*Author:*
**Koolen, Lucas A E**

*Title:*
**Effects of Serotonin 1A Receptor Transmission on Neural Control of Respiration**

# Effects of Serotonin 1A Receptor Transmission on Neural Control of Respiration

Lucas André Elies Koolen

Student ID number: P1562742

A dissertation submitted to the University of Bristol in accordance with the requirements for award of the degree of PhD in the Faculty of Life Sciences (Physiology, Pharmacology, and Neuroscience), March 2021

word count: 64.248

# ABSTRACT

Agonists of inhibitory serotonin 1A receptors (5-$HT_{1A}$R) may have therapeutic potential for their ability to enhance and stabilize respiration These effects are suggested to be mediated by inhibition of inhibitory interneurons of the respiratory control network. However, precise effects of selective 5-$HT_{1A}$R agonism on this network are poorly understood. The main aim of the thesis was to establish the effects of systemic 5-$HT_{1A}$R transmission on respiratory motor drives, during rest and homeostatic respiratory reflexes, as generated by the intact respiratory control network in rats.

Systemic administration of selective 5-$HT_{1A}$R agonist NLX-101 in rats *in situ* resulted in: enhanced respiratory rate due to shortening of the expiratory phase; promoted late-expiratory abdominal activity; and enhanced respiratory patterns in phrenic and abdominal, but not hypoglossal and vagal nerve motor outputs. Homeostatic respiratory reflex responses were not altered by systemic NLX-101. Fluorescent *in* situ hybridization indicated that 5-$HT_{1A}$R RNA is present in SLC32A1-positive (i.e. glycinergic and/or GABAergic) neurones and SLC32A1-negative neurones, broadly distributed across key regions of the respiratory control network. Extracellular recordings of functionally identified respiratory neurones in the ventral respiratory column, combined with juxta-cellular pico-ejection of NLX-101, indicated that 5-$HT_{1A}$ R expressing neurones are also broadly distributed across functional subpopulations of respiratory neurones.

The broad expression of 5-$HT_{1A}$R across anatomical regions and functional subpopulations of respiratory neurones indicates that the observed enhanced respiratory drive after systemic 5-$HT_{1A}$ transmission is likely an emergent network effect mediated by action at multiple neurone populations and mechanisms throughout the respiratory network. Based on the signature of functional effects of systemic NLX-101, I propose several candidate contributing mechanisms.

The thesis contributes to establishing the role of 5-$HT_{1A}$R in respiratory control, and ultimately, the therapeutic potential of 5-$HT_{1A}$R transmission in the reversal of opioid induced respiratory depression and the treatment of respiratory control disorders such as Rett syndrome.

## AUTHOR'S DECLARATION

I declare that the work in this dissertation was carried out in accordance with the requirements of the University's Regulations and Code of Practice for Research Degree Programmes and that it has not been submitted for any other academic award. Except where indicated by specific reference in the text, the work is the candidate's own work. Work done in collaboration with, or with the assistance of, others, is indicated as such. Any views expressed in the dissertation are those of the author.

SIGNED: ..... DATE: …….

.

## DEDICATION

This work, and all good that may come from it, is dedicated to my wife Fenfang and our son Lei. I cannot stress enough how much I appreciate the love, support, and inspiration you give me.

## ACKNOWLEDGEMENTS

Firstly, I am extremely grateful to my supervisor, Dr. Ana Abdala for her advice, continuous support, and patience during my PhD study. Dr. Abdala has been very generous with her time, support, and expert advice. She has taught me skills and a mindset that I will continue to use in my working life. I am also grateful to Prof. Julian Paton, who has advised me as a supervisor in the earlier stages of my PhD, and to Prof. Sergey Kasparov, who has kindly taken over this role after Prof. Paton left the University of Bristol. I would like to thank Dr. Daniel Zoccal at São Paulo State University, and Dr Yaroslav Molkov and Dr. William Barnett at Georgia State University, for their feedback and advice in discussing presentations, experiments, and research ideas throughout this PhD. Thank you, Ian Charles, for your support and good company during the day-to-day activities in the lab. And a special thanks to my parents Truus and Theo, and my aunt Mia, who were so generous to provide not only moral support, but also financial support in the final year of this PhD. Above all, however, I would like to thank my wife Fenfang. The past years have been very challenging. Fenfang likes to joke that without her, and without the arrival of our baby boy, I would have finished this thesis at least a year earlier. The contrary is far more likely. Without her love, support, and encouragement, I am not so sure if I'd have been able to see this through in the first place.

# TABLE OF CONTENTS

# LIST OF FIGURES

# LIST OF TABLES

# LIST OF ABBREVIATIONS

**abbreviation : explanation** **page for context**

# Chapter 1: General Introduction

## 1.1 General overview

Oxygen and carbon dioxide homeostasis are essential to life for two reasons. First, every cell in your body requires $O_2$ for the formation of adenosine triphosphate through aerobic metabolism. Second, the $CO_2$ produced in this process promotes hypercapnic acidosis. Acidosis, too, influences cellular functions throughout the body, and only a limited pH range is compatible with life. Respiration, along with blood circulation, is one of two principle processes though which $O_2$ enters, and $CO_2$ exits the bloodstream, and blood gas homeostasis is maintained (Davies and Moores, 2010).

Central control of respiration involves a semi-autonomous neural network in the brainstem known as a central pattern generator (CPG). The generation of respiratory rhythm in this network involves dynamic modulation from other brainstem regions in the medulla and pons, and from central and peripheral chemo-, and mechanoreceptor afferents in order to continuously adapt respiratory activity to changing metabolism and maintain blood-gas-, and acid-base homeostasis. Optimal homeostasis requires dynamic pulmonary gas exchange, with matched control of blood perfusion. Therefore, not surprisingly, respiratory control is coupled to sympathetic cardiovascular control. The various neural network interactions involved in sympathetic and respiratory control are modulated by a variety of neurotransmitters. Serotonergic transmission has been of interest for its apparent role in respiratory control in health and disease. This thesis concerns the role serotonin 1A receptor (5-$HT_{1A}$R) transmission in eupnoeic (healthy, resting state) respiratory control and chemoreceptor-mediated respiratory and sympathetic reflexes from a systems neuroscience perspective.

The present 'General Introduction' addresses the current understanding of the brainstem network interactions underlying respiratory and sympathetic control which are relevant to the aims of this thesis. Section 1.2 describes the phases of the respiratory cycle as categorised by neural and motor activity patterns, and it discusses the core CPG neural network interactions thought to underlie these patterns. Subsequent sections describe modulation of respiratory CPG activity through mechanisms that affect respiratory phase transitioning (section 1.3), and through feedback from central chemoreceptors (section 1.4) and peripheral chemoreceptors (section 1.5). Section 1.6 describes neural

mechanisms by which respiratory control is coupled to sympathetic control. Modulation of respiratory activity by serotonergic transmission, specifically by 5-$HT_{1A}$R transmission, is addressed in section 1.7. Section 1.8 addresses therapeutic potential of 5-$HT_{1A}$ transmission in the treatment of respiratory control disorders. Ultimately, thesis aims and hypotheses are outlined in section 1.9.

## 1.2 GENERATION OF THE RESPIRATORY RHYTHM

### *1.2.1 Phases of the respiratory cycle, cognate peripheral nerve outputs, and their physiological significance*

*The eupnoeic respiratory cycle consists of three phases.*

Eupnoea, or normal restful breathing is typically described as a cyclic sequence that can be divided into three phases: inspiration (I); post-inspiration (Post-I), which is the first stage of expiration; and a second expiratory phase (E2). Each of these phases is marked by distinct activity patterns of respiratory control centres in the brainstem, and of cranial and spinal nerves (Smith et al., 2013, Dhingra et al., 2020).

*Motor patterns of the respiratory cycle and their physiological significance.*

Cranial and spinal nerves drive activity of two functionally distinct groups of muscles: those controlling thoracic pressure and those controlling upper airway resistance. An overview of motor and sympathetic nerve activity patterns over the course of the various phases of the respiratory cycle is presented in **figure 1-1A**. During eupnoea in mammals, the main pump muscle activated with every single inspiration is the diaphragm, which is innervated by the phrenic nerve (PN). Activity in the PN can be recorded as an appropriate surrogate for the determination of the neural phase of inspiration (Dutschmann et al., 2014b). Upper airway resistance is largely determined by laryngeal adductor and abductor muscles, and by the genioglossus muscle. The former two are innervated by the recurrent laryngeal nerve (RLN), which is a branch of the cervical vagus nerve (cVN). The genioglossus muscle is innervated by the hypoglossal nerve (HN). An increase in HN activity immediately prior to, and during, inspiration results in a stabilization of the airway, thereby preventing its collapse under negative inspiratory pressure (Bailey, 2011). In eupnoeic breathing, expiratory airflow is driven by release of the potential energy stored in the contracted diaphragm as it returns to its former position, as well as by recoil of the expanded lung tissue and chest wall. Post-I is an early expiratory phase that spans the transition between inspiration and E2 phases. During post-I phase, laryngeal adductor

muscles contract to counteract passive expiratory airflow and thereby control its pattern and duration. This activity slows the release of air during early stages of expiration and controls time for gas exchange in the lungs. Post-I activity is usually determined from recordings of the cervical vagal nerve (cVN) or the recurrent laryngeal nerve (Dutschmann et al., 2014b). During post-I, low amplitude discharge is also observed in the lower branches of thoraco-abdominal nerves (T13-L1, hencerforth referred to as AbN), including the iliohypogastric, which innervate the transverse abdominal muscles (Abdala et al., 2009). The second stage of expiration (E2) is largely a passive process at rest. However, in conditions of high metabolic demand, e.g. during exercise, abdominal expiratory contraction emerges during the E2 phase, in association with reduced upper airway resistance and increased sympathetic outflow (Abdala et al., 2009, de Britto and Moraes, 2017, Molkov et al., 2011). This activity, referred to as late expiration (Late-E), decreases lung volume below functional residual capacity so that the inspiratory volume of the subsequent breathing cycle can be increased (Abdala et al., 2009). Late-E motor activity, like abdominal post-I activity, can be recorded from the lower branches of thoraco-abdominal nerves (T13-L1). Late-E sympathetic activity can be recorded at nerves of the thoracic sympathetic trunk (tSN).

Respiratory neurones are named based on their discharge patterns relative to the respiratory cycle

Extracellular and single cell recordings reveal that the above respiratory phases and motor outputs are reflected in rhythmic activity patterns of distinct functional subpopulations of respiratory neurones in the brainstem (Segers et al., 2008, Alheid and McCrimmon, 2008, Smith et al., 2007, Schwarzacher et al., 1991, Ezure, 1990). These respiratory subpopulations are typically named based on the respiratory phase during which they display peak activity, as well as the patterning of their discharge (e.g. incrementing or decrementing). The following functional subpopulations can be identified among neurones involved in respiratory control: pre-inspiratory and inspiratory (pre-I/I) phase spanning neurones, whose discharge starts shortly prior to inspiration and proceeds into early phases of inspiration; early-inspiratory (Early-I) neurones; incrementing, or ramping inspiratory (Ramp-I) neurones; post-inspiratory (Post-I) neurones, which have a decrementing discharge pattern that spans the Post-I phase only; decrementing expiratory (Dec-E) neurones, which are similar to Post-I neurones but their discharge spans the Post-I and E2 phases; incrementing, or augmenting expiratory (Aug-E) neurones, which show peak activity during E2; and late-expiratory (late-E) neurones. A

schematic representation of burst patterns of respiratory subpopulations relative to phases of the respiratory cycle is provided in **Figure 1-1B**. It should be noted that whether Post-I neurones (Richter, 1982) and Dec-E neurones (Manabe and Ezure, 1988) are indeed distinct populations is not clear, and the two populations are often pooled under the term 'Post-I neurones' in the respiratory literature. In the same vein, although categorization by discharge pattern can facilitate intuitive understanding of neural network dynamics, it is important to always be aware that 'populations' of a shared functional phenotype should not be presumed homogenous. Neurones with a common discharge pattern can differ in properties such as receptor expression, neurotransmitter release, and efferent connectivity.

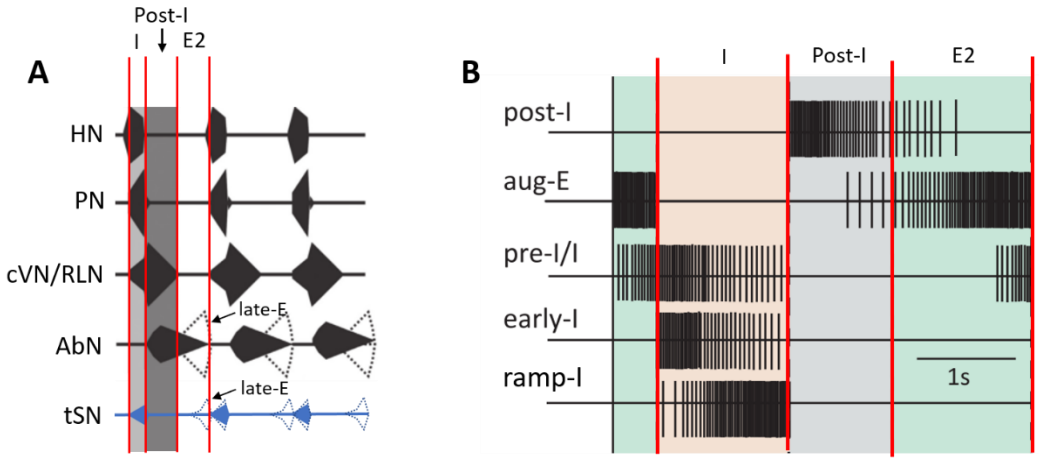


**Figure 1-1:** Eupnoeic respiratory and sympatho-respiratory activity patterns in peripheral nerves and in respiratory neurone populations.
**(A)** Schematic representation of the eupnoeic respiratory and sympatho-respiratory pattern and rhythm as recorded from cranial and spinal motor nerves and the thoracic sympathetic trunk. Dotted lines represent late-E activity, which is absent in eupnoeic respiration, but emerges in conditions of high respiratory drive (adapted from Dutschmann and Dick (2012)) **(B)** Schematic representation of discharge patterns relative to the respiratory cycle of various functional subtypes of respiratory neurones (adapted from Smith et al. (2013)). See text in section 1.2.1.for further detail. Abbreviations: HN = hypoglossal nerve; PN = phrenic nerve; cVN = cervical vagus nerve; RLN = recurrent laryngeal nerve; AbN = abdominal nerve; tSN = thoracic sympathetic nerve; Post-I = post-inspiratory neurones (or phase); Aug-E = augmenting expiratory neurones; Pre-I/I = pre-inspiratory/inspiratory phase spanning neurones; Early-I = early inspiratory neurones; Ramp-I = ramping inspiratory neurones.

### *1.2.2 Principle mechanisms of rhythm generating neural networks*

The respiratory motor outputs associated with each respiratory phase are generated by a central pattern generator (CPG). CPG's are neural networks that generate a behaviourally relevant rhythmic pattern of activity, even when isolated from all other central and peripheral rhythmic inputs (Bucher et al., 2015). CPGs exist for most, if not all, rhythmic motor behaviors in invertebrates and vertebrates (e.g. walking, flying, swimming, feeding behaviours, enteric rhythms, respiration) (Bucher et al., 2015, Marder and Bucher, 2001). Despite the diversity of animals and behaviours in which CPGs are involved, it appears CPG networks commonly adhere to either or both of two principal mechanisms for rhythm generation. Firstly, many CPGs rely on so called 'pacemaker neurones' to drive autorhythmic activity. Such pacemaker neurones have intrinsic properties by which they produce oscillations of the membrane potential that usually result in action potentials. Often, such pacemaker neurones are co-active with non-pacemaker neurones through excitatory synapses or gap junctions, giving rise to so called 'pacemaker groups' (Bucher et al., 2015). A second common mechanism is that rhythmicity can emerge from synaptic interactions of neurones that do not necessarily show oscillatory properties in isolation. Such emergent network rhythmicity is often a function of reciprocal synaptic inhibition between neurones, combined with post-inhibitory rebound properties of CPG neurones and/or excitatory drives, which results in alternating bouts of activity and suppression (Bucher et al., 2015). Over a century ago, Brown (1911) suggested that the alternate flexion and extension of leg muscles in walking could be produced by rhythmic central circuits in which the antagonistic muscles were driven by neurones that inhibited each other. This concept was later developed into the notion of 'inhibitory half-centre oscillators', i.e. two or more neurones, or synchronized neurone populations, that make reciprocally inhibitory synaptic connections and produce out-of-phase rhythmic oscillations. Both pacemaker driven CPGs and inhibitory half-centre oscillators are capable of generating rhythmic activity independently, but it is important to note that the two mechanisms are not mutually exclusive, and both can contribute to rhythm generation in a CPG network.

### *1.2.3 The respiratory central pattern generator (CPG)*

The mechanistic underpinnings of rhythm generation in the respiratory CPG is a topic of ongoing debate. Most current evidence suggests that rhythmic activity in the respiratory CPG is likely shaped by a combination of both pacemaker neurones, as well as emergent network properties.

Auto-rhythmic populations in the respiratory CPG

The core circuitry of the mammalian respiratory CPG is located in a bilateral ventral respiratory column (VRC) in the ventrolateral medulla. The VRC is a collection of brainstem nuclei involved in respiratory control organized in a rostral-to-caudal orientation (see **figure 1-2A**). Expiratory populations involved in rhythm generation are concentrated in rostral regions of the VRC: the parafacial respiratory group (pFRG, contains late-E neurones) (Abdala et al., 2009, Moraes et al., 2013, Silva et al., 2016, Pagliardini et al., 2011); the post-inspiratory complex (PiCo, contains Post-I neurones) (Anderson et al., 2016); and the Bötzinger Complex (BötC, contains Post-I and Aug-E neurones) (Alheid and McCrimmon, 2008, Segers et al., 2008, Tian et al., 1999, Ezure et al., 1988). Inspiratory rhythmogenic VRC populations (Pre-I/I and Early-I) are concentrated in the pre-Bötzinger complex (pre-BötC) (Smith et al., 1991, Guyenet and Wang, 2001, Sun et al., 1998, Alheid and McCrimmon, 2008, Ezure et al., 1988). Most caudally, the rostral-, and caudal ventral respiratory group (RVRG and CVRG) contain transmission circuitry which relays inputs from rhythmogenic populations to various (pre-)motor neurones (Ezure et al., 1988, Alheid and McCrimmon, 2008). In rats and mice, three of the above VRC regions – the pFRG, the PiCo, and the pre-BötC – are reported to contain neurone populations with autonomous rhythm generating properties. The pFRG contains auto-rhythmic glutamatergic neurones that are thought to be suppressed during eupnoeic breathing, but that generate rhythmic activity in conjunction with AbN late-E activity under specific conditions (e.g. conditions of high respiratory drive (Pagliardini et al., 2011, Abdala et al., 2009, Huckstepp et al., 2015). The PiCo is a region with auto-rhythmic glutamatergic-cholinergic neurones that fire in phase with Post-I motor output (Anderson et al., 2016). Lastly, the pre-BötC contains auto-rhythmic glutamatergic neurones derived from developing brain homeobox protein 1 (Dbx1) expressing progenitor cells that are essential for inspiratory rhythm generation (Smith et al., 1991, Gray et al., 2010).

By far the most research on putative mechanisms underlying autorhythmic populations in the respiratory CPG has focused on the pre-BötC. Nonetheless, the mechanisms underlying auto-rhythmic inspiratory activity in the pre-BötC remains subject of debate (Del Negro et al., 2018, Ramirez and Baertsch, 2018b, Phillips et al., 2019) Pacemaker theories (Del Negro et al., 2010, Toporikova and Butera, 2011, Phillips et al., 2019) assume that persistent sodium currents ($I_{NaP}$) and calcium activated nonselective cation currents ($I_{CAN}$), drive slow-wave oscillations of the membrane potential of excitatory pacemaker neurones in the pre-BötC, resulting in their endogenous rhythmic bursting. These

pacemaker neurones, combined with recruitment of additional excitatory neurones, are believed to form a pacemaker group with a pre-I/I discharge pattern that provides the principal auto-rhythmic excitatory drive for inspiratory rhythm generation. Alternatively, the 'burstlet theory' (Kam et al., 2013a, Feldman and Kam, 2015) posits that burst associated conductances are important for robust inspiratory activity, but that Pre-I/I bursts are not themselves auto-rhythmic. Rather, the principle auto-rhythmic mechanism underlying inspiration is reflected in low frequency Pre-I burstlets observed through field potential recordings of the pre-BötC in rhythmic brain slice preparations of mice and in rats *in vivo*, which may or may not develop into higher frequency pre-I/I bursts that propagate to other regions in the CPG (Kam et al., 2013a, Kam et al., 2013b). The mechanisms underlying burstlet generation, as well as those underlying development of burstlets into bursts remain to be determined. It has been suggested that burstlets are generated by synchronization of convergent subsets of excitatory neurones through emergent network properties in the pre-BötC microcircuitry (Kam et al., 2013b, Feldman and Kam, 2015). Development of burstlets into bursts is suggested to be a threshold process involving $I_{NaP}$ and $I_{CAN}$ and the recruitment of additional neurones (Feldman and Kam, 2015, Del Negro et al., 2018). Thus, burstlet theory posits that pre-I burstlets and bursts are separable components. Inspiratory bursts are triggered by burstlets, and only the latter is a true auto-rhtyhmic activity.

Current theories on the coordination of multiphasic respiratory activity

Despite being important rhythmogenic microcircuits, neither the pFRG, the PiCo, nor the pre-BötC can generate multiphasic respiratory activity in isolation. To generate multiphasic respiratory activity, the respiratory CPG must coordinate rhythmic alternation of the respiratory phases and activities (I, Post-I, E2 or late-E) within each respiratory cycle. The two prevailing theories on the coordination of multiphasic respiratory activity are the inhibitory ring model (Rybak et al., 2004, Rybak et al., 2007, Smith et al., 2007, Smith et al., 2009, Smith et al., 2013), and the triple oscillator theory (Anderson et al., 2016, Anderson and Ramirez, 2017, Ramirez and Baertsch, 2018a).

The inhibitory ring model posits that the coordination of alternating inspiratory and expiratory activities in eupnoeic breathing is mediated by antagonistic interactions between specific functional subpopulations of respiratory neurones in the fashion of an inhibitory half-centre oscillator. This model hypothesises that the minimal network architecture of the VRC rhythmogenic circuitry can be described as an auto-rhythmic Pre-I/I population of glutamatergic neurones observed in the pre-BötC (Gray et al., 2010,

Bouvier et al., 2010), which is interconnected to three GABA-ergic and glycinergic respiratory subpopulations that form a ring of mutually inhibiting neurones comprising Post-I and Aug-E neurones in the BötC (Alheid and McCrimmon, 2008, Burke et al., 2010, Smith et al., 2007), and Early-I neurones in the pre-BötC (Winter et al., 2009, Morgado-Valle et al., 2010, Kuwana et al., 2006, Koizumi et al., 2013) (see **Figure 1.2B**). The three phases of eupnoeic respiration (I, Post-I, E2) are marked by predominant activity of either of the three neurone populations in the inhibitory ring (Early-I, Post-I, and Aug-E, respectively). Inhibitory neurones of the BötC and pre-BötC (notably Post-I and Early-I neurones) are suggested to also contribute to the suppression of the pFRG auto-rhythmic late-E activity during eupnoeic breathing (Barnett et al., 2018, Flor et al., 2020) (via mechanisms discussed in section 1.4.4). Onset of inspiration is suggested to be mediated, in part, by the interplay between glutamatergic (auto-rhythmic and other) populations in the pre-BötC and inhibitory drive to the pre-BötC from expiratory populations in the BötC (Smith et al., 2013, Marchenko et al., 2016) . Rhythmic excitatory drive from the pontine parabrachial complex to Post-I neurones in the VRC is suggested to play an important role in inspiratory to expiratory phase transitioning (Dutschmann and Dick, 2012, Molkov et al., 2013) (via mechanisms discussed in section 1.3).

Multi-level computational simulations of the inhibitory ring model are able to generate rhythmic activity patterns at the level of individual neurones and at the network level (motor outputs) that are consistent with experimentally observed eupnoeic respiratory activity patterns (Smith et al., 2007), respiratory reflex responses (Barnett et al., 2017, Molkov et al., 2013), and responses to various experimental manipulations of the CPG (Shevtsova et al., 2011, Shevtsova et al., 2014, Richter and Smith, 2014, Smith et al., 2007, Dhingra et al., 2019) in rats and mice *in vivo*, and in *in situ* working heart-brainstem preparations (WHBP) of mice and rat. *In* situ WHBP are decerebrated, $pO_2$ and $pCO_2$ clamped preparations of rats and mice on cardio-pulmonary bypass which allow simultaneous recordings of brainstem neurones and of multiple cranial and spinal nerve outputs generated by the intact, unanaesthetised respiratory CPG (Paton, 1996b). The model's assumptions on how distinct populations in various pontine and medullary anatomical regions contribute to the coordination of respiratory phases is also consistent with the spatio-temporal activity pattern observed in field potential recordings with multi-electrode arrays spanning the entire respiratory CPG network in *in situ* WHBP (Dhingra et al., 2020). Experiments to test the role of inhibition in the VRC as postulated in the inhibitory ring model have predominantly employed pharmacological and optogenetic

manipulations of glycinergic and/or GABAergic transmission, or activity of glycinergic and/or GABAergic neurones in either the BötC or the pre-BötC in rats and mice *in vivo* or in *in situ* WHBP. Generally, the hypothesis in such experiments is that inhibitory transmission in the pre-BötC and/or activity of inhibitory neurones in the BötC each promote expiratory (Post-I and E2) activity and supress inspiratory activity. Conversely, inhibitory transmission in the BötC, and activity of inhibitory neurones in the pre-BötC are hypothesised to promote inspiratory activity and suppress expiratory activity. Multiple such pharmacological (Bongianni et al., 2010, Pierrefiche et al., 1998, Marchenko et al., 2016) and optogenetic (Ausborn et al., 2018, Sherman et al., 2015, Alsahafi et al., 2015) studies report findings in rats, mice, cats, and rabbits *in vivo* and *in situ t*hat are consistent with the above hypothesis. Nonetheless, the role of inhibitory transmission in the coordination of respiratory phases is disputed. Marchenko et al. (2016) and Janczewski et al. (2013) performed identical manipulations of pharmacological excitation, inhibition, and blockade of inhibition in either the BötC or the pre-BötC in anesthetised rats *in vivo* in which peripheral feedback to the respiratory CPG was removed through vagotomisation. Whereas findings of the former study are consistent with the general hypothesis described above, Janczewski et al. (2013) report that disruption of inhibitory transmission has no significant effect on respiratory rhythm generation in the absence of peripheral feedback. This discrepancy is not readily resolved and remains to be further explored in future studies. Perhaps the greatest obstacle in the verification of the inhibitory ring model, however, is that the hypothesised connectivity of functional subpopulations in the VRC remains to be mapped experimentally. This is partly because the relevant functional subpopulations are, as yet, not exclusively associated with specific biochemical markers that can be utilized in connectivity studies.

An alternative model of the respiratory CPG, although with a similar principal network structure, is the triple oscillator theory. The triple oscillator theory (Anderson and Ramirez, 2017) was proposed in response to the recent discovery of auto-rhtyhmic excitatory Post-I neurones in the PiCo (Anderson et al., 2016). This theory assumes that the three autorhythmic populations in the respiratory CPG – the pre-BötC, the PiCo, and the pFRG - each provide excitatory drive for I, Post-I and late-E activity, respectively. Similar to the inhibitory ring model, each of these respiratory phases and activities are marked by dominance of its cognate rhythmogenic populations, which is suggested to be coordinated through reciprocal inhibitory connections between the three oscillators (see **figure 1-2C**). In conditions of eupnoeic respiratory drive, activity of the pFRG remains

suppressed by inhibition from both inspiratory and Post-I neurone populations. Optogenetic activation of cholinergic (ChAT-positive) PiCo neurones delays the onset of the subsequent inspiratory burst *in vivo* in mice (Anderson et al., 2016). Conversely, in *in vitro* horizontal slice preparations that encompass the VRC of mice, inspiratory Dbx1-positive pre-BötC neurones simultaneously inhibit and excite PiCo neurones via GABAergic and glutamatergic transmission, with inhibitory drive being dominant (Anderson et al., 2016). These findings are consistent with the theory's hypothesis that temporal coordination of inspiratory and expiratory activity is mediated by mutually inhibitory interactions between PiCo and pre-BötC populations. The mutually inhibitory interactions between PiCo and the pFRG, as proposed in the triple oscillator theory, remain to be experimentally verified.

The triple oscillator theory and the inhibitory ring model both emphasise the role of reciprocal inhibitory connections between inspiratory and expiratory populations in the coordination of multiphasic respiratory activity. Despite their shared features, there are also notable contrasts between the inhibitory ring model and the triple oscillator theory. A key difference is that the triple oscillator theory emphasizes the role of auto-rhythmic PiCo neurones as an independent source of excitatory drive for Post-I activity. In contrast, current iterations of the inhibitory ring model do not incorporate the PiCo, but emphasize the role of ponto-medullary interactions as a source of excitatory drive to BötC Post-I neurones. Furthermore, the triple oscillator theory does not account for the E2 respiratory phase or its neurophysiological correlates (Aug-E neurone activity). Nonetheless, the two theories are theoretically reconcilable. The existence of auto-rhythmic excitatory Post-I neurones is not principally incompatible with the inhibitory ring model. PiCo neurones could hypothetically contribute to inspiratory-to-expiratory phase transitioning through excitatory drive to inhibitory BötC post-I interneurones, directly or via pontine circuitry. Likewise, the network structure of the triple oscillator theory does not preclude implementation of mutually inhibitory interactions between Post-I and Aug-E neurones that could account for the experimentally observed antagonistic activity patterns of these respiratory subpopulations (Tian et al., 1999). Further exploring the role of the PiCo in respiratory control will be important in determining the mechanisms underlying coordination of multiphase respiratory activity, and in exploring if the inhibitory ring model and the triple oscillator theory can be integrated.

To conclude, the mechanisms underlying respiratory rhythmogenesis are a topic of ongoing debate. Primary components of respiratory rhythms likely originate from an

interplay of glutamatergic autorhythmic populations and emergent network properties. Phasic synaptic inhibition appears to be critically involved in coordinating these drives and shaping the three-phase pattern of respiratory activity during normal breathing by controlling which populations are active and inactive during each phase.

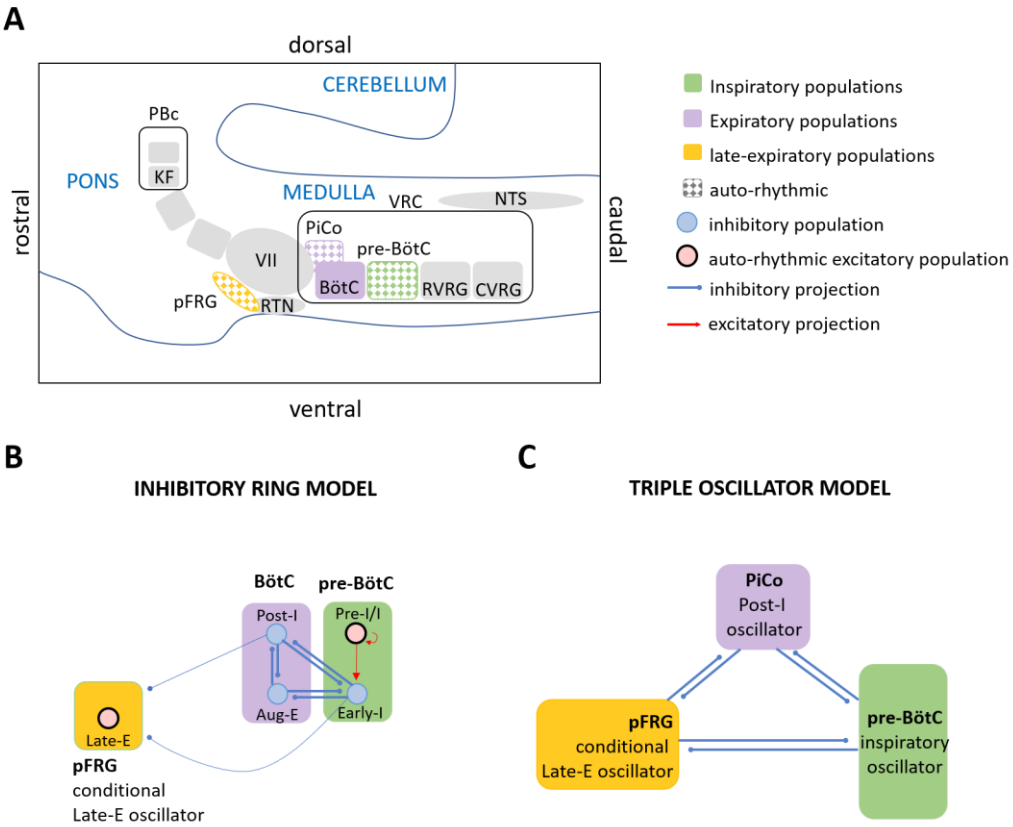


**Figure 1-2:** key brainstem regions of the respiratory CGP, and principle respiratory CPG network architecture according to the inhibitory ring model and the triple oscillator theory.

Schematic representations of: **(A)** key neuroanatomical regions of the respiratory CPG; **(B)** principal network interactions involved in the coordination multiphase respiratory activity according to the inhibitory ring model; or **(C)** according to the triple oscillator theory. See text in section 1.2.3 for a description of the anatomy and postulated network interactions. Abbreviations: PBc = parabrachial complex; KF = Kölliker-Fuse nucleus; pFRG = parafacial respiratory group; RTN = retrotrapezoid nucleus; VII = facial nucleus; PiCo = post-inspiratory complex; BötC = Bötzinger Complex; pre-BötC = pre-Bötzinger complex; RVRG = rostral ventral respiratory group; CVRG = caudal ventral respiratory complex; VRC = ventral respiratory column; NTS = nucleus tractus solitarius; Post-I = post-Inspiratory neurons; Pre-I/I = pre-inspiratory/inspiratory phase spanning neurones; Early-I = early-inspiratory neurons; Aug-E =augmenting expiratory neurons; late-E = late-expiratory neurones.

## 1.3 CONTROL OF RESPIRATORY PHASE TRANSITION

The respiratory rhythm continuously adapts to changes in environment (informed by sensory input from e.g. chemoreceptors, mechanoreceptors, and nociceptors) and behaviour (e.g. mastication, swallowing, vocalization, coughing, sneezing, and diving reflex). One mechanism by which such adaptation occurs is through control of respiratory phase transitioning. The importance of mechanisms of phase transitioning is clearly illustrated in the case of Rett syndrome, a neurological disorder in which disruptions of phase transitioning mechanisms can promote potentially lethal forms of respiratory dysrhythmia (Abdala et al., 2014a, Ramirez et al., 2013) (discussed further in section 1.8.2). The current section describes the Herring-Breuer reflex and interactions between the VRC and regions in the pontine parabrachial complex. These are two mechanisms which provide input to the core rhythmogenic circuitry in the VRC and act complementary to mediate the inspiratory-to-expiratory phase transition, and the duration of inspiratory-, and expiratory phases.

### *1.3.1 The Hering-Breuer Reflex*

The Hering-Breuer reflex (HBR) is a lung inflation induced activation of pulmonary stretch (mechano-) receptors (PSR) that elicits termination of inspiration, facilitation of the post-inspiratory respiratory phase, and prolongation of expiration (Clark and von Euler, 1972, Luck, 1970, Kubin et al., 2006). Simply put, the HBR acts to prevent over-inflation of the lungs. In rats, cats, and dogs PSR axons travel via the cVN to form excitatory synapses with excitatory and inhibitory pump cells in the nucleus tractus solitarius (NTS), which then relay PSR feedback to respiratory regions in the VRC and the pontine parabrachial complex. Experimental studies (reviewed in (Kubin et al., 2006, Dutschmann and Dick, 2012)) and computational simulations based on the inhibitory ring model (Molkov et al., 2013), suggest that PSR feedback promotes inspiratory-to-expiratory phase transition through NTS pump cell mediated excitation of Post-I neurones in the BötC, and inhibition of Early-I neurones in the pre-BötC.

### *1.3.2 Pontine control of phase transition*

The pontine parabrachial complex (PBc) contains respiratory neurones that have been implicated in shaping the eupnoeic respiratory pattern and rhythm through the promotion of inspiratory-to-expiratory phase transition, much like the HBR. In *in* situ WHBP of rats, despite the lack of HBR feedback due to removal of the lungs and of vagal afferent inputs, a normal three-phase pattern of respiratory activity can be observed in

electrophysiological recordings of respiratory neurones and the cranial and spinal nerves relevant for respiratory motor activity. Neurones of the PBc were reported to demonstrate phase modulation of their firing patterns, and a substantial amount of these neurones showed activity patterns centred around inspiratory-to-expiratory phase transitions (Dhingra et al., 2020, Alheid et al., 2004). Further, transection of the PBc, which constitutes removal of pontine input to the medullary rhythmogenic circuitry, results in apneustic breathing in vagotomised *in situ* WHBP of neonatal (Dutschmann et al., 2000) or juvenile (Smith et al., 2007) rats.

The PBc is a term used to describe the collective parabrachial nuclei (medial parabrachial nucleus; internal-, central-, and external parts of the lateral parabrachial nucleus) and the Kölliker-Fuse (KF) nucleus in the dorsolateral pons. The KF, in particular, plays an essential role in the suppression of inspiration and providing drive for Post-I activity. Pharmacological excitation or disinhibition of neurones in the KF parenchyma in the absence of pulmonary feedback, promotes tonic excitation of post-I activity in the cVN and/or the RLN, promotes premature termination of inspiration and inspiratory-to-expiratory phase transitioning, and prolongs expiratory phase duration (Abdala et al., 2016, Dutschmann and Herbert, 2006, Bonis et al., 2013, Barnett et al., 2018). Pharmacological inhibition of the KF in the absence of pulmonary feedback, on the other hand, prolongs inspiration and eliminates the post-I component of cVN activity (Dutschmann and Herbert, 2006, Levitt et al., 2015, Jenkin et al., 2017). Tract tracing studies show that neurones in the KF and select nearby parabrachial nuclei (medial parabrachial nucleus, external part of the lateral parabrachial nucleus, and internal part of the lateral parabrachial nucleus) collectively are reciprocally connected to a multitude of respiratory areas such as the rhythmogenic areas in the VRC (BötC, pre-BötC, rVRG, and cVRG), and the NTS (Dutschmann and Dick, 2012, Ezure and Tanaka, 2006, Song et al., 2015). Projections from the KF, specifically, to rhythmogenic VRC regions are thought to be mainly excitatory (Ezure and Tanaka, 2006, Geerling et al., 2017, Rosin et al., 2006). Based on the anatomy and functional interactions as described above, computational models based on the inhibitory ring model suggested that inputs from the PBc, and notably the KF, shape respiratory phase durations and inspiratory-to-expiratory phase transitioning through the activation of post-I and Aug-E neurones in the BötC, and inhibition of Early-I neurones in the pre-BötC (Molkov et al., 2013) (see **figure 1-3**). This was later supported by cross-correlational analysis of timing specific and response specific discharge patterns in response to electrical stimulation and/or pharmacological inhibition

performed among pairs of KF and BötC neuronal pools. The experiments confirmed an excitatory functional connection between neurones in the KF with an early expiratory (Early-E) discharge pattern that project to glycinergic Post-I neurones in the BötC (Song et al., 2015).

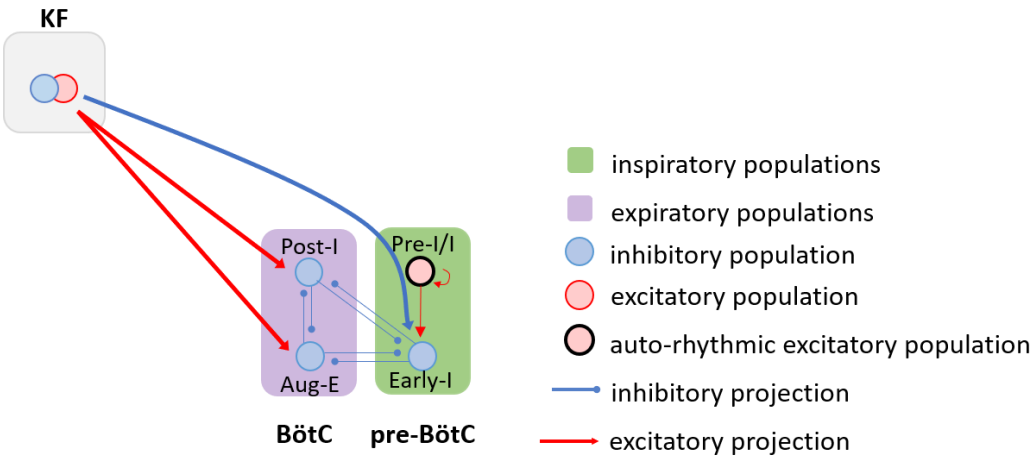


**Figure 1-3:** Ponto-medullary interactions that mediate inspiratory-to-expiratory phase transitioning.

Schematic representation projections from the KF to regions in the medullary VRC that mediate inspiratory-to-expiratory phase transitioning as suggested in a computational simulation based on the inhibitory ring model (Molkov et al., 2013). The schematics do not show the complete model but highlight selected elements of it for the sake of visual clarity. See text of section 1.3.2 for further details. Abbreviations: KF = Kölliker-Fuse; BötC = Bötzinger Complex, Pre-BötC = pre-Bötzinger Complex, Pre-I/I = pre-inspiratory/inspiratory phase spanning neurones; Early-I = early inspiratory neurones; Aug-E = augmenting expiratory neurones; Post-I = post-inspiratory neurones.

### *1.3.3 Interactions between peripheral feedback and PBc control*

Both peripheral and pontine controls described above appear to mediate the duration of respiratory phases and inspiratory-to-expiratory phase transitions via the same mechanisms: excitation of Post-I neurones in the BötC, and inhibition of Early-I neurones in the pre-BötC. The two mechanisms appear to interact. This notion is supported by the finding that activity of respiratory phase spanning neurones in the PBc is found to be increased in vagotomized animals or preparations (Feldman and Gautier, 1976, Dick et al., 2008). Further, tract tracing studies that show the NTS and the parabrachial complex are reciprocally connected (reviewed in (Dutschmann and Dick, 2012)), and that GABAergic neurones of NTS are in contact with KF neurones projecting to the VRC in rats (Yokota et al., 2008). Computational simulations suggest that respiratory-modulated activity in the PBc may be suppressed by inhibitory pump cells in the NTS projecting to the pons (Molkov et al., 2013).

Suppression of the ponto-medullary control loop by NTS pump cells suggests that the HBR may be the dominant mechanism to mediate respiratory phase transitions. However, experiments with vagal stimulation in *in situ* WHBP of rats across different stages of postnatal development show that, while neonates exhibit HBR stimulus-dependent prolongation of expiration, significant habituation occurs following repetitive vagal stimulation in preparations of juvenile rats (PND >16) (Dutschmann et al., 2014a, Dutschmann et al., 2009a). In light of this, it has been suggested that the HBR habituates during early development and that control of inspiratory-to-expiratory phase transitioning shifts from the HBR to ponto-medullary mechanisms during postnatal development (Dutschmann et al., 2014a, Dutschmann et al., 2009a).

.

## 1.4 CENTRAL CHEMORECEPTOR FEEDBACK MECHANISMS IN RESPIRATORY CONTROL

Respiratory pattern and rhythm generation is to a large extent controlled by feedback mechanisms in which chemoreceptor cells relay information regarding levels of $O_2$, $CO_2$ and pH to brainstem regions of respiratory control. There are central and peripheral components to ventilatory chemoreflexes. The current section addresses the former and section 1.5, the latter.

The respiratory central chemoreflex is defined as the process by which $CO_2$, or hypercapnic acidification, in cerebrospinal fluid interacts with chemoreceptor cells in the brainstem and promotes augmented respiratory drive and enhanced sympathetic activity. Hypercapnic acidification is the result of the interconversion of $CO_2$ and water into carbonic acid, protons, and bicarbonate ions. Enhanced respiratory drive in response to $CO_2$ promotes an increase in lung ventilation, which contributes to the maintenance of $O_2$/$CO_2$/pH equilibrium through a wash out of $CO_2$ and influx of $O_2$. This increased lung ventilation occurs in conjunction with an increase in sympathetic activity that promotes vasoconstriction and enhanced cardiac output, which results in increased blood perfusion (this will be discussed in detail in section 1.6). Additionally, enhanced sympathetic activity can promote arousal, which can act to stimulate breathing (Kaur et al., 2013). Large, acute increases in partial pressure of arterial $CO_2$ ($paCO_2$) can lead to high arousal/panic responses, some of which are adaptive behaviours in the case of airway blockade (e.g. arousal from sleep, postural changes) (Taugher et al., 2014).

The currently prevailing view is that the brainstem mediators of the respiratory central chemoreflex are concentrated in - though not exclusively to - the retrotrapezoid nucleus (RTN), and serotonergic (5-HT) neurones in the raphe nuclei. It should be noted that there are other $CO_2$ chemosensitive cell populations that may modulate the hypercapnic respiratory response: noradrenergic neurones in the Locus Coeruleus (reviewed in Guyenet (2014)); Orexigenic neurones (reviewed in Carrive and Kuwaki (2017); and stimulation of respiratory neurones by $CO_2$ dependent astrocyte activities (Beltran-Castillo et al., 2017, Howarth et al., 2017, Wenker et al., 2010). This section will focus on the role of the RTN and of chemoreceptive serotonergic neurones in the hypercapnic respiratory response, which have been described in most detail and appear to provide a greater contribution to the overall ventilatory response to hypercapnia and/or low pH.

### *1.4.1 Central chemoreceptors in the RTN*

*Anatomical location, phenotype, and connectivity of RTN chemoreceptor neurones*

The retrotrapezoid nucleus (RTN) is historically defined as a cluster of chemoreceptive cells in the region ventral and caudal to the facial nucleus (the ventral parafacial nucleus, $pF_V$) . Recent phenotyping studies of the cells responsive to changes in $CO_2$ in this region have helped more specifically define the RTN as a group of cells that express vesicular glutamate transporter 2 (VGluT2), transcription factor paired-like homeobox 2b (Phox2B), and neurokinin 1 (NK-1) receptors. They contain RNA transcripts for pituitary adenylate cyclase-activating peptide (PACAP) and Neuromedin B, and the majority of RTN neurones (>80%) also contain transcripts for TASK-2 and G-protein coupled receptor 4 (GPR4), proteins that contribute to their pH sensitivity. Furthermore, RTN neurones lack the defining markers of catecholaminergic, serotonergic, cholinergic, GABAergic, and glycinergic neurones. Axons of RTN neurones spread out to innervate various brainstem regions involved in respiratory rhythm generation, such as: the BötC, pre-BötC, RVRG, CVRG, NTS, and the KF (for review, see: Guyenet et al. (2019)).

*Physiological role of RTN neurones in the central chemoreflex respiratory response.*

The physiological role of RTN neurones as mediators of the respiratory hypercapnic response is well established and reviewed in Guyenet et al. (2019) and Guyenet and Bayliss (2015). This section provides a brief summary of some findings that demonstrate RTN chemosensitivity, and that RTN neurones drive breathing in proportion to $paCO_2$.

Single unit electrophysiological recordings of RTN neurones in anaesthetized rats show that the RTN neurone discharge pattern tracks the end-expiratory $CO_2$ concentration (a proxy measure for $paCO_2$), with higher firing frequencies as the $CO_2$ concentrations of expired air increase. This effect is maintained after intracerebral administration of glutamate receptor antagonist (kynurenate) to eliminate excitatory input from other putative central and peripheral chemoreceptor sites (Mulkey et al., 2004). Also, acute brain slices with RTN neurones from neonatal mice respond to acidification in the presence of synaptic blockers, and these neurones maintain pH sensitivity after acute dissociation (Mulkey et al., 2004, Onimaru et al., 2014). These findings suggest that RTN neurones respond to local brain $pCO_2$, and likely have intrinsic $CO_2$/pH sensitivity.

Unilateral optogenetic stimulation of RTN neurones with Channelrhodopsin-2 (ChR2), a light sensitive depolarizing cation channel, expressed under a promoter selective of Phox2B expressing neurones (PRSx8) results in enhanced lung ventilation as observed in

plethysmography recordings of anesthetized rats (Burke et al., 2015). Conversely, bilateral inhibition of RTN neurones through optic stimulation of Arch2.0, a light-sensitive hyperpolarizing proton pump, of which expression was driven by the PRSx8 promotor, resulted in reduction of breathing when arterial pH was 7.44, but not when arterial pH is 7.59. Arterial pH was manipulated by changing the fraction of inspired $O_2$ ($FiO_2$) or by systemic administration of acetazolamide, an inhibitor of carbonic anhydrase, an enzyme that assists interconversion of carbonic acid into water and carbon dioxide (Basting et al., 2015). Transgenic Phox2b knockout mice ($Phox2b^{27alacki}$;;$Egr\text{-}2^{Cre}$ mice) hypoventilate at rest and do not increase breathing rate when exposed to high concentrations of $CO_2$ (Ramanantsoa et al., 2011). Similarly, lesioning of RTN neurones in rats, via local injections of SSP-saporin (a toxin that eliminates cells expressing the NK-1 receptor, of which expression in the RTN/$pF_V$ region is unique to RTN neurones), leads to hypoventilation at rest, and a reduction in the hypercapnic ventilatory response in accordance with the percentage RTN neurones lesioned (Souza et al., 2018). Together, these findings indicate that RTN neurones mediate the central chemoreflex respiratory response.

### *1.4.2 Central chemoreceptors in the raphe nuclei*

Serotonergic neurones are located in following anatomical regions in the mature rodent brain: the raphe pallidus (RPa); the raphe obscurus (ROb); the raphe magnus (RMg); periaqueductal grey structures; the pontine raphe; the dorsal raphe; the median raphe; and the medial lemniscus (Harding et al., 2004).

*Physiological role of serotonergic raphe neurones in the central chemoreflex respiratory response.*

The above regions are derived from several embryonic rhombomeres of the neural tube. Brust et al. (2014) performed a series of pharmacogenetic experiments in which various 5-HT populations defined by embryonic origin, were each selectively inhibited in mice through activation of hyperpolarizing 'designer receptors exclusively activated by designer drugs' (DREADD) hM4Di (a $G_{i/o}$ protein-coupled receptor with selectivity for a biologically inert synthetic ligand), upon which the hypercapnic response was queried *in vivo* via plethysmography recordings in room air (0% $FiCO_2$) vs. hypercapnic air (5% $FiCO_2$). The authors demonstrated that exclusively Egr2-, and Pet1-positive (Egr2-Pet1) serotonergic neurones derived from rhombomeres 3 and 5 (r3/r5) were necessary for the full hypercapnic response *in* vivo in awake adult mice. Patch clamp recordings in acute brain slices in the presence of synaptic blockers revealed that Egr2-Pet1 serotonergic

neurones had intrinsic $CO_2$/pH chemosensitivity (Brust et al., 2014). The anatomical locations of this subset of serotonergic neurones correspond to the caudal end of the medial lemniscus and median raphe nucleus (for r3 derived Egr2-Pet1 neurones), and the rostral end of the raphe magnus and raphe pallidus (for r5 derived Egr2-Pet1 neurones) (**figure 1-4**). Rhombomeric lineage also appears to determine the innervation patterns of serotonergic neurones. Serotonergic neurones derived from r3/r5 selectively innervated brainstem nuclei involved in chemosensory processing, but not various respiratory (pre)motor nuclei (**figure 1-4**). The findings by Brust et al. (2014) are in line with earlier findings that indicate that, in rodents, serotonergic neurones in the raphe magnus can be activated by $CO_2$, whereas serotonergic neurones in the raphe obscurus are less responsive to changes in $CO_2$/pH (Depuy et al., 2011, Mulkey et al., 2004, Hodges et al., 2005, Iceman et al., 2013).

Using an experimental protocol similar to Brust et al. (2014), Hennessy et al. (2017) found that pharmacogenetic (hM4Di-mediated) inhibition of Tachykinin positive and Pet1 positive (Tac1-Pet1) serotonergic neurones blunted the *in* vivo hypercapnic respiratory response to 5% pi$CO_2$ vs. 0% pi$CO_2$ in mice. The authors did not report any experiments to confirm whether Tac1-Pet1 neurones lacked intrinsic chemosensitivity, as would be expected from the findings of Brust et al. (2014). Tac1-Pet1 neurones populated the raphe obscurus and raphe pallidus (Okaty et al., 2015, Hennessy et al., 2017). Tac1-Pet1 axonal boutons were found sparsely in respiratory control areas (e.g. pre-BötC), but densely in respiratory motor regions (Hennessy et al., 2017). Hennessy et al. (2017) suggest Tac1-Pet1 neurones may act downstream of Egr2-Pet1 serotonergic neurones, which do not innervate respiratory motor nuclei. Thus, intrinsic $CO_2$/pH sensitivity in serotonergic neurones appears specific to the Egr2-Pet1 neurones derived from r3/r5, but serotonergic transmission by other raphe neurones may facilitate a respiratory reflex initiated by $CO_2$/pH sensors elsewhere.

### *1.4.3 Molecular mechanisms of $CO_2$ chemosensitivity*

RTN neurones and a subset of serotonergic neurones are thought to have intrinsic $CO_2/H^+$ sensitivity. The mechanism underlying Erg2-Pet1 neurone $CO_2/H^+$ sensitivity is currently not yet identified. However, in RTN neurones, double knockout of two proton detectors, potassium channel TASK-2 and G protein coupled receptor 4 (GPR4), nearly eliminates the hypercapnic respiratory response in mice *in vivo* (Wang et al., 2013, Kumar et al., 2015) , whereas mice in which either TASK-2 or GPR4 is knocked out separately show a 65%

reduction of the hypercapnic respiratory response (Guyenet et al., 2016, Kumar et al., 2015, Gestreau et al., 2010). In acute brain slices of wild type mice, incubation of GRP4 antagonists reduced the proportion of pH sensitive RTN neurones (Kumar et al., 2015, Dong et al., 2017), and systemic administration of a GPR4 antagonist (NE 52-QQ57) attenuated the respiratory response to $CO_2$ in unanaesthetised waking rats and mice (Hosford et al., 2018). Conversely, selective reintroduction of GPR4 expression in RTN neurones of GPR4 KO mice restores the respiratory chemoreflex *in vivo* and the ability of hypercapnia to elicit Fos expression (a metabolic marker) in RTN neurones (Kumar et al., 2015). These findings indicate that intrinsic $CO_2$ chemosensitivity in the RTN is mediated by proton pump TASK-2 and GPR4, in response to hypercapnic acidification. Although TASK-2 and GPR4 are present in high levels in RTN neurones, it should be noted that TASK-2 expression is also reported outside the RTN (Gestreau et al., 2010), and GPR4 may be expressed in low levels by subsets of serotonergic neurones and the brain vascular endothelium (Hosford et al., 2018, Shi et al., 2017, Kumar et al., 2015).

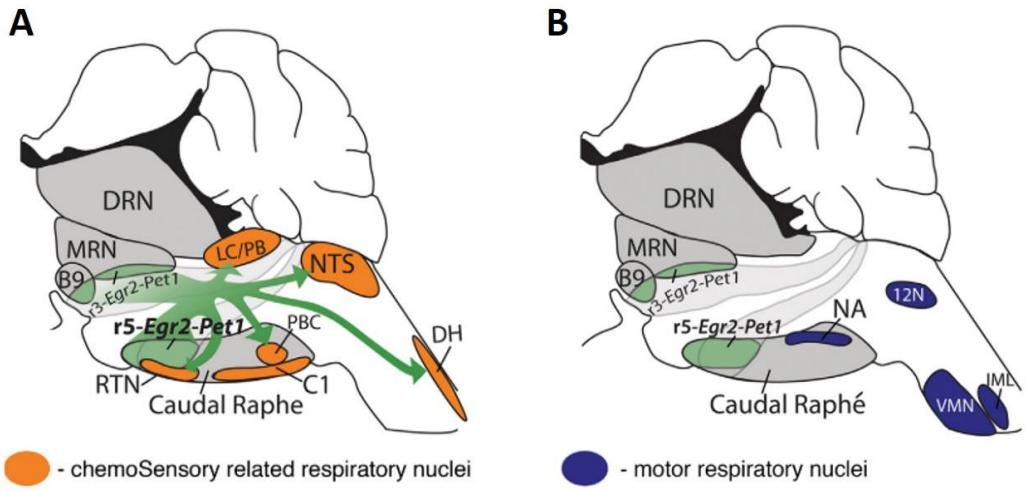


**Figure 1-4:** Anatomical location and projection sites of $CO_2$ sensitive serotonergic neurones.
Schematic representation of anatomical location and projections of Egr2-Pet1 serotonergic neurones derived from embryonic rhombomeres r3 and r5 that are found be unique among 5-HT neurones to have intrinsic $CO_2$ sensitivity. **(A)** raphe (grey) and r3-Egr2-Pet1 and r5-Egr2-Pet1 5-HT neurones (green) with intrinsic $CO_2$ sensitivity map onto the caudal parts of the median lemniscus and the median raphe, and onto the rostral parts of the caudal raphe (raphe magnus and raphe pallidus). Egr2-Pet1 5-HT neurones derived from r3/r5 selectively innervate brainstem nuclei involved in chemosensory processing (orange), but not various analysed respiratory (pre)motor nuclei (**B**, blue regions). Abbreviations: DRN = dorsal raphe nucleus; MRN = median raphe nucleus; LC/PB = locus corealeus/parabrachial nucleus; NTS nucleus tractus solitarius; RTN = retrotrapezoid nucleus; PBC = pre-Botzinger Complex; DH = dorsal horn; NA = nucleus ambiguous; 12N = Vagal nucleus; VMN = ventral spinal motor neurones; IML = intermediolateral cell column of the spinal cord. Figures adapted from Brust et al. (2014).

### *1.4.4 Contributions of the RTN to emergence of late-E activity in hypercapnic conditions.*

Under conditions of high metabolic demand, such as hypercapnia, late-E activity can emerge as a result of activity of a conditional expiratory oscillator located in the pFRG (see section 1.2) (Huckstepp et al., 2015, Zoccal et al., 2018). The pFRG houses a population of neurones, named 'late-E neurones', that fire exclusively in phase with late-E activity recorded in the AbN and have been identified as a critical source of late-E AbN activity under hypercapnic conditions (Abdala et al., 2009, Moraes et al., 2013, Silva et al., 2016, Pagliardini et al., 2011). The respiratory network interactions that - in response to CO2 chemoreceptor activation – lead to the emergence of late-E burst of abdominal nerve activity are suggested to constitute combined excitation and disinhibition of late-E neurones. Under resting conditions, late-E neurone activity is thought to be suppressed by inhibitory synaptic inputs from glycinergic Post-I neurones in the BötC, and Early-I neurones in the pre-BötC (Molkov et al., 2010).

Optogenetic inhibition via selective expression of a light-sensitive inhibitory $Cl^-$ channel (eNpHR3.0) in glycinergic neurones of the BötC during the post-I phase evoked generation of late-E abdominal nerve activity in *in situ* WHBP of rats. In contrast, optogenetic excitation of glycinergic BötC neurones via a light-sensitive cation channel (ChETA) during the post-I phase suppressed late-E abdominal nerve activity in hypercapnic conditions (Moraes et al., 2014a). In the same *in situ* preparations, intracellular recordings of pFRG late-E neurones confirmed that inhibitory input during the post-I phase prevents generation of late-E neurone activity under eucapnic conditions (Moraes et al., 2014a). Excitatory drive to late-E neurones, on the other hand, may come from glutamatergic $CO_2$-sensitive RTN neurones. Late-E activity emerges in hypercapnic conditions, when $CO_2$ sensitive drive to late-E neurones is increased beyond the threshold value to overcome their inhibitory input. Optogenetic stimulation of Phox2B expressing RTN neurones with pacing stimulation of ChR2 elicits late-expiratory airflow in conscious rats under normocapnic conditions (Abbott et al., 2011). Conversely, pharmacogenetic inhibition of Phox2B expressing RTN neurones with G-protein-coupled Drosophila allatostatin receptor prevents the development of late-E abdominal activity under hypercapnic conditions in anesthetised rats and in *in situ* WHBP of rats (Marina et al., 2010, Abbott et al., 2011). Thus, emergence of late-E AbN activity is suggested to be the result of interplay between inhibitory- (from BötC post-I neurones) and excitatory (from RTN glutamatergic $CO_2$ chemosensitive neurones) inputs to pFRG late-E neurones (see **figure 1-5**). Late-E activity

is inhibited in resting conditions, but can emerge as a result of enhanced excitatory chemoreceptor drive to late-E neurones, or as a result of reduced inhibition of late-E neurones from Post-I neurones.

*The Kölliker-Fuse nucleus modulates late-E motor output.*

Given that activity of BötC post-I neurones inhibits late-E activity, and given that the pontine KF plays an important role in the emergence of post-I activity (see section 1.3.2), it is possible that the KF plays an indirect role in the control of late-E activity. Recent pharmacological experiments with focal micro-injections in the KF confirm that disinhibition of the KF with $GABA_A$ antagonist gabazine increases cVN post-I activity and attenuates the emergence of AbN late-E bursts in hypercapnic conditions (Barnett et al., 2018). Conversely, augmented inhibition of the KF via micro-injection in the KF of $GABA_A$ receptor agonist isoguvacine resulted in reduced cVN post-I activity and advanced the onset of late-E abdominal bursts in hypercapnic conditions (Jenkin et al., 2017). Based on computational modeling simulations it was suggested that excitatory neurones in the KF stimulate post-I neurones in the BötC, which in their turn inhibit late-E neurones in the pFRG (see **figure 1-5**). Via reduction of excitatory input from KF neurones to VRC post-I neurones, inhibition of the KF is suggested to indirectly disinhibit late-E neurones (Barnett et al., 2018). Thus, late-E activity is thought to stem from interactions between the KF, the BötC and pre-BötC, the pFRG, and $CO_2$ chemosensitive neurones of the RTN. The pFRG houses an expiratory oscillator that is suppressed under eupnoeic conditions. Emergence and timing of late-E activity is a function of inhibitory inputs to the pFRG from the VRC Post-I and Early-I neurones – which in their turn are modulated by KF efferents – and excitatory drive from central chemoreceptors in the RTN.

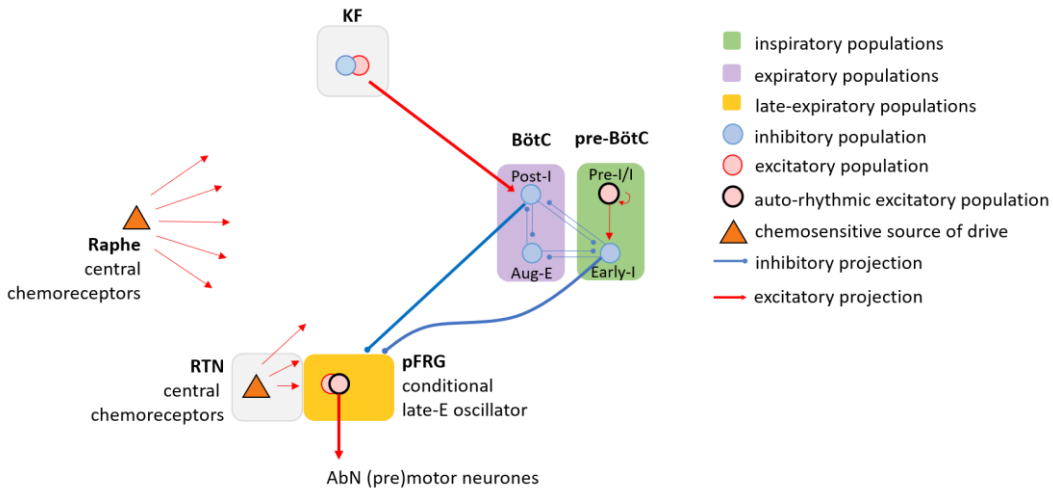


**Figure 1-5:** Pathways suggested to mediate emergence of late-E activity

Schematic representation of interactions between the pontine KF, the VRC, and $CO_2$ chemosensitive neurones that are thought to affect the emergence and timing of late-E activity. The interactions displayed in figure are as suggested in the computational model by (Barnett et al., 2018). The schematic does not show the complete model but highlight selected elements of it for the sake of visual clarity. Justification for all suggested projections and an explanation of the interactions is provided in section 1.4.4. Abbreviations: KF = Kölliker-Fuse; BötC = Bötzinger Complex, Pre-BötC = pre-Bötzinger Complex, RTN = retrotrapezoid nucleus; pFRG = parafacial respiratory group.

## 1.5 PERIPHERAL CHEMORECEPTOR FEEDBACK MECHANISMS IN RESPIRATORY CONTROL

### *1.5.1 Oxygen sensing in the Carotid Bodies.*

*Multisensory chemoreceptors in the carotid-, and aortic bodies mediate the peripheral chemoreflex response.*

The peripheral chemoreflex is the sympathetic and respiratory response activated by chemosensory cells located in the carotid bodies, and to a lesser extent, the aortic bodies (reviewed in Costa et al. (2014)). The carotid bodies are located bilaterally in the bifurcation of the common carotid artery, whereas the aortic bodies are located along the aortic arch. Both carotid and aortic bodies are multifunctional receptors that sense multiple modalities (e.g. blood gases, arterial pressure, blood pH, glucose and circulating signalling molecules), and can evoke multiple reflex responses, likely via distinct signalling pathways (reviewed in Zera et al. (2019)). Stimulation of peripheral chemoreceptors results in increased respiratory rate and tidal volume (or physiological surrogates thereof), combined with enhanced post-I activity (observed in AbN, HN, and cVN), sympathetic and respiratory late-E activity (observed in AbN and thoracic sympathetic nerve activity), overall sympatho-activation, and bradycardia followed by tachycardia (Lindsey et al., 2018, Dick et al., 2004, Moraes et al., 2012a, Barnett et al., 2017, Abdala et al., 2009). Carotid bodies (CB) are the main peripheral sites for chemoreceptor cells that sense low $paO_2$ and high $paCO_2$/pH. Only a sparse number of chemoreceptor cells have been identified in the aortic arch region of rats (Easton and Howe, 1983), and they may be entirely absent from mice (Chalmers et al., 1967). The remainder of this section will focus on carotid body chemoreceptors and their downstream neural architecture as the main mediators of the peripheral chemoreflex.

Molecular mechanisms of $O_2$ and $CO_2$ sensing in the carotid bodies

The carotid bodies are uniquely sensitive to even modest changes in $paO_2$ (e.g. from ~100 to 80 mmHg) (Prabhakar et al., 2006). The CB are made up of a dense network of capillaries that supply blood to clusters of chemoreceptor glomus cells, also known as type 1 cells, and supportive sustentacular type 2 cells. The glomus cells can be directly sensitive to both low $O_2$ and high $CO_2$/pH (Lahiri et al., 2006) and, upon stimulation, secrete neurotransmitters (e.g. ATP, acetylcholine, dopamine, 5-HT, and substance-P) that excite adjacent afferent terminals of petrosal ganglia neurones (Vicario et al., 2000, Costa et al., 2014) with axons that project via the carotid nerve to the NTS. Type 2 cells, although

electrophysiologicaly unresponsive to hypoxia or hypercapnic acidosis, are purported to have a glia-like paracrine role in the CB (Kumar and Prabhakar, 2012). The exact molecular mechanisms by which glomus cells may sense a decline in $O_2$ is still a matter of debate. Most theories rely on the integration of mitochondrial $O_2$ sensing with transduction mechanisms that interact with membrane ion channels (reviewed in Rakoczy and Wyatt (2018)). There is consensus that acute $O_2$ sensing by glomus cells is mediated by several types of outward rectifying $K^+$ channels that are reversibly inhibited by decreases in $pO_2$. Closure of these $K^+$ channels results in the membrane depolarization that opens $Ca^{2+}$ channels to trigger exocytosis of synaptic vesicles. (reviewed in Teppema and Dahan (2010), Lopez-Barneo et al. (2016)). Sensitivity of glomus cells to hypercapnic acidosis is dependent on acid-sensing ion channel 3 (ASIC3) (Lu et al., 2013, Tan et al., 2010). Interestingly, ASIC3 mediated sensitivity to low pH is reciprocally related to sensitivity to hypoxia. That is, with increasing expression of ASIC3 or increasing sensitivity to low pH, the response magnitude to low $pO_2$ decreases (Lu et al., 2013). This suggests the existence of distinct $O_2$ vs. $CO_2$ 'sensitivity profiles' among various glomus cells.

### *1.5.2 Respiratory peripheral chemoreflex mechanisms: interactions between the Nucleus Tractus Solitarius and the Ventral Respiratory Column.*

Anatomical studies suggest the peripheral chemoreflex response is mediated, at least in part, by interactions between NTS and VRC neurones. Retrograde labelling with wheat germ agglutinin and horseradish peroxidase conjugates injected into vascularly isolated CB *in* situ in rats revealed most CB afferents first synapse in the commissural and medial subnuclei of the NTS, with some fibres projecting to areas in the ventral and ventrolateral medulla (e.g. area postrema, the dorsal motor nucleus of the vagus nerve, the caudal ventrolateral medulla, and the nucleus ambiguus) (Mifflin, 1992). These findings are in line with those of immunohistochemical labelling of Fos protein after hypoxia or electrical stimulation of the carotid sinus nerve in rat (Erickson and Millhorn, 1994, Erickson and Millhorn, 1991). Through projections to various brainstem circuits, second order neurones in the NTS form multiple pathways to modulate respiratory rhythm and pattern and, concurrently, the sympathetic and parasympathetic outflows that mediate cardiac output and vascular tone (sympathetic reflexes will be discussed in section 1.6). The respiratory response to CB activation is likely reliant on second order NTS neurones that project directly to various respiratory regions in the VRC. The majority of such NTS neurones innervate the RTN/pFRG area, the RVRG, the CVRG, the RVLM, and to a lesser extent the BötC and pre-BötC regions (Alheid et al., 2011, Yang et al., 2020).

In addition to anatomical studies, functional studies provide further support for the notion that the peripheral chemoreflex respiratory response is mediated by interactions between NTS and VRC neurones. *In vivo* single unit recordings in rats show that stimulation of peripheral chemoreceptors through brief periods of normocapnic hypoxia or through intravenous injection of sodium cyanide (NaCN) results in the activation of RTN neurones (Takakura et al., 2006). This activation requires the integrity of the carotid sinus nerves and the NTS (Takakura et al., 2006, Guyenet et al., 2018). NTS neurones with projections to the RTN/pFRG area show Fos expression after hypoxia, and ninety percent of these NTS neurones are glutamatergic (contain VGLUT2 mRNA) (Takakura et al., 2006). Inhibition of the pre-BötC and RVRG, through local injections of $GABA_A$ receptor agonist (muscimol) until complete loss of PN activity, had no effect on the excitatory response of RTN neurones to peripheral chemoreceptor activation in anaesthetised rats (Takakura et al., 2006). Local pharmacological inhibition of the RTN, on the other hand, abolished the late-E sympathetic and respiratory components of the peripheral chemoreflex upon CB stimulation, but did not affect the Post-I respiratory response (Moraes et al., 2012a). Based on these findings it has been suggested that the late-E response to peripheral chemoreceptor activation is independent from VRC circuits underlying eupnoeic respiratory activity and is likely mediated by projections from NTS neurones to the RTN/pFRG regions, resulting in excitation of late-E neurones (see **figure 1-6**) (Barnett et al., 2017). Furthermore, late-E activity and post-I activity in response to peripheral chemoreceptor activation are thought to be mediated by distinct pathways. Computational simulations based on the inhibitory ring model suggest that excitatory projections of second order peripheral chemoreceptor neurones in the NTS to post-I neurones in CVRG transmission circuitry may contribute to the peripheral chemoreceptor induced motor activity during Post-I phase (see **figure 1-6**) (Barnett et al., 2017).

### *1.5.3 Pontine contribution to the respiratory peripheral chemoreflex.*

Besides respiratory regions in the ventrolateral medulla, the KF and parabrachial nuclei of the pons, too, have been found to receive inputs from NTS neurones that relay signals from CB afferents. This innervation originates in part from commissural NTS neurones that express Fos after hypoxia (Herbert et al., 1990, Song et al., 2011). The KF and parabrachial nuclei are known to be involved in respiratory phase transitioning, control of the duration of the respiratory cycle (see section 1.3), and the promotion of late-E activity through disinhibition of RTN neurones (see section 1.4.4)**.** Transverse sectioning at the ponto-medullary junction to remove inputs from the pons resulted in a loss of AbN post-I and

late-E activity, and of cVN post-I activity that could not be reinstated by hypercapnia, hypoxia, anoxia, or peripheral chemoreceptor activation with NaCN in *in situ* WHBP of rats (Abdala et al., 2009). KF neurones are activated during hypoxia and carotid sinus nerve stimulation (Erickson and Millhorn, 1994), and pharmacological inhibition through local muscimol injections in the KF attenuated the sympathetic and respiratory responses to intra-arterial KCN injections or to hypoxia in anaesthetized, and unanaesthetised rats, respectively (Damasceno et al., 2014, Damasceno et al., 2015). Furthermore, the lateral parabrachial nucleus is suggested to mediate shortening of expiratory phase duration in response to hypoxia, as uni-, or bilateral lesion of this region resulted in an attenuation of this expiratory phase shortening in anesthetized rats (Song and Poon, 2009). Taken together, these findings indicate that respiratory regions in the parabrachial complex mediate the respiratory response to peripheral chemoreceptor activation. This could be via a pathway in which NTS neurones relay peripheral chemoreceptor afferents to the parabrachial complex, which then interacts with rhythmogenic circuitry in the VRC as described in section 1.3 (see **figure 1-6**).

To summarize, the respiratory late-E component of the peripheral chemoreflex is dependent on RTN and pFRG function and is likely mediated by excitatory projections from the NTS to the RTN/pFRG regions. The post-I respiratory response and tachypnoea in response to peripheral chemoreceptor activation is mediated by a separate pathway, which is hypothesised to involve excitatory projections from NTS neurones to transmission circuitry of the CVRG. This latter pathway remains to be experimentally verified. The respiratory response to peripheral chemoreceptor activation is also found to be dependent on intact ponto-medullary interactions.

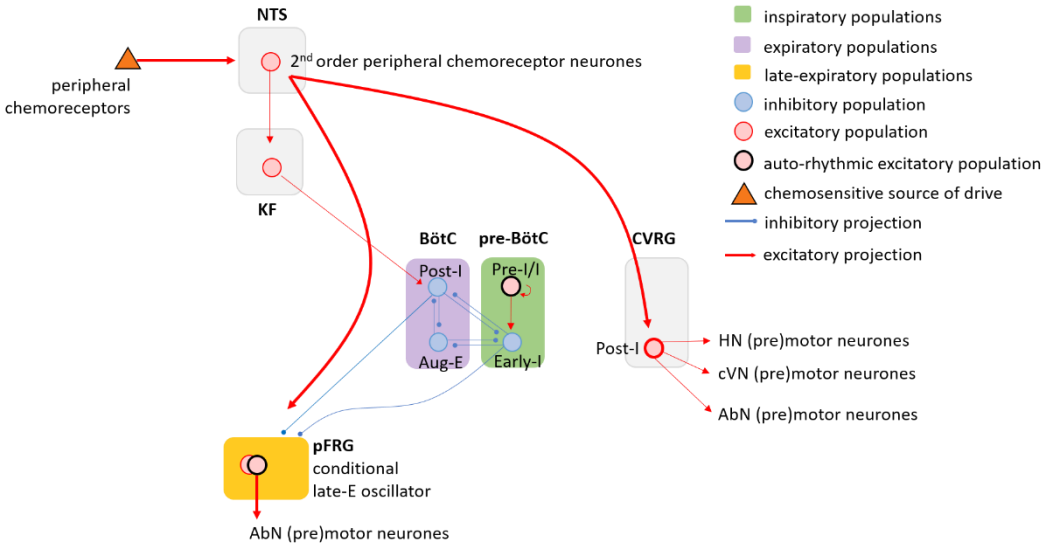


**Figure 1-6:** Pathways suggested to mediate respiratory responses to peripheral chemoreceptor activation

Schematic representation of interactions between the NTS, the VRC, and the pFRG (thick lines) that mediate the emergence of late-E activity and Post-I activity in response to peripheral chemoreceptor activation as suggested in the computational inhibitory ring model by Barnett et al. (2017). The schematics do not show the complete model but highlight selected elements of it for the sake of visual clarity. Late-E and post-I activity in response to peripheral chemoreceptor activation are suggested to be mediated by separate pathways. Justification for all suggested projections and an explanation of the interactions is provided in sections 1.5.2 and 1.5.3. Abbreviations: NTS = Nucleus tractus solitarius; KF = Kölliker-Fuse; VRC = ventral respiratory column, BötC = Bötzinger Complex, Pre-BötC = pre-Bötzinger Complex, CVRG = caudal ventral respiratory group, pFRG = parafacial respiratory group.

## 1.6 ENTRAINMENT OF RESPIRATORY AND SYMPATHETIC ACTIVITY

Blood circulation and pulmonary ventilation are modulated in a coordinated fashion to optimally maintain oxygen-, and pH homeostasis in bodily tissues under continuously changing conditions of metabolic demand. Not surprisingly, central mechanisms of cardiovascular and respiratory control interact. Central cardiovascular control is largely mediated via sympathetic outflow to the heart and vasculature, where it modulates cardiac output and vasoconstriction.

### *1.6.1 Distinct patterns of sympatho-respiratory coupling occur depending on metabolic state*

Under eupnoeic conditions, sympathetic nerve activity in mammals exhibits positive modulation during I and Post-I phases of the respiratory cycle (Dick et al., 2014, Baekey et al., 2008, Malpas, 1998, Malpas, 2010, Zoccal et al., 2008, Zoccal et al., 2009a, Zoccal et al., 2009b). This results in respiratory-rhythm-entrained oscillations in baseline heart rate (known as respiratory sinus arrhythmia) and in arterial pressure levels (known as Traube-Hering waves) (**figure 1-7**) (Moraes et al., 2012b, Bazilio et al., 2019).

The pattern of sympathetic output changes with alterations in respiratory rhythm and pattern. Suppression of respiratory activity via exposure to hypocapnia reversibly reduces sympathetic outlflow, heart rate, baseline levels of arterial pressure, and Traube-Hering waves in *in situ* WHBP of rats (Simms et al., 2009). Conversely, in conditions of high respiratory drive (hypoxia and/or hypercapnia), the emergence of AbN late-E bursts (addressed in sections 1.4.4 and 1.5) is coupled with concomitant sympathetic late-E activity, which contributes to an overall increase in sympathetic drive (Zoccal et al., 2008, Dick et al., 2004, Mandel and Schreihofer, 2009, Molkov et al., 2011).

Stimulation of peripheral chemoreceptors by short periods of hypoxia or intra-arterial cyanide administration in anesthetized rats (Dick et al., 2004, Mandel and Schreihofer, 2006) or in *in* situ WHBP of rats (Costa-Silva et al., 2010, Moraes et al., 2012a) gives rise to yet another distinct pattern of sympatho-respiratory coupling. Section 1.5 mentions that the respiratory response to peripheral chemoreceptor activation includes enhanced post-I activity observed in AbN, HN, and cVN in *in* situ preparations of rats. This response to peripheral chemoreceptor activation is coupled with high amplitude sympathetic bursts during post-I followed by inhibition of sympathetic output during early inspiration. (Dick et al., 2004, Costa-Silva et al., 2010, Mandel and Schreihofer, 2009, Moraes et al., 2012a, Barnett et al., 2017, Braga et al., 2007).

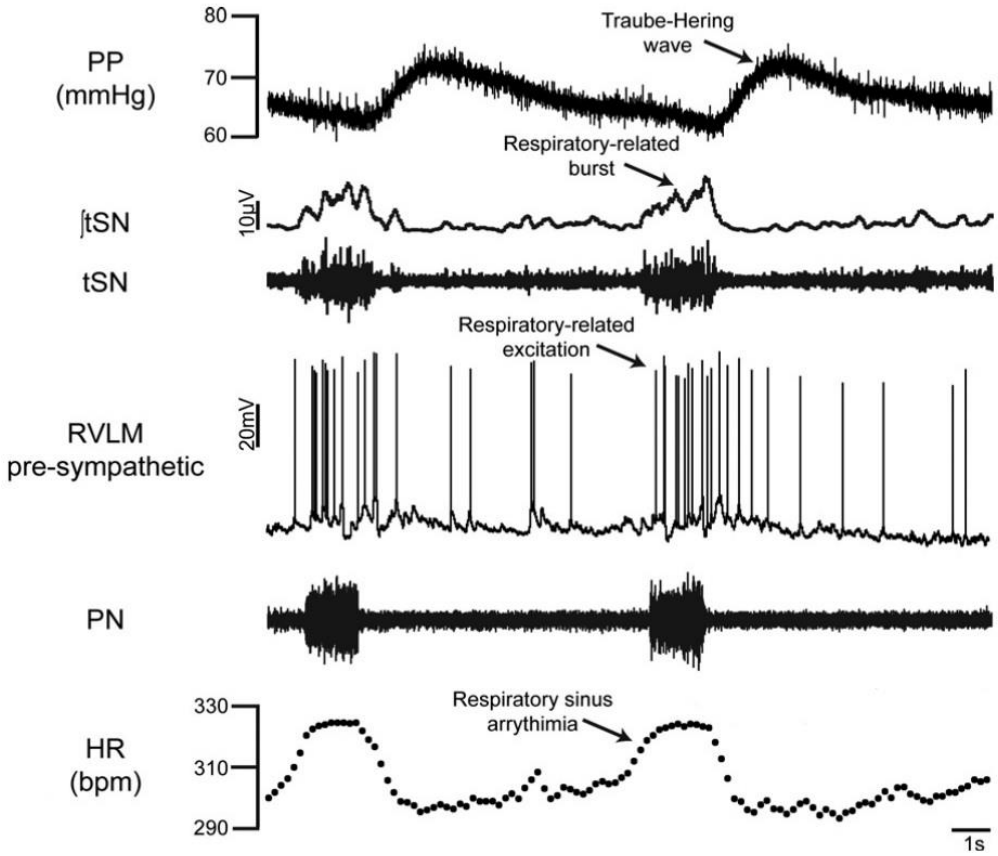


**Figure 1-7**: Example traces of sympathetic activity entrained with the respiratory cycle.

Sympathetic activity is entrained with the respiratory cycle. Specifically, during eupnoeic breathing sympathetic activity is upregulated during late stages of the inspiratory phase. This results in respiratory sinus arrhthmia, and a delayed peak in perfusion pressure (Traube-Hering waves). From top to bottom, traces show perfusion pressure (PP), sympathetic nerve activity, RVLM pre-sympathetic neurone activity, phrenic nerve activity, and heart rate. Figure is adapted from Machado et al. (2017)

*Sympathetic ganglionic efferents control long- and short term blood pressure regulation.*

Sympathetic control of circulation operates via three main classes of sympathetic ganglionic neurone efferents: thermosensitive, glucosensitive, and barosensitive (Guyenet, 2006). Thermosensitive sympathetic efferents consist primarily of hypothermia-activated cutaneous vasoconstrictors (Janig and Habler, 2003, Vallbo et al., 2004). Glucosensitive sympathetic efferents are activated by hypoglycaemia and physical exercise, and mediate adrenaline release from the adrenal glands (Cao and Morrison, 2001). Activity of barosensitive sympathetic ganglionic efferents can be mediated by arterial baroreceptors located in the aortic arch and the carotid sinus, of which vagal efferents project to the NTS (Guyenet, 2006). The group of barosensitive neurones is the largest group of sympathetic efferents, and is thought to play a dominant role in both short-, and long term blood pressure regulation (Janig and Habler, 2003, Guyenet, 2006).

They control cardiac output, vasoconstriction (except for cutaneous arteriole constriction), the kidneys (renin secretion, renal sodium reabsorption, and renal blood flow (DiBona and Kopp, 1997)), and noradrenaline release from a subset of adrenal gland chromaffin cells (Janig and Habler, 2003). These sympathetic efferents show ongoing activity at rest (sympathetic tone), and their discharge patterns are highly synchronised with respiratory rhythm (Janig and Habler, 2003, Vallbo et al., 2004, Dempsey et al., 2002).

*Excitatory pre-sympathetic neurones in the rostral ventrolateral medulla drive activity of sympathetic efferents*

A nodal point for respiratory reflexes mediated by barosensitive sympathetic efferents is found in the rostral ventrolateral medulla (RVLM), which houses two major populations of pre-sympathetic neurones. The first is a population of catecholaminergic neurones, denoted C1, which express all the enzymes required for synthesizing adrenaline, and the second is a population of non-catecholaminergic (non-C1) neurones (Ross et al., 1984, Schreihofer and Guyenet, 1997, Schreihofer et al., 2000). RVLM C1 and non-C1 pre-sympathetic neurones are glutamatergic, as evidenced by expression of vesicular glutamate transporter-2 (VGLUT2) RNA (Stornetta et al., 2002b, Stornetta et al., 2002a). They lack markers of inhibitory neurones such as glycine transporter 2 (GlyT2) and glutamic acid decarboxylase (GAD) (Comer et al., 1999, Schreihofer et al., 1999, Stornetta and Guyenet, 1999, Stornetta et al., 2002b, Stornetta et al., 2002a). C1 Pre-sympathetic neurones are the major source of monosynaptic excitatory input to sympathetic preganglionic neurones in the intermediolateral column of the spinal cord (Guyenet et al., 2013, Stornetta et al., 2016, Stornetta, 2009, Stornetta et al., 2002b, Moraes et al., 2017, Marina et al., 2011) which, in their turn, drive the barosensitive sympathetic ganglionic efferents described above (Guyenet et al., 2013).

*Contributions of RVLM C1 pre-sympahtetic neurones to sympatho-respiratory coupling*

In pioneering studies on the role of RVLM neurones on cardiovascular control, micro-injection of L-glutamate in the RVLM resulted in increased arterial pressure in rodents (Dampney, 1981, Dampney et al., 1982, Ross et al., 1984). Catecholaminergic brainstem neurones express transcription factor Phox2B, which allows for their genetic targeting via Phox2B selective artificial promoter PRSx8 (Marina et al., 2011, Hwang et al., 2001, Duale et al., 2007). Optogenetic gain of function experiments have targeted RVLM C1 neurones via focal viral vector delivery of a transgene that drives expression of ChR2 under control of the PRSx8 promoter. These studies showed that selective stimulation of RVLM C1 neurones increased sympathetic activity, heart rate, and arterial pressure under resting

conditions in anesthetised (Abbott et al., 2009), and unanaesthetised (Abbott et al., 2013, Burke et al., 2014, Kanbar et al., 2010) rats, and in *in situ* preparations of rats (Menuet et al., 2014). The sympathetic responses evoked by C1 photo-stimulation in anesthetized rats (a rise in blood pressure and reflex bradycardia) were similar to those evoked by hypoxia, and were also occluded by hypoxia, while they persisted under hypercapnia (Burke et al., 2014). Conversely, loss of function studies show that blocking glutamatergic transmission via local micro-injection of glutamate receptor antagonist (kynurenic acid) in the RVLM results in the elimination of sympathetic reflex responses to brief hypoxia in urethane anesthetized rats (Koshiya et al., 1993).

Pharmacogenetic loss of function studies have utilised the PRSx8 promoter to target RVLM C1 neurones for expression of the inhibitory *drosophila* allatostatin receptor, which can be activated by administration of exogenous allatostatin peptide (Tan et al., 2006). Pharmacogenetic inhibition of RVLM C1 cells with allatostatin resulted in large reductions of eucapnic sympathetic nerve activity and arterial pressure in urethane anesthetized rats (Marina et al., 2011), in freely moving unanaesthetised rats (Moraes et al., 2017), and in *in situ* WHBP of rats (Marina et al., 2011, Moraes et al., 2017). In anesthetized and peripheral chemoreceptor denervated rats, systemic hypercapnia still evoked vigorous sympathetic and cardiovascular chemoreflex responses after allatostatin induced inhibition of RVLM C1 neurones (Marina et al., 2011). In line with this, allatostatin-mediated inhibition did not reduce late-E sympathetic activity, but did inhibit I/Post-I sympathetic activity after exposure to hypercapnia in *in situ* WHBP of rats (Moraes et al., 2017). Allatostatin-mediated inhibition also significantly reduced the inspiratory sympathetic, but not the late-E sympathetic responses to peripheral chemoreflex activation *in situ* (Moraes et al., 2017). Findings of a recent optogenetic inhibition study also point towards a role of RVLM C1 neurones in cardiovascular control under conditions of peripheral chemoreceptor activation, but not under conditions of central chemoreceptor activation. Light-stimulation of inhibitory proton pump ArchaeorhodopsinT-3.0, expressed in the RVLM under the PRSx8 promoter, resulted in a large decrease in blood pressure under conditions of brief hypoxia, but had little effect under hypercapnic- or resting conditions in unanaesthetised rats (Wenker et al., 2017). Furthermore, the authors report that under the effect of isoflurane anaesthesia, C1 inhibition did result in a significant drop in blood pressure under resting conditions. They suggest that the contribution of C1 activity to cardiovascular control under resting conditions may have been overestimated by experiments using anaesthesia.

Nevertheless, the lack of a significant hypotensive effect of optogenetic C1 inhibition under resting conditions in unanaesthetised rats contrasts with the earlier-mentioned large reductions in sympathetic activity and arterial pressure observed after allatostatin-mediated inhibition of C1 neurones under similar conditions (Moraes et al., 2017).

To summarize, the above findings of RVLM C1 gain- or loss of function studies collectively suggest that the (I/Post-I) sympathetic activity in response to peripheral and/or central chemoreceptor activation is dependent on RVLM C1 neurone function, but that late-E sympathethic activity in response to central chemoreceptor activation is not. Interestingly, pharmacogenetic (allatostatin) inhibition (Moraes et al., 2017) and optogenetic (archaeorhodopsinT3.0) inhibition (Wenker et al., 2017) experiments in unanaesthetised rats *in vivo* suggest differing degrees of contribution of RVLM C1 neurones to cardiovascular control under resting conditions. This discrepancy calls for further experimental validation of the contribution of C1 neurone activity to cardiovascular control under resting conditions in unanaesthetised rats *in vivo*.

### *1.6.2 Sympatho-respiratory coupling is the result of interactions between brainstem networks of sympathetic and respiratory control*

Respiratory modulation of sympathetic activity was found to persist after vagotomy and decerebration (reviewed in Molkov et al. (2014b). This suggests that sympatho-respiratory coupling occurs through interactions between brainstem circuits of sympathetic and respiratory control. The exact neural mechanisms that give rise to the various patterns of sympatho-respiratory coupling addressed in section 1.6.1 are not fully understood. The distinct patterns of sympatho-respiratory coupling under the various states of respiratory drive conditions (normoxia/eucapnia, hypoxia, hypercapnia), along with the differing contributions of C1 pre-sympathetic neurones to these patterns, suggests that there are multiple pathways along which sympatho-respiratory coupling can occur.

*Functional and anatomical connectivity underlying eupnoeic sympatho-respiratory coupling.*

RVLM C1 and non-C1 pre-sympathetic neurones exhibit distinct respiratory modulation. Extracellular recordings in combination with peripheral nerve recordings showed that RVLM neurone activity patterns were phase-locked with the respiratory cycle (Haselton and Guyenet, 1989). Intracellular recordings in *in situ* WHBP of rats combined with peripheral nerve recordings showed that all recorded RVLM C1 and non-C1 pre-

sympathetic neurones presented $I_{NaP}$ intrinsic pacemaker activity, and confirmed that many cells also exhibit spontaneous excitatory post-synaptic potentials and synaptic inhibition in different phases of the respiratory cycle (Moraes et al., 2013, Moraes et al., 2017). Specifically, 3 groups of pre-sympathetic neurones were identified that showed distinct patterns of respiratory modulation, which corresponded to the sympathetic activity recorded at various sympathetic nerves. A fourth group showed no respiratory modulation (Moraes et al., 2013). IHC labelling for tyrosine hydroxylase (TH) after intracellular recordings in *in situ* WHBP of rat showed that all recorded inspiratory modulated RVLM cells were C1 (TH positive, and positive for a transgene expressed under the PRSx8 promoter), and that all recorded Post-I modulated RVLM cells were non-C1 (TH negative, and negative for a transgene expressed under the PRSx8 promoter) (Moraes et al., 2017). These findings indicate that: (1) RVLM pre-sympathetic cells receive input from respiratory neurones; (2) RVLM C1 pre-sympathetic neurones contribute specifically to inspiratory modulation of sympathetic activity; and (3) RVLM non-C1 pre-sympathetic neurones may contribute specifically to post-I modulation of sympathetic activity.

The RVLM lies immediately dorsal to the ventral respiratory column in close proximity to, and even partly intermingled with, neurones of the rythmogenic BötC region (Stornetta et al., 2016, Stornetta et al., 2002a, Stornetta et al., 2002b, Guyenet et al., 2013). Due to this anatomical proximity, it has been suggested that the respiratory modulation of pre-sympathetic RVLM neurones may be in part mediated by direct synaptic connections with rhythmogenic respiratory neurones of the ventral respiratory column (Zoccal et al., 2008, Zoccal et al., 2014). Indeed, anatomical studies have reported BötC neurone axon varicosities in close apposition to RVLM neurones, suggesting synaptic contacts between both regions (Sun et al., 1997).

Another source of respiratory modulation to RVLM neurone activity is introduced by a population of GABA-ergic neurones in the caudal ventrolateral medulla (CVLM), a region immediately caudal to the RVLM at the level of the pre-BötC. CVLM GABA-ergic neurones establish synaptic inputs with RVLM neurones (Schreihofer and Guyenet, 2003). Micro-injection of L-glutamic acid in the CVLM (Willette et al., 1983), or $GABA_A$ receptor antagonist bicuculine in the RVLM (Monnier et al., 2003, Guyenet et al., 1990) results in inhibition of sympathetic output and a drop in arterial pressure. CVLM GABA-ergic input to the RVLM is crucial to negative feedback control of sympathetic activity via the sympathetic baroreflex (Schreihofer and Guyenet, 2003). Afferents of arterial baroreceptors synapse at 2$^{nd}$ order baroreceptor neurones in the NTS, which project

(directly or indirectly) to CVLM GABA-ergic neurones (Schreihofer and Guyenet, 2002, Molkov et al., 2014b), that, in turn, inhibit the pre-sympathetic neurones of the RVLM (Dampney, 1994a, Molkov et al., 2014b). Among CVLM GABA-ergic neurones, 4 groups of neurones were identified that exhibit distinct patterns of respiratory modulation (Mandel and Schreihofer, 2006). This suggests that respiratory-phase-locked inhibition from CVLM neurones can contribute to the respiratory modulation of RVLM neurone activity.

Sympatho-respiratory coupling is dependent on pontine input, directly and/or via VRC respiratory populations. Experiments in *in situ* WHBP of rats showed that pontomedullary transection, which constitutes removal of pontine input to medullary respiratory and sympathetic circuitry, eliminated eupneic respiratory modulation of sympathetic activity and its cardiovascular derivatives (Traube-Hering waves, and respiratory sinus cardiac arrhythmia), and it attenuated the cardiovascular response to stimulation of peripheral chemoreceptors with cyanide (Baekey et al., 2008). This suggests that input from pontine respiratory neurones contributes to sympatho-respiratory coupling. Anatomical studies have indicated the existence of pontine projections to medullary VRC neurones (see section 1.3), that, in turn, may interact with pre-sympathetic neurones of the RVLM (Stornetta et al., 2016). Tracing experiments have reported direct projections between the pontine KF and parabrachial nuclei and RVLM C1 pre-sympathetic neurones (Stornetta et al., 2016). Computational models based on the inhibitory ring model suggest that pontine inspiratory-expiratory phase spanning respiratory neurones projecting to the RVLM may contribute to the enhanced I/Post-I sympathetic activity observed under eupnoeic conditions (Barnett et al., 2017).

Besides GABA-ergic and glutamatergic input from respiratory neurones, it should be noted that RVLM pre-sympathetic neurones are also reported to receive inputs from the hypothalamus (orexinergic and oxytocinergic), from the medullary raphe (serotonergic and substance P), and cholinergic inputs (Dampney, 1994a, Dampney, 1994b, Guyenet, 2006). It is possible that the function of such inputs relates to the regulation of sympathetic activity in accordance to wakefulness and vigilance (hypothalamic orexigenic input), and central chemoreflex activation (medullary raphe serotonergic input), but their role is currently not well understood.

To summarize, converging evidence of anatomical, functional, and computational studies suggest that sympatho-respriatory coupling occurs, at least in part, through interactions of rhythmogenic respiratory neurones of the VRC and of respiratory neurones of the

dorsolateral pons with RVLM pre-sympahtetic neurones. Furthermore, RVLM pre-sympathetic neurones receive respiratory rhythm-entrained inhibitory input from GABA-ergic neurones in the CVLM. (see **figure 1-8A**) Besides GABA-ergic and glutamatergic inputs, RVLM pre-sympathetic neurone activity is possibly regulated by a host of other transmitters (e.g. orexin, substance P, serotonin) of which the contribution and function in sympatho-respiratory interactions is currently poorly understood.

*Late-E sympatho-respiratory coupling in response to hypercapnia and peripheral chemoreceptor activation likely share common pathways.*

RVLM C1 gain/loss of function studies and single cell recordings of RVLM C1 neurones, both discussed in section 1.6.2, suggest that sympathetic Late-E activity and sympathetic I/Post-I activity are mediated by distinct pathways. Sympathetic late-E activity is likely not mediated by C1 pre-sympathetic neurones, but may be mediated by RVLM non-C1 pre-sympathetic neurones. Respiratory (AbN) Late-E activity in response to peripheral and central chemoreceptor activation is thought to have its origin in activity of late-E neurones in the pFRG region (see sections 1.4.4 and 1.5.2). Because sympathetic late-E activity appears in conjunction with respiratory late-E activity, it has been suggested that late-E sympathetic activity is likely a consequence of excitatory projections from pFRG late-E neurones to pre-sympathetic neurones in the RVLM which lies adjacent (Baekey et al., 2010, Molkov et al., 2011, Molkov et al., 2014a). The notion of a common pFRG drive for late-E sympathetic and respiratory activity, that is distinct from the drive of sympathetic I/Post-I activity, is supported by the finding that local injection of $GABA_A$ receptor agonist muscimol in the RTN/pFRG inhibited both the late-E respiratory and sympathetic responses, but did not affect the post-I sympathetic response to peripheral chemoreceptor activation (Moraes et al., 2012a). Carotid body stimulation was found to activate neurones in the RTN/pFRG region via direct projections from glutamatergic $2^{nd}$ order peripheral chemoreceptor neurones of the NTS in rats (Takakura et al., 2006). Computational models based on the inhibitory ring model were able to reproduce sympathetic and respiratory reflex responses to peripheral chemoreflex stimulation and hypercapnia with a model that assumes that enhanced excitatory drive from central chemoreceptors to pFRG late-E neurones drives the hypercapnic late-E sympathetic and respiratory response, and that excitation of pFRG late-E neurones via a direct excitatory projection from peripheral chemoreceptor neurones of the NTS drives the late-E sympathetic and respiratory response to peripheral chemoreceptor activation (see **figure 1-8B**) (Barnett et al., 2017).

*Functional connectivity underlying sympatho-respiratory coupling observed during peripheral chemoreceptor stimulation.*

The phasic post-I sympathetic activity pattern observed after peripheral chemoreceptor activation likely originates from 2nd order NTS peripheral chemoreceptor neurones that project to pontomedullary respiratory circuitry, of which output is projected to RVLM pre-sympathetic neurones. Section 1.5.2 addressed a computational modelling study which suggests that projections from excitatory second order peripheral chemoreceptor neurones in the NTS to post-I neurones in CVRG transmission circuitry may contribute to respiratory post-I bursts observed in the AbN, cVN, and HN after peripheral chemoreceptor activation (Barnett et al., 2017). This modelling study also assumes tSN post-I activity in response to peripheral chemoreceptor activation originates from excitatory drive of these CVRG post-I neurones to RVLM pre-sympathetic neurones (see **figure 1-8C**). These assumptions still require experimental verification. Nevertheless, they are plausible given that the model was comprised of minimal additions to a well validated framework, and the model allowed for *in silico* reproduction of experimentally observed sympathetic and respiratory activity under eucapnic/normoxic, hypercapnic, and hypoxic conditions. The RVLM C1 neurone loss-, and gain of function studies and single cell recordings addressed in section 1.6.2 suggest that the sympathetic peripheral chemoreflex is mediated by RVLM C1 pre-sympathetic neurones. Thus, one putative pathway via which Post-I sympathetic activity may occur is via excitatory drive from a population of Post-I neurones in cVRC transmission circuitry to C1 neurones in the RVLM.

Finally, there is support for a second source of tSN drive in response to peripheral chemoreceptor activation. This pathway is rather straightforward, and is comprised of a direct projection from commissural NTS neurones that receive input from CB afferents and have a direct glutamatergic projection to C1 pre-sympathetic neurones of the RVLM. This projection could be considered to underlie sympatho-respiratory coupling, as it involves sympathetic activity in response to peripheral chemoreceptor activation. However, it is thought to drive tonic, respiratory-independent, sympathetic excitation (Koshiya and Guyenet, 1996, Koshiya et al., 1993, Mandel and Schreihofer, 2009, Moraes et al., 2012b, Barnett et al., 2017).

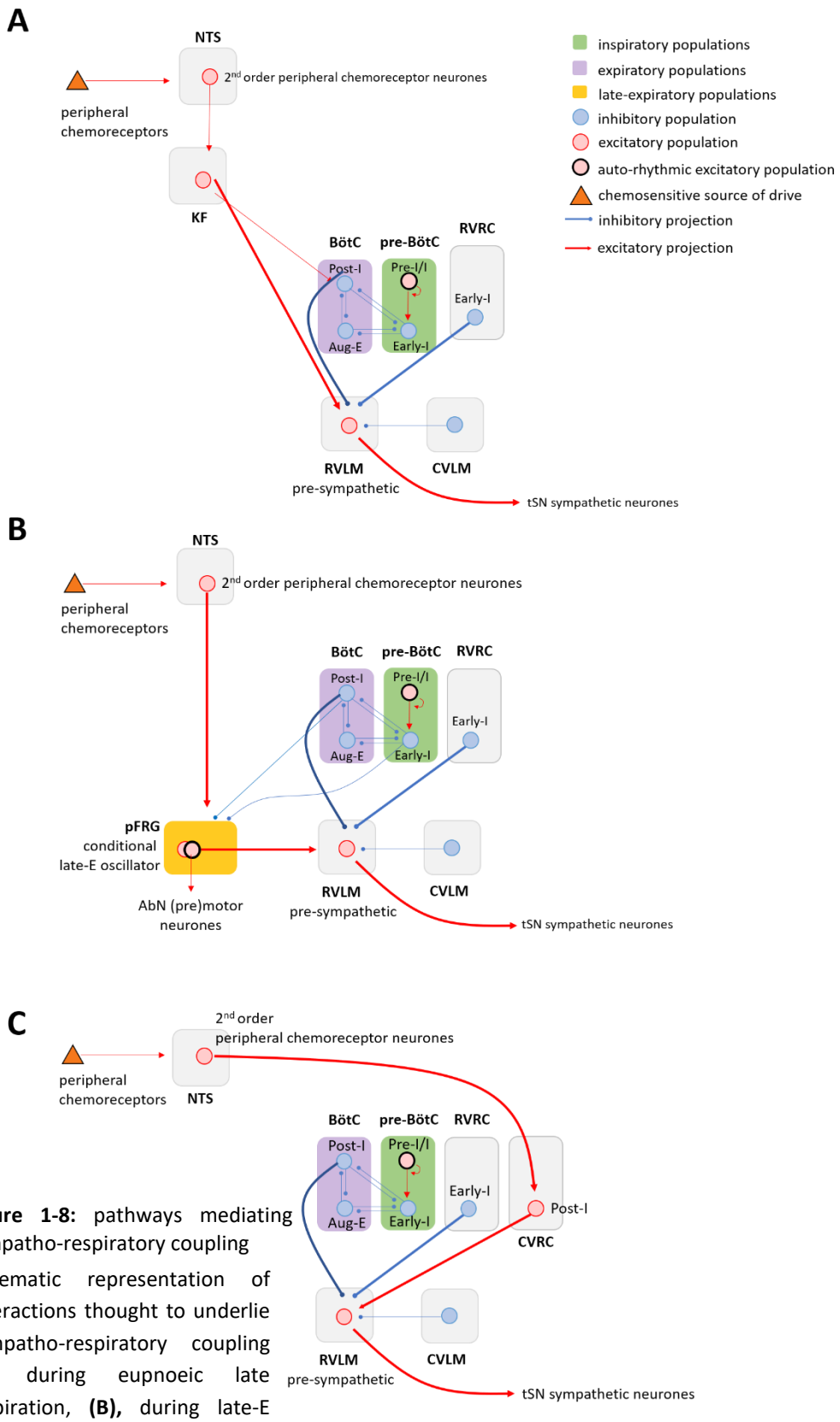


**Figure 1-8:** pathways mediating sympatho-respiratory coupling

Schematic representation of interactions thought to underlie sympatho-respiratory coupling **(A)** during eupnoeic late inspiration, **(B),** during late-E activity; **(C)** and during Post-I activity in the peripheral chemoreflex response. This figure legend is continued on the next page.

**Figure 1-8 caption, continued from previous page:** All interactions are originally proposed in a computational model by Barnett et al. (2017), which is an expansion of the inhibitory ring model. The schematics do not show the complete model but highlight selected elements of it for the sake of visual clarity. **(A)** Excitatory projections from inspiratory-to-expiratory phase spanning neurones of the KF to RVLM pre-sympathetic neurones are suggested to mediate eupnoeic sympatho-respiratory activity during late stages of inspiration. **(B)** Excitatory projections from pFRG late-E neurones to RVLM pre-sympathetic neurones are suggested to underlie late-E sympathetic activity. Excitatory projections from NTS 2$^{nd}$ order peripheral chemoreceptor neurones to the pFRG are suggested to mediate late-E sympathetic activity in response to peripheral chemoreceptor activation. **(C)** Excitatory projections from a hypothetical cVRG Post-I population are suggested to underlie Post-I sympatho-respiratory coupling in response to peripheral chemoreflex activation. Justification for all suggested projections and an explanation of the interactions is provided in section 1.6.2. Abbreviations: RVLM = rostral ventrolateral medulla; CVLM = caudal ventrolateral medulla; NTS = Nucleus tractus solitarius; KF = Kölliker-Fuse; VRC = ventral respiratory column, BötC = Bötzinger Complex, Pre-BötC = pre-Bötzinger Complex, RVRG = rostral ventral respiratory group, CVRG = caudal ventral respiratory group, pFRG = parafacial respiratory group.

## 1.7 SEROTONERGIC MODULATION OF RESPIRATORY CONTROL

The review of central chemoreflex mechanisms in respiratory control (section 1.4) addressed evidence for a role of raphe serotonergic (5-HT) neurones in respiratory control. The present section will further explore the role of 5-HT transmission in general, and 5-$HT_{1A}$ transmission in particular, in respiratory control.

### *1.7.1 Serotonergic transmission: a brief overview of cellular and physiological functions*

When considering the role of 5-HT transmission in respiratory control, it is important to be aware of its wide range of effects on cellular and physiological mechanisms. Before addressing the role of 5-HT transmission in respiratory control specifically, this section will briefly address some general properties of the serotonergic system that contribute to a better understanding of its role in respiratory control.

Serotonergic transmission has been implicated in the regulation of respiratory-, (Cummings and Hodges, 2019, Hodges and Richerson, 2008) and cardiovascular control (Watts et al., 2012), along with a wide range of other behaviours and physiological functions (i.e. the regulation of sleep, memory, feeding, mood regulation, sexual behaviour, temperature regulation, and pain signalling (Sahu et al., 2018). In addition, during development and in adult mammals, 5-HT signalling mediates trophic effects (e.g. cell proliferation, migration, differentiation, synaptogenesis, neurogenesis, cortical network organization) and influences synaptic plasticity (Sahu et al., 2018). The wide range of processes in which the serotonergic system is involved can be partly explained by a high variability and heterogeneity in terms of neuronal properties and receptor subtypes, and the serotonergic system's extensive connections with other brain regions.

To date, fifteen 5-HT receptor subtypes have been identified (5-$HT_{1A-F}$, 5-$HT_{2A-B}$, 5-$HT_3$, 5-$HT_4$, 5-$HT_{5A-B}$, 5-$HT_6$, and 5-$HT_7$). All 5-HT receptors are G-protein coupled receptors (GPCRs), with the exception of 5-$HT_3$ receptors, which are depolarizing ligand gated $Na^+$ and $K^+$ channels. 5-$HT_{1A,B,D-F}$, 5-$HT_{4B}$, and 5-$HT_5$ receptors classically couple with $G_{i-o}$ proteins, 5-$HT_{2A-C}$ receptors couple with $G_q$ proteins, and receptors 5-$HT_{4A}$, 5-$HT_6$, and 5-$HT_7$ couple with $G_s$ (Hannon and Hoyer, 2008). Through activation of various distinct G-protein-activated intracellular signalling cascades, 5-HT signalling can mediate a wide range of cellular functions. Grossly simplified, 5-$HT_1$ and 5-$HT_5$ signalling acts to inhibit neuronal activity via a decrease in cellular levels of cAMP, whereas 5-$HT_{2,4,6,7}$ signalling

typically results in neuronal excitation via increasing cellular cAMP (Hannon and Hoyer, 2008, Hodges and Richerson, 2008).

5-HT belong to a class of signalling molecules known as neuromodulators. That is, by driving biochemical changes (e.g. cAMP production, intracellular $Ca^{2+}$ levels, phosphorylation), 5-HT transmission has the ability to alter ion channel properties in target neurones and change their response to traditional neurotransmitters (Hodges and Richerson, 2008).

Within the central nervous system, serotonin is synthesized by raphe neurones in the midbrain, pons, and medulla which have extensive projections throughout the brain and spinal cord. This includes projections to regions of respiratory and sympathetic control in the medulla and pons (Richter et al., 2003)**.** Raphe neurones have a tonic activity pattern which can be modulated by sleep state, environmental cooling, repetitive motor activities (e.g. locomotion or mastication), and changes in $pCO_2$/pH (see section 1.4) (Richter et al., 2003). Peripherally, serotonin acts as a hormone, or auto- or paracrine factor, and is synthesized by both enteric neurones and enterochromaffin cells located in the gastrointestinal system (Jenkins et al., 2016). Systemic and central serotonin pools are separated by the blood brain barrier.

### *1.7.2 Broad serotonergic transmission in respiratory control*

*The role of the serotonergic system in respiratory control: evidence from complete loss of serotonergic function studies.*

5-HT knockout mouse models have been developed to assess the role of 5-HT transmission in respiratory control *in vivo*. One such 5-HT KO mouse model is derived from deletion of transcription factor Pet-1, which is uniquely expressed in all 5-HT neurones (Hendricks et al., 2003, Cheng et al., 2003). Pet-$1^{-/-}$ mice lack ~70% of their brainstem 5-HT neurones, and function of the residual 5-HT neurones is compromised (Hendricks et al., 2003). Pet-$1^{-/-}$ mice show prolonged apnoea (cessation of breathing), and a reduced respiratory frequency, both of which improve after the first 2 weeks of life (Erickson et al., 2007). More complete loss of 5-HT neurones was achieved in Lmx1b$^{f/f/p}$ mice which had conditional knockout of the LIM homeobox transcription factor (Lmx1b) gene exclusively in Pet-1 expressing cells. Lmx1b$^{f/f/p}$ mice have complete (~99%) and specific loss of central 5-HT neurones, and have severely reduced levels of central 5-HT (Zhao et al., 2006). They, too, show frequent apnoea and breathing arrhythmias that improve with age (after the first 2 weeks of life) (Hodges et al., 2009). In both Pet-$1^{-/-}$ and Lmx1b$^{f/f/p}$

mice, respiratory dysrhythmias could be reverted to a more regular respiratory pattern by central administration of 5-$HT_{2A}$ receptor agonist 2,5-dimethoxy-iodoamphetamine (DOI), substance P (SP) (alone or in combination with DOI), or 5-HT (Hodges et al., 2009). Despite normalization of baseline respiratory activity with age, both Pet-$1^{-/-}$ and $Lmx1b^{f/f/p}$ mice have significantly reduced ventilatory responses to hypercapnia as adults (Hodges et al., 2008, Cerpa et al., 2017). Intracerebroventricular infusion of 5-HT in $Lmx1b^{f/f/p}$ mice is reported to restore the hypercapnic ventilatory response to near control levels (Hodges et al., 2008).

Large scale genetic KO of all serotonergic neurones is a multifaceted manipulation of the central nervous system, and one cannot exclude developmental effects and/or compensatory mechanisms to occur. In an effort to overcome these caveats, acute loss of function studies have been performed utilizing inhibitory DREADD hM4Di receptors expressed in all 5-HT neurones (targeted by serotonin transporter SLC6A4 gene expression) in adult mice (Ray et al., 2011). Similar to the effect of 5-HT KO in adult mice, acute pharmacogenetic inhibition of 5-HT activity had no effect on baseline respiratory activity, but did reduce the central chemoreflex in adult mice *in vivo*.

To conclude, 5-HT KO mouse studies suggest that broad 5-HT transmission is involved in the central chemoreflex, but also in baseline respiratory control, at least during neonatal development. The ability to normalize baseline respiratory activity and the central chemoreflex by simply replacing missing neurotransmitters suggests the dysrhythmias in 5-HT KO mice are not due to trophic effects (e.g. altered developmental network formation). Acute loss of function of the serotonergic system via activation of DREADD hM4Di expressed in all 5-HT neurones in adult mice resulted in a similar respiratory pattern as seen in adult 5-HT KO mice: normal baseline activity but a reduced hypercapnic response. This suggests that the normalization of baseline respiratory activity observed in KO mice is likely not the result of a compensatory mechanism. These findings have been interpreted to suggest that the general function of the serotonergic system as a whole in respiratory control switches from providing tonic respiratory drive during the neonatal period, to providing $CO_2$ chemosensitive drive past neonatal age (Cerpa et al., 2017).

*Evidence for a role of serotonergic transmission in respiratory drive via mechanisms distinct from central chemoreceptor drive in rodents past neonatal age.*

The net effect of loss of function of the complete serotonergic system appears to affect central chemoreception, but not baseline respiratory activity. Nevertheless, more

selective manipulations of specific 5-HT receptor subtypes have been found to affect baseline respiratory activity in rats past neonatal age.

In *in situ* WHBP of juvenile rats, systemic administration of 5-$HT_4$ (GR113808) or 5-$HT_{2A}$ antagonist (MDL 11399) significantly reduced or completely eliminated the amplitude of integrated HN and PN burst activity, yet did not significantly affect HN and PN burst frequency (i.e. respiratory rate). In contrast, systemic administration of 5-$HT_{2C}$ antagonist (RS 102221) significantly decreased HN and PN burst frequency, and decreased their integrated burst amplitude. All three antagonists reduced population potential amplitudes and burst frequencies of pre-BötC inspiratory neurones in accordance with cognate effects observed in peripheral nerves (Ptak et al., 2009). In the same study, electrophysiological and IHC experiments indicate that direct 5-HT release from spontaneously active raphe obscurus neurones acts on 5-$HT_{2A/2C/4}$ receptors in the pre-BötC and HN motor nucleus in rhythmically active acute slices (Ptak et al., 2009). The rhythmically active slices were of neonatal rats, but the pharmacology in these slices is in line with that in the *in* situ preparations of juvenile rats. It is therefore possible that the mechanisms observed in slices of neonates are also preserved in the *in situ* preparations of juvenile rats. Together, these findings indicate that respiratory activity in rats is dependent on endogenous 5-HT transmission, with distinct effects mediated by various 5-HT receptor subtypes.

Gain of function via ChR2-mediated rhythmic stimulation of Pet-1 expressing 5-HT neurones of the raphe obscurus showed an increase in respiratory frequency and diaphragmatic EMG amplitude in adult mice in vivo (Depuy et al., 2011). This breathing stimulation was attenuated, but not abolished (-55%) by methysergide (an antagonist for all 5-HT receptors except 5-$HT_{1A/4}$). The residual potentiation may be dependent on 5-$HT_{1A/4}$ receptor transmission. Elevated $FiCO_2$ (8%) was still able to potentiate further (+16%) respiratory activity. Extracellular single unit recordings of ChR2 expressing 5-HT neurones in the raphe obscurus showed that these did not respond to hypercapnia (up to 10% $CO_2$) in anesthetized rats *in vivo*. Correspondingly, ChR2 stimulation of Pet-1 5-HT neurones in the raphe obscurus did not potentiate the hypercapnic (8% $CO_2$) respiratory response *in vivo*. Thus, serotonergic raphe obscurus neurones enhance respiratory drive via a mechanism distinct from that underlying respiratory central chemoreflex responses.

### *1.7.3 Serotonin 1A receptor transmission in respiratory control*

The subtype of 5-HT receptor that is most extensively expressed in the respiratory network is 5-$HT_{1A}$ (Richter et al., 2003). There is increasing interest in 5-$HT_{1A}$ receptor transmission for its ability to stabilize respiratory dysrhythmia, presumably through depression of inhibitory neurones in the network. The current section will review the evidence for the effect of 5-$HT_{1A}$ transmission on respiratory activity, and the mechanisms thought to underlie this effect.

*Molecular mechanisms by which 5-$HT_{1A}$ R transmission exerts inhibition of neurones.*

The primary signalling cascade by which 5-$HT_{1A}$ agonism affects intracellular processes is via an exchange of GDP for GTP on the α subunit of the inhibitory $G_{i/o}$ protein, which results in inhibition of adenylyl cyclase (AC), which then results in a decrease of cyclic adenosine monophosphate (cAMP) production, and ultimately, reduced protein kinase A (PKA) activity (Cooper and Londos, 1982). 5-$HT_{1A}$ receptors are also able to activate G protein-coupled inwardly rectifying potassium channels (GIRKs) (reviewed in Polter and Li (2010)). GIRK activation profoundly hyperpolarizes neurones and inhibits neuronal firing. GIRK activation is primarily mediated by G protein $\beta_\gamma$ subunits (Clarke et al., 1987). Also mediated by the G protein $\beta_\gamma$ subunit in response to 5-$HT_{1A}$ receptor activation, is the inhibition of voltage-gated $Ca^{2+}$ channel activity (Chen and Penington, 1996, Bayliss et al., 1997a). This results in a reduction of calcium entry. Thus, $G_{i\alpha}$ / $G_{o\alpha}$ activity in response to 5-$HT_{1A}$ receptor binding results in inhibition of intracellular mechanisms that are mediated by the AC-cAMP-PKA pathway. In addition, activation of G protein $\beta_\gamma$ subunits in response to 5-$HT_{1A}$ receptor activation results in activation of GIRK channels and inhibition of voltage gated $Ca^{2+}$ channels which results in direct inhibition of neuronal firing. A schematic representation of these signalling mechanisms in response to 5-$HT_{1A}$ receptor activation is provided in **figure 1-9.**

It should be noted that these are not the only mechanisms by which 5-$HT_{1A}$ receptors affect their host cells. In fact, 5-$HT_{1A}$ receptors are coupled to the broadest range of second messengers of all serotonergic receptors. Other intracellular pathways regulated by regulated by 5-$HT_{1A}$ receptors include, but are not limited to: the mitogen-activated protein kinases (MAPK/ERK) pathway; and the phosphoinositide 3-kinase (PI3K) and protein kinase B/Akt pathway (reviewed in Chilmonczyk et al. (2015)). Given their relevance to neural excitability, emphasis in the present thesis is on 5-$HT_{1A}$ mediated inhibition of the AC-cAMP-PKA pathway, activation of GIRKs, and inhibition of voltage gated $Ca^{2+}$ channels.

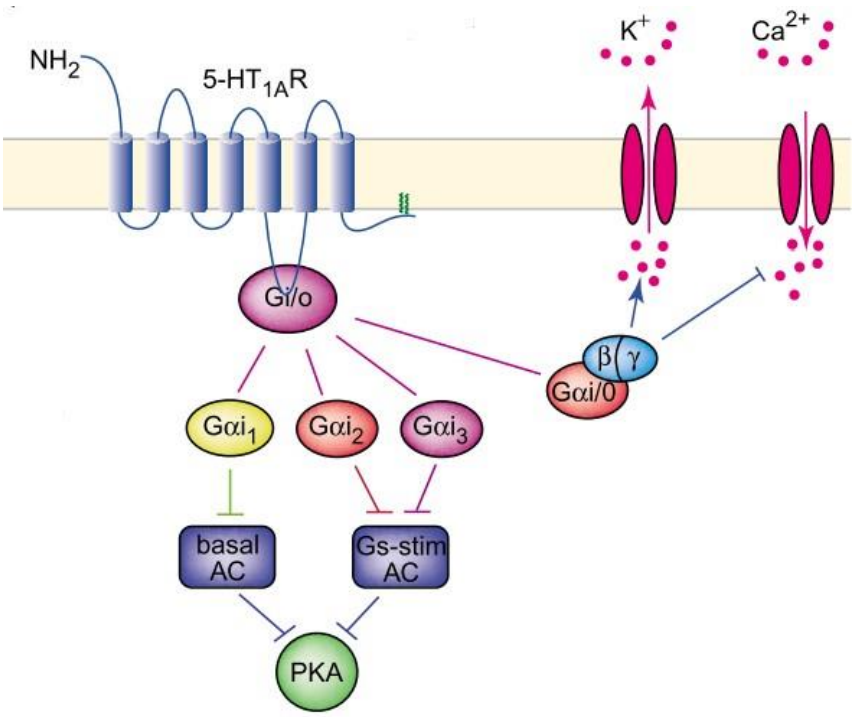


**Figure 1-9:** Signalling pathways regulated by the 5-$HT_{1A}$ receptor.

Giα/Goα activity in response to 5-$HT_{1A}$R binding results in inhibition of intracellular mechanisms that are mediated by the AC-cAMP-PKA pathway (left). In addition, activation of G protein βγ subunits in response to 5-HT1A receptor activation results in activation of GIRK channels and inhibition of voltage gated $Ca^{2+}$ channels which results in direct inhibition of neuronal firing (right). Figure adapted from Richter et al. (2003).

*Many studies report augmented respiratory activity in response to 5-$HT_{1A}$ R agonist treatment*

The majority of studies performed to investigate the effect of 5-$HT_{1A}$ receptors on respiratory activity has utilized the drug (R)-(+)-8-hydroxy-2-(di-n-propylamino) tetralin hydrobromide (8-OH-DPAT). This drug has high affinitiy for 5-$HT_{1A}$ receptors, but it is also reported to have moderate affinity for 5-$HT_7$ receptors in both rat (Hedlund et al., 2004) and human receptors (in human, 5-$HT_{1A}$ R pKi ranges from 8.4-9.4, and 5-$HT_7$ R pKi ranges from 6.3-7.6 (guidetopharmacology.org, ligand ID: 7)). Systemic or central administration of 8-OH-DPAT results in augmented amplitude and/or frequency of integrated respiratory muscle and/or motor nerve activity and in spontaneously breathing anesthetized adult rats and cats (Szereda-Przestaszewska and Kaczynska, 2007, Valic et al., 2008, Besnard et al., 2012, Besnard et al., 2009, Manzke et al., 2009) or in *in situ* WHBP of rats and mice (Manzke et al., 2009, Manzke et al., 2010). Subsequent administration of 5-$HT_{1A}$R antagonist and dopamine receptor D4 agonist WAY-100635 (Chemel et al., 2006, Martel et al., 2007) abolished these effects (Szereda-Przestaszewska and Kaczynska, 2007, Valic et al., 2008). Administration of WAY-100635 without any prior administration of 8-OH-DPAT reduced upper airway muscle respiratory activity in anesthetized rats (Besnard et al., 2012, Besnard et al., 2007)**,** and phrenic nerve activity in *in situ* WHBP of rats (Manzke et al., 2009) to below baseline levels. Thus, 5-$HT_{1A}$ receptors are endogenously active under baseline conditions and have an excitatory role in resting respiratory activity in *in vivo* and in *in situ* in rodents. The net effect of activation of 5-$HT_{1A/7}$ receptors with 8-OH-DPAT is also enhanced respiratory drive.

In an effort to get an impression of the relative contributions of 5-$HT_{1A}$ transmission and 5-$HT_7$ transmission to the effects on respiratory activity of 8-OH-DPAT administration, (Manzke et al., 2009) recorded phrenic nerve activity before and after administering 5-$HT_{1A}$ R or 5-$HT_7$ R agonists or antagonists in *in situ* WHBP of rats. Application of 5-$HT_7$R agonist (5-CT) significantly reduced minute respiratory activity derived from phrenic nerve activity. Respiratory activity was suppressed further after additional block of 5-$HT_{1A}$ receptor transmission with antagonist WAY-100635. Conversely, minute respiratory activity was enhanced when 8-OH-DPAT was administered after initial administration of 5-$HT_7$R antagonist (SB269970). Thus, while the net effect of 5-$HT_{1A/7}$ receptor activation with 8-OH-DPAT is a stimulation of respiratory activity, the effect of 5-$HT_7$ activation appears to be a reduction of respiratory drive. The increased respiratory activity observed after administration of 8-OH-DPAT appears attributable to activation of 5-$HT_{1A}$ receptors.

The effects of 8-OH-DPAT administration on resting respiratory activity in anaesthetised rats persisted after vagotomization, but carotid body denervation prevented the increase in breathing rate (Szereda-Przestaszewska and Kaczynska, 2007). Comparison of Fos expression in 8-OH-DPAT treated rats versus controls revealed significant increases in Fos expression after 8-OH-DPAT administration in the nucleus tractus solitarius, nucleus raphe pallidus, retrotrapezoid nucleus, lateral parabrachial, and Kölliker-Fuse nuclei (Besnard et al., 2012). 5-$HT_{1A}$ Receptors are expressed in the BötC, and pre-BötC (Manzke et al. 2009; Manzke et al. 2010), and commissural NTS of rats (Vantrease et al., 2015). Together, these findings suggest that key components of peripheral chemoreflex respiratory response circuitry (carotid bodies and NTS) are involved in the respiratory response to 8-OH-DPAT. By extension of the above findings, the peripheral chemoreflex response may be affected by 8-OH-DPAT. However, possible effects of 5-$HT_{1A}$ transmission on the peripheral respiratory chemoreflex remain unexplored to date. The central chemoreflex, on the other hand, is reported to be significantly attenuated (22% reduction) by microdialysis of 8-OH-DPAT in the proximity of the rostral raphe pallidus and raphe magnus regions in conscious rats (Li et al., 2006). Systemic administration of 8-OH-DPAT in *in situ* WHBP of juvenile rats results in a loss of the hypercapnic respiratory response (Corcoran et al. 2013). Finally, administration (i.v.) of 8-OH-DPAT resulted in a fall of arterial pressure in anesthetized rats (Szereda-Przestaszewska and Kaczynska, 2007). The mechanisms underlying this effect are currently unknown.

*5-$HT_{1A}$ autoreceptors and 5-$HT_{1A}$ heteroreceptors have opposing effects on respiratory control*

Serotonin 1A receptors can be found post-synaptically in various brainstem regions involved in respiratory control (BötC and pre-BötC (Manzke et al., 2009, Manzke et al., 2010), but they are also found in high numbers pre-synaptically in serotonergic raphe neurone somata and dendrites (Beaudoin-Gobert and Sgambato-Faure, 2014, Sotelo et al., 1990). The pre-synaptic 5-$HT_{1A}$ receptors are referred to as 5-$HT_{1A}$ autoreceptors, whereas post-synaptic 5-$HT_{1A}$ receptors on non-serotonergic neurones are denoted hetero-receptors. From a network perspective, 5-$HT_{1A}$ hetero-receptors and auto-receptor transmission have inverse effects. 5-$HT_{1A}$ auto-receptor activation decreases serotonergic tone and inhibits further 5-HT release, and thereby constitutes a negative feedback loop that inhibits the entire 5-HT system. This means that 5-$HT_{1A}$ auto-receptor activation can result in reduction of 5-$HT_{1A}$ heteroreceptor activation (Chilmonczyk et al., 2015).

Until recently, little was known about the relative contribution of both populations of receptors to the net effect of 5-$HT_{1A}$ agonism on respiratory control. In order to differentiate auto-receptor versus hetero-receptor effects of 8-OH-DPAT on respiratory drive, Corcoran et al. (2014) used rhythmically active medullary slices with HN rootlets from WT mice and from Lmx1bf/f/p neonatal mice which had a complete absence of central 5-HT neurones (i.e. no 5-HT1a auto-receptors, only hetero-receptors) and recorded the HN respiratory output in response to 8-OH-DPAT *in vitro*. 8-OH-DPAT bath application promoted increased hypoglossal nerve burst frequency in slices from $Lmx1b^{f/f/p}$ mice, but not in slices from WT mice. This effect was abolished by blockade of synaptic inhibition via bath co-administration of $GABA_A$-, and glycine receptor antagonists (gabazine, CPG 55845, and strychnine). Interestingly, after 10 minutes of 8-OH-DPAT administration, HN burst frequency returned to baseline levels in slices from $Lmx1b^{f/f/p}$ mice, but was depressed in slices from WT rats. The authors concluded that 5-$HT_{1A}$ hetero-receptors and auto-receptors may have physiologically competing effects: fast-onset stimulation of breathing due to hetero-receptor mediated inhibition of glycinergic and GABAergic respiratory interneurones (disinhibition), and slow-onset inhibition due to auto-receptor agonism.

*5-$HT_{1A}$ transmission may enhance respiratory drive through suppression of inhibitory respiratory interneurones.*

5-$HT_{1A}$ receptor transmission inhibits its host neurones, yet the effect of 8-OH-DPAT administration on the respiratory network is stimulatory. The augmented respiratory drive has been postulated to be the result of augmented glycinergic transmission in inhibitory respiratory interneurones, leading to disinhibition of their post-synaptic targets (Shevtsova et al., 2011, Manzke et al., 2009, Manzke et al., 2010).

*In vivo* patch clamp recordings of Post-I neurones in the BötC, combined with simultaneous recordings of the phrenic nerve in anesthetised cats revealed that systemic administration of 8-OH-DPAT increases excitability of these neurones. This effect was most pronounced in post-I neurones, which are putatively glycinergic (Ezure et al., 2003, Schmid et al., 1991). The recorded Post-I neurones exhibited a release from inspiratory inhibitory input, causing them to advance the onset of their bursting activity far into the preceding inspiratory phase of the respiratory cycle. At higher concentrations of 8-OH-DPAT, this release of inspiratory inhibition was combined with a hyperpolarizing $K^+$ current that suppressed action potentials of these post-I neurones throughout most of the respiratory cycle (low levels of late inspiratory activity persisted, coincident with

depolarizing post-synaptic currents). At the network level, the authors also observed a shortening of both the inspiratory and expiratory phase, which resulted in an increase in PN burst frequency, after administration 8-OH-DPAT. The responses to systemic 8-OH-DPAT at the network level (PN output) and at the cellular level (Post-I neurone activity) observed by Manzke et al. (2009) were reproduced *in silico* in computational simulations based on extensions of the inhibitory ring model (Shevtsova et al., 2011). This computational model hypothesises that systemic administration of 8-OH-DPAT at low concentrations results in 5-$HT_{1A}$R mediated augmentation of glycine α3 receptor (Gly$\alpha_3$R) inhibitory currents in Early-I and Aug-E neurones. This was suggested to contribute to the shortening of inspiratory and expiratory phase durations observed in PN activity. Additionally, suppression of Early-I neurones was hypothesised to result in a release from post-synaptic inhibition of Post-I neurones during inspiration. This release from inspiratory inhibition is suggested to underlie the advancement of Post-I neurone activity into the inspiratory phase. The near-complete silencing of Post-I neurones through hyperpolarizing $K^+$ currents, which was observed at higher concentrations of 8-OH-DPAT, was suggested to be the result of 5-$HT_{1A}$ R mediated activation of GIRK channels in Post-I neurones.

The notion that the augmented respiratory drive is mediated by modulation of glycinergic transmission is inspired by the finding that 8-OH-DPAT directly induced dephosphorylation of $Gly_{\alpha3}$R's, which augmented glycine-activated inhibitory $Cl^-$ currents in HEK293 cells co-expressing 5-$HT_{1A}$ and $Gly_{\alpha3}$R's (Manzke et al., 2010). Further, 8-OH-DPAT mediated enhancement of PNA frequency was abolished when glycine receptors were blocked by systemic application of strychnine before or after administration of 8-OH-DPAT *in situ* and *in vivo* in rats (Manzke et al., 2010, Manzke et al., 2009). The latter findings, however, are difficult to interpret, as systemic blockade of glycinergic transmission likely has confounding effects on respiratory CPG network interactions. With regard to the computational model by Shevtsova et al. (2011), it should be noted that the assumed distribution of $Gly_{\alpha3}$R and 5-$HT_{1A}$ Receptor (co)expression in various VRC respiratory neurone functional subpopulations is not experimentally verified. Furthermore, potential effects of 5-$HT_7$ transmission on the respiratory network, or potential 5-$HT_{1A}$-mediated modulation of receptors other than $Gly_{\alpha3}$R's are not taken into account. Nonetheless, the model is able to reproduce experimental findings at both the cellular and network level, and it provides testable hypotheses on putative mechanisms by which systemic 5-$HT_{1A}$ transmission may affect respiratory activity.

## 1.8 THERAPEUTIC RELEVANCE OF 5-HT$_{1A}$ TRANSMISSION

Recently, there is increased interest in the therapeutic potential of 5-HT$_{1A}$ receptor agonists for treatment of breathing abnormalities. This section will discuss the potential of 5-HT$_{1A}$ agonists in the in the treatment of opioid induced respiratory depression, and in symptomatic treatment of respiratory dysrhythmia in Rett syndrome.

### *1.8.1 Therapeutic relevance of 5-HT$_{1A}$ transmission in averting opioid induced respiratory depression.*

Opioid-based analgesics are the most often used therapeutic drugs for the relief of moderate to severe nociceptive pain that may occur following surgical operation or major trauma, or for the management of chronic nociceptive pain. An opioid-related adverse effect is respiratory depression due to inhibitory μ-opioid receptor (μOR) activation in brainstem regions of respiratory control (Dahan et al., 2018). This is of particular concern to clinicians as respiratory depression is potentially lethal. Outside the clinic, too, overdose of prescription or illicit opioids, or co-administration of opioids with central nervous system depressants may evoke respiratory depression. One strategy to mitigate opioid induced depression is to counteract it through co-treatment with respiratory stimulants. To be effective, the respiratory stimulants should prevent respiratory depression, without affecting the analgesic effect of opioids.

The augmented respiratory drive in response to 5-HT$_{1A}$ receptor agonists reveals a potential strategy to avert opioid-induced respiratory depression. 5-HT$_{1A/7}$ agonist 8-OH-DPAT has been postulated to enhance respiratory drive via augmented glycinergic (Shevtsova et al., 2011, Manzke et al., 2009, Manzke et al., 2010) transmission in inhibitory respiratory interneurones, leading to disinhibition of their post-synaptic targets (see section 1.7.3). Systemic administration 8-OH-DPAT is reported to also counteract respiratory depression in response to fentanyl (μOR agonist) in *in situ* WHBP of juvenile rates in *in vivo* rats (Manzke et al., 2009, Shevtsova et al., 2011, Dutschmann et al., 2009b, Guenther et al., 2009), without antagonising anti-nociception (Guenther et al., 2009). Enhancement of respiratory drive in response to 8-OH-DPAT administration is suggested to be mediated by 5-HT$_{1A}$ transmission induced dephosphorylation of Gly$_{\alpha 3}$ receptors, which resulted in augmented glycinergic inhibition (Shevtsova et al., 2011, Manzke et al., 2009, Manzke et al., 2010) (see section 1.7.3). This notion is consistent with the finding that 5-HT$_{1A}$ receptor activation with 8-OH-DPAT failed to counteract opioid reduced respiratory depression in Gly$_{\alpha 3}$ receptor deficient mice (Manzke et al., 2010). Since 5-HT$_{1A}$

R mediated potentiation of glycinergic currents is a pathway distinct from opioid receptor activation, it is plausible that 5-$HT_{1A}$ transmission can enhance respiratory drive without interfering with opioid analgesic effects. Therefore, 5-$HT_{1A}$ receptor agonists may have potential for clinical use in prevention of opioid-induced depression.

The problem with most available 5-$HT_{1A}$ receptor agonists today is insufficient selectivity (Dahan et al., 2018). Sufficient efficacy is also important, as the selective, but partial 5-$HT_{1A}$ receptor agonist buspirone was found not effective to reverse morphine induced respiratory depression in humans (Oertel et al., 2007). 8-OH-DPAT is not available for clinical use and has moderate affinity for 5-$HT_7$ receptors. A recently developed highly selective 5-$HT_{1A}$ full agonist NLX-112 (also known as befiradol or F13640) was reported to induce robust reduction of fentanyl induced respiratory depression in rats. However, in contrast to earlier findings with 8-OH-DPAT by Guenther et al. (2009), the authors also report concomitant decreases in fentanyl-induced analgesia, and altered nociception (Ren et al., 2015). The underlying mechanisms for the latter are as yet unclear.

### *1.8.2 Therapeutic relevance of 5-$HT_{1A}$ transmission in rescue from respiratory dysrhythmia symptoms in Rett syndrome.*

Rett syndrome (RTT) is a neurological disorder most often caused by loss of function of transcriptional regulator methyl-CpG-binding protein 2 (MeCP2) (Chahrour et al., 2008, Percy, 2016, Young et al., 2005). RTT is most often linked to mutations in the X linked gene that encodes MeCP2, and it affects 1 in ~10,000 live female births (Chahrour and Zoghbi, 2007). RTT in males is rare, as most boys with MECP2 mutations die in utero or early infancy (Jiang et al., 2017). Symptoms in humans start at 6-18 months after birth, and include severe mental disability, epilepsy (Dolce et al., 2013), and dystonia, and dyskinesia (Chahrour and Zoghbi, 2007). An additional, life-threatening symptom of RTT is breathing abnormalities as a result of brainstem dysfunction. Breathing abnormalities account for ~26% of sudden and unexpected deaths in RTT patients (Weese-Mayer et al., 2006, Bissonnette and Knopp, 2006). The severity and development of clinical symptoms in RTT are variable, putatively as a result of random X-chromosome inactivation (Nagarajan et al., 2008), but respiratory abnormalities typically include: apneusis (abnormally prolonged inspiration producing breath-holding, followed by inadequate expiration) or episodic apnoea (cessation of breathing); Valsalva breathing (active expiration against a closed glottis); air swallowing; gasping; and Cheyne-Stokes breathing (alternating hyper- and

hypoventilation) (Ramirez et al., 2013, Bissonnette and Knopp, 2006, Weese-Mayer et al., 2006)

The symptoms of respiratory dysrhythmia in humans with RTT can be reliably mimicked by knockout or loss-of-function mutations of the MeCP2 gene in female (MeCP2 $^{-/+}$) or male (MeCP2$^{-/Y}$) mice (reviewed in Jiang et al. (2017)). Even though complete loss of MeCP2 is lethal in human males, hemizygous MeCP2$^{-/Y}$ male mice can survive up to twelve weeks. MeCP$^{-/Y}$ mice develop breathing abnormalities from 2-3 weeks of age, and experience phenotypic regression which ultimately becomes lethal. Female Mecp$^{+/-}$ mice, on the other hand, have a normal lifespan and develop breathing abnormalities after 6-7 months of age (Abdala et al., 2010, Levitt et al., 2013, Samaco et al., 2013, Schmid et al., 2012). Male Mecp$^{-/Y}$ mouse models present a relatively homogenous pathological phenotype compared to humans with RTT (Chao et al., 2007), which is useful for systematic dissection of the mechanisms underlying the symptoms in this mouse model. However, as RTT occurs primarily in human females, Mecp2$^{-/Y}$ mice provide limited translational applicability. Therefore, therapeutic strategies derived from experiments with Mecp$^{-/y}$ mice need to be validated in Mecp2$^{+/-}$ females.

*Chemoreflex function disturbances are thought to underlie frequent apnoea in mouse and human*

Two known contributing factors to the respiratory symptoms in RTT mouse models and humans with RTT are reduced $CO_2$ sensitivity, and a disruption of interactions between pontine and medullary regions of respiratory control. The current section will address the reduced $CO_2$ sensitivity, the section thereafter will address the disruption of ponto-medullary interactions.

The prevalence of breathing dysrhythmia in humans and RTT mice appears negatively correlated with the $CO_2$ sensitivity of the respiratory network. Both male Mecp2$^{-/Y}$ (Zhang et al., 2011b) and female Mecp2$^{+/-}$ mice (Bissonnette et al., 2014) show reduced $CO_2$ sensitivity. Specifically, Mecp2$^{-/Y}$ mice fail to increase ventilation in response to moderate hypercapnia (1-3% $PCO_2$), and only respond with increased tidal volume and respiratory rate to severe hypercapnia (6-9% $PCO_{2)}$ (Zhang et al., 2011b). Crucially, enhanced respiratory drive in response to high $pCO_2$ was coupled with a drastic inhibition of breathing irregularity in male Mecp2$^{-/Y}$ mice (Zhang et al., 2011b). Consistent with these findings, brainstem expression of multiple $CO_2$/pH sensitive ion channels is altered in a way that results in reduced pH sensitivity of their host neurones in male Mecp2$^{-/Y}$ mice

(Zhang et al., 2011b). In humans (Smeets et al., 2006, Halbach et al., 2012) as well as Mecp2$^{+/-}$ mice (Bissonnette and Knopp, 2006), periods of hyperventilation and forceful breathing often alternate with periods of hypoventilation and apnoea. The repeated alternation between hyper- and hypoventilation is thought to be exacerbated by reduced $CO_2$ sensitivity. Episodes of forceful breathing and hyperventilation result in hypocapnia. This, in combination with an upwards-shifted apnoeic threshold due to reduced $CO_2$ sensitivity then promotes episodes of apnoea (Bissonnette and Knopp, 2006, Toward et al., 2013), which leads to oxygen desaturation (Southall et al., 1988) and likely contributes to repetition of hyperventilation. Thus, in both humans with RTT, and in male and female Mecp2 deficient mice, reduced $CO_2$ sensitivity leads to an increased apnoeic threshold. This can promote apnoea and contribute to repeated alternation of hyper- and hypoventilation.

*Pontine contributions to respiratory dysrhythmia in Rett syndrome*

In *in situ* WHBP of Mecp2$^{-/Y}$ male mice, and Mecp2$^{+/-}$ female mice, apnoea are characterized by enhanced activity and duration of Post-I activity in the cVN during the initial portion of the apnoea (Stettner et al., 2007, Abdala et al., 2010), combined with tonic discharge of the HN throughout the apnoea (Abdala et al., 2010). As addressed in section 1.1.2 Post-I cVN activity is linked to contraction of the laryngeal adductors that control expiratory airflow via closure of the glottis.

Section 1.3.2, describes how Post-I activity is mediated by excitatory drive from the pontine KF to post-I neurones in the BötC. Active breath-hold, apnoea, and Valsalva manoeuvres through laryngeal adductor contraction, common features of disordered breathing in RTT, are suggested to be the result of disrupted ponto-medullary gating of Post-I activity (Abdala et al., 2014a, Ramirez et al., 2013). Ponto-medullary gating of Post-I activity is also thought to control inspiratory to expiratory phase transitioning and the duration of inspiratory and expiratory phases (Barnett et al., 2018) (see section 1.3.2). Disruption of pontomedullary mechanisms for inspiratory-to-expiratory phase transitioning can result in the respiratory dysrhythmia often observed in the RTT respiratory phenotype, as it leads to disrupted timing of termination of the inspiratory phase, and expiratory phase duration irregularity. Thus, disruptions in the rhythm and pattern of excitatory drive from KF neurones projecting to BötC Post-I neurones are thought to contribute to RTT respiratory symptoms related to control of laryngeal contraction and disruptions in respiratory phase transitioning.

Excitatory drive from the KF to post-I BötC neurones can be mediated by inhibitory transmission in the parabrachial complex. Previous sections (section 1.4.4) reviewed evidence that modulation of inhibitory transmission in the KF via focal administration of $GABA_A$ agonist or antagonist inhibits and enhances, respectively, Post-I activity in *in situ* WHBP of rats (Jenkin et al., 2017, Abdala et al., 2016). $Mecp2^{+/-}$ mice show deficiency of GABA perisomatic bouton-like puncta in the KF (Abdala et al., 2016). It is therefore plausible that deficits in synaptic inhibition in the KF underlie the exacerbation in Post-I activity which contributes to the breathing abnormalities in RTT. Indeed, systemic administration of GABA reuptake blocker (NO-711 hydrochloride) markedly reduced occurrence of central apnoea in Mecp2 deficient mice (Abdala et al., 2010). This effect was recapitulated with focal micro-injections of NO-711 in the KF of $Mecp2^{+/-}$ mice (Abdala et al., 2016). Conversely, blockade of $GABA_A$ receptors in the KF of WT rats with micro-injections of $GABA_A$ antagonist bicuculline mimicked the RTT respiratory phenotype of recurrent central apnoea and prolonged Post-I activity (Abdala et al., 2016). Therefore, pharmacotherapeutic enhancement of synaptic inhibition in the KF may be an effective strategy for reversal of respiratory abnormalities in Rett syndrome.

*Therapeutic potential of 5-$HT_{1A}$ agonists in symptomatic treatment of abnormal breathing in Rett syndrome*

Deficits in inhibitory transmission could be treated with drugs that augment GABAergic transmission. Benzodiazepines, positive modulators of $GABA_A$ receptors, can be effective in reversing respiratory dysrhythmia (Abdala et al., 2010), yet they are suboptimal for clinical application due to their addictive and sedative properties. Moreover, GABA is one of the main inhibitory neurotransmitters and it has an important role in the generation of respiratory rhythm (and many other functions in the brain), it is therefore not a suitable therapeutical target for selective stabilization of respiratory rhythm. Indeed, although augmented GABAergic transmission can reduce isolated apnoea and periodic breathing in $Mecp2^{+/-}$ mice, it also results in a distorted respiratory pattern relative to that of naive WT mice (Abdala et al., 2010). This prompted the search for alternative inhibitory neurotransmitters that might be of clinical relevance to reverse abnormal breathing patterns in RTT.

Deficiencies of 5-HT neurotransmission have been found in Mecp2 deficient mice, and in humans with RTT. In humans suffering from RTT, deficiency of 5-hydroxyindoleacetic acid (5-HIAA), a 5-HT metabolite, was found in spinal fluid (Samaco et al., 2009). Similarly, low brain concentrations of 5-HT were found in $Mecp2^{-/Y}$ male mice, and this deficiency

progressed with age (Ide et al., 2005, Viemari et al., 2005). In Mecp2$^{-/Y}$ mice, brain concentrations of 5-HT precursor tryptophan were comparable to WT mice, which suggests 5-HT deficiencies in these mice are due to a failure in 5-HT biosynthesis (Ide et al., 2005, Viemari et al., 2005). Systemic administration of citalopram, a selective serotonin reuptake inhibiter, was found to reverse reduced $CO_2$ sensitivity in Mecp2 deficient conscious mice (Toward et al., 2013). Further, systemic administration (Abdala et al., 2010) or focal micro-injection in the KF (Abdala et al., 2014b) of 5-HT$_{1A/7}$ receptor agonist (8-OH-DPAT) can depress respiratory apnoea in Mecp2$^{-/+}$ conscious mice and *in situ* WHBP of Mecp2$^{+/-}$ mice, respectively. It is, therefore, suggested that restoration of KF inhibitory transmission can also be mediated by augmented transmission of inhibitory 5-HT$_{1A}$ receptors, resulting in a clinically relevant stabilization of the respiratory pattern in mouse models of RTT (Abdala et al., 2014a, Wittman et al., 2019). Together, these findings suggest that manipulation of 5-HT transmission may be an effective strategy for symptomatic treatment of breathing abnormalities in RTT.

The search for 5-HT$_{1A}$ R agonists with clinical potential to stabilize respiratory activity and enhance respiratory drive is still ongoing. Sarizotan is a clinically approved 5-HT and D2-Like receptor agonist previously tested for L-dopa induced dyskinesia in the treatment of Parkinson's disease (Goetz et al., 2007). In separate 7 day and 14 day studies, sarizotan reduced the incidence of apnoea (to 15% of pre-treatment level) and irregular breathing in three different female mouse models of RTT in conscious animals (Abdala et al., 2014b). This indicates that sarizotan is a viable candidate for clinical treatment of abnormal breathing in RTT. However, a phase 2/3 clinical trial with sarizotan for the symptomatic treatment of respiratory dysrhythmia in Rett syndrome has recently been terminated due to lack of efficacy (ClinicalTrials.gov Identifier: NCT02790034).

A second family of 5-HT$_{1A}$ receptor agonists that may have clinical potential are 1-(1-benzoylpiperidin-4-yl)methanamine derivates, of which drug discovery and clinical development is an ongoing process (Sniecikowska et al., 2019a, Sniecikowska et al., 2019b). One 1-(1-benzoylpiperidin-4-yl)methanamine derivate of note is the selective 5-HT$_{1A}$R agonist NLX-101 (formerly named F15599). In rat cortex, striatum, and hippocampal tissue, NLX-101 showed 1000-fold higher binding affinity for 5-HT$_{1A}$ receptors over other 5-HT receptors, and over dopamine-, and adrenoreceptors *in vitro*. In addition, NLX-101 did not interact with a wide range of other receptors, ion channels, or monoamine transporters (Newman-Tancredi et al., 2009). Given its high selectivity for 5-HT$_{1A}$ receptors, this novel compound may also have therapeutic potential for treatment

of respiratory symptoms in Rett syndrome. Systemic administration of NLX-101 was found to reduce apnoea and improve breath irregularity in unanaesthetised male $Mecp2^{-/Y}$ and female $Mecp2^{-/+}$ mice *in* vivo in a dose dependent manner (Levitt et al., 2013). Interestingly, NLX-101 is reported to preferentially activate Gαi subunits over Gαo subunits at 5-$HT_{1A}$ receptors *in vitro* (Newman-Tancredi et al., 2009). Differences in host cell environment can determine which G-proteins interact with a G-protein coupled receptor (GPCR). This can result in differential recruitment of intracellular responses in response to GPCR agonism across neural subpopulations. *In vivo* and *ex vivo* experiments in rats reveal that NLX-101 induces hetero-receptor mediated responses with greater potency than it induces auto-receptor mediated responses (Llado-Pelfort et al., 2010). Similarly, pharmacological magnetic resonance imaging (phMRI) and positron emission tomography (PET) studies in cats and rats reveal that systemic administration of NLX-101 results in anatomical patterns of energy metabolism that suggest preferential activation of cortical regions over raphe regions (Becker et al., 2016, Levigoureux et al., 2019, Vidal et al., 2018, Vidal et al., 2020). Based on these findings, it has been suggested that the preferential activation of Gαi subunits over Gαo subunits at 5-$HT_{1A}$ receptors may translate to a functional bias of NLX-101 for hetero-receptors over auto-receptors (Llado-Pelfort et al., 2010). It should be noted that, from a clinical perspective, functional bias of a drug is only relevant when one can achieve clinical efficacy at the desired cell population without also saturating the response of the less responsive populations. To illustrate, in the above-mentioned experiments by Levitt et al. (2013), despite putative selectivity for hetero-receptors, the experimental dose (1μM) of NLX-101 was sufficient to activate 5-$HT_{1A}$ auto-receptor mediated G protein-coupled inwardly rectifying potassium channels (GIRK) conductance in all recorded (n=7) dorsal raphe neurones. Whether the suggested functional bias for hetero-receptor activation of NLX-101 is clinically relevant, remains to be established.

## 1.9 THESIS AIMS

The previous sections of this general introduction outlined how eupnoeic breathing and respiratory reflex responses are the result of an interplay between medullary rhythmogenic circuitry, pontine inputs, inputs from central chemoreceptor neurones in the RTN and raphe nuclei, and CB peripheral chemoreceptor input relayed via the NTS. Furthermore, interactions between the respiratory CPG, the CVLM, and RVLM pre-sympathetic neurones mediate the coupling of respiratory activity to sympathetic activity. 5-$HT_{1A}$ R transmission is thought to modulate the respiratory control network. However, the precise effects of selective 5-$HT_{1A}$R transmission on respiratory and respiratory-entrained sympathetic output, and the putative mechanisms from which such effects arise, are poorly understood.

### *1.9.1 5-$HT_{1A}$ transmission in respiratory control: current knowledge of its effects and mechanisms, and the gaps in understanding.*

Systemic administration of 5-$HT_{1A}$ R agonists is reported to enhance respiratory drive (Szereda-Przestaszewska and Kaczynska, 2007, Valic et al., 2008, Besnard et al., 2012, Besnard et al., 2009, Manzke et al., 2009, Manzke et al., 2010) (see section 1.7.3) and stabilize the respiratory rhythm (Abdala et al., 2010, Abdala et al., 2014b, Abdala et al., 2014a, Levitt et al., 2013) (see section 1.8.2). Pharmacological therapies targeting 5-$HT_{1A}$ transmission are therefore thought to have therapeutic potential for the treatment of respiratory depression or respiratory dysrhythmia. Various mechanisms have been proposed to explain these effects, many of which rely on 5-$HT_{1A}$ R mediated inhibition of inhibitory neurones, resulting in disinhibition of inspiratory populations (Shevtsova et al., 2011). A feature that the mechanisms suggested to underlie 5-$HT_{1A}$ mediated enhancement of respiratory drive and stabilization of respiratory rhythm have in common, is that they are linked to activity at 5-$HT_{1A}$ heteroreceptors, i.e. 5-$HT_{1A}$ receptors expressed on non-serotonergic neurones. Moreover, activity at auto-receptors, i.e. those expressed on serotonergic neurones, could have negative effects on ventilation thwarting some of the expected therapeutic benefit. For instance, 5-$HT_{1A}$ transmission at the rostral raphe pallidus and raphe magnus is reported to affect the respiratory central chemoreflex response in rats (Li et al., 2006) (see section 1.7.3). It has been proposed that activation of 5-$HT_{1A}$ auto-receptors at chemosensitive raphe neurones, would reduce 5-HT release at their target sites, thereby reducing central chemoreceptor tonus and reflex responses (Corcoran et al., 2014). Activity at these pathways is expected to produce negative effects on ventilation, since activity of central chemosensory neurones provides an essential tonic

drive to inspiratory neurones (see section 1.4). The simultaneous recruitment of physiologically antagonistic pathways by 5-$HT_{1A}$ agonists imposes significant limitations on the interpretation of literature data, especially since the most commonly used pharmacological tools had a less than ideal selectivity profile and no evidence of heteroreceptor bias.

Previously, effects of 5-$HT_{1A}$ transmission on respiratory drive have predominantly been assessed with the use of a non-selective 5-$HT_{1A/7}$ agonist (8-OH-DPAT). Some studies have used cocktails of 5-$HT_{1A/7}$R agonist and 5-$HT_7$ antagonist, or selective 5-$HT_7$R agonists to establish the relative contributions of each receptor type to the effect of 8-OH-DPAT (Manzke et al., 2009). However, the suppression of 5-$HT_7$ transmission itself in such experiments introduces confounding manipulations of the respiratory network, and one should be cautious to interpret the effects of 5-$HT_7$ antagonism combined with 5-$HT_{1A/7}$ agonism as if it were a selective manipulation of 5-$HT_{1A}$ transmission. Thus, direct experimental evidence of the effect of selective 5-$HT_{1A}$ R agonism on resting breathing, central and peripheral chemosensory control, and sympatho-respiratory coupling remains to be established. Such information would be relevant to assess the therapeutic potential and potential adverse effects of 5-$HT_{1A}$ agonists in the treatment of respiratory rhythm disorders. Further, proposed theories on putative mechanisms underlying the effect of 5-$HT_{1A}$ transmission on respiratory control assume an important role for 5-$HT_{1A}$ mediated inhibition of inhibitory neurones in the respiratory CPG. However, the 5-$HT_{1A}$ R expression profile throughout key brainstem regions of the respiratory CPG, and the further phenotype of neurones expressing 5-$HT_{1A}$ receptors (e.g. whether they are inhibitory neurones), is currently largely unknown. Finally, the current model describing putative network interactions suggested to underlie the effect of 5-$HT_{1A}$ transmission on respiratory control assumes expression of 5-$HT_{1A}$ R (and Glyα3 R) at specific respiratory neurone subpopulations (e.g. Pre-I/I-, Early-I-, Ramp-I-, Post-I/Dec-E, and Aug-E neurones) (Manzke et al., 2009, Manzke et al., 2010, Shevtsova et al., 2011) (see section 1.7.3). However, the distribution of 5-$HT_{1A}$R among these functional respiratory neurone subtypes is yet to be experimentally established.

### *1.9.2 Thesis aim and general hypothesis*

The overarching aim of this thesis is to establish the effects of systemic administration of selective 5-$HT_{1A}$ R agonist (NLX-101) on respiratory motor outputs and respiratory modulation of sympathetic activity, during rest and homeostatic respiratory reflexes, as

generated by the intact respiratory CPG network in *in situ* WHBP of juvenile rats. NLX-101 is a highly selective 5-$HT_{1A}$ R full agonist with suggested biased agonism properties that are thought to translate to preferential activation of 5-$HT_{1A}$ hetero-receptors over auto-receptors (Llado-Pelfort et al., 2010, Newman-Tancredi et al., 2009) (see section 1.8.2). Whether NLX-101's pharmacology involves biased agonism or another mechanism is yet uncertain, but its reported effects are consistent with selective activity at of 5-$HT_{1A}$ heteroreceptors in other brain regions, with reduced recruitment of auto-receptors.

The overarching hypothesis is that systemic administration of this selective 5-$HT_{1A}$R agonist will result in net enhanced respiratory drives that are determinant of enhanced ventilation.

### *1.9.3 Chapter aims*

The general thesis aim is addressed through experiments that are presented in chapters 3, 4, and 5. Experiments in these chapters have the following aims:

- Experiments in Chapter 3 aim to assess effects of systemic administration of selective 5-$HT_{1A}$ receptor agonist (NLX-101) on eupnoeic respiratory activity (recorded at PN, HN, cVN, and AbN) and the respiratory and sympathetic responses (recorded at PN, cVN, AbN, and tSN) to peripheral chemoreceptor stimulation and to hypercapnia *in situ* WHBP of juvenile rats.
- Experiments in Chapter 4 aim to map key anatomical components of the respiratory system that (co-)express 5-$HT_{1A}$ receptor RNA and SLC32A1 RNA. The SLC32A1 gene encodes for vesicular inhibitory amino acid transporter, which is a marker of inhibitory GABA-ergic and/or glycinergic neurones
- Experiments in Chapter 5 aim to identify which functional subtypes of respiratory neurones in the VRC are responsive to juxta-cellular pico-ejection of 5-$HT_{1A}$ R agonist, which is an indication of 5-$HT_{1A}$ R expression in these neurones.

# Chapter 2: GENERAL METHODS

To avoid repetitions in the methods sections of results chapters, this general methods section will address elements of the experimental methods that apply to multiple chapters.

## 2.1 ANIMALS AND ETHICAL APPROVAL

All experimental procedures conformed to the UK Animals (Home Office Scientific Procedures) Act 1986 and were approved by the University of Bristol Animal Welfare and Ethics Review Body (AWERB).

The experiments in this thesis involve use of male Wistar rats, and they include procedures carried out on animals that are covered under Dr. Ana Abdala's Home Office license. The highest severity procedures carried out on animals in the studies reported here are 'mild'. The system and interactions under study in this thesis involves interactions of elements along various levels of organization: i.e. circuit-level dynamics, modulated by peripheral cues (central-, and peripheral chemoreceptor activation) and serotonergic transmission, that control whole-organism physiological states. Such interactions, and their net outcome, can only truly be probed in a system in which these interactions still function, i.e. animals and *in situ* preparations derived from animals. A large body of research leading up to the aims and hypotheses in this thesis is based on computational modelling of known, and putative brainstem network interactions. Verification of the hypotheses supported by these computational models requires the use of animals as proposed in the current studies. Our data is shared with a collaborating group of computational modellers to optimally utilize the data acquired through the experimental procedures. The use of rats is most appropriate for these studies as for this species we can utilize a well-established *in situ* preparation that enables comprehensive monitoring of respiratory activities in each experiment, and it allows us to capitalize on a large body of existing experimental data obtained in the same species. The use of *in situ* preparations of rats ensures a relatively high level of refinement and reduction of the use of animals in our research.

## 2.2 *IN SITU* WORKING HEART BRAINSTEM PREPARATIONS (WHBP)

### *2.2.1 In Situ WHBP background and justification.*

All electrophysiological recordings reported in chapters 3 and 5 were performed using the *in situ* perfused working heart-brainstem preparation (WHBP) of juvenile rats (Paton, 1996b). This is a transcardially perfused preparation of a decerebrate rat with an otherwise intact rostral neuraxis, and an intact brainstem respiratory network. The *in situ* WHBP allows simultaneous electrophysiological recording of respiratory and sympathetic nerves: the PN, the cVN, the HN, the AbN, and the SN without the requirement of anaesthetics. Simultaneous recording of multiple peripheral nerves provides a comprehensive image of respiratory network activity and of potential changes in respiratory network function induced by experimental manipulations. Absence of anaesthesia is important as some anaesthetics are known to dampen respiratory (Dahan et al., 2018) and sympathetic (Wenker et al., 2017) network activity. The brainstem was exposed for electrophysiological recordings (field potential, extracellular single unit recordings) and focal micro-ejections or pico-ejections of drugs directly in the brain. Drugs can also be administered systemically via the perfusate. The metabolic state of preparations was controlled by changing $CO_2$ and $O_2$ levels in the perfusate. Peripheral chemoreceptors were stimulated via intra-arterial bolus injections of cyanide salt solution (see **Figure 2-1**).

### *2.2.2 Anaesthesia, euthanasia, and surgical procedures for in situ WHBP.*

Male Wistar juvenile (50-90g, PND 21-29) rats received an I.P. injection of heparin sodium salt (1000 I.U.) and were subsequently deeply anesthetised with isoflurane until loss of paw withdrawal reflex. The rats were killed through exsanguination via a cut in the descending aorta and bisected below the L1 spinal region. Anaesthesia was subsequently withdrawn and the head and thorax was placed in ice-chilled carbogenated Ringer solution (for composition, see section 2.2.3). The preparation was de-cerebrated, skinned, and visceral organs were removed. Thoracic phrenic (PN), cervical vagus (cVN), hypoglossal (HN), thoraco-lumbar (T12–L1) abdominal iliohypogastric (AbN), and thoracic (T9-T10) sympathetic trunk (tSN) nerves were exposed and distally cut. The preparation was then transferred to a recording chamber, where a double lumen catheter (DLR-4, Braintree Scientific, Braintree, USA) was inserted into the descending aorta for retrograde transcardiac perfusion. One lumen of the catheter was used for transcardiac perfusion (25-30 mL/min) with carbogenated (95% $O_2$; 5% $CO_2$) Ringer solution with 1.25%

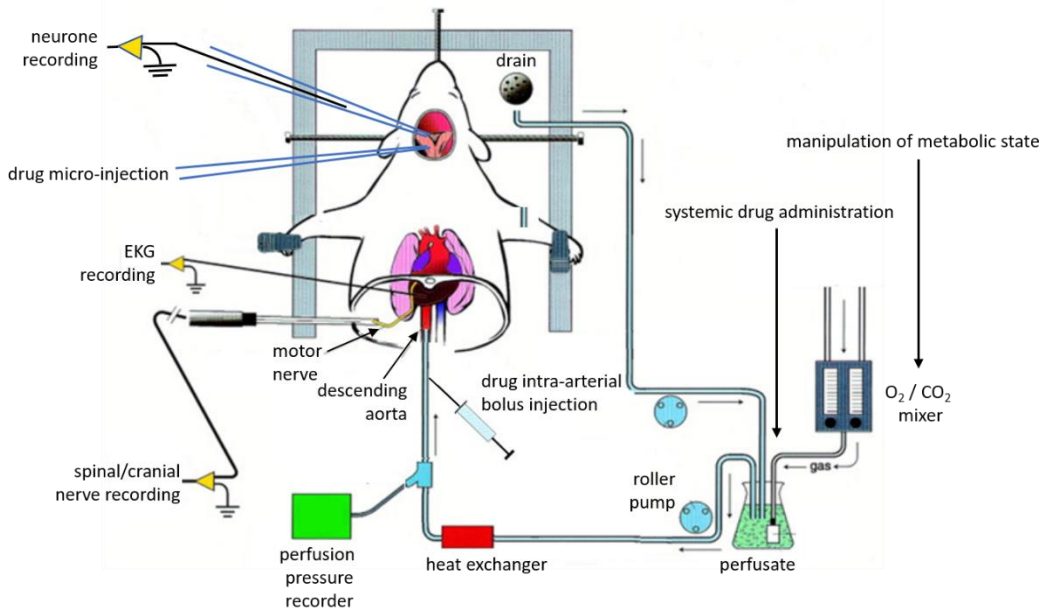


**Figure 2-1:** The *in situ* working heart-brainstem preparation (WHBP) of rat.

Schematic representation of the *in situ* WHBP, a decerebrate transcardially perfused preparation which allows simultaneous electrophysiological recording of output from the intact respiratory network via multiple cranial, and spinal motor nerves and of the sympathetic trunk without the requirement of anaesthetics. The brainstem can be exposed for electrophysiological recordings (patch-clamp, field potential, extracellular single unit recordings) and focal micro-ejections or pico-ejections of drugs directly in the brain. Drugs can also be administered systemically via the perfusate. The metabolic state of preparations can be controlled by changing $CO_2$ and $O_2$ levels in the perfusate. Peripheral chemoreceptors can be stimulated via intra-arterial bolus injections of cyanide salt solution.

polyethylene glycol (PEG) 20,000 oncotic agent (Fisher Scientific UK Ltd. Loughborough, UK) at a temperature of 31°C. The other lumen was attached to a pressure transducer for continuous measurement of perfusion pressure simultaneously with perfusion. Perfusate flow was controlled with a peristaltic pump (Watson-Marlow 505D, Falmouth, Cornwall, UK) and drawn from a reservoir flask, via a heat exchanger, through a particulate filter (25 µm polypropylene screen filter, Merck Millipore Ltd., Burlington, U.S.A) and a bubble trap before entering the preparation. Circulated perfusate was recycled from the preparation chamber back to the reservoir. The volume of perfusate circulated through the setup was 200mL. To ensure adequate brain perfusion, vasopressin (Tocris, Bristol, UK) stock solution (5mM) in saline was added to the perfusate to make up 0.5-3nM vasopressin in perfusate (200mL), and perfusion pressure was maintained between 50-90 mmHg. 500µL Vecuronium Bromide (Abcam, Cambridge, UK) stock solution (2mg/mL) was added to the perfusate (200mL) to block neuromuscular transmission. From the moment of exsanguination to the onset of perfusion, the surgical procedure was performed in under 20 minutes. To optimise access to the desired nerves or to the brainstem for extracellular

recordings, the animal was placed in lateral position (for experiments in Chapter 3), or prone with their head fixed using ear bars and a snout clamp to ensure the brainstem was orientated similarly in all preparations (for experiments in chapter 5).

### *2.2.3 Solutions and pharmacological agents.*

The composition of Ringer solution is as follows: 1.25 mM $MgSO_4.7H_2O$; 1.25 mM $KH_2PO_4$ (ACROS organics, Geel, Belgium); 3.95 mM KCl; 25 mM $NaHCO_3$; 125 mM NaCl; 2.5 mM $CaCl_2.H_2O$; 10 mM D-Glucose. All reagents were from Fisher Scientific UK Ltd. (Loughborough, UK) unless stated otherwise. Perfusate was made by adding 1.25% Oncotic agent PEG 20.000 (Fisher Scientific UK Ltd., Loughborough, UK) to freshly made Ringer solution, then filtering it (5-13µm pore size general purpose filter paper, Fisherbrand™, Pittsburg, U.S.A).

### *2.2.4 Electrodes, Apparatus and software used for in situ WHBP peripheral nerve recordings.*

Custom made bipolar suction electrodes were positioned to record from each cut and exposed nerve. These electrodes were pulled from borosilicate glass (GC150-F10, Harvard Apparatus), broken back and fire-polished to the appropriate diameter for a tight seal around the recorded nerve. The recording electrodes were bipolar. That is, a silver recording wire (AG005130, Goodfellow Cambridge Ltd., Huntingdon, United Kingdom) was placed inside the glass capillary, and a reference insulated silver wire (AG005842, Goodfellow Cambridge Ltd., Huntingdon, United Kingdom) was fitted to the outside of the glass capillary in such a manner that the wire end, bared of insulator, could be placed in close apposition to the nerve. The use of a reference wire, along with a tight seal around the nerve, improved the signal-to-noise ratio obtained with the electrodes. Electrodes were mounted on separate mechanical 3-D micromanipulators (U31CF micromanipulator, Narishige International LTD., London, United Kingdom). Electrophysiological recordings of peripheral nerves were x10k amplified (A-M systems Model 1700, Sequim, USA), bandwidth filtered (PN, VN, AbN, tSN at 300-5000 Hz, and HN 100-5000 Hz). A-D conversion was performed using a Micro 1401 data-acquisition unit (Cambridge Electronic Design, Cambridge, UK) and Spike2 data acquisition software (Cambridge Electronic Design Ltd., Cambridge, UK). Raw recording data was converted to integrated nerve traces through the following online processing steps: direct current (DC) offset removal ($\tau$= 10 ms); rectification; and integration ($\tau$= 50 ms). Offline data processing and analysis was

performed with Spike2 with the use of a custom script (Abdala Sheikh, 2020) and will be addressed in further detail in methods section of Chapter 3.

## 2.3 JUSTIFICATION FOR THE USE OF 5-HT$_{1A}$ RECEPTOR AGONIST NLX-101.

As addressed in the general introduction, the majority of studies performed to investigate the role of 5-HT$_{1A}$ receptor agonism in respiratory and sympathetic control has utilized the drug (R)-(+)-8-hydroxy-2-(di-n-propylamino) tetralin hydrobromide (8-OH-DPAT). This drug has high affinity for 5-HT$_{1A}$ receptors, but it is also reported to have moderate affinity for 5-HT$_7$ receptors (See General Introduction, section 1.7.3) Experiments with co-administration of 8-OH-DPAT with 5-HT$_7$ agonist (5-CT), 5-HT$_7$ antagonist (SB269970), or 5-HT$_{1A}$ receptor antagonist (WAY-100635) have provided indications of the role of 5-HT$_{1A}$ in respiratory control, but effects on sympathetic and respiratory control of selective 5-HT$_{1A}$ activation without confounding factors from other pharmacological manipulations are currently not yet established. The proprietary selective 5-HT$_{1A}$ receptor agonist NLX-101 (formerly named F15599) facilitates investigation of the effect of 5-HT$_{1A}$ receptor activation on respiratory control with a specificity that was hitherto not possible (proprietor of NLX-101 is Neurolixis Inc. Dana Point, USA). NLX-101 is a highly selective 5-HT$_{1A}$R agonist. In rat cortex, striatum, and hippocampal tissue, NLX-101 showed 1000-fold higher binding affinity for 5-HT$_{1A}$ receptors over other 5-HT receptors, and over dopamine-, and adrenoreceptors in vitro. In addition, NLX-101 did not interact with a wide range of other receptors, ion channels, or monoamine transporters (Newman-Tancredi et al., 2009). Additionally, NLX-101 is suggested to have functional selectivity for 5-HT$_{1A}$ hetero-receptors (Llado-Pelfort et al., 2010). This may be of clinical relevance as 5-HT$_{1A}$ auto-receptor and hetero-receptor activation are reported to have opposing effects: fast onset stimulation of respiratory activity in response to hetero-receptor activation, and slow onset inhibition of respiratory activity in response to auto-receptor activation (see General introduction section 1.7.3). Thus, NLX-101 enables the hitherto limited investigation of the role of highly selective 5-HT$_{1A}$ activation in respiratory and sympathetic control.

# Chapter 3: EFFECTS OF 5-HT$_{1A}$ TRANSMISSION ON RESPIRATORY MOTOR AND SYMPATHETIC NETWORK OUTPUT IN RAT *IN SITU*

## 3.1 CHAPTER INTRODUCTION

The present chapter presents a series of experiments performed to assess the role of 5-HT$_{1A}$ transmission in eupnoeic respiratory control and in the respiratory and sympathetic responses to chemoreceptor activation in the *in situ* WHBP. The subsections in this chapter introduction will present a brief review of relevant literature to outline the present understanding, and gaps therein, regarding the role of 5-HT$_{1A}$ transmission in eupnoeic respiratory activity (section 3.1.1), in the respiratory responses to hypercapnia (3.1.2) and to peripheral chemoreceptor activation (section 3.1.3), and in the coupling of sympathetic and respiratory activity (section 3.1.4). Section 3.1.5 addresses the chapter aims and hypotheses based on the findings addressed in the preceding sections.

### *3.1.1 5-HT$_{1A}$ transmission in eupnoeic respiratory control*

Effects of 5-HT$_{1A}$ transmission on eupnoeic respiratory activity

Systemic or central administration of 5-HT$_{1A/7}$ agonist (8-OH-DPAT) results in augmented amplitude and/or frequency of integrated bursts of the PN in mice, rats, cats, and dogs *in vivo* (Valic et al., 2008, Szereda-Przestaszewska and Kaczynska, 2007, Radocaj et al., 2015), or in *in situ* WHBP of rats and mice (Manzke et al., 2009, Manzke et al., 2010). In line with these findings, plethysmography recordings in anesthetized vagotomised rats *in* vivo revealed increases in breathing rate and tidal volume after systemic administration of 8-OH-DPAT (Szereda-Przestaszewska and Kaczynska, 2007). Systemic administration of 8-OH-DPAT is also reported to result in augmented electromyographic activity of upper airway muscles in anesthetized rats *in vivo* (Besnard et al., 2012, Besnard et al., 2007). In a subset of these experiments, 8-OH-DPAT induced stimulation of respiratory activity was reported to be abolished by subsequent administration of 5-HT$_{1A}$R antagonist and dopamine receptor D4 agonist WAY-100635 (Szereda-Przestaszewska and Kaczynska, 2007, Valic et al., 2008). Administration of WAY-100635 without any prior administration of 8-OH-DPAT reduced upper airway muscle respiratory activity in anesthetized rats (Besnard et al., 2012, Besnard et al., 2007)**,** and phrenic nerve activity in *in situ* WHBP of rats (Manzke et al., 2009) to below baseline levels. Systemic administration 8-OH-DPAT is reported to also counteract respiratory depression in response to fentanyl (μ-opioid

receptor agonist) in *in situ* WHBP and in *in vivo* rats (Manzke et al., 2009, Shevtsova et al., 2011, Dutschmann et al., 2009b, Guenther et al., 2009). Comparisons of the effect of 8-OH-DPAT in rhythmically active acute brainstem slices from WT and from Lmx1b$^{f/f/p}$ neonatal mice, which had a complete absence of Raphe serotonergic neurons (i.e. no 5-$HT_{1A}$ auto-receptors), suggest that pre-synaptic 5-$HT_{1A}$ auto-receptors and post-synaptic hetero-receptors may have physiologically competing effects. That is, 8-OH-DPAT transiently increased burst frequency from the HN nerve rootlet, a measure of respiratory drive, in slices from Lmx1b$^{f/f/p}$ neonatal mice, but not in WT slices. This excitation was abolished when synaptic inhibition was blocked by bath administration of a mixture of $GABA_A$-, and glycine receptor antagonists (gabazine, CPG 55845, and strychnine). Conversely, after 10 min of application, respiratory frequency in Lmx1b$^{f/f/p}$ slices had returned to baseline levels, whereas it was significantly depressed in WT slices. This pattern of activity was interpreted to be reflective of rapid stimulation of breathing due to hetero-receptor mediated inhibition of glycinergic and GABA-ergic respiratory interneurons (disinhibition), and delayed inhibition due to auto-receptor agonism (Corcoran et al., 2014) (see section 1.7.3).

To summarize, 5-$HT_{1A}$ receptors are endogenously active under baseline conditions and have an excitatory role in resting respiratory activity. The net effect of stimulation of 5-$HT_{1A/7}$ transmission with 8-OH-DPAT was enhanced respiratory drive. 5-$HT_{1A}$ auto-receptors and hetero-receptors are suggested to have physiologically competing effects: rapid onset stimulation of breathing due to hetero-receptor mediated inhibition of inhibitory interneurons (disinhibition), and delayed inhibition due to auto-receptor agonism.

<u>Gaps in understanding with regard to the effect of systemic 5-$HT_{1A}$ transmission on the eupnoeic respiratory rhythm and pattern</u>

There are multiple sites and mechanisms in the respiratory CPG at which 5-$HT_{1A}$ transmission can affect eupnoeic respiratory rhythm and pattern (e.g. inhibition in the KF, inhibition of rhythmogenic subpopulations in the VRC). Previous experiments describing the effect of systemic 5-$HT_{1A}$R agonism on respiratory activity have focused on specific elements of respiratory rhythm and pattern (e.g. respiratory rate and pattern derived from PN discharge recordings, upper airway resistance derived from upper airway muscle tonus recordings, etc.), often recorded from distinct animal models, preparations, and experimental conditions, and have typically used a non-selective 5-$HT_{1A}$ agonist. What is currently still lacking, is a comprehensive assessment of the effect of selective 5-$HT_{1A}$

agonism on the intact respiratory CPG, free from possible confounds introduced by anaesthesia or the requirement to translate findings between various animal models, recording techniques, and experimental conditions. Such assessment can be obtained from experiments with simultaneous recordings of all relevant motor nerve outputs (i.e. the PN, HN, cVN, and AbN) combined with systemic administration of a selective 5-$HT_{1A}$ agonist, NLX-101, in the *in situ* WHBP. Because the various recorded nerve outputs are interdependent and shaped by network interactions relatively well described in the inhibitory ring model, and because all nerve recordings are simultaneously obtained under identical experimental conditions, such a dataset could be interpreted in the context of the inhibitory ring model to inform hypotheses regarding putative mechanisms by which 5-$HT_{1A}$ transmission affects the respiratory CPG. Furthermore, the physiologically antagonistic effects of 5-$HT_{1A}$ auto-receptor vs. hetero-receptor activation complicate interpretations of effects of 5-$HT_{1A}$R agonists. The use of the proposed hetero-receptor biased 5-$HT_{1A}$R agonist NLX-101 facilitates assessment of the effect of hetero-receptor activation on respiratory activity with reduced interference from auto-receptor activation.

### *3.1.2 5-$HT_{1A}$ transmission in the hypercapnic respiratory response*

Serotonergic transmission affects central $CO_2$ chemoreceptor function in respiratory control

The respiratory central chemoreflex is primarily mediated by populations of RTN neurones (see section 1.4.1), and raphe serotonergic neurones (see section 1.4.2) both thought to have intrinsic $CO_2$/pH sensitivity. Genetic KO mouse models with near complete loss of 5-HT neurones show reduced $CO_2$ sensitivity persisting into adult age (Hodges et al., 2008, Cerpa et al., 2017). Similarly, acute pharmacogenetic inhibition of 5-HT (SLC6A4-expressing) neurones with DREADD hM4Di activation has no effect on baseline respiratory activity, but attenuates the hypercapnic respiratory response in vivo in adult mice (Ray et al., 2011) (see section 1.7.2). Selective pharmacogenetic inhibition of 5-HT neurone subpopulations, targeted by genetic markers of rhombomeric lineage, identified Raphe serotonergic neurones derived from embryonic rhombomeres 3 (r3 Egr2-Pet1 neurones) and 5 (r5 Egr2-Pet1 neurones) exclusively to have intrinsic $CO_2$/pH chemosensitive properties. The anatomical locations of these subpopulations of Raphe serotonergic neurones correspond to the caudal end of the medial lemniscus and median Raphe nucleus (for r3 Egr2-Pet1 neurones), and the rostral end of the caudal Raphe nuclei, i.e. Raphe magnus and Raphe pallidus (for r5 Egr2-Pet1 neurones). These serotonergic

neurones derived from r3/r5 selectively innervated brainstem nuclei involved in chemosensory processing, but not various respiratory (pre-)motor nuclei (Brust et al., 2014) (see section 1.4.2).

A second subpopulation of serotonergic raphe neurones reported to contribute to the central chemoreflex respiratory response is made up of tachykinin (tac1) positive raphe serotonergic neurones (Tac1-Pet1 neurones). The anatomical location of the Tac1-Pet1 population maps primarily onto the raphe obscurus and caudal raphe pallidus. Whether these neurones have intrinsic $CO_2$ chemosensitive properties is not directly established, but the findings by Brust et al. (2014) suggest they are not. Pharmacogenetic inhibition of this population, however, resulted in blunted respiratory rate and tidal volume components of the hypercapnic ventilatory response in mice *in vivo*. These neurones were observed to project to the pre-BötC, to various (pre-)motor nuclei within in the brainstem, and to pre-sympathetic C1 neurones in the RVLM. The authors suggest that Tac1-Pet1 raphe serotonergic neurones act downstream of r3/r5 Egr2-Pet1 neurones to modulate respiratory (pre-)motor output in response to hypercapnic acidosis (Hennessy et al., 2017) (see section 1.4.2).

Late-E activity appears to also be mediated by serotonergic transmission in the RTN/pFRG region. Episodic micro-injections of 5-HT in the RTN/pFRG region resulted in a lasting (30 min) stimulation of abdominal expiratory activity under resting conditions, and a potentiation of abdominal late-E activity in response to hypercapnia in anesthetised rats (Lemes et al., 2016b). This effect was blocked when antagonist to excitatory 5-$HT_2$ receptors (ketanserin) was administered to the RTN/pFRG region prior to the 5-HT micro-injections. It is currently not established whether this excitatory serotonergic drive to the pFRG stems from intrinsically chemosensitive serotonergic neurones. However, late-E activity emerges under hypercapnic conditions which also stimulate serotonergic chemoreceptor neurones, and late-E activity appears to be promoted by excitatory serotonergic transmission in the RTN/pFRG. It is conceivable that the promotion of late-E activity via stimulation of post-synaptic 5-$HT_2$ receptors in the RTN/pFRG may be mediated by serotonin release from intrinsically chemosensitive serotonergic neurones.

Thus, serotonergic mechanisms thought to contribute to the central chemoreflex response include: $CO_2$/pH chemosensory input to the CPG from r3/r5 Egr2-Pet1 raphe serotonergic neurones; modulation of respiratory motor output during the hypercapnic

ventilatory response by Tac1-Pet1 Raphe neurons; and promotion of late-E activity mediated by excitatory 5-$HT_2$R transmission in the RTN/pFRG.

5-$HT_{1A}$ mediated modulation of the central chemoreflex respiratory response

5-$HT_{1A}$ auto-receptors are widely expressed in Raphe neurones, and the central chemoreflex is significantly attenuated (22% reduction) by microdialysis of 5-$HT_{1A/7}$ receptor agonist (8-OH-DPAT) in the proximity of the rostral raphe pallidus and raphe magnus regions in conscious rats (Li et al., 2006) (section 1.7.3). However, the effect of 5-$HT_{1A}$ transmission can differ across brainstem regions. For example, blockade of 5-$HT_{1A}$ transmission in the LC through focal administration of 5-$HT_{1A}$R antagonist and dopamine receptor D4 agonist (WAY-100635) attenuates the hypercapnic response in anesthetised rats. Activity of noradrenergic neurones in the locus coeruleus (LC) is thought to stimulate the hypercapnic response (reviewed in Guyenet (2014)), but 5-HT release in the LC is thought to attenuate the hypercapnic response (de Souza Moreno et al., 2010). The observed attenuation of the hypercapnic response observed after administration of WAY-100635 in the LC is suggested to be caused by blockade of local 5-$HT_{1A}$ auto-receptors of serotonergic neurones that synapse in the LC, and the resulting disinhibition of 5-HT release in the locus coeruleus (de Souza Moreno et al., 2010). Thus, local pharmacological manipulations of 5-$HT_{1A}$ transmission indicate that 5-$HT_{1A}$ transmission can have opposing effects on the respiratory hypercapnic response, depending on the regions and mechanisms affected. Despite the above, systemic administration of 5-$HT_{1A/7}$R agonist 8-OH-DPAT in *in situ* WHBP of juvenile rats results in a loss of the hypercapnic respiratory response (Corcoran et al. 2013). This suggests that the net effect of systemic 5-$HT_{1A}$ transmission is an attenuation of the hypercapnic response.

To conclude, 5-$HT_{1A}$R transmission (and blockade thereof) appears to differentially contribute to the hypercapnic response in distinct regions. The net effect of systemic administration of a selective 5-$HT_{1A}$R agonist or antagonist on the central chemoreflex respiratory response remains, to the best of my knowledge, unexplored. However, systemic 5-$HT_{1A/7}$R agonism results in attenuation of the hypercapnic response. Current evidence suggests that effects of 5-$HT_{1A}$ transmission on the hypercapnic response are chiefly mediated by action at 5-$HT_{1A}$ auto-receptors. Candidate contributors to the observed effects of systemic 5-$HT_{1A/7}$R agonism are 5-$HT_{1A}$ auto-receptor mediated inhibition of $CO_2$ chemosensitive r5-Egr2-Pet1 raphe serotonergic neurones and/or 5-$HT_{1A}$ auto-receptor mediated inhibition of Tac1-Pet1 neurones in the caudal raphe pallidus or raphe obscurus. A further mechanism that could hypothetically contribute to the

attenuation of the hypercapnic response observed after systemic 5-$HT_{1A/7}$R agonism, is 5-$HT_{1A}$ auto-receptor mediated reduction of 5-HT release in the RTN. Despite evidence of attenuation of the hypercapnic response after local administration of WAY-100635 in the LC, it is possible that the net effect of systemic administration of 5-$HT_{1A}$ antagonist results in potentiation of the hypercapnic response through auto-receptor mediated disinhibition of raphe neurones.

### *3.1.3 5-$HT_{1A}$ transmission in the peripheral chemoreflex respiratory response*

Peripheral chemoreflex function is dependent on $O_2$ and $CO_2$ sensitive glomus cells in the carotid bodies (CB), which can be stimulated by intra-arterial bolus injections of cyanide salt (NaCN or KCN) solution (reviewed in Lahiri et al. (2006)). Stimulation of peripheral chemoreceptors results in increased respiratory rate and tidal volume, large post-I bursts (in HN, cVN, and AbN) without elongation of the post-I phase, and late-E activity (in AbN and tSN) (see section 1.5.1).

Key brainstem components of the peripheral chemoreflex respiratory response

CB afferents project to the NTS (Mifflin, 1992, Erickson and Millhorn, 1994, Erickson and Millhorn, 1991), from which second order peripheral chemoreceptor neurones relay information to key regions of the respiratory CPG (predominantly to the RTN/pFRG region, the rVRG and cVRG, and the RVLM) (Alheid et al., 2011, Yang et al., 2020). Ablation or inhibition of CB and/or NTS eliminates the chemoreflex response to hypoxia or intra-arterial cyanide altogether (Takakura et al., 2006, Guyenet et al., 2018, Mulkey et al., 2004). Late-E activity in response to peripheral chemoreceptor activation is thought to be mediated by direct glutamatergic projections from NTS second order chemoreceptor neurones to the RTN (Takakura et al., 2006, Moraes et al., 2012a, Barnett et al., 2017). The late-E response, but not the Post-I response, to CB activation is dependent on RTN function (Moraes et al., 2012a). The Post-I response has been suggested to be mediated by direct projections from second order chemoreceptor neurones to post-I neurones in pre-motor transmission circuitry in the VRC (Barnett et al., 2017). Recordings of respiratory motor output after ponto-medullary transections in *in situ* WHBP of juvenile rats indicate that both post-I and late-E activity in response to peripheral chemoreceptor activation with NaCN bolus administrations are dependent on intact ponto-medullary interactions (Gandini et al., 2009). In summary, pharmacological inhibition studies and lesioning/transection studies indicate that the CB, NTS, RTN/pFRG, VRC, and pontine regions provide contributions necessary for distinct elements of the respiratory response to peripheral chemoreceptor activation.

Potential involvement of 5-$HT_{1A}$ transmission in the peripheral chemoreflex respiratory response

Comparison of Fos expression (a metabolic marker) in 5-$HT_{1A/7}$ agonist (8-OH-DPAT) treated rats versus controls revealed significant increases in Fos expression after 8-OH-DPAT administration in the NTS, RTN, and lateral parabrachial and KF nuclei (Besnard et al., 2012). 5-$HT_{1A}$ Receptors are expressed in the commissural NTS of rats (Vantrease et al., 2015), and RT-PCR indicates that 5-$HT_{1A}$R RNA is present in the cytosol of $O_2$ chemosensitive isolated glomus cells from rats (Yokoyama et al., 2015). To the best of my knowledge, effects of 5-$HT_{1A}$ transmission on the peripheral chemoreflex respiratory response have never been established. In light of the findings above, however, it is plausible that systemic administration of 5-$HT_{1A}$ agonist could result in suppression of neurones involved in the peripheral chemoreflex, and thereby attenuate the respiratory responses to peripheral chemoreceptor challenges.

### *3.1.4 5-$HT_{1A}$ transmission in control of sympatho-respiratory coupling*

Distinct patterns of sympatho-respiratory coupling occur during different respiratory behaviours

Sympathetic activity drives cardiac output and vasoconstriction, and it thereby acts to upregulate arterial perfusion. Sympathetic output exhibits entrainment with the respiratory cycle and the pattern of this sympatho-respiratory coupling changes with alterations in metabolic state, and respiratory rhythm and pattern. Under eupnoeic conditions, sympathetic nerve activity in mammals exhibits positive modulation during late-I and early Post-I phases of the respiratory cycle (Bazilio et al., 2019, Moraes et al., 2012a) (see section 1.6.1). In *in situ* WHBP of juvenile rats, hypercapnia leads to augmented sympathetic drive via the emergence of late-E activity in the tSN which occurs concomitantly with AbN late-E bursts. (Zoccal et al., 2008, Dick et al., 2004, Mandel and Schreihofer, 2009, Molkov et al., 2011). Peripheral chemoreceptor activation also promotes AbN and tSN late-E activity, along with high amplitude sympathetic bursts during post-I followed by inhibition of sympathetic output during early inspiration. The Post-I tSN response to peripheral chemoreceptor activation occurs concomitantly with the augmented Post-I respiratory motor activity observed in the cVN, HN, and AbN (Dick et al., 2004, Costa-Silva et al., 2010, Mandel and Schreihofer, 2009, Moraes et al., 2012a, Barnett et al., 2017, Braga et al., 2007).

Mechanisms underlying sympatho-respiratory modulation

A nodal point for sympathetic efferents is the RVLM, a region in which catecholaminergic (C1) and non-catecholaminergic—pre-sympathetic neurones exhibit respiratory modulation through excitatory and inhibitory inputs from various sources in the respiratory CPG. Converging evidence of anatomical, functional, and computational studies suggest that sympatho-respiratory coupling occurs, at least in part, through interactions of rhythmogenic respiratory neurones of the VRC (Zoccal et al., 2008, Zoccal et al., 2014) and of respiratory neurones of the dorsolateral pons with RVLM pre-sympathetic neurones (Baekey et al., 2008, Stornetta et al., 2016, Barnett et al., 2017). In addition, RVLM pre-sympathetic neurones receive respiratory rhythm-entrained inhibitory input from GABA-ergic neurones in the CVLM (Schreihofer and Guyenet, 2003, Willette et al., 1983, Guyenet et al., 1990, Monnier et al., 2003), which in turn receive excitatory input from the NTS (Schreihofer and Guyenet, 2002, Molkov et al., 2014b). (see section 1.6.2, **figure 1-8A**). Late-E and Post-I sympathetic activities in response to chemoreceptor activation appear mediated by distinct pathways. Late-E sympathetic activity is likely a consequence of excitatory projections from pFRG late-E neurones to non-C1 pre-sympathetic neurones in the RVLM (Baekey et al., 2010, Molkov et al., 2010, Molkov et al., 2011). Converging evidence from anatomical, pharmacological, pharmacogenetic, optogenetic, and computational modelling studies suggests that enhanced excitatory drive from central chemoreceptors to pFRG late-E neurones drives the hypercapnic late-E sympathetic and respiratory response, and that excitation of pFRG late-E neurones via an excitatory projection from 2$^{nd}$ order peripheral chemoreceptor neurones of the NTS drives the late-E sympathetic and respiratory response to peripheral chemoreceptor activation (Barnett et al., 2017) (see section 1.6.2, **figure 1-8B**). Post-I sympathetic activity in response to peripheral chemoreceptor activation, on the other hand, has been hypothesized to be mediated by excitatory drive from Post-I neurones in VRC transmission circuitry to C1 neurones in the RVLM (Barnett et al., 2017). The RVLM Post-I neurones were suggested to receive peripheral chemoreceptor drive from the NTS (see section 1.6.2, **figure 1-8C**). Finally, commissural NTS neurones that receive input from the CB provide direct glutamatergic drive to C1 pre-sympathetic neurones in the RVLM. This pathway is thought to underlie a tonic, non-respiratory dependent, component of augmented sympathetic activity in response to peripheral chemoreceptor activation (see section 1.6.2).

Putative role of 5-$HT_{1A}$ transmission in sympatho-respiratory coupling

Respiratory regions thought to be critical components of various pathways for sympatho-respiratory coupling are: the PBc, the NTS, the pFRG/RTN region, and various regions of the VRC (see section 1.6.2). Histological-, *in situ* hybridization-, and PCR experiments indicate that 5-$HT_{1A}$R are expressed in the BötC and pre-BötC (Manzke et al., 2009, Manzke et al., 2010), and the NTS (Vantrease et al., 2015). Further, the NTS, RTN, lateral parabrachial nucleus, and the KF showed increased fos expression in 5-$HT_{1A/7}$ agonist (8-OH-DPAT) treated rats versus controls revealed (Besnard et al., 2012). This suggests modulation of activity in these regions in response to systemic 5-$HT_{1A}$R transmission. Intravenous administration of 8-OH-DPAT resulted in a fall of arterial pressure in anesthetized rats (Szereda-Przestaszewska and Kaczynska, 2007). However, there is currently little known about the effects of 5-$HT_{1A}$ transmission on sympatho-respiratory coupling. Given the above findings, it is conceivable that 5-$HT_{1A}$ transmission influences respiratory rhythm entrained patterns of sympathetic activity.

### *3.1.5 Chapter aims and hypotheses*

**Chapter aim:** The aim this chapter is to assess effects of systemic administration of selective 5-$HT_{1A}$ receptor agonist NLX-101 on restful eupnoeic respiratory activity (recorded at PN, HN, cVN, and AbN) in *in situ* WHBP of rats. I also aim to evaluate the effects of 5-$HT_{1A}$ transmission on respiratory and respiratory-entrained sympathetic responses (recorded at PN, cVN, AbN, and the tSN) to hypercapnia and to peripheral chemoreceptor activation in *in situ* WHBP of rats.

**Experiments**: To assess the effects of 5-$HT_{1A}$ transmission on eupneic respiratory activity, we systemically administered selective 5-$HT_{1A}$R full agonist NLX-101 or vehicle while performing a comprehensive assessment of respiratory motor output through simultaneous recordings of PN, HN, cVN, and AbN discharge in *in situ* WHBP of juvenile rats. NLX-101 or vehicle was administrated in a concentration-response experiment, and respiratory motor output patterns after NLX-101 administration were compared to those of vehicle controls.

Effects of 5-$HT_{1A}$ transmission on the hypercapnic respiratory and sympathetic responses were assessed through recordings of the hypercapnic respiratory and sympathetic response in the PN, cVN, AbN, and tSN to normoxic hypercapnia (8% $CO_2$, $O_2$-balanced) before and after systemic administration of 5-$HT_{1A}$ agonist NLX-101, 5-$HT_{1A}$ R antagonist WAY-100635, or vehicle in *in situ* WHBP of rats. Any effects of drugs (WAY-100635 or NLX-

101) on the hypercapnic response were expected to be revealed as a significant effect of drug versus vehicle.

Effects of 5-$HT_{1A}$ transmission on the peripheral chemoreflex were evaluated through recordings of the respiratory and sympathetic responses in the PN, cVN, AbN, and tSN to intra-arterial bolus adminitration of NaCN solution before and after systemic administration of 5-$HT_{1A}$ agonist NLX-101, or vehicle in *in situ* WHBP of rats. Any effects of NLX-101 on the respiratory and sympathetic responses to peripheral chemoreceptor activation were expected to be revealed as a significant effect of NLX-101 versus vehicle post-treatment.

**Hypotheses:** The hypothesis of this chapter is that systemic administration of 5-$HT_{1A}$R agonist increases the respiratory drive, reflected in an augmented respiratory rate. Sympathetic and respiratory responses to peripheral chemoreceptor activation are hypothesized to be attenuated through inhibition of peripheral chemoreceptors and/or excitatory neurones downstream of chemoreceptors (e.g. in the NTS). Current evidence for a role of 5-$HT_{1A}$ transmission in the hypercapnic respiratory response suggests that systemic 5-$HT_{1A}$R agonism attenuates the hypercapnic response, chiefly through activation of 5-$HT_{1A}$ auto-receptors at raphe neurones (see section 3.1.2). Because NLX-101 is believed to act as a 5-$HT_{1A}$ hetero-receptor biased agonist, we expect low-level activation of raphe neurone 5-$HT_{1A}$ auto-receptors. Therefore, sympathetic and respiratory responses to hypercapnia are hypothesized to be unaffected by systemic administration of NLX-101. We hypothesised that the net effect of systemic administration of WAY-100635 is an augmented respiratory and sympathetic hypercapnic response due to disinhibition of raphe chemoreceptor neurones and disinhibition of 5-HT mediated chemosensitive mechanisms downstream of raphe neurones (see section 3.1.2).

## 3.2 CHAPTER METHODS

This chapter describes three experiments with the *in situ* working heart-brainstem preparation (WHBP). The first experiment consists of simultaneous recordings of the PN, cVN, HN, and AbN while performing a concentration-response experiment with systemic administration via the perfusate of selective 5-$HT_{1A}$ receptor agonist NLX-101 or vehicle. The second and third experiments consist of simultaneous recordings of the PN, cVN, AbN, and tSN during hypercapnia or peripheral chemoreflex stimulation, respectively, before and after systemic administration via the perfusate of NLX-101 or vehicle. This section describes: methods of central and peripheral chemoreceptor activation (3.2.1); solutions and pharmacological agents specific to experiments in this chapter (3.2.2); respiratory and sympathetic output parameters analysed (3.2.3), experimental procedures, data processing, and analysis for the NLX-101 concentration response curve experiment (3.2.4); experimental procedures, data processing, and analysis for the NLX-101 hypercapnic response experiment (3.2.5), and experimental procedures, data processing, and analysis for the NLX-101 peripheral chemoreflex experiment (3.2.6).

### *3.2.1 $CO_2$ chemoreceptor and Peripheral chemoreceptor activation*

$CO_2$ chemoreceptor activation

$CO_2$ chemoreceptors were stimulated through a change in the partial pressures of $CO_2$ in the perfusate. Two perfusate solutions were prepared, stored in separate reservoir flasks, and pumped through parallel recirculating perfusion circuits that could be alternated to feed into the preparation with the use of a 4-way stopcock switch at the level of the aortic catheter. One reservoir was bubbled with 5% $CO_2$ ($O_2$ balanced), whereas the other was bubbled with 8% $CO_2$ ($O_2$ balanced). $CO_2$ concentrations of the gas mixture were determined with the use of a $CO_2$ gas sensor (P.K. Morgan Ltd., Kent, U.K.). Beyond differing partial pressures of $CO_2$ and $O_2$, both volumes of perfusate were kept identical in composition (i.e. if drugs were added to one volume, they were also added to the other), and were controlled by the same peristaltic pump (i.e. perfusion flow rates were identical). This setup facilitated selective and reversible manipulation of $CO_2$ chemosensitive drive through acute alternation between normocapnic (5% $CO_2$, $O_2$ balanced) and hypercapnic (8% $CO_2$, $O_2$ balanced) perfusate flowing into the preparation.

Peripheral chemoreceptor activation

Peripheral chemoreceptors were stimulated with the use of intra-arterial boluses of sodium cyanide (0.03%) dissolved in saline (0.9% NaCl, pH = 7.3).

The peripheral chemoreflex is mediated through stimulation of neurosecretory type 1 glomus cells in the carotid body and aortic bodies that sense hypoxia or hypercapnic acidosis. A decline in $PaO_2$ is thought to result in membrane depolarization and synaptic vesicle release in Type 1 glomus cells through inhibition of $K^+$ channels that is mediated by mitochondrial $O_2$-sensing mechanisms (see section 1.5.1). Sensitivity of glomus cells to hypercapnic acidosis is mediated by acid-sensing ion channel 3 (ASIC3) (see section 1.5.1). Cyanide inhibits mitochondrial electron transport through the inhibition of mitochondrial enzyme cytochrome c-oxidase. As a result, intracellular oxygen utilization (oxidative phosphorylation), and production of ATP, is inhibited**.** This causes acute inhibition of $O_2$ regulated $K^+$ channels in a manner similar to that observed in conditions of oxidative stress. Additionally, inhibition of oxidative phosphorylation forces cells into anaerobic metabolism, creating lactic acid and leading to acid-base imbalances and metabolic acidosis (reviewed in Lu et al. (2013) and Leavesley et al. (2008)). The latter can stimulate ASIC3 acid sensing channels. Intra-arterial bolus injections of small volumes (25-75µL) of cyanide salt solution (0.03%) results in acute stimulation of peripheral chemoreceptors with immediate washout. It is therefore a suitable method for repeated peripheral chemoreceptor stimulation.

### *3.2.2 Solutions and Pharmacological Agents*

NLX-101 fumarate (Neurolixis Inc. Dana Point, USA) was dissolved in saline to make a 100µM (free base) working solution from which to add to the perfusate in *in situ* WHBP experiments. WAY-100635 maleate (Abcam Biochemical, Cambridge, United Kingdom) was dissolved in $H_2O$ to make a 10mM working solution from which to add to the perfusate in *in situ* WHBP experiments. Intra-arterial cyanide boluses were performed with the use of NaCN (Sigma-Aldrich, Steinham, Germany) solution (0.03%) in 0.9% sodium chloride (Hameln Pharmaceuticals Ltd, Gloucester, UK).

### *3.2.3 Descriptions of sympatho-respiratory, and respiratory motor output parameters*

Offline data processing and analysis was performed with Spike2 (version 8.16) with the use of a custom script (Abdala Sheikh, 2020). Parameters describing respiratory rhythm (phase durations, AbN late-E and PN discharge rates (bpm), and latencies to peak burst amplitude (s)) were obtained from integrated discharge patterns from all respiratory motor nerves (∫PN, ∫HN, ∫cVN, ∫AbN). Additionally, respiratory and sympathetic waveform patterns (area under the curve, and/or peak and trough amplitude values) were obtained per respiratory phase for ∫PN, ∫HN, ∫cVN, ∫AbN, and ∫tSN discharge patterns. The current

section provides a description of how each respiratory and sympathetic output parameter is obtained from integrated nerve activity traces.

Phrenic nerve respiratory parameters

For each respiratory cycle, the start and end of ∫PN inspiratory bursts were detected through marking the points at which ∫PN rises above ('PN-start', see **figure 3-1A**) or falls below ('PN-end', see **figure 3-1A**) an amplitude (μV) threshold value (PN-threshold, see **figure 3-1A**) manually set just above noise levels. The interval between 'PN-start' to 'PN-end' is the duration of the inspiratory phase of the respiratory cycle (PN dur. I (s)). The end of the respiratory cycle was marked by the onset of the next ∫PN inspiratory burst ('cycle-end', see **figure 3-1A**). The interval between 'PN-end' to 'cycle-end' is the duration of the expiratory phase (PN dur. E(s), comprising both Post-I and E2). The interval between 'PN-start' and 'end-cycle' marks was the total duration of the respiratory cycle, and is used to calculate the respiratory rate (PN rate (bpm). The latency between the 'PN-start' and the timepoint at which ∫PN reached its peak amplitude (relative to 'PN-expiratory trough') during the inspiratory phase was denoted PN Tpeak (s). The peak amplitude (PN amplitude I (μV)) and area under the curve (AUC) of ∫PN inspiratory bursts, were obtained relative to 'PN expiratory trough'. The AUC of the PN burst is normalised by inspiratory phase duration to generate PN normalised AUC I.

Hypoglossal nerve respiratory parameters

In the ∫HN trace, trough and peak amplitudes were measured relative to a running minimum ∫HN amplitude (HN zero), measured per respiratory cycle in the expiratory phase of the preceding respiratory cycle. The maximum amplitude of ∫HN activity relative to 'HN zero' (HN amplitude (μV), see **figure 3-1A**) was obtained within the time period from 0.3 seconds prior to 'PN-start' to 0.2 seconds later than 'PN-end'. In the eupnoeic respiratory rhythm, the onset of HN bursts slightly precedes that of PN bursts. HN burst onset (HN-start, see **figure 3-1A**) was defined as the timepoint of 97% repolarization from 'HN amplitude (μV)'to 'HN zero (μV)' occurring in the expiratory phase of the preceding respiratory cycle (i.e. between the preceding cycle's 'PN-end' and the present cycle's 'PN-start'). The duration of pre-inspiratory HN discharge (HN dur. Pre-I (s)) was defined as the interval between 'HN-start' and 'PN-start'. In addition to the absolute duration of HN pre-I activity, it was also expressed relative to inspiratory phase duration by dividing 'HN dur. Pre-I (s)' by 'PN dur. I (s)' (HN dur.pre-I : dur.I (%)).The latency between onset of the HN burst (HN-start) and the timepoint at which the maximum HN amplitude (HN amplitude (μV)) was measured is referred to as 'HN Tpeak (s)'. ∫HN AUC was obtained in the interval

from 'HN-start' to 'PN end', and measured relative to 'HN zero'. ∫HN AUC was normalised over inspiratory phase duration to generate HN normalised AUC I.

Cervical vagus nerve respiratory parameters

In the ∫cVN trace, a baseline amplitude value (cVN-zero) was obtained by measuring the minimum value in a manually selected 10-minute epoch of eupnoeic respiratory activity during baseline. In each respiratory cycle analysed, the maximum amplitude of ∫cVN activity and the minimum amplitude (see figure 3-1B) during the expiratory phase are measured relative to cVN zero to obtain 'cVN amplitude PI (μV)' and cVN Trough (μV), respectively (see **figure 3-1B**). The end of the Post-I phase (PI-end, see **figure x**) was defined as the timepoint at which ∫cVN reaches 97% repolarisation from 'cVN amplitude PI' (μV) relative to the 'cVN-trough' amplitude (μV) (see **figure 3-1B**). Post-inspiratory phase duration (cVN dur. PI (s)) was defined as the interval between 'PN-end' and 'PI-end' (see **figure 3-1B**).

In addition to obtaining the absolute duration (s) of the post-I phase, it's duration was also expressed relative to expiratory phase duration as a whole by dividing 'cVN dur. PI (s)' by 'PN dur. E (s)', this parameter was denoted 'cVN dur.PI : dur.E (%)'. The ∫cVN AUC during the inspiratory phase (from 'PN-start' till 'PN-end' timepoints) was obtained relative to 'cVN-zero', and normalised by 'PN dur. I (s)' to obtain the cVN normalised AUC during the inspiratory phase (cVN normalised AUC I) (see **figure 3-1B**). Similarly, ∫cVN AUC during the post-inspiratory phase was obtained relative to 'cVN-zero', and normalised by 'cVN dur. PI (s)' to get the cVN normalised AUC during the post-inspiratory phase (cVN normalised AUC PI).

Iliohypogastric (abdominal) nerve respiratory parameters

To measure parameters derived from ∫AbN and tSN discharge, the expiratory phase was divided at two-third of its duration (2/3-expiration, see fig-3-1C). This division provided estimates of E1 phase duration (the first 2/3$^{rd}$ of the expiratory phase) and of E2 phase duration (the latter 1/3$^{rd}$ of the expiratory phase) centrally. Inspiratory and expiratory phase durations are derived from simultaneous recordings of the PN. The arithmetic estimation of the E1 and E2 phases based on PN discharge patterns allowed for the calculation of respiratory and sympathetic rhythm and pattern parameters independent of changes in cVN cycle duty. These definitions for the respiratory phases were used to obtain the following AbN pattern parameters per respiratory phase: ∫AbN peak amplitude values (AbN amplitude I (μV), AbN amplitude PI (μV), AbN amplitude E2 (μV)); AbN trough

amplitude values (AbN trough I (μV), AbN trough PI (μV), AbN trough E2 (μV)); and AbN normalised AUC values (AbN normalised AUC I, AbN normalised AUC PI, AbN normalised AUC E2). All amplitude, trough, and AUC values are measured relative to the minimum amplitude recorded in ∫AbN (AbN-zero) during a manually selected 10-minute epoch during baseline of eupnoeic respiratory activity. The occurrence of late-E bursts was also detected by the rise of ∫AbN discharge amplitude above a threshold amplitude value (AbN late-E threshold, see **figure 3-1C**) during the interval between final '1/3-expiration' and the subsequent 'PN-start' + 0.2s. The late-E threshold value was manually set at a constant value, above baseline noise and below late-E peak amplitudes, for the duration of the whole recording. Identified AbN Late-E bursts were used to calculate the late-E rate over the duration of the recording sample selected for analysis (AbN late-E rate (bpm)). In respiratory cycles where late-E activity was detected, the AbN late-E amplitude (μV) (relative to 'AbN-zero') was also obtained.

Sympatho-respiratory parameters obtained from thoraco-sympathetic nerve recordings

From the ∫tSN trace, peak amplitude, trough amplitude, and normalised AUC parameters were obtained per respiratory phase in a fashion identical to that described for AbN parameters (see **figure 3D**). Definitions for respiratory phase durations were identical to those used to obtain AbN parameters. All AbN amplitude, trough, and AUC values were measured relative to the minimum amplitude recorded in ∫tSN (tSN-zero) during a manually selected 10-minute epoch of eupnoeic respiratory and sympathetic activity during baseline. The following tSN parameters were obtained: tSN amplitude I (μV), tSN amplitude PI (μV), tSNN amplitude E2 (μV)); tSN trough I (μV), tSN trough PI (μV), tSN trough E2 (μV)); tSN normalised AUC I, tSN normalised AUC PI, and tSN normalised AUC E2.

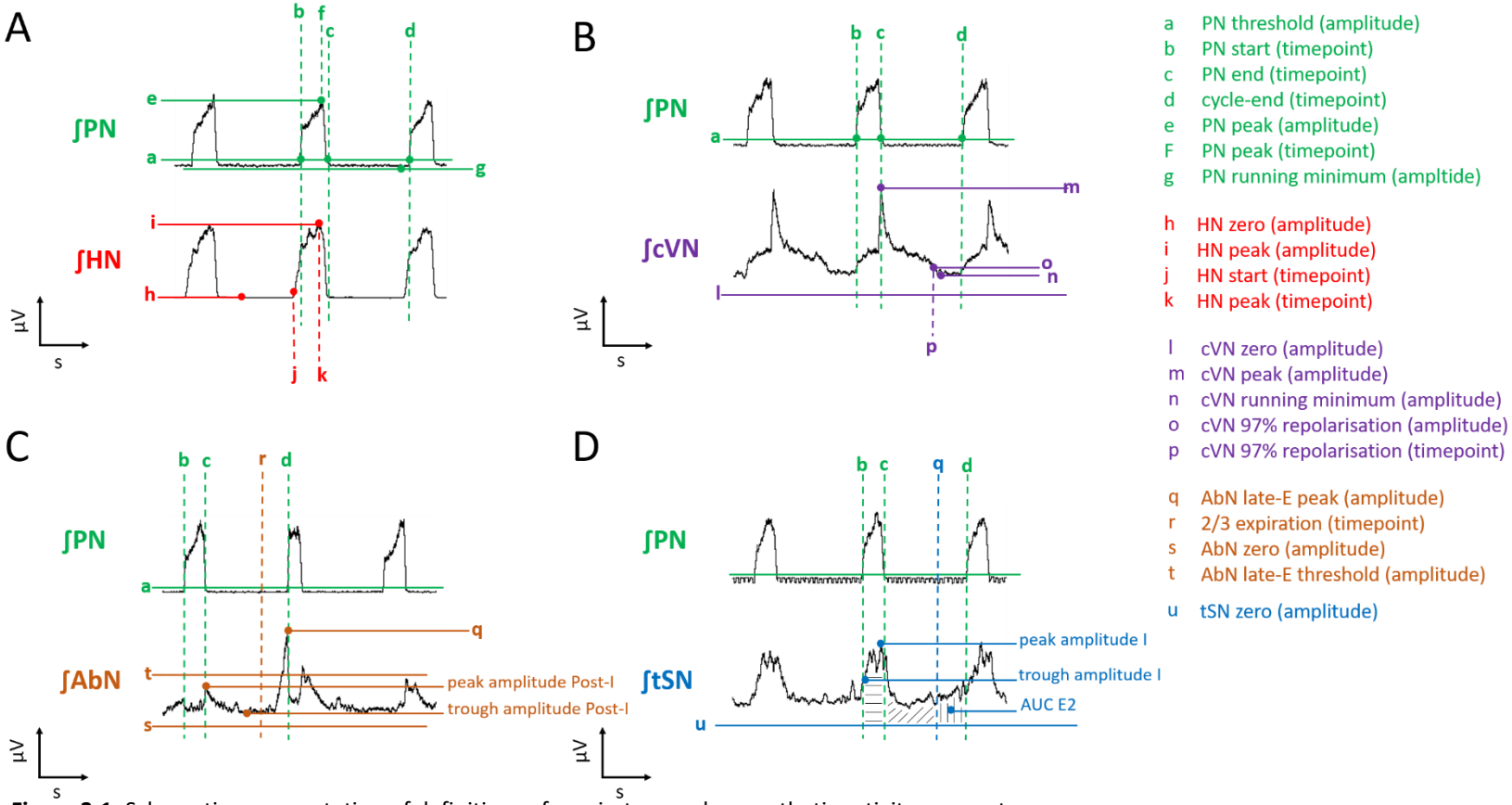


**Figure 3-1:** Schematic representation of definitions of respiratory and sympathetic activity parameters

Figures show integrated nerve traces annotated with amplitude or timepoint measurements (letters) of events relevant for the calculation of respiratory and sympathetic activity parameters from ∫PN (**A**, green), ∫HN (**A**, red), ∫cVN (**B**, purple), ∫AbN (**C**, orange), and ∫tSN (**D**, blue) traces. See text (section 3.2.3) for a detailed description of respiratory and sympatho-respiratory parameters, and how they are calculated with measurements depicted in this figure. I = inspiratory phase, AUC = area under the curve.

### *3.2.4 Experimental procedures, data acquisition, processing, and analysis for the NLX-101 concentration response curve experiment*

Experimental procedures

For experiments concerning the effect of 5-$HT_{1A}$R agonism on eupnoeic respiratory activity, rats were randomly allocated to one of two treatment groups: exposure to NLX-101 fumarate, or to 0.9% NaCl (vehicle). In *situ* WHBP of male juvenile rats (50-90g) for simultaneous recordings of PN, HN, cVN, and AbN were prepared as described in the General Methods (section 2.2.2). Once a stable eupnoeic respiratory pattern was established, a 15-minute baseline recording was made. In preparations of the NLX-101 exposure group, the baseline recording was followed by cumulative additions of NLX-101 working solution (100µM in Saline) to the circulating perfusate (200mL) to achieve perfusate concentrations of 1nM, 10nM, 100nM, 500nM, and 1µM in succession. At each concentration, a 15-minute recording was performed before proceeding to the next concentration. In the control group, 0.9 % NaCl (Hameln pharmaceuticals Ltd., Gloucester, UK) was added in volumes that corresponded to the volumes added in the NLX-101 concentration response curve and the same recording times were allowed.

Data acquisition, processing and analysis

Data acquisition parameters and the hardware and software used are described in the General Methods (section 2.2.4). Offline data processing and analysis was performed with Spike2 with the use of a custom script. With this script respiratory parameter values were obtained per respiratory cycle (see section 3.2.3). A 5-minute epoch, 10 minutes after each drug addition to the reservoir, was selected for analysis. For each respiratory parameter analysed, an average of all respiratory cycles in the sample was taken. Plots and statistical analysis were performed with Graphpad Prism (GraphPad Sotfware, Inc., La Jolla, USA). Recordings were excluded from statistical analysis if stability of respiratory output was inadequate from the onset of recording (e.g. displaying a biphasic respiratory pattern) or if general stability of the preparation deteriorated (usually indicated by a loss of perfusion pressure). Individual nerve recordings could be selectively excluded from a recording in the case of a loss of signal due to mechanical disconnection of a nerve from the suction electrode. These exclusion criteria apply for all *in situ* WHBP experiments described in this chapter (details on excluded recordings are provided in results sections 3.3.1-3.3.2). Statistical analysis was done with Two-Way Repeated Measures 2-Way ANOVA ($\alpha = 0.05$) with a Holm-Sidak correction for multiple comparisons of drug vs saline

at each step in the concentration-response relationship. The saline experiments served as a temporal control. This approach was chosen instead of comparison of NLX-101 at each concentration vs NLX-101 at the pre-treatment condition, in order to control for potential deterioration of the preparation over the course of the experiment.

### *3.2.5 Experimental procedures, data processing, and analysis for experiments assessing effects of NLX-101 on the hypercapnic response.*

Experimental procedures

For experiments concerning the effect of 5-$HT_{1A}$ transmission on the hypercapnic sympathetic and respiratory responses, rats were allocated to one of three treatment groups: exposure to NLX-101 (10nM), to WAY-100635 (300nM), or to 0.9% NaCl (vehicle, equivalent volume to NLX-101 concentration). In *situ* WHBP of male juvenile rats (50-90g) for simultaneous recordings of PN, cVN, AbN, and tSN were prepared as described in the General Methods (section 2.2.2). In experiments with administration of WAY-100635, only the PN and AbN were recorded. For each hypercapnic response experiment, perfusate was prepared in duplicate: one reservoir of eucapnic/normoxic perfusate (5% $CO_2$, $O_2$ balanced; 200mL); and one of hypercapnic perfusate (8% $CO_2$, $O_2$ balanced;200mL) (see section 3.1.1). Accordingly, drugs additions were made to both reservoirs (see section 3.1.1). After establishing stable eupnoeic outputs from all recorded nerves under perfusion with eucapnic/normoxic perfusate, a 5-minute recording of baseline respiratory and sympathetic activity was obtained. This was followed by an acute switch from normocapnic to hypercapnic (8% CO2; 92 % O2) perfusion, with hypercapnic perfusion maintained for 5 minutes before acute reversion to normocapnic perfusate, after which another 5-minute recovery period was recorded. Then, depending on the treatment group, either NLX-101 (10nM), WAY-100635 (300nM), or saline was added to the arterial perfusate, in the equivalent volumes. Ten minutes were allowed to reach steady-state after drug or vehicle administration. Then, the hypercapnic state switch sequence was repeated post-treatment: 5-minute baseline recording; followed by 5-minute hypercapnic perfusion; followed by recovery to eucapnic/normoxic perfusate and an additional 5-minute recording. **Figure 3-2** provides a schematic representation of this experimental protocol.

*Data acquisition, processing and analysis*

Data acquisition parameters and the hardware and software used are described in the General Methods (section 2.2.4). Data processing and analysis of sympatho-respiratory parameters was performed in Spike2 with the same custom script as described in section 3.1.3. The last 3 minutes from each 5-minute recording block (pre-treatment normocapnic; pre-treatment hypercapnic; NLX-101 normocapnic; NLX-101 hypercapnic) were selected to calculate state averages for sympatho-respiratory parameters for statistical analysis (see **figure 3-2**). For each sympatho-respiratory parameter, the hypercapnic responses were expressed as the change from the immediately preceding baseline sample (i.e. pre-treatment hypercapnic response = pre-treatment hypercapnic sample average - pre-treatment baseline sample average, and post-treatment hypercapnic response = post-treatment hypercapnic sample average - post-treatment baseline sample average). Statistical analysis was performed with repeated measures ANOVA ($\alpha$ =.05), with holm-Sidak comparison of drug (NLX-101 or WAY-100635) groups versus the vehicle group per treatment condition (pre-treatment or post-treatment). Any effects of drugs (WAY-100635 or NLX-101) on the hypercapnic response were expected to be revealed as a significant effect of drug versus vehicle in the post-treatment condition. As a supplementary analysis, the pre-treatment hypercapnic response in all recordings (irrespective of drug treatment group) was quantified by comparison of pre-treatment baseline sample averages versus pre-treatment hypercapnic sample averages with a repeated measures t-test ($\alpha$ =.05).

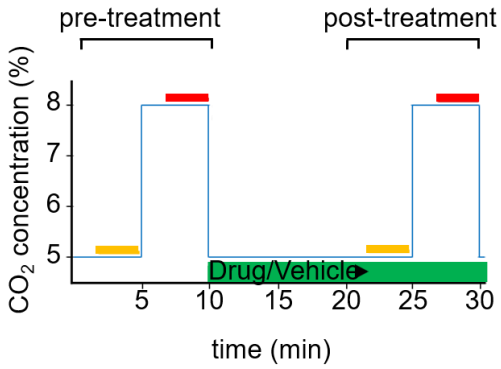


**Figure 3-2:** Recording protocol to assess effects of $5HT_{1A}R$ agonism and antagonism respiratory and sympatho-respriatory hypercapnic responses.

Recordings consisted of two normocapnia-hypercapnia sequences: the first during pre-treatment conditions, and a second after administration of NLX-101 (10nM), WAY100635 (300nM), or vehicle to the perfusate. For every respiratory/sympathetic output parameter, the response to hypercapnia was defined per treatment condition (pre-treatment vs. post-treatment) by subtracting the average of a 3-minute normocapnic sample (yellow line) from the average of the corresponding 3-minute hypercapnic sample (red line). The blue line represents the $CO_2$ concentration in the perfusate.

### *3.2.6 Experimental procedures, data processing, and analysis for analysis for experiments assessing effects of NLX-101 on the peripheral chemoreflex response*

Experimental procedures

For experiments concerning the effect of 5-$HT_{1A}$ transmission on the sympatho-respiratory response to peripheral chemoreflex activation, rats were allocated to one of three treatment groups: exposure to low concentration NLX-101 (10nM), exposure to high concentration NLX-101 (100nM); and exposure to NaCl (vehicle, in equivalent volume). In *situ* WHBP of male juvenile rats (50-90g) for simultaneous recordings of PN, cVN, AbN, and tSN were prepared as described in the General Methods (section 2.2.2). After establishing stable eupnoeic outputs from all recorded nerves, recordings commenced with a 7.5-minute baseline recording followed by a series of three pre-treatment intra-arterial bolus injections of 25, 50, and 75µL NaCN (0.03%) in saline (0.9% NaCl) solution. The bolus injections were interspersed with a 7.5-minute interval. After the final bolus injection of the pre-treatment series, a 5-minute interval followed. Depending on treatment conditions, low concentration NLX-101 (10nM), high concentration NLX-101 (100nM), or saline (0.9% NaCl) was then administrated and another 10-minute interval followed to establish a post-treatment steady-state. The series of three intra-arterial bolus injections (25, 50, and 75 µL) was performed again post-treatment. A schematic representation of this experimental protocol is provided in **Figure 3-3**.

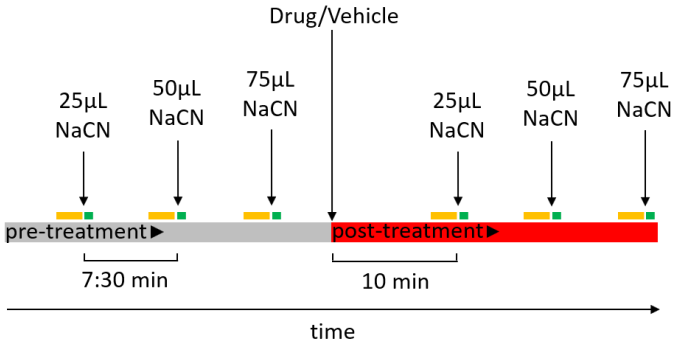


**Figure 3-3:** Recording protocol to assess effects of 5$HT_{1A}$R agonism on respiratory and sympatho-respiratory NaCN responses.

Experiments consisted of two series of intra-arterial NaCN solution (0.03%) boluses of incremental volumes (25, 50, and 75µL): the first series during pre-treatment conditions, and a second series after administration of NLX-101 (10nM or 100nM) or vehicle to the perfusate. For every respiratory/sympathetic output parameter, we calculated the change in each respiratory cycle during the first 20 seconds after NaCN administration (green bars) relative to its corresponding 60s baseline average (yellow bars). For each respiratory parameter, two types of NaCN response data were analysed: the 'maximum response', and the 'delay to maximum response'. The 'maximum response' value is the greatest change from baseline observed in any of the respiratory cycles during the first 20s after NaCN administration. The 'delay to maximum response' is the interval (s) between onset of NaCN bolus administration and the onset of the respiratory cycle in which the 'maximum response' value is observed.

*Data acquisition, processing and analysis*

Data acquisition parameters and the hardware and software used are described in the General Methods (section 2.2.4). Data processing and analysis of sympatho-respiratory parameters was performed in Spike2 with the same custom script as described in section 3.1.3. For every respiratory/sympathetic output parameter, we calculated the change in each respiratory cycle during the first 20 seconds after NaCN administration relative to its corresponding 60s baseline average (see Figure 3-3). For each respiratory parameter, two types of NaCN response data were analysed: the 'maximum response', and the 'delay to maximum response'. The 'maximum response' value was the greatest change from baseline observed in any of the respiratory cycles during the first 20s after NaCN administration. The 'delay to maximum response' is the interval (s) between onset of NaCN bolus administration and the onset of the respiratory cycle in which the 'maximum response' value is observed. For each respiratory and sympathetic output parameter, statistical analysis was performed separately for pre-, vs. post-treatment peripheral chemoreflex responses. Statistical analysis was performed with a 2-way repeated measures ANOVA ($\alpha = 0.05$) with Sidak correction for comparisons of either NLX-101 group (10nM or 100nM) vs. Vehicle per NaCN bolus (25µL vs. 50µL vs. 75µL). Any effects of drugs (NLX-101 10nM or NLX-101 100nM) versus vehicle on the sympatho-respiratory response to peripheral chemoreceptor activation were expected to be revealed as a significant effect of drug versus vehicle in the post-treatment condition. As a supplementary analysis, the pre-treatment NaCN responses in all recordings (irrespective of drug treatment group) were quantified by comparison of pre-treatment baseline sample averages versus pre-treatment NaCN bolus (25µL, 50µL, or 75µL) maximum response values with a 2-way repeated measures ANOVA with Geisser-Greenhouse correction and Holm-Sidak correction for multiple comparisons ($\alpha = .05$).

## 3.3 RESULTS

### *3.3.1 NLX-101 enhanced normocapnic respiratory drive in a concentration-dependent manner*

Through simultaneous recordings of the PN, cVN, HN, and AbN we performed an assessment of the effects on respiratory motor output of systemic administration of selective 5-$HT_{1A}$ receptor agonist NLX-101 versus vehicle controls in incremental concentrations in the *in situ* WHBP of juvenile rats.

*Sample sizes and excluded recordings.*

For the NLX-101 treatment group in concentration-response experiments, eight *in situ* WHBP recordings were obtained that were stable throughout the duration of the recording protocol. In six of these *in situ* WHBP experiments, simultaneous recordings of the PN, HN, cVN, and AbN were performed. In the remaining two experiments, HN recordings were not obtained (tSN was recorded instead, data not shown). One AbN recording, one cVN recording, and one HN recording were excluded from analysis due to mechanical and electrical recording issues unrelated to *in situ* WHBP viability and stability (i.e. loss of nerve recording due to poor electrode fit, or baseline shifts due to drifts in seal resistance of that nerve). Thus, for the concentration response experiments, the resulting sample sizes per nerve in the NLX-101 treatment group were: PN n=8; HN n=5; cVN n=7; and AbN n=7. For the vehicle treatment group, five *in situ* WHBP with recordings of PN, HN, cVN, and AbN were obtained.

*Pre-treatment discharge patterns of the PN, cVN, HN, and AbN in in situ WHBP reflect eupnoeic respiratory activity.*

In pre-treatment conditions, PN, HN, cVN, and AbN activities were identical to the typical eupnoeic respiratory activity (see section 1.2.1 for a detailed description of eupnoeic respiratory activity). Briefly, PN displayed a ramping burst pattern; HN displayed a similar pattern with onset slightly prior to inspiratory PN activity; cVN showed ramping inspiratory activity followed by decrementing post-I discharge that terminated at approximately two third of expiratory phase duration, and AbN showed low amplitude post-I discharge but no appreciable late-E activity (see **figure 3-4$A_1$/$B_1$** for pre-treatment example traces).

*Systemic administration of NLX-101 resulted in increased respiratory rate due to shortening of expiratory phase duration.*

**Figure 3-5** shows concentration-response relationships for respiratory rhythm parameters in response to NLX-101 or vehicle. **Table 3-1** can be referenced for the M and SEM values used to make the plots in figure 3-5.

Systemic administration of NLX-101 results in a concentration-dependent increase of the respiratory rate (PN rate (bpm), see **figure 3-5A$_1$** and **Table 3-1**) with a statistically significant increase relative to vehicle controls at 1μM NLX-101 (36.60 ± 2.82 vs. 24.34 ± 4.56, P=0.031; NLX-101 vs. vehicle group respectively). This increased respiratory rate appears to be mediated to a greater extent by shortening of expiratory phase duration (PN dur. E (s), see **figure 3-5A$_3$** and **table 3-1**) than by shortening of inspiratory phase duration phase (PN dur. I (s), see **figure 3-5A$_2$** and **table 3-1**) in the NLX-101 treatment group compared to vehicle controls. However, neither PN dur. E (s) and PN dur. I (s) were significantly altered in the NLX-101 treatment group relative to vehicle controls. The expiratory phase can be subdivided into duration of the Post-I phase (dur. PI), and duration of the second expiratory phase (dur. E2). Systemic administration of NLX-101 did not result in a significant reduction of cVN dur. PI (s) relative to vehicle controls (see **figure 3-5B$_1$**, and **table 3-1**). Ultimately, the Post-I duty cycle (cVN dur.PI : dur.E (%), see **figure 3-5B$_2$**, and **table 3-1**) was not significantly changed. This suggests that the duration of E2 is reduced to a similar extent as the duration of Post-I.

*Systemic administration of NLX-101 resulted in a shortening of time to peak in the hypoglossal motor output.*

Both in the Phrenic nerve (PN Tpeak (s), **figure 3-5A$_4$** and **table 3-1**) and the HN nerve (HN Tpeak (s), **figure 3-5C$_3$** and **table 3-1**), the average Tpeak(s) value for (pre-)inspiratory burst activity appears shortened after administration of NLX-101 in a concentration dependent fashion. Statistically significant shortening of Tpeak (s) in the NLX-101 treatment group vs vehicle controls is observed in the HN nerve at 100nM (NLX-101 vs. vehicle group M±SEM are 0.34 ± 0.05 vs. 0.71 ± 0.05, respectively; P=0.025), 500nM (NLX-101 vs. vehicle group M±SEM are 0.24 ± 0.03 vs. 0.63 ± 0.04, respectively; P=0.019), and 1μM (NLX-101 vs. vehicle group M±SEM are 0.22 ± 0.04 vs. 0.59 ± 0.05, respectively; P=0.029). The duration of pre-inspiratory activity in the HN burst was not significantly affected by NLX-101 relative to vehicle controls (HN dur. pre-I (s), **figure 3-5C$_1$** and **table 3-1**). Similarly, HN pre-I duty cycle was not significantly affected by administration of NLX-

101 (HN dur.pre-I : dur.I (%), See **figure 3-5C$_2$** and **table 3-1**). This suggests that the duration of HN burst activity during the inspiratory phase remained unchanged.

*Systemic administration of NLX-101 does not significantly increase the frequency of late-E activity*

The representative traces from the NLX-101 treatment group versus vehicle controls show that NLX-101 promoted the emergence of late-E activity in the abdominal nerve (see **figure 3-4**). Further, a large increase in mean AbN late-E activity (AbN late-E rate (bpm)) was seen in the NLX-101 treatment group compared to baseline (see **figure 3-5D$_1$**, and **table 3-1**). Interestingly, this increase in AbN late-E rate in the NLX-101 treatment group was not significant when compared to vehicle controls.

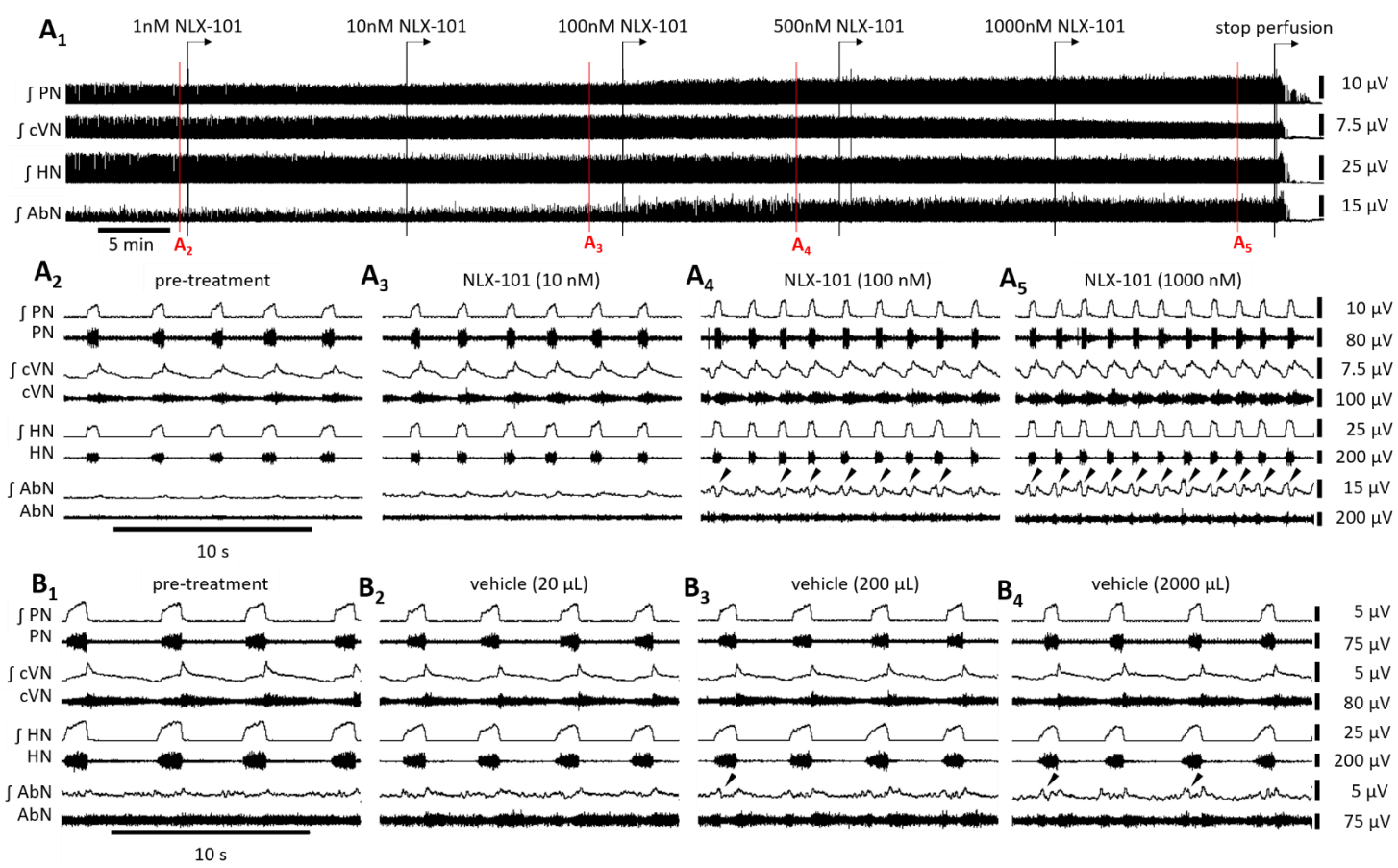


**Figure 3-4:** representative traces of *in situ* WHBP respiratory response to systemic administrations of NLX-101 vs. vehicle.

Peripheral nerve recordings of the PN, cVN, HN, and AbN in two *in situ* WHBP illustrate the dose-dependent effect of NLX-101 (**A**) vs. volume-matched vehicle (0.9% saline) administration (**B**) on respiratory motor nerve output. Activity in each nerve is represented by raw recording traces and integrated (∫) activity traces. The full time-course of a recording with NLX-101 is presented (**$A_1$**), with red annotation to indicate 10s sections depicted in more detail below (**$A_{2-5}$**). NLX-101 concentrations and vehicle volumes annotated on the figure describe the subsequent cumulative doses systemically applied via the perfusate as the recording progresses. NLX-101 enhances respiratory drive in a dose-dependent manner compared to vehicle controls. This is apparent in the dose-dependent increase of respiratory rate and the emergence of late-E discharges (black arrows) in the abdominal nerve in the NLX-101 treated *in situ* preparation (**$A_{1-5}$**), when compared to the vehicle control recording (**$B_{1-4}$**).

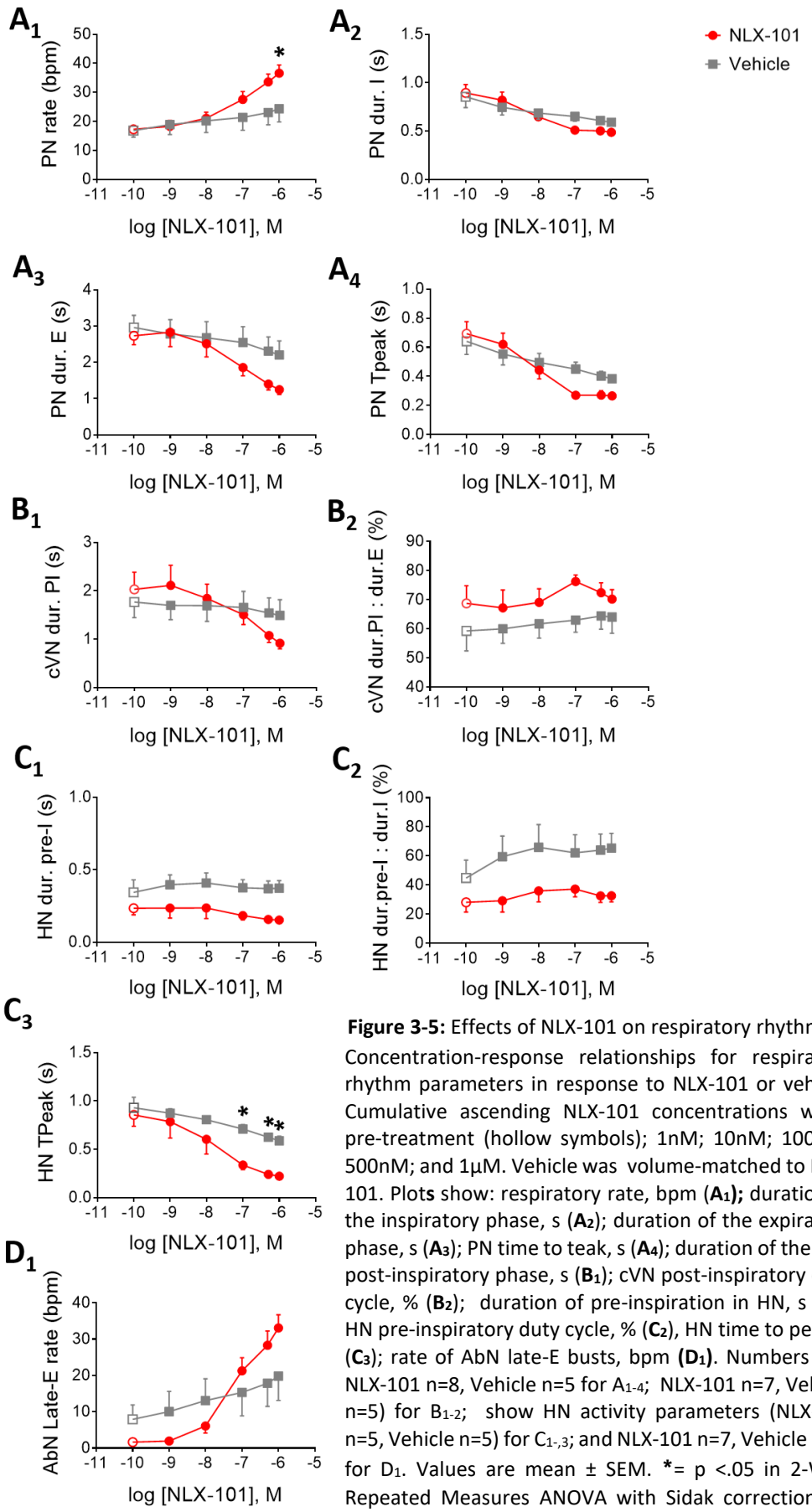


**Figure 3-5:** Effects of NLX-101 on respiratory rhythms**.** Concentration-response relationships for respiratory rhythm parameters in response to NLX-101 or vehicle. Cumulative ascending NLX-101 concentrations were: pre-treatment (hollow symbols); 1nM; 10nM; 100nM; 500nM; and 1µM. Vehicle was volume-matched to NLX-101. Plots show: respiratory rate, bpm (**$A_1$**)**;** duration of the inspiratory phase, s (**$A_2$**); duration of the expiratory phase, s (**$A_3$**); PN time to teak, s (**$A_4$**); duration of the cVN post-inspiratory phase, s (**$B_1$**); cVN post-inspiratory duty cycle, % (**$B_2$**); duration of pre-inspiration in HN, s (**$C_1$**); HN pre-inspiratory duty cycle, % (**$C_2$**), HN time to peak, s (**$C_3$**); rate of AbN late-E busts, bpm **($D_1$)**. Numbers are: NLX-101 n=8, Vehicle n=5 for $A_{1\text{-}4}$; NLX-101 n=7, Vehicle n=5) for $B_{1\text{-}2}$; show HN activity parameters (NLX-101 n=5, Vehicle n=5) for $C_{1\text{-},3}$; and NLX-101 n=7, Vehicle n=5) for $D_1$. Values are mean ± SEM. *****= p <.05 in 2-WAY Repeated Measures ANOVA with Sidak correction for comparisons of NLX-101 group vs. vehicle control.

**Table 3-1** Group means for concentration-response relationships of NLX-101 or vehicle on respiratory rhythms.
Values are mean ± SEM values per treatment group. Significantly different group means (NLX-101 vs. vehicle controls, $p<0.05$) are annotated in **bold red text**.

| Nerve | parameter | pre-treatment | | 1nM | | 10nM | | 100nM | | 500nM | | 1µM | |
|---|---|---|---|---|---|---|---|---|---|---|---|---|---|
| | | NLX-101 | vehicle | NLX-101 | vehicle | NLX-101 | vehicle | NLX-101 | vehicle | NLX-101 | vehicle | NLX-101 | vehicle |
| PN | rate (bpm) | 17.29 ±1.14 | 16.81 ±2.23 | 18.28 ±2.06 | 18.88 ±3.49 | 21.05 ±2.10 | 20.20 ±4.07 | 27.56 ±2.72 | 21.36 ±4.41 | 33.58 ±2.73 | 23.04 ±4.21 | **36.60 ±2.82** | 24.34 ±4.56 |
| | dur. I (s) | 0.89 ±0.09 | 0.85 ±0.11 | 0.82 ±0.08 | 0.75 ±0.08 | 0.65 ±0.07 | 0.69 ±0.07 | 0.51 ±0.03 | 0.65 ±0.05 | 0.50 ±0.04 | 0.61 ±0.04 | 0.49 ±0.04 | 0.59 ±0.04 |
| | dur. E (s) | 2.73 ±0.25 | 2.96 ±0.34 | 2.83 ±0.40 | 2.78 ±0.39 | 2.51 ±0.36 | 2.68 ±0.45 | 1.86 ±0.23 | 2.55 ±0.44 | 1.40 ±0.16 | 2.31 ±0.39 | 1.24 ±0.13 | 2.20 ±0.38 |
| | Tpeak (s) | 0.69 ±0.08 | 0.64 ±0.09 | 0.62 ±0.08 | 0.55 ±0.08 | 0.44 ±0.06 | 0.50 ±0.06 | 0.27 ±0.03 | 0.45 ±0.05 | 0.27 ±0.03 | 0.40 ±0.03 | 0.27 ±0.03 | 0.38 ±0.03 |
| HN | dur. pre-I (s) | 0.24 ±0.05 | 0.34 ±0.09 | 0.24 ±0.07 | 0.40 ±0.07 | 0.24 ±0.07 | 0.41 ±0.07 | 0.18 ±0.03 | 0.38 ±0.06 | 0.16 ±0.02 | 0.37 ±0.05 | 0.15 ±0.37 | 0.37 ±0.05 |
| | dur.pre-I : dur.I (%) | 28.23 ±6.70 | 44.84 ±12.29 | 29.30 ±7.80 | 59.52 ±14.15 | 36.02 ±7.57 | 65.92 ±15.61 | 37.28 ±5.36 | 62.24 ±12.42 | 32.65 ±4.54 | 64.05 ±10.99 | 32.73 ±4.30 | 65.48 ±10.13 |
| | Tpeak (s) | 0.86 ±0.12 | 0.93 ±0.11 | 0.79 ±0.17 | 0.87 ±0.05 | 0.60 ±0.15 | 0.81 ±0.03 | **0.34 ±0.05** | 0.71 ±0.05 | **0.24 ±0.03** | 0.63 ±0.04 | **0.22 ±0.04** | 0.59 ±0.05 |
| cVN | dur. PI (s) | 2.03 ±0.36 | 1.77 ±0.32 | 2.11 ±0.42 | 1.70 ±0.30 | 1.84 ±0.30 | 1.69 ±0.33 | 1.51 ±0.20 | 1.65 ±0.33 | 1.07 ±0.15 | 1.54 ±0.31 | 0.91 ±0.12 | 1.49 ±0.33 |
| | dur-PI : dur.E (%) | 68.78 ±6.04 | 59.30 ±6.89 | 67.21 ±6.16 | 61.72 ±4.92 | 69.11 ±4.66 | 61.72 ±4.92 | 76.29 ±2.27 | 63.00 ±4.20 | 72.43 ±3.38 | 64.42 ±4.56 | 70.25 ±3.26 | 64.08 ±5.61 |
| AbN | late-E rate (bpm) | 1.65 ±1.21 | 7.93 ±3.98 | 1.95 ±1.14 | 10.06 ±5.56 | 6.08 ±1.94 | 13.09 ±6.01 | 21.30 ±3.63 | 15.32 ±6.42 | 28.33 ±3.94 | 17.85 ±6.37 | 33.08 ±3.64 | 19.80 ±6.71 |

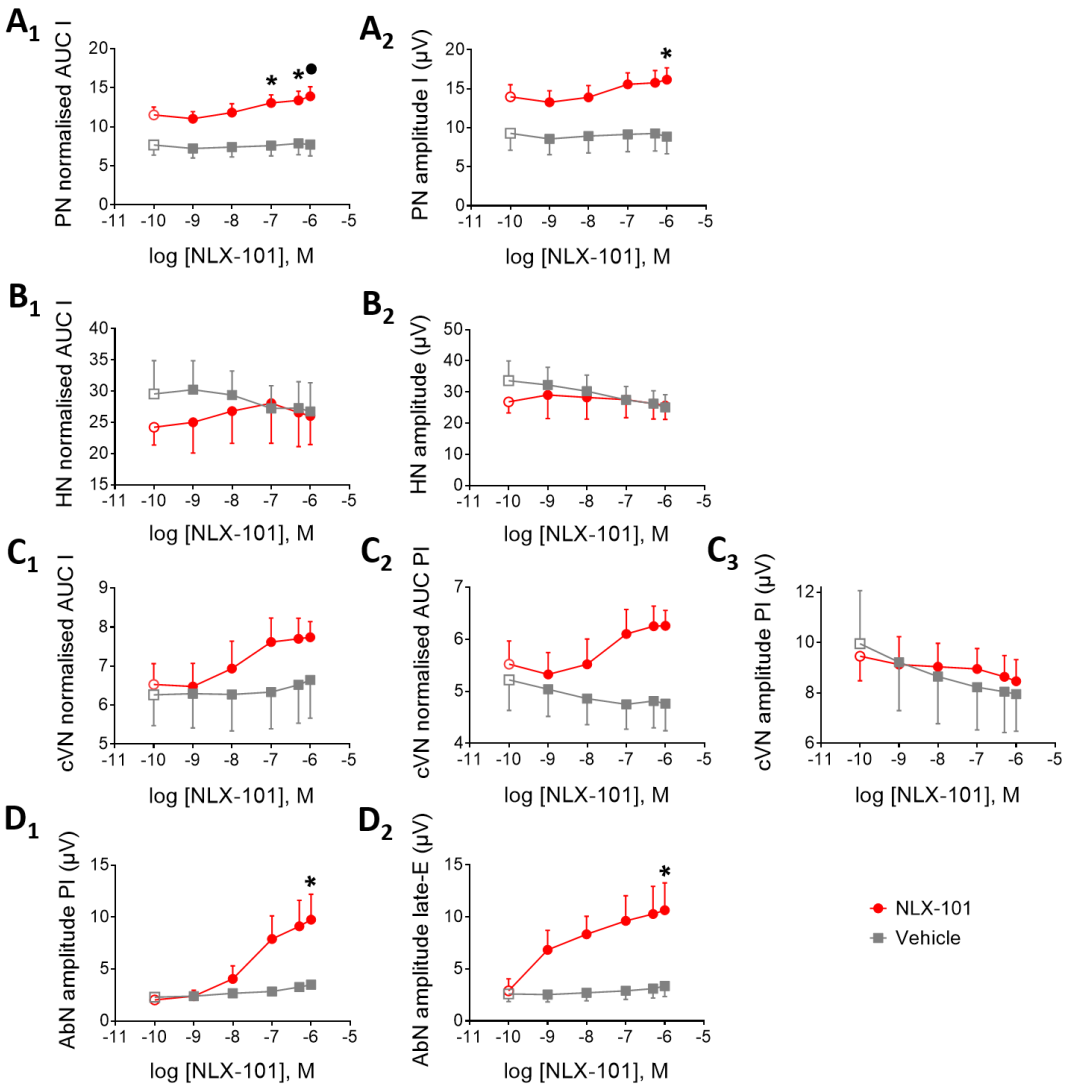


**Figure 3-6:** Effects of NLX-101 on respiratory patterns.

Concentration-response relationships for respiratory pattern parameters in NLX-101 or vehicle. Cumulative NLX-101 concentrations were: pre-treatment (hollow symbols); 1nM; 10nM; 100nM; 500nM; and 1µM. Vehicle was volume matched to NLX-101. Plots show: area under the curve of PN bursts, normalised to inspiratory phase duration in seconds (**$A_1$**); PN burst peak amplitude (**$A_2$**); area under the curve of HN bursts, normalised to inspiratory phase duration in seconds (**$B_1$**); HN burst peak amplitude, µV (**$B_2$**); cVN area under the curve during inspiration, normalised to inspiratory phase duration in seconds (**$C_1$**); cVN area under the curve during Post-I, normalised to Post-I phase duration in seconds (**$C_2$**); cVN burst peak amplitude during Post-I, µV (**$C_3$**); AbN burst peak amplitude during Post-I, µV (**$D_1$**); AbN late-E burst peak amplitude, µV (**$D_2$**). Numbers are: NLX-101 n=8, Vehicle n=5 for $A_{1\text{-}2}$; NLX-101 n=5, Vehicle n=5 for $B_{1\text{-}2}$; NLX-101 n=7, Vehicle n=5 for $C_{1\text{-}3}$ and $D_{1,2}$. Values are mean ± SEM. *= p <.05, • = p<.01 in 2-WAY Repeated Measures ANOVA with Sidak correction for comparisons of NLX-101 group vs. vehicle control.

**Table 3-2:** Group means for concentration-response relationships of NLX-101 or vehicle on respiratory waveform patterns.

Values are mean ± SEM values per treatment group. Significantly different group means (NLX-101 vs. vehicle controls, $p<0.05$) are annotated in **bold red text**.

| Nerve | parameter | pre-treatment | | 1nM | | 10nM | | 100nM | | 500nM | | 1µM | |
|---|---|---|---|---|---|---|---|---|---|---|---|---|---|
| | | NLX-101 | vehicle | NLX-101 | vehicle | NLX-101 | vehicle | NLX-101 | vehicle | NLX-101 | vehicle | NLX-101 | vehicle |
| PN | normalised AUC I | 11.53 ±1.01 | 7.68 ±1.31 | 11.04 ±0.90 | 7.23 ±1.22 | 11.83 ±1.13 | 7.41 ±1.28 | **13.05 ±1.04** | 7.59 ±1.32 | **13.39 ±1.16** | 7.88 ±1.46 | **13.91 ±1.22** | 7.73 ± 1.45 |
| | amplitude I (µV) | 13.97 ±1.55 | 9.29 ±2.17 | 13.27 ±1.46 | 8.58 ±2.02 | 13.91 ±1.50 | 8.93 ±2.17 | 15.58 ±1.48 | 9.16 ±2.22 | 15.77 ±1.57 | 9.28 ±2.26 | **16.18 ±1.51** | 8.86 ±2.20 |
| HN | normalised AUC I | 24.22 ±2.86 | 29.56 ±5.35 | 25.02 ±4.93 | 30.23 ±4.63 | 26.80 ±5.17 | 29.38 ±3.84 | 28.07 ±6.42 | 27.24 ±3.62 | 26.58 ±5.46 | 27.28 ±4.23 | 26.04 ±4.59 | 26.74 ±4.61 |
| | amplitude (µV) | 26.88 ±3.62 | 33.65 ±6.35 | 29.05 ±7.59 | 32.26 ±5.67 | 28.28 ±6.96 | 30.28 ±5.18 | 27.54 ±5.80 | 27.48 ±4.30 | 26.27 ±4.93 | 26.27 ±4.14 | 25.64 ±4.42 | 25.06 ±4.11 |
| cVN | Normalised AUC-I | 6.53 ±0.53 | 6.27 ±0.79 | 6.48 ±0.59 | 6.30 ±0.88 | 6.94 ±0.70 | 6.28 ±0.94 | 7.62 ±0.61 | 6.33 ±0.94 | 7.70 ±0.53 | 6.52 ±0.98 | 7.74 ±0.40 | 6.64 ±0.98 |
| | Normalised AUC-PI | 5.52 ±0.45 | 5.22 ±0.59 | 5.33 ±0.42 | 5.04 ±0.52 | 5.52 ±0.49 | 4.86 ±0.51 | 6.10 ±0.47 | 4.75 ±0.48 | 6.25 ±0.38 | 4.82 ±0.52 | 6.26 ±0.30 | 4.76 ±0.52 |
| | ampliktude PI (µV) | 9.46 ±0.98 | 9.95 ±2.10 | 9.13 ±1.11 | 9.22 ±1.92 | 9.04 ±0.93 | 8.65 ±1.87 | 8.95 ±0.81 | 8.23 ±8.23 | 8.65 ±0.84 | 8.05 ±1.62 | 8.47 ±0.86 | 7.96 ±1.48 |
| AbN | amplitude PI (µV) | 2.03 ±0.35 | 2.30 ±0.35 | 2.39 ±0.56 | 2.40 ±0.26 | 4.06 ±1.26 | 2.67 ±0.24 | 7.89 ±2.23 | 2.84 ±0.14 | 9.12 ±2.51 | 3.27 ±0.27 | **9.75 ±2.44** | 3.49 ±0.36 |
| | amplitude Late-E (µV) | 2.89 ±1.15 | 2.60 ±0.75 | 6.83 ±1.88 | 2.54 ±0.75 | 8.33 ±1.73 | 2.71 ±0.78 | 9.62 ±2.42 | 2.89 ±0.82 | 10.28 ±2.65 | 3.10 ±0.90 | **10.65 ±2.63** | 3.35 ±1.02 |

*Systemic administration of NLX-101 altered PN and AbN respiratory patterns*

Systemic administration of NLX-101 in the *in situ* WHBP resulted in altered PN and AbN respiratory patterns compared to vehicle controls. Peak amplitude of the PN inspiratory burst was increased compared to vehicle controls (PN amplitude I (μV), see **figure 3-6A$_2$** and **table 3-2**), with statistically significant difference in NLX-101 vs. vehicle treatment group means at 1μM (NLX-101 vs. vehicle group, 16.18 ± 1.51 vs. 8.86 ± 2.20, respectively; p=0.034)**.** Similarly, PN normalised AUC (see **figure 3-6A$_1$** and **table 3-2**) was increased after administration of NLX-101 with significant increase relative to vehicle controls at 100nM **(**NLX-101 vs. vehicle group M±SEM are 13.05 ± 1.04 vs. 7.59 ± 1.32, respectively; p=0.014), 500nM **(**NLX-101 vs. vehicle group M±SEM are 13.39 (1.16) vs. 7.88 (1.46), respectively; p=0.013**)**, and 1μM **(**M (NLX-101 vs. vehicle group M±SEM are 13.91 (1.22) vs. 7.73 (1.45), respectively; p=0.004**)**.

The average maximum amplitude of Post-I bursts in the cVN (cVN amplitude PI (μV), see **figure 3-6C$_3$** and **table 3-2**), was not significantly affected by NLX-101 administration relative to vehicle controls. Similarly, normalised AUC values in the cVN both during the inspiratory phase (cVN normalised AUC-I, see **figure 3-6C$_1$** and **table 3-2**), and during the post-inspiratory phase (cVN normalised AUC-PI, see **figure 3-6C$_2$** and **table 3-2**) were not significantly changed in the NLX-101 group relative to vehicle controls.

Peak amplitudes of AbN activity during post-I phase (AbN amplitude PI (μV), see **figure 3-6D$_1$** and **table 3-2**) and during late-E phase (AbN amplitude late-E (μV), see **figure 3-6D$_1$** and **table 3-2**) were both significantly increased compared to vehicle controls at 1μM NLX-101 (AbN amplitude PI (μV): NLX-101 vs. vehicle group 9.75 ±2.44 vs. 3.49 ±0.36, respectively, p=0.031. AbN amplitude late-E (μV): NLX-101 vs. vehicle group M±SEM are 10.65 ± 2.63 vs. 3.35 ± 1.02, respectively, p=0.048).

Hypoglossal nerve respiratory patterns did not change significantly. Both the peak amplitude (HN amplitude I (μV), see **figure 3-6B$_2$** and **table 3-2**) and normalised AUC values (HN normalised AUC I, see **figure 3-6B$_2$** and **table 3-2**) in the HN were not affected significantly after administration of NLX-101 relative to vehicle controls.

*The eupnoeic three-phase respiratory pattern persisted after systemic administration of NLX-101*

Previous studies had reported inhibition of post-inspiratory neurones in response to systemic administration of 5-$HT_{1A/7}$ agonist 8-OH-DPAT (Manzke et al., 2009, Shevtsova et al., 2011), which could result in a biphasic respiratory pattern. The biphasic respiratory pattern can be recognised in *in situ* WHBP peripheral nerve output patterns by the loss of cVN Post-I activity, and a square-wave (as opposed to ramping) discharge pattern in PN bursts. In none of the recordings *in situ* WHBP in the NLX-101 treatment group (n=8) did we observe a transition to a biphasic respiratory pattern. The typical response to NLX-101 is illustrated in the representative traces in **figure 3-4**, which shows an increased respiratory rate, but without abolishing cVN Post-I activity, and with retention of the ramping PN burst shape. As addressed above, the NLX-101 treatment group average for cVN post-I phase duration (**figure 3-5B$_1$**, and **table 3-1**) is not significantly reduced relative to the vehicle group average, and duty cycle is unchanged. Furthermore, the normalised AUC of the cVN Post-I burst is not reduced in the NLX-101 treatment group relative to vehicle controls (see **figure 3-6C$_2$**, and **table 3-2**.

### *3.3.2 Effects of NLX-101 on sympatho-respiratory response to hypercapnia*

Through simultaneous recordings of the PN, cVN, AbN, and tSN we performed an assessment of the effects of systemic administration of 5-$HT_{1A}$R agonist NLX-101 (10nM) or 5-$HT_{1A}$R antagonist WAY-100635 (300nM) versus vehicle controls on the respiratory and sympathetic hypercapnic response in the *in situ* WHBP of juvenile rats.

*Sample sizes and excluded recordings*

The NLX-101 (10nM) treatment group in hypercapnic response experiments consisted of 7 *in situ* WHBP experiments, where PN, AbN, and tSN were simultaneously recorded. Cervical vagus nerve recordings were also obtained in all i*n situ* WHBP, with the exception of one recording. Thus, the sample sizes for the NLX-101 (10nM) treatment group in hypercapnic response experiments are: PN n=7; cVN n=6; AbN n=7; tSN n=7). The WAY-100635 (300nM) treatment group in hypercapnic response experiments consisted of 7 *in situ* WHBP experiments in which only PN and AbN recordings were obtained. The vehicle control group in hypercapnic response experiments consisted of 7 *in situ* WHBP in which PN, cVN, AbN, and tSN were recorded. Of these, one PN recording and one AbN recording were excluded from analysis due to inadequate recording quality for reasons unrelated to viability and stability of the preparation (i.e. due to suboptimal seal of the electrode to the nerve). In addition to these recordings, an additional five *in situ* WHBP experiments were performed in which only PN and AbN were recorded. This results in the following sample sizes for the vehicle group in hypercapnia experiments: PN n=11; cVN n=7; AbN n=11; tSN n=7). For comparison of pre-treatment eucapnic and hypercapnic respiratory and sympathetic activity, recordings from all treatment groups were pooled. Sample sizes for this comparison were: PN n=25; cVN = 13; AbN n=25; tSN n=14)

*Pre-treatment hypercapnic rhythms and patterns of the PN, cVN, AbN, and tSN*

The hypercapnic response in *in* situ WHBP of juvenile rats has previously been described as an increase in respiratory rate and pattern, combined with the emergence of AbN and tSN late-E activity (Abdala et al., 2009, Marina et al., 2010, Molkov et al., 2011). The pre-treatment hypercapnic response in recordings of the present chapter was consistent with this description (see representative traces in **figure 3-7A$_{1-2}$**). Mean values of pre-treatment baseline and pre-treatment hypercapnic respiratory and sympathetic activity, and statistical comparisons thereof, are reported in **Supplementary Tables S1-S2** (See appendix: supplementary data).

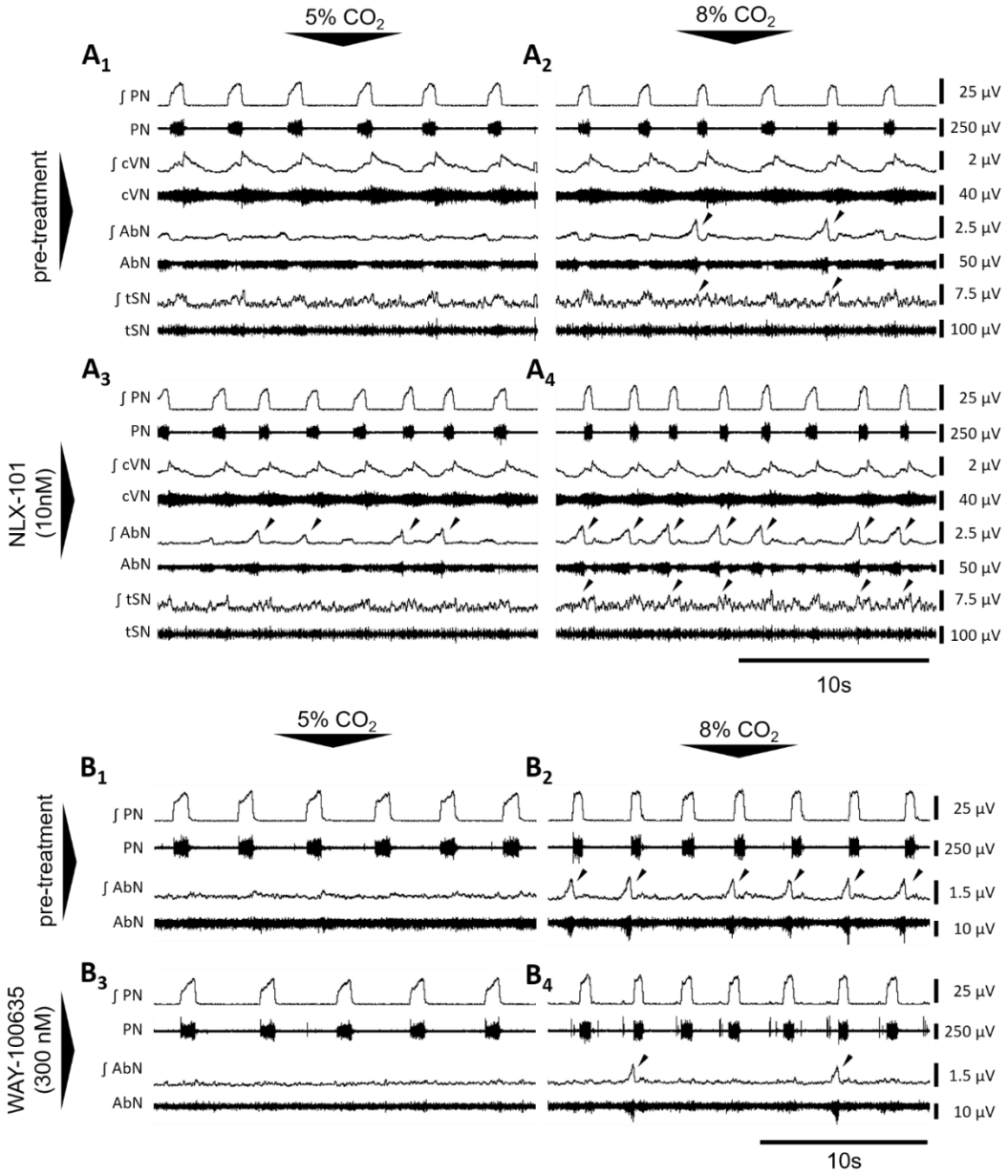


**Figure 3-7:** Representative traces of effect of NLX-101 and WAY-100635 on the sympathetic and respiratory hypercapnic response.

(**$A_{1-4}$**) PN, cVN, AbN, and tSN raw and integrated (∫) traces obtained from a single *in situ* WHBP recording illustrate sympathetic and respiratory activity during: pre-treatment eucapnic conditions (5% $CO_2$, $O_2$-balanced) (**$A_1$**); pre-treatment hypercapnic conditions (8% $CO_2$, $O_2$-balanced) (**$A_2$**); eucapnic conditions after systemic administration of NLX-101 (10nM) (**$A_3$**); and hypercapnic conditions after administration of NLX-101 (10nM) (**$A_4$**). Similarly, (**$B_{1-4}$**) show PN and AbN raw and integrated (∫) traces obtained from an *in situ* WHBP recording under normocapnic and hypercapnic conditions, before and after systemic administration of WAY-100635 (300nM). Arrows indicate AbN late-E bursts and concurrent augmented late-E tSN activity. Mean values and statistical comparisons of pre-treatment baseline vs. hypercapnic respiratory activities obtained from all recordings pooled are reported in **Supplementary Table S1** (see appendix).

*Systemic administration of NLX-101 did not affect the respiratory response to hypercapnia*

**Figure 3-8** shows plots for pre-treatment and post-treatment respiratory hypercapnic rhythms between the different treatment groups. Mean values of changes from eucapnia pre- and post-treatment are provided for each treatment group (NLX-101 10nM; WAY-100635 300nM; vehicle) in **table 3-3**.

For none of the analysed respiratory rhythm parameters, and for neither post-, nor pre-treatment comparisons, statistically significant differences in the mean hypercapnic response of the NLX-101 (10nM) treatment group or the WAY-100635 (300nM) treatment group were found when compared to vehicle controls (see **figure 3-8** and **table 3-3**).

**Figure 3-9** shows plots for pre-treatment and post-treatment comparisons of the hypercapnic response in the drug treatment groups (NLX-101 10nM; WAY-100635 (300nM)) vs. vehicle controls for PN, cVN, and AbN respiratory patterns (Δ normalised AUC and Δ maximum amplitude (μV), per respiratory phase, per motor nerve). Corresponding pre-, and post-treatment group means and SEM values for each hypercapnic response parameter are listed in **table 3-4**. No significant differences between the mean hypercapnic responses for the drug treatment groups vs. vehicle controls was observed in respiratory patterns. Thus, systemic administration of NLX-101 or WAY-100635 did not affect the respiratory response to hypercapnia in *in situ* WHBP of juvenile rats.

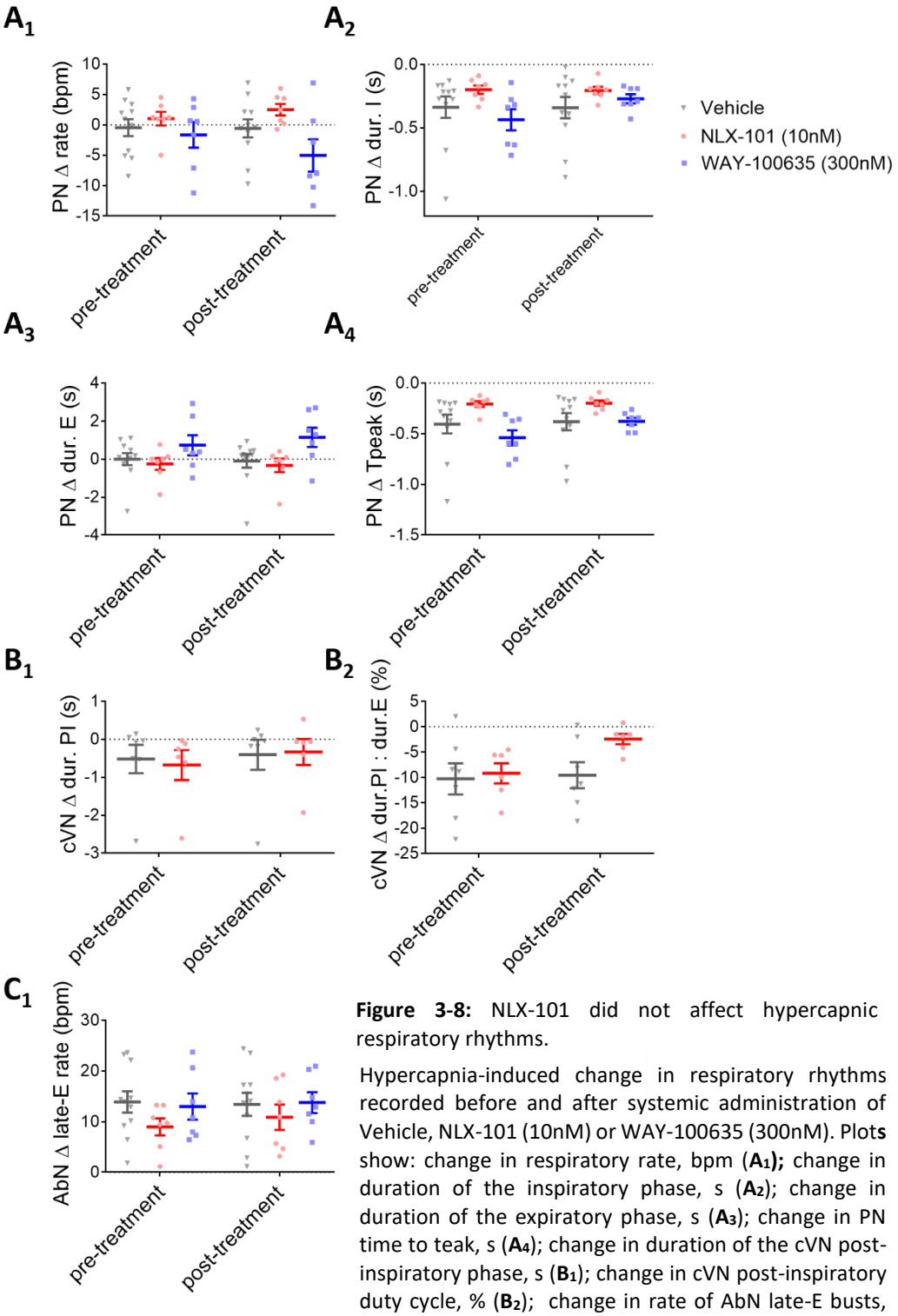


**Figure 3-8:** NLX-101 did not affect hypercapnic respiratory rhythms.

Hypercapnia-induced change in respiratory rhythms recorded before and after systemic administration of Vehicle, NLX-101 (10nM) or WAY-100635 (300nM). Plots show: change in respiratory rate, bpm (**$A_1$**); change in duration of the inspiratory phase, s (**$A_2$**); change in duration of the expiratory phase, s (**$A_3$**); change in PN time to teak, s (**$A_4$**); change in duration of the cVN post-inspiratory phase, s (**$B_1$**); change in cVN post-inspiratory duty cycle, % (**$B_2$**); change in rate of AbN late-E busts, bpm (**$C_1$**). Numbers are: Vehicle n=11, NLX-101 n=7, WAY-100635 n=7 for $A_{1-4}$ and $C_1$; Vehicle n=6, NLX-101 n=6 for $B_{1-2}$. Values are mean ± SEM. 2-WAY Repeated Measures ANOVA with Sidak correction for comparisons of NLX-101 or WAY-100635 vs. vehicle group vs. vehicle per treatment condition (pre- vs. post-treatment) yields no significant results. Mean values and statistical comparisons of pre-treatment baseline vs. hypercapnic respiratory activities are reported in **Supplementary Table S1** (see appendix).

**Table 3-3** Group means for hypercapnic respiratory rhythm responses pre- and post-treatment with NLX-101 (10nM), WAY-100635 (300nM) or Vehicle.

Values are mean **±** SEM values per treatment group. NLX-101 (10nM) or WAY-100635 (300nM) group means are not significantly different from Vehicle group means.

| | | pre-treatment | | | post-treatment | | |
|---|---|---|---|---|---|---|---|
| **nerve** | **parameter** | **WAY-100635 (300nM)** | **vehicle** | **NLX-101 (10nM)** | **WAY-100635 (300nM)** | **vehicle** | **NLX-101 (10nM)** |
| **PN** | **Δ rate (bpm)** | −1.65 ±2.11 | −0.47 ±1.40 | 1.01 ±1.12 | −5.04 ±2.65 | −0.59 ±1.48 | 2.49 ±0.96 |
| | **Δ dur. I (s)** | −0.44 ±0.08 | −0.34 ±0.09 | −0.19 ±0.03 | −0.27 ±0.04 | −0.34 ±0.08 | −0.20 ±0.03 |
| | **Δ dur. E (s)** | 0.73 ±0.53 | −.002 ±0.32 | −0.25 ±0.31 | 1.15 ±0.51 | −0.10 ±0.36 | −0.33 ±0.35 |
| | **Δ Tpeak (s)** | −0.54 ±0.08 | −0.40 ±0.09 | −0.21 ±0.03 | −0.38 ±0.03 | −0.38 ±0.09 | −0.20 ±0.03 |
| **cVN** | **Δ dur. PI (s)** | - | −0.52 ±0.37 | −0.68 ±0.40 | - | −0.41 ±0.40 | −0.34 ±0.34 |
| | **Δ dur.PI : dur.E (%)** | - | −10.28 ±3.07 | −9.17 ±1.99 | - | −9.55 ±2.57 | −2.43 ±1.02 |
| **AbN** | **Δ late-E rate (bpm)** | 13.00 ±2.58 | 13.90 ±2.11 | 8.98 ±1.67 | 13.78 ±2.06 | 13.44 ±2.27 | 13.78 ±2.06 |

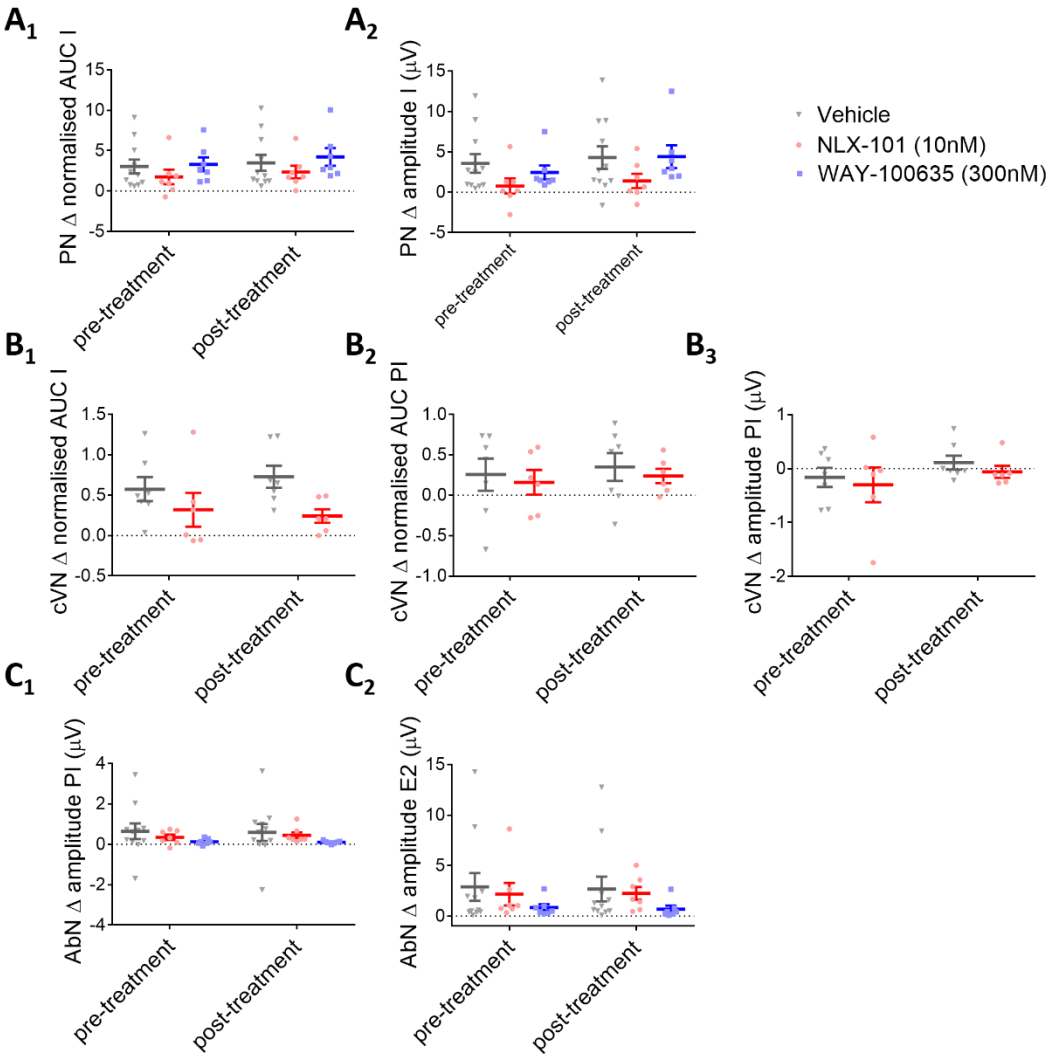


**Figure 3-9:** NLX-101 did not affect hypercapnic respiratory patterns.

Hypercapnia-induced change in respiratory patterns recorded before and after systemic administration of vehicle, NLX-101 (10nM) or WAY-100635 (300nM).Plots show: change in area under the curve of PN bursts, normalised to inspiratory phase duration in seconds (**$A_1$**); change in PN burst peak amplitude (**$A_2$**); change in cVN area under the curve during inspiration, normalised to inspiratory phase duration in seconds (**$B_1$**); change in cVN area under the curve during Post-I, normalised to Post-I phase duration in seconds (**$B_2$**); change in cVN burst peak amplitude during Post-I, μV (**$B_3$**); change in AbN burst peak amplitude during Post-I, μV (**$D_1$**); change in AbN E2 burst peak amplitude, μV (**$D_2$**).Numbers are: Vehicle n=11, NLX-101 n=7, WAY-100635 n=7 for $A_{1-2}$ and $C_{1-2}$; Vehicle n=6, NLX-101 n=6 for $B_{1-3}$. Values are mean ± SEM. 2-WAY Repeated Measures ANOVA with Sidak correction for comparisons of NLX-101 or WAY-100635 vs. vehicle group vs. vehicle per treatment condition (pre- vs. post-treatment) yields no significant results. Mean values and statistical comparisons of pre-treatment baseline vs. hypercapnic respiratory activities are reported in **Supplementary Table S1** (see appendix).

**Table 3-4:** Group means for hypercapnic respiratory patterns pre- and post-treatment with NLX-101 (10nM), WAY-100635 (300nM) or Vehicle.

Values are mean **±** SEM values per treatment group. Values are mean **±** SEM values per treatment group. NLX-101 (10nM) or WAY-100635 (300nM) group means are not significantly different from vehicle group means.

| | | **pre-treatment** | | | **post-treatment** | | |
|---|---|---|---|---|---|---|---|
| **nerve** | **parameter** | **WAY-100635 (300nM)** | **vehicle** | **NLX-101 (10nM)** | **WAY-100635 (300nM)** | **vehicle** | **NLX-101 (10nM)** |
| **PN** | **Δ normalised AUC I** | 3.31 ±0.86 | 3.04 ±0.86 | 1.76 ±0.89 | 4.22 ±1.08 | 3.50 ±0.99 | 2.37 ±0.77 |
| | **Δ amplitude I (μV)** | 2.45 ±0.87 | 3.58 ±1.15 | 0.78 ±0.96 | 4.40 ±1.41 | 4.30 ±1.39 | 1.41 ±0.88 |
| **cVN** | **Δ normalised AUC I** | - | 0.58 ±0.15 | 0.32 ±0.21 | - | 0.73 ±0.14 | 0.24 ±0.08 |
| | **Δ normalised AUC PI** | - | 0.26 ±0.20 | 0.16 ±0.15 | - | 0.35 ±0.17 | 0.24 ±0.09 |
| | **Δ amplitude PI (μV)** | - | −0.16 ±0.18 | −0.30 ±0.32 | - | 0.11 ±0.13 | −0.06 ±0.11 |
| **AbN** | **Δ amplitude PI (μV)** | 0.13 ±0.06 | 0.65 ±0.39 | 0.35 ±0.13 | 0.10 ±0.03 | 0.59 ±0.42 | 0.45 ±0.15 |
| | **Δ late-E amplitude (μV)** | 13.00 ±2.58 | 13.90 ±2.11 | 8.98 ±1.67 | 13.78 ±2.06 | 13.44 ±2.27 | 10.89 ±2.50 |

*Systemic administration of NLX-101 did not affect the sympathetic response to hypercapnia*

**Figure 3-10** shows the sympathetic hypercapnic responses as recorded from the tSN before (pre-treatment) and after (post-treatment) systemic administration of NLX-101 (10nM) or vehicle. Changes in sympathetic activity in response to hypercapnia were analysed for each phase of the respiratory cycle (I, Post-I, and E2) for the following tSN parameters: peak amplitude (μV) (Δ tSN amplitude I (μV), Δ tSN amplitude PI (μV), Δ tSN amplitude E2 (μV)); trough amplitude (μV) (tSN Δ trough I (μV), tSN Δ trough PI (μV), tSN Δ trough E2 (μV)); and normalised AUC values (tSN Δ normalised AUC I, tSN Δ normalised AUC PI, tSN Δ normalised AUC E2). Mean and SEM for hypercapnic response values per treatment group (NLX-101 10nM vs. vehicle) are listed in **table 3-5**. Hypercapnia resulted in significantly increased sympathetic activity in all sympathetic activity parameters (see **supplementary table S2** in appendix). Two-way repeated measures ANOVA with Sidak correction for comparisons of the NLX-101 (10nM) group versus vehicle controls ($\alpha = 0.05$), performed separately with pre-treatment and post-treatment hypercapnic response values, did not reveal significant treatment group differences in the mean hypercapnic response for each of the analysed sympathetic parameters. Thus, systemic administration of NLX-101 did not affect the sympathetic response to hypercapnia in *in situ* WHBP of juvenile rats.

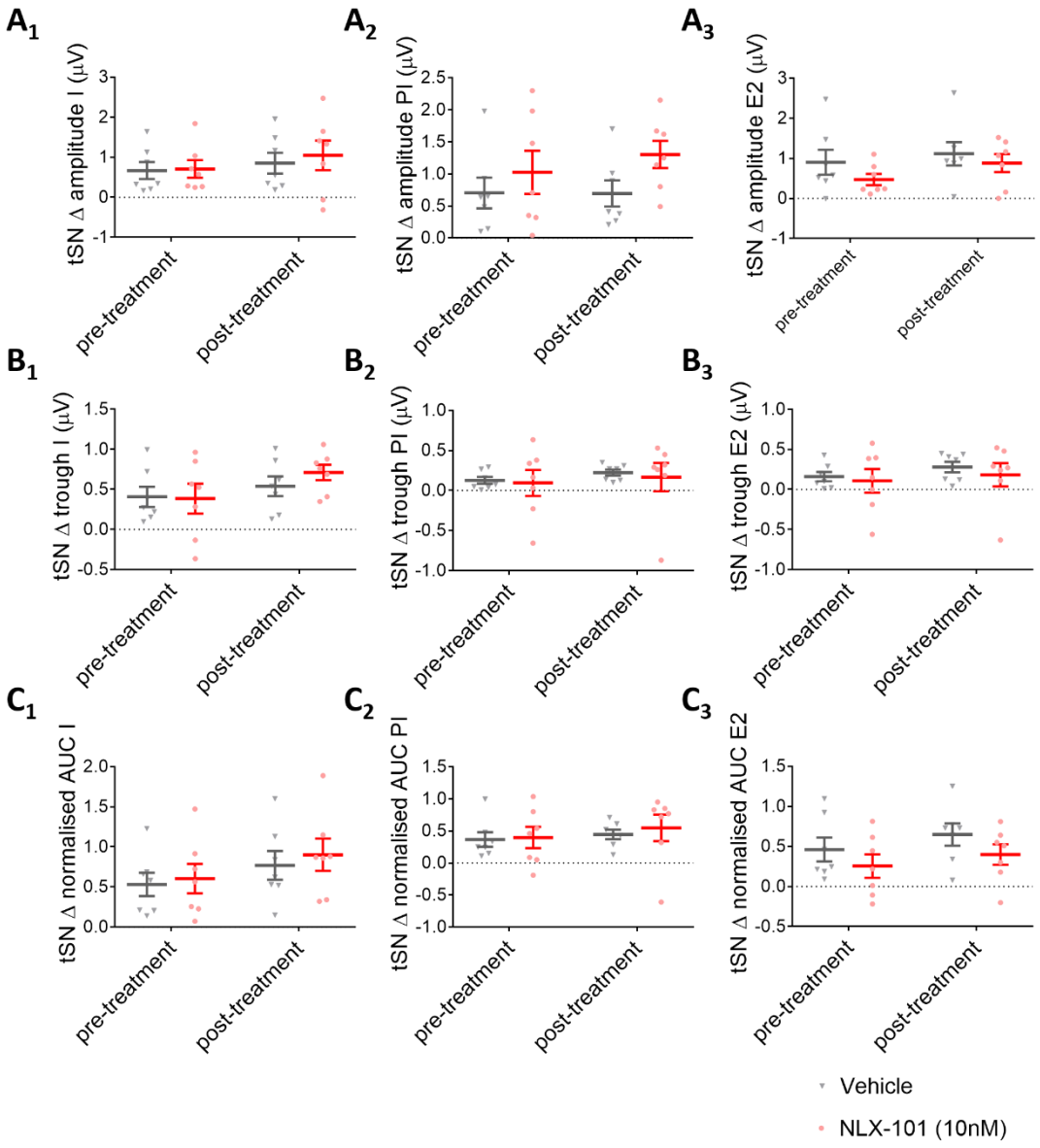


**Figure 3-10:** NLX-101 did not affect sympathetic hypercapnic responses.

Hypercapnia-induced changes in the sympatho-respiratory patterns from tSN traces recorded before and after systemic administration of Vehicle (n=7) or NLX-101 (10nM, n=7). Plot**s** show **A**$_{1\text{-}3}$ show change in peak amplitude (μV) during inspiration, post-inspiration, and E2. Plots **B**$_{1\text{-}3}$ show change in trough (minimum) amplitude (μV) during inspiration, post-inspiration, and E2). Plots **C**$_{1\text{-}3}$ show change in area under the curve normalised by phase duration in seconds during inspiration, post-I, and E2. Values are mean ± SEM. 2-WAY Repeated Measures ANOVA with Sidak correction for comparisons of NLX-101 or WAY-100635 vs. vehicle group vs. vehicle per treatment condition (pre- vs. post-treatment) yields no significant results. Mean values and statistical comparisons of pre-treatment baseline vs. hypercapnic sympathetic activities are reported in **Supplementary Table S**2 (see appendix).

**Table 3-5:** Group means for sympathetic hypercapnic responses pre- and post-treatment with NLX-101 (10nM) or Vehicle.
Values are mean **±** SEM values per treatment group. NLX-101 (10nM) group means are not significantly different from Vehicle group means.

| | **pre-treatment** | | **post-treatment** | |
|---|---|---|---|---|
| **tSN parameter** | **Vehicle** | **NLX-101 (10nM)** | **Vehicle** | **NLX-101 (10nM)** |
| **Δ amplitude I (μV)** | 0.67 ±0.21 | 0.71 ±0.22 | 0.85 ±0.26 | 1.05 ±0.37 |
| **Δ amplitude PI (μV)** | 0.70 ±0.24 | 1.03 ±0.34 | 0.70 ±0.20 | 1.30 ±0.21 |
| **Δ amplitude E2 (μV)** | 0.90 ±0.31 | 0.47 ±0.14 | 1.11 ±0.29 | 0.88 ±0.22 |
| **Δ trough I (μV)** | 0.41 ±0.13 | 0.39 ±0.19 | 0.54 ±0.12 | 0.71 ±0.10 |
| **Δ trough PI (μV)** | 0.13 ±0.04 | 0.10 ±0.16 | 0.22 ±0.04 | 0.17 ±0.18 |
| **Δ trough E2 (μV)** | 0.16 ±0.06 | 0.11 ±0.15 | 0.28 ±0.07 | 0.18 ±0.15 |
| **Δ normalised AUC I** | 0.53 ±0.15 | 0.61 ±0.18 | 0.77 ±0.18 | 0.90 ±0.20 |
| **Δ normalised AUC PI** | 0.37 ±0.11 | 0.40 ±0.17 | 0.45 ±0.07 | 0.55 ±0.21 |
| **Δ normalised AUC E2** | 0.46 ±0.15 | 0.26 ±0.15 | 0.65 ±0.14 | 0.40 ±0.13 |

### *3.3.3 NLX-101 did not affect sympatho-respiratory responses to peripheral chemoreflex stimulation*

Through simultaneous recordings of the PN, cVN, AbN, and tSN we performed an assessment of the effects of systemic administration of NLX-101 (10nM or 100nM) versus vehicle controls on the respiratory and sympathetic response to peripheral chemoreceptor activation with intra-arterial bolus administration (25, 50, or 75µL) of NaCN solution (0.03%) in *in situ* WHBP of juvenile rats.

*Sample sizes and excluded recordings*

The NLX-101 (10nM) treatment group in NaCN intra-arterial bolus response experiments consisted of 7 *in situ* WHBP experiments, in each of which PN, AbN, cVN and tSN were simultaneously recorded with no exclusions. The NLX-101 (100nM) treatment group consisted of 8 *in situ* WHBP experiments. In each of these experiments, PN, cVN, AbN, and tSN discharge was simultaneously recorded, with the exception of AbN activity in one recording. This AbN recording was excluded from analysis due to inadequate recording quality for reasons unrelated to viability and stability of the preparation (i.e. due to suboptimal seal of the electrode to the nerve). This resulted in the following sample sizes for the NLX-101 (100nM) treatment group in NaCN bolus response experiments: PN n=8 cVN n=8; AbN n=7; tSN n=8). Finally, the vehicle control group in NaCN intra-arterial bolus response experiments consisted of 7 *in situ* WHBP experiments, in each of which PN, AbN, cVN and tSN were simultaneously recorded with no exclusions. For comparison of pre-treatment baseline sympatho-respiratory activities vs. maximum sympatho-respiratory activities elicted by pre-treatment NaCN bolus adminsirations (25µL, 50µL, or 75µL), recordings from all treatment groups were pooled. Sample sizes for this comparison were: PN n=22; cVN = 22; AbN n=21; tSN n=22.

*Pre-treatment and post-treatment respiratory patterns of in response to NaCN*

In pre-treatment conditions, PN, cVN, AbN, and tSN respiratory and sympathetic response to peripheral chemoreceptor activation were as described in the previous literature (reviewed in General Introduction, section 1.5.1). That is, intra-arterial bolus injection (25, 50, or 75µL) of NaCN solution (0.03% in saline) elicited a concentration dependent acute transient response (~10s) of increased respiratory rate, increased Post-I discharges in the cVN and AbN, sympatho-respiratory late-E activity in the AbN and tSN, and augmented I/post-I sympathetic activity in the tSN (see **figure 3-12A$_{1-3}$**). Mean values of pre-treatment baseline respiratory and sympathetic activity and of maximum NaCN-elicited activities,

and statistical comparisons thereof, are reported in **Supplementary Tables S3-S5** (See appendix: supplementary data).

*Systemic administration of NLX-101 altered respiratory rhythms elicited by intra-arterial NaCN bolus*

Potential treatment group differences in the respiratory response to NaCN bolus injections were quantified trough comparison of group mean values for the 'maximum response' for each analysed respiratory parameter (see **figure -3-12** and section 3.2.5 for explanations of how 'maximum response' values are obtained). Statistical analysis was performed with a 2-way repeated measures ANOVA with Sidak correction for comparisons ($\alpha = 0.05$) of either NLX-101 (10nM) or NLX-101 (100nM) vs. Vehicle per NaCN bolus (25µL vs. 50µL vs. 75µL). Any effects of drugs (NLX-101 10nM or NLX-101 100nM) versus vehicle on the sympatho-respiratory response to peripheral chemoreceptor activation were expected to be revealed as a significant effect of drug versus vehicle in the post-treatment condition.

**Figure 3-11** and **Table 3-6** show the mean maximum responses to NaCN intra-arterial bolus concentration (25, 50, or 75µL) per treatment group (NLX-101 10 nM; NLX-101 100nM; vehicle). NaCN bolus injections caused a shortening of the PN inspiratory phase (see **figure 3-11B$_1$** and **table 3-6**), which did not differ significantly between pre-treatment groups. However, the shortening in PN inspiration to 25µL and 50µL NaCN was significantly attenuated after treatment with NLX-101 (100nM) versus vehicle (at post-treatment 25µL NaCN, NLX-101 100nM vs vehicle group M±SEM is −0.06±0.01 vs. −0.20 ± 0.06, respectively, p=0.044; at post-treatment 50µL NaCN, NLX-101 100nM vs vehicle group M±SEM is −0.06±0.02 vs. −20±.04, respectively, p=0.047) ( see **figure 3-11B$_{1-2}$** and **table 3-6**). Duration of the PN expiratory phase (see **figure 3-11C** and **table 3-6**) was also shortened in response to NaCN bolus administrations, and this effect was significantly attenuated by NLX-101 (10 nM) compared to vehicle at post-treatment 25µL and 50µL NaCN (at post-treatment 25µL NaCN bolus, NLX-101 10nM vs vehicle group M±SEM is −1.61 ± 0.31 vs. −0.64 ± 0.18, respectively, p=0.013; at post-treatment 50µL NaCN bolus, NLX-101 10nM vs vehicle group M±SEM is −1.54±0.32 vs. −0.62±0.14, respectively, p=0.020**) (figure 3-11C$_2$** and **table 3-6**). However, the expiratory duration response to 50µL (NLX-101 100nM vs vehicle group M±SEM is −2.29±0.30 vs. −0.66±0.14, respectively, p=0.032) and 75µL NaCN (NLX-101 100nM vs vehicle group M±SEM is −2.40±0.53 vs. −0.82±0.19, respectively, p=0.041) was different pre-treatment with the higher concentration of NLX-101. The presence of pre-treatment group differences in this

parameter limits our ability to interpret the cognate post-treatment responses. The time to PN peak amplitude was significantly shortened in response to NaCN bolus administration (see **figure 3-11D** and **table 3-6**), and this response was not significantly affected post-treatment in NLX-101 and vehicle groups.

**Table 3-6:** Group means for respiratory rhythms elicited by intra-arterial NaCN pre- and post-treatment with NLX-101 (10nM, or 100nM) or Vehicle.
Values are mean ± SEM values per treatment group. Significantly different group means (NLX-101 10nM or 100nM vs. vehicle controls, $p<0.05$) are annotated in **bold red text**.

| | | pre-treatment | | | post-treatment | | |
|---|---|---|---|---|---|---|---|
| **PN parameter** | **NaCN dose** | **Vehicle** | **NLX-101 (10nM)** | **NLX-101 (100nM)** | **Vehicle** | **NLX-101 (10nM)** | **NLX-101 (100nM)** |
| **Δ rate (bpm)** | **25 µL** | 24.89 ±4.14 | **39.11 ±4.36** | 18.80 ±3.63 | 28.78 ±4.78 | 34.73 ±2.67 | 37.10 ±5.19 |
| | **50 µL** | 29.52 ±3.39 | 36.04 ±3.50 | 35.51 ±2.60 | 33.73 ±5.29 | 37.44 ±3.68 | 38.61 ±2.35 |
| | **75 µL** | 35.48 ±4.70 | 40.59 ±2.24 | 37.69 ±2.82 | 32.16 ±5.87 | 34.35 ±4.58 | 44.88 ±6.20 |
| **Δ dur. I (s)** | **25 µL** | −0.26 ±0.05 | −0.28 ±0.03 | −0.19 ±0.05 | −0.20 ±0.06 | −0.13 ±0.05 | **−0.06 ±0.01** |
| | **50 µL** | −0.29 ±0.05 | −0.28 ±0.05 | −0.30 ±0.05 | −0.20 ±0.04 | −0.09 ±0.02 | **−0.06 ±0.02** |
| | **75 µL** | −0.28 ±0.05 | −0.25 ±0.05 | −0.27 ±0.07 | −0.16 ±0.04 | −0.10 ±0.04 | −0.08 ±0.04 |
| **Δ dur. E (s)** | **25 µL** | −0.83 ±0.20 | −2.36 ±0.51 | −2.05 ±0.52 | −0.64 ±0.18 | **−1.61 ±0.31** | −1.21 ±0.12 |
| | **50 µL** | −0.66 ±0.14 | −2.02 ±0.44 | **−2.29 ±0.30** | −0.62 ±0.14 | **−1.54 ±0.32** | −1.30 ±0.12 |
| | **75 µL** | −0.82 ±0.19 | −2.11 ±0.44 | **−2.40 ±0.53** | −0.62 ±0.18 | −1.31 ±0.30 | −1.17 ±0.11 |
| **Δ Tpeak (s)** | **25 µL** | −0.25 ±0.03 | −0.33 ±0.02 | −0.21 ±0.06 | −0.21 ±0.04 | −0.17 ±0.02 | −0.17 ±0.01 |
| | **50 µL** | −0.34 ±0.03 | −0.35 ±0.03 | −0.34 ±0.06 | −0.28 ±0.03 | −0.20 ±0.02 | −0.21 ±0.03 |
| | **75 µL** | −0.34 ±0.05 | −0.32 ±0.03 | −0.43 ±0.08 | −0.28 ±0.04 | −0.21 ±0.03 | −0.21 ±0.03 |

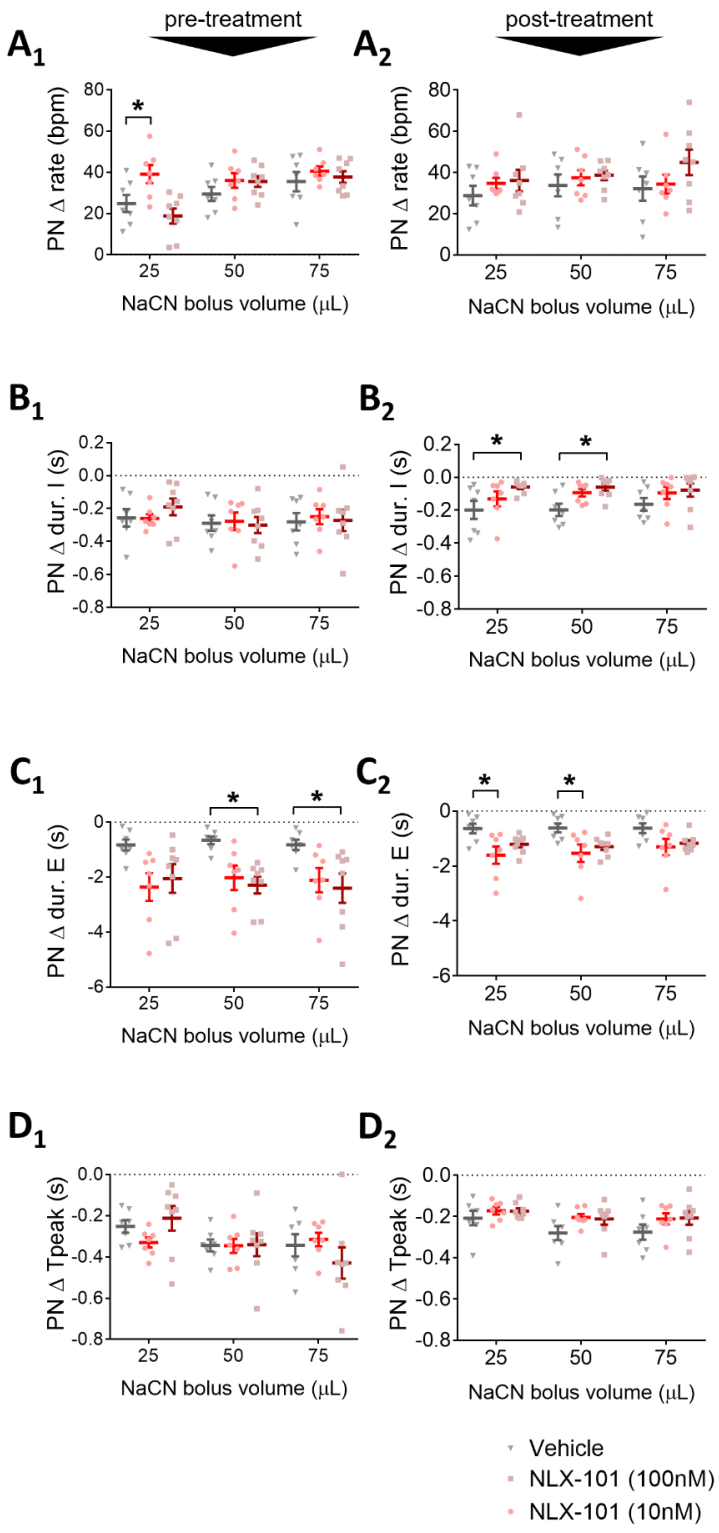


**Figure 3-11:** NLX-101 alters respiratory rhythms elicited by intra-arterial NaCN.

Plots show greatest change-from-baseline values in respiratory rhythm observed in the PN response to NaCN (25µL, 50µL, and 75µL) before and after systemic administration of Vehicle (n=7), NLX-101 (10nM, n=7) or NLX-101 (100nM, n=8). Plots **$A_{1,2}$** show greatest NaCN induced increase in respiratory rate (bpm) before (**$A_1$**) and after (**$A_2$**) administration of NLX-101 or vehicle. Plots **$B_{1,2}$** show greatest NaCN induced shortening of inspiratory phase (s) before **($B_1$)** and after (**$B_2$**) administration of NLX-101 or vehicle. Plots **$C_{1,2}$** show greatest NaCN induced shortening in expiratory phase duration (s) before **($C_1$)** and after (**$C_2$**) administration of NLX-101 or vehicle. Plots **$D_{1,2}$** show greatest NaCN induced shortening of PN time to peak (s) before **($D_1$)** and after (**$D_2$**) administration of NLX-101 or vehicle. Values are mean ± SEM. *****= p <.05 in 2-WAY Repeated Measures ANOVA with Sidak correction for comparisons of NLX-101 groups (10nM or 100nM) vs. vehicle control. Statistical analysis is performed separately for each NaCN (25 µL, 50 µL, or 75µL) response. Mean values of pre-treatment baseline respiratory rhythm responses and of maximum NaCN-elicited rhythm responses, and statistical comparisons thereof, are reported in **Supplementary Table S3** (See appendix).

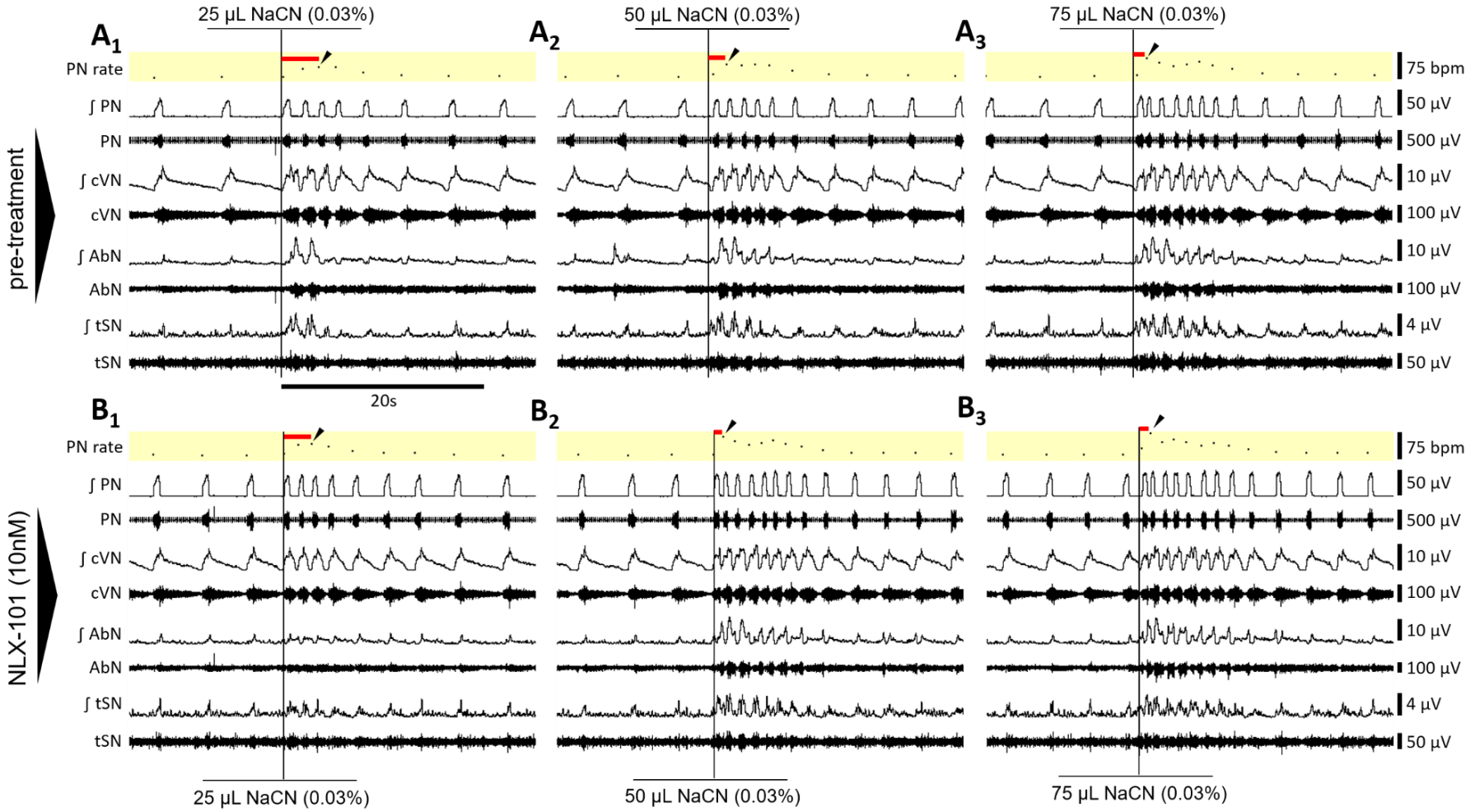


**Figure 3-12:** example traces of sympatho-respiratory response to intra-arterial NaCN administration before and after systemic administration of NLX-101 (10nM).

Nerve recordings of the PN, cVN, AbN, and tSN illustrating typical sympatho-respiratory responses to intra-arterial boluses of 25µL (**$A_1$**) 50µL (**$A_2$**) and 75µL **($A_3$**) of NaCN (0.03%) administered before, and after (**$B_{1,2,3}$**) systemic NLX-101 (10nM) or vehicle. Black arrows indicate the maximum response observed in PN rate, relative to pre-NaCN baseline. Red lines illustrate the delay to maximum response. Detailed descriptions for how 'maximum response' and 'delay-to-maximum response' values are obtained are provided in section 3.2.6.

*Systemic administration of NLX-101 did not affect NaCN-elicited changes in burst amplitude and normalised burst envelopes in integrated respiratory motor nerve activities.*

**Figure 3-13** shows plots for pre-treatment and post-treatment comparisons between the respiratory pattern changes in response to NaCN bolus administrations (25,50, and 75µL) observed in NLX-101 (10nM or 100nM) treatment groups vs. vehicle controls. The design of these plots is identical to the design described for NaCN responses observed in respiratory rhythm parameters. Pre-, and post-treatment group means and SEM values of the NaCN respiratory pattern responses are listed in **table 3-7A-B.**

In the PN, the increase in the inspiratory burst amplitude (PN Δ amplitude (µV), see **figure 3-13A$_{1-2}$** and **table 3-7A**), as well as the increase in normalised inspiratory AUC (PN Δ normalised AUC I, see **figure 3-13B$_{1-2}$** and **table 3-7A**) in response to NaCN bolus injections were not significantly affected by systemic administration of NLX-101 (10nM or 100nM) compared to vehicle.

In the cVN, NaCN bolus administrations resulted in an increase in the normalised AUC during inspiratory discharge (cVN Δ normalised AUC I, see **figure 3-13E$_{1-2}$** and **table 3-7B**). This response was found to be significantly increased pre-treatment relative to vehicle in the NLX-101 (100nM) group (at post-treatment 75µL NaCN bolus, NLX-101 100nM vs vehicle group M ± SEM is 2.83 ± 0.72 vs. 1.40 ± 0.29, respectively, p=0.022). However, no significant differences in cVN normalised AUC I in NaCN responses were observed between NLX-101 treatment groups (10nM or 100nM) vs. vehicle post-treatment. The amplitude of cVN post-inspiration burst was increased in response to NaCN bolus administrations (see **figure 3-13F$_{1-2}$** and **table 3-7B**). There were, however, no significant differences between NLX-101 treatment groups (10 nM or 100nM) versus the vehicle controls with regard to the increases in cVN post-I amplitude post-treatment (**figure 3-13F$_{1-2}$** and **table 3-7B**). cVN trough (µV) values reflect baseline activity of the cVN nerve per respiratory cycle. NaCN bolus administrations resulted in an increase of cVN trough (µV) values (see **figure 3-13G$_{1-2}$** and **table 3-7B**). No statistically significant differences were observed between NLX-101 treatment groups (10 nM or 100nM) versus the vehicle controls with regard to increase in cVN post-treatment (**figure 3-13G$_{1-2}$** and **table 3-7B**).

In the AbN, the amplitude of post-I activity (see **figure 3-13C$_{1-2}$** and **table 3-7A**) and activity during E2 (see **figure 3-13D$_{1-2}$** and **table 3-7A**) in response to NacN bolus was not significantly altered after treatment with NLX-101 when compared to vehicle controls.

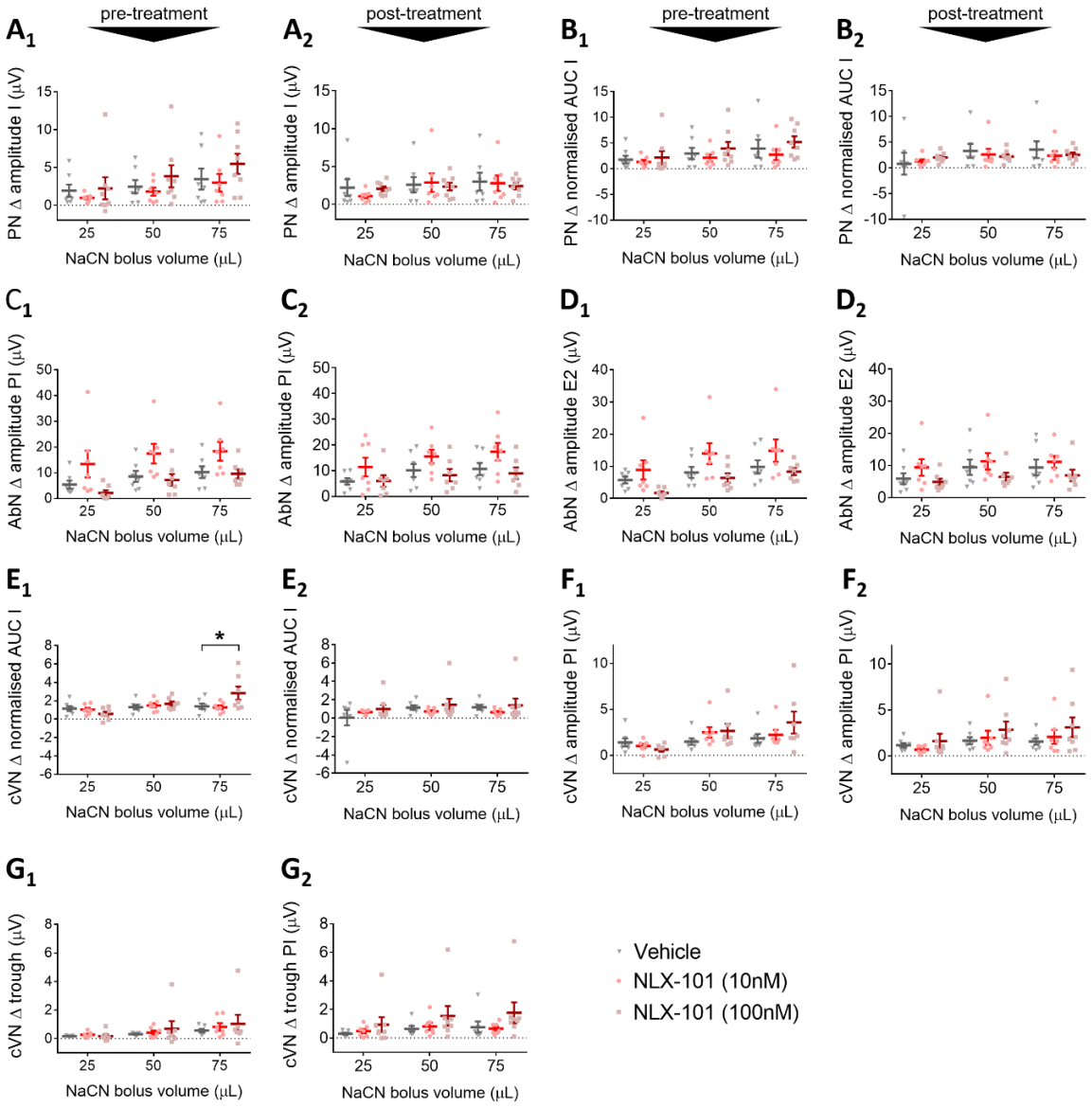


**Figure 3-13:** NLX-101 did not affect respiratory patterns elicited by intra-arterial NaCN.

Plots show greatest change-from-baseline values in respiratory patterns observed in the PN response to NaCN (25μL, 50μL, and 75μL) before and after systemic administration of Vehicle or NLX-101 (10nM, or 100nM). Plots **$A_{1,2}$** show greatest NaCN induced increase in PN burst amplitude (μV) before (**$A_1$**) and after (**$A_2$**) administration of NLX-101 or vehicle. In a similar manner, plots **$B_{1,2}$-$I_{1,2}$** describe the NaCN response greatest change-from-baseline values for the following nerves and parameters: (**$B_{1,2}$**) PN burst area under the curve (AUC) normalised to inspiratory phase duration in seconds; (**$C_{1,2}$**) AbN peak amplitude (μV) during post-I phase; (**$D_{1,2}$**) AbN peak amplitude (μV) during E2 phase ; (**$E_{1,2}$**) cVN inspiratory AUC, normalised to inspiratory phase duration in seconds; (**$F_{1,2}$**) peak amplitude of post-inspiratory cVN discharge; (**$G_{1,2}$**) cVN trough (minimum) amplitude (μV)). Numbers are: Vehicle n=7, NLX-101 (10nM) n=7 , NLX-101 (100nM) n=7, for $C_{1,2}$ and $D_{1,2}$; Vehicle n=7, NLX-101 (10nM) n=7 , NLX-101 (100nM) n=8, for $A_{1,2}$, $B_{1,2}$, $E_{1,2}$, $F_{1,2}$, and $G_{1,2}$.Values are mean ± SEM. *= $p < .05$ in 2-WAY Repeated Measures ANOVA with Sidak correction for comparisons of NLX-101 groups (10nM or 100nM) vs. vehicle control. Statistical analysis is performed separately for each NaCN (25 μL, 50 μL, or 75μL) response. Mean values of pre-treatment baseline respiratory patterns and of maximum NaCN-elicited patterns, and statistical comparisons thereof, are reported in **Supplementary Table S4** (See appendix).

**Table 3-7A:** Group means for respiratory patterns elicited by intra-arterial NaCN pre- and post-treatment with NLX-101 (10nM, or 100nM) or Vehicle.

Values are mean ± SEM per treatment group. Significantly different group means (NLX-101 10nM or 100nM vs. Vehicle, p.05) are annotated in **bold red text**. Table is continued on next page (**Table 3-7B**).

| | | | pre-treatment | | | post-treatment | | |
|---|---|---|---|---|---|---|---|---|
| **Nerve** | **parameter** | **NaCN dose** | **Vehicle** | **NLX-101 (10nM)** | **NLX-101 (100nM)** | **Vehicle** | **NLX-101 (10nM)** | **NLX-101 (100nM)** |
| **PN** | **Δ amplitude I (μV)** | **25 μL** | 1.93 ±0.80 | 0.99 ±0.20 | 2.25 ±1.45 | 2.21 ±1.11 | 1.09 ±0.28 | 2.07 ±0.31 |
| | | **50 μL** | 2.47 ±0.87 | 1.82 ±0.54 | 3.85 ±1.46 | 2.61 ±1.01 | 2.89 ±1.23 | 2.36 ±0.51 |
| | | **75 μL** | 3.48 ±1.39 | 2.99 ±1.16 | 5.49 ±1.33 | 3.00 ±1.18 | 2.82 ±1.03 | 2.41 ±0.43 |
| | **Δ normalised AUC I** | **25 μL** | 1.77 ±0.76 | 1.33 ±0.40 | 2.18 ±1.27 | 0.80 ±2.12 | 1.26 ±0.39 | 2.01 ±0.34 |
| | | **50 μL** | 2.97 ±1.11 | 2.13 ±0.68 | 3.92 ±1.29 | 3.29 ±1.37 | 2.59 ±1.11 | 2.23 ±0.43 |
| | | **75 μL** | 3.91 ±1.72 | 2.76 ±1.06 | 5.20 ±1.09 | 3.53 ±1.64 | 2.39 ±0.85 | 2.54 ±0.46 |
| **AbN** | **Δ ampltitude PI (μV)** | **25 μL** | 5.43 ±1.57 | 13.37 ±5.18 | 2.12 ±1.06 | 5.79 ±1.28 | 11.43 ±3.65 | 5.98 ±2.24 |
| | | **50 μL** | 8.54 ±2.13 | 17.39 ±3.82 | 7.25 ±2.27 | 10.10 ±2.56 | 15.50 ±2.57 | 8.25 ±2.39 |
| | | **75 μL** | 10.20 ±2.30 | 18.31 ±3.67 | 9.56 ±1.80 | 10.67 ±2.34 | 17.36 ±3.43 | 8.99 ±2.27 |
| | **Δ ampltitude E2 (μV)** | **25 μL** | 5.74 ±1.03 | 8.90 ±2.97 | 1.69 ±0.54 | 5.88 ±1.72 | 9.41 ±2.58 | 4.88 ±1.05 |
| | | **50 μL** | 8.10 ±1.68 | 13.97 ±3.21 | 6.37 ±1.47 | 9.46 ±2.38 | 11.33 ±2.56 | 6.44 ±1.30 |
| | | **75 μL** | 9.82 ±2.08 | 14.85 ±3.48 | 8.36 ±1.06 | 9.39 ±2.46 | 11.15 ±1.82 | 6.90 ±1.80 |

**Table 3-7B** Group means for respiratory patterns elicited by intra-arterial NaCN pre- and post-treatment with NLX-101 (10nM, or 100nM) or Vehicle.

Continuation of **Table 3-7A**. Values are mean **±** SEM per treatment group. Significantly different group means (NLX-101 10nM or 100nM vs. Vehicle, p.05) are annotated in **bold red text**.

| | | | pre-treatment | | | post-treatment | | |
|---|---|---|---|---|---|---|---|---|
| **Nerve** | **parameter** | **NaCN dose** | **Vehicle** | **NLX-101 (10nM)** | **NLX-101 (100nM)** | **Vehicle** | **NLX-101 (10nM)** | **NLX-101 (100nM)** |
| **cVN** | **Δ normalised AUC I** | **25 µL** | 1.15 ±0.27 | 1.03 ±0.20 | 0.56 ±0.25 | 0.05 ±0.84 | 0.66 ±0.10 | 0.99 ±0.44 |
| | | **50 µL** | 1.31 ±0.24 | 1.50 ±0.24 | 1.67 ±0.24 | 1.14 ±0.25 | 0.73 ±0.13 | 1.45 ±0.66 |
| | | **75 µL** | 1.40 ±0.29 | 1.28 ±0.20 | **2.83 ±0.72** | 1.18 ±0.25 | 0.63 ±0.14 | 1.40 ±0.74 |
| | **Δ amplitude PI (µV)** | **25 µL** | 1.40 ±0.44 | 1.01 ±0.23 | 0.64 ±0.23 | 1.15 ±0.25 | 0.68 ±0.15 | 1.61 ±0.78 |
| | | **50 µL** | 1.49 ±0.36 | 2.49 ±0.58 | 2.65 ±0.78 | 1.65 ±0.38 | 1.96 ±0.78 | 2.83 ±0.90 |
| | | **75 µL** | 1.84 ±0.47 | 2.23 ±0.53 | 3.57 ±1.21 | 1.55 ±0.36 | 2.06 ±0.76 | 3.10 ±1.07 |
| | **Δ trough (µV)** | **25 µL** | 0.17 ±0.01 | 0.28 ±0.07 | 0.17 ±0.13 | 0.30 ±0.07 | 0.48 ±0.15 | 0.93 ±0.51 |
| | | **50 µL** | 0.31 ±0.04 | 0.43 ±0.14 | 0.70 ±0.53 | 0.64 ±0.19 | 0.81 ±0.26 | 1.54 ±0.68 |
| | | **75 µL** | 0.57 ±0.11 | 0.82 ±0.26 | 1.04 ±0.64 | 0.76 ±0.39 | 0.65 ±0.15 | 1.76 ±0.73 |

*Systemic administration of NLX-101 does not affect the onset of respiratory responses to intra-arterial NaCN bolus*

To assess whether 5-$HT_{1A}$R agonism affected the onset of the respiratory response to peripheral chemoreceptor activation, we quantified the delay to the timepoint of maximum response (delay-to-max) for respiratory parameters of the PN response to each of three intra-arterial boluses (25µL, 50µL, and 75µL) with NaCN (0.03%) before and after systemic Vehicle, NLX-101 (10nM) or NLX-101 (100nM) in in situ WHBP from juvenile rats. See **figure 3-12** and section 3.2.5 for a more detailed account of how 'delay-to-max' values are obtained. **Figure 3-14** and **table 3-8** provide delay-to-max mean and SEM for the PN response to pre- and post-treatment 25, 50, or 75µL NaCN bolus injections for each treatment group (NLX-101 10nM, NLX-101 100nM, vehicle). For each of the above respiratory parameters, no significant differences between NLX-101 treatment groups (10nM or 100nM) vs. vehicle controls were observed in the delay-to-max (s) values for respiratory responses to pre- , or post-treatment NaCN bolus injections. Thus, systemic administration of NLX-101 (10nM or 100nM) vs. vehicle controls did not affect the onset of the respiratory response to peripheral chemoreceptor activation with NaCN bolus injections.

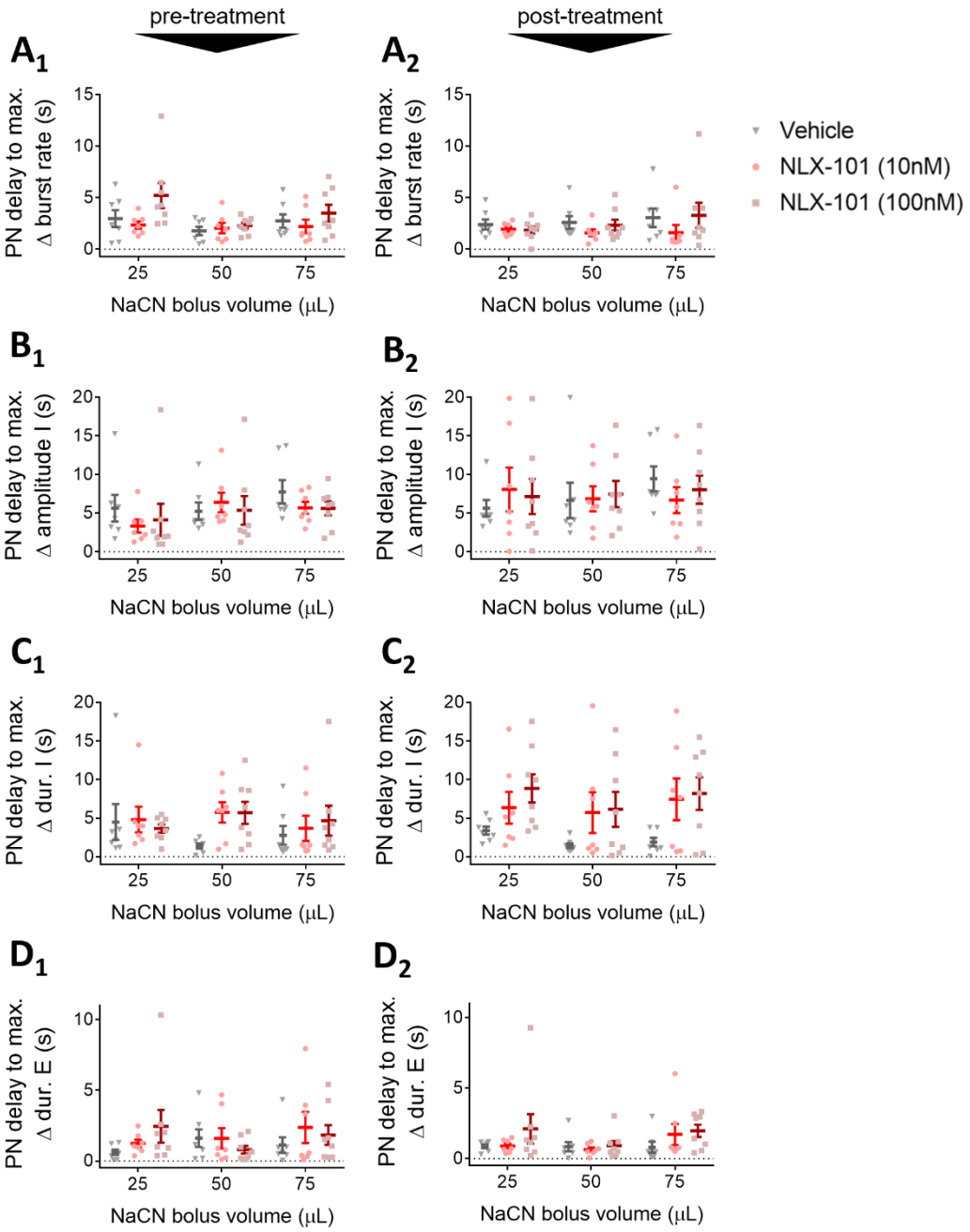


**Figure 3-14:** NLX-101 did not affect the delay to maximum PN respiratory response to intra-arterial NaCN.

Delay to the timepoint of maximum response (delay-to-max) values were obtained for respiratory parameters of the PN response to NaCN (25µL, 50µL, and 75µL) before and after systemic administration of Vehicle (n=7), NLX-101 (10nM, n=7), or NLX-101 (100nM, n=7). Plots **$A_{1,2}$** show the delay-to-max (s) for the change in PN rate in response to NaCN before (**$A_1$**) and after (**$A_2$**) administration of Vehicle or NLX-101 (10nM or 100nM). In identical fashion, the delay-to-max (s) values are provided for: the increase in burst amplitude (**$B_{1,2}$**); the shortening of inspiratory phase duration (**$C_{1,2}$**) ;and the shortening expiratory phase duration (**$D_{1,2}$**). Values are mean ± SEM. 2-WAY Repeated Measures ANOVA with Sidak correction for comparisons of NLX-101 groups (10nM or 100nM) vs. vehicle control yielded no significant results. Statistical analysis is performed separately for each NaCN (25 µL, 50 µL, or 75µL) response.

**Table 3-8:** Group means for the delay to maximum PN respiratory response to intra-arterial NaCN.

Values are mean **±** SEM for the delay to maximum PN responses (s) elicited by intra-arterial NaCN pre- and post-treatment with NLX-101 (10nM or 100nM) or vehicle. NLX-101 (10nM or 100nM) group means are not significantly different from Vehicle group means.

| | | pre-treatment | | | post-treatment | | |
|---|---|---|---|---|---|---|---|
| **PN parameter** | **NaCN dose** | **Vehicle** | **NLX-101 (10nM)** | **NLX-101 (100nM)** | **Vehicle** | **NLX-101 (10nM)** | **NLX-101 (100nM)** |
| **delay to max. Δ rate (s)** | **25 µL** | 2.97 ±0.82 | 2.35 ±0.36 | 5.20 ±1.20 | 2.40 ±0.49 | 1.94 ±0.23 | 1.85 ±0.35 |
| | **50 µL** | 1.78 ±0.40 | 2.06 ±0.51 | 2.29 ±0.29 | 2.59 ±0.62 | 1.60 ±0.33 | 2.33 ±0.53 |
| | **75 µL** | 2.73 ±0.64 | 2.21 ±0.65 | 3.50 ±0.81 | 3.05 ±0.90 | 1.61 ±0.74 | 3.29 ±1.21 |
| **delay to max. Δ amplitude I (s)** | **25 µL** | 5.63 ±1.72 | 3.34 ±0.84 | 4.13 ±2.07 | 5.64 ±1.07 | 8.05 ±2.83 | 7.15 ±2.27 |
| | **50 µL** | 5.25 ±1.12 | 6.38 ±1.26 | 5.35 ±1.85 | 6.65 ±2.28 | 6.85 ±1.62 | 7.46 ±1.69 |
| | **75 µL** | 7.75 ±1.52 | 5.70 ±0.78 | 5.61 ±0.89 | 9.43 ±1.60 | 6.68 ±1.67 | 8.02 ±1.82 |
| **delay to max. Δ dur. I (s)** | **25 µL** | 4.49 ±2.32 | 4.82 ±1.66 | 3.65 ±0.54 | 3.39 ±0.53 | 6.34 ±2.05 | 8.85 ±1.84 |
| | **50 µL** | 1.38 ±0.32 | 5.75 ±1.31 | 5.69 ±1.43 | 1.44 ±0.31 | 5.71 ±2.64 | 6.13 ±2.25 |
| | **75 µL** | 2.77 ±1.22 | 3.67 ±1.64 | 4.67 ±1.93 | 1.89 ±0.55 | 7.44 ±2.70 | 8.18 ±2.12 |
| **delay to max. Δ dur. E (s)** | **25 µL** | 0.61 ±0.19 | 1.24 ±0.27 | 2.45 ±1.16 | 0.87 ±0.13 | 0.90 ±0.17 | 2.11 ±1.05 |
| | **50 µL** | 1.61 ±0.62 | 1.60 ±0.72 | 0.79 ±0.28 | 0.85 ±0.33 | 0.65 ±0.15 | 0.92 ±0.33 |
| | **75 µL** | 1.12 ±0.55 | 2.37 ±1.10 | 1.84 ±0.69 | 0.81 ±0.39 | 1.72 ±0.76 | 1.97 ±0.44 |

*Systemic administration of NLX-101 did not affect sympathetic response to intra-arterial NaCN*

**Figure 3-15** shows plots for pre-treatment and post-treatment comparisons between the different treatment groups for the maximum response in tSN. The organisation of plots and design of statistical comparisons of treatment groups tests is identical to that previously described for maximum respiratory response values. **Tables 3-10A-B** list the maximum response mean and SEM values per NaCN (0.03%) intra-arterial bolus dose (25, 50, or 75µL) and per treatment group (NLX-101 10 nM; NLX-101 100Nm; vehicle controls) for each of the above tSN parameters.

NaCN bolus administration resulted in an increase of the maximum tSN amplitude (µV), trough value (µV), and normalised AUC values. Mean values of pre-treatment baseline vs. maximum NaCN-elicited sympathetic activities, and statistical comparisons thereof, are reported in **Supplementary Tables S5A/B** (see appendix). This increase in sympathetic activity in response to peripheral chemoreceptor activation is also illustrated in representative traces of the tSN (see **figure 3-11**). No significant differences between NLX-101 treatment groups (10nM or 100nM) vs. vehicle controls were observed in the tSN parameters for sympathetic responses to post-treatment NaCN bolus injections. Thus, systemic administration of NLX-101 (10nM or 100nM) vs. vehicle controls did not affect the sympathetic response to peripheral chemoreceptor activation as observed in maximum responses to intra-arterial bolus injections (25, 50, or 75µL) with NaCN solution (0.03%).

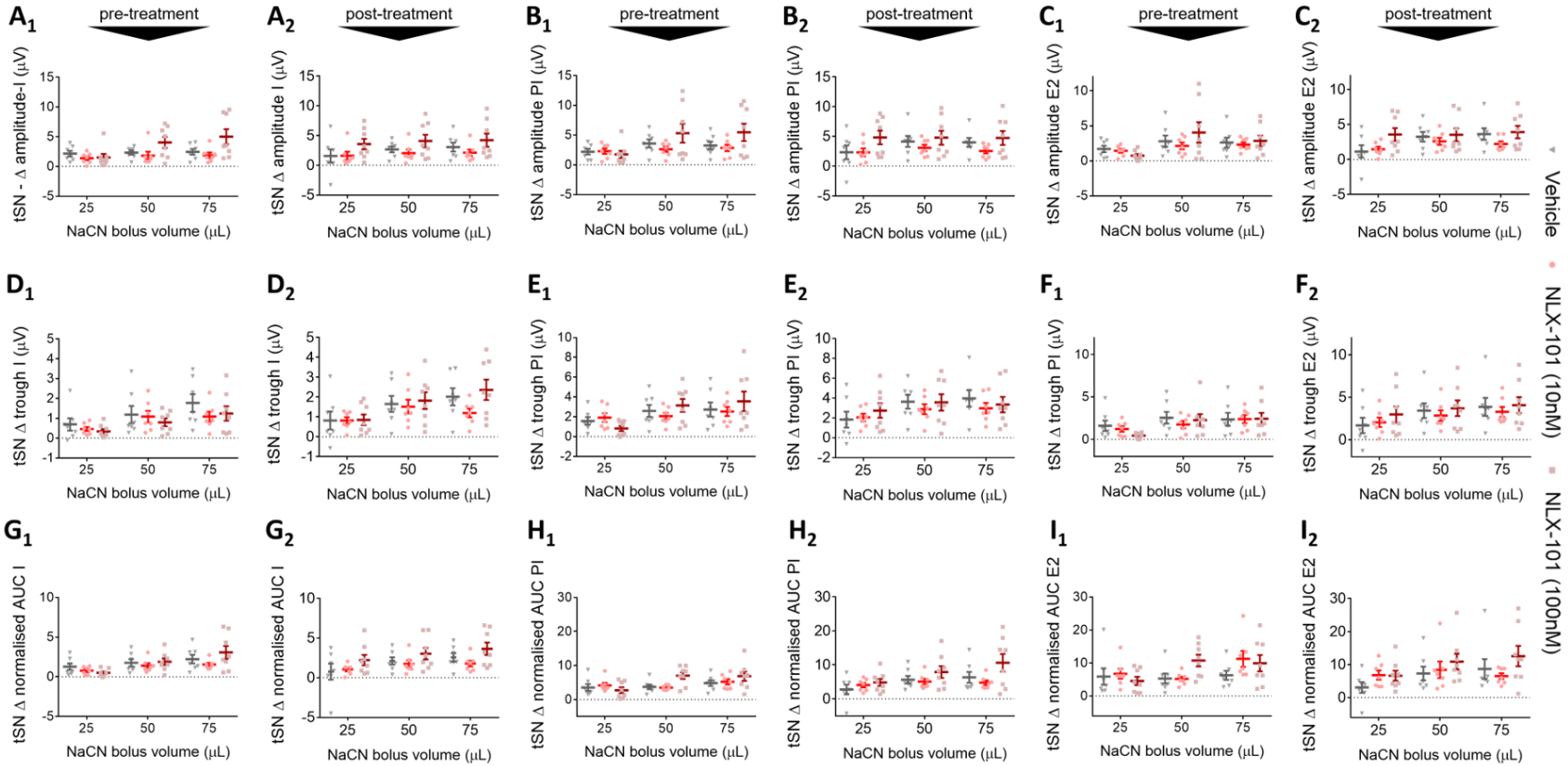


**Figure 3-15:** NLX-101 did not affect the thoracic Sympathetic nerve sympatho-respiratory response to intra-arterial administration of sodium cyanide.

Plots show greatest change-from-baseline values observed in thoracic Sympathetic nerve (tSN) recordings of the sympatho-respiratory response to NaCN (25μL, 50μL, and 75μL) before and after systemic administration of Vehicle (n=7), NLX-101 (10nM, n =8)) or NLX-101 (100nM, n=8). Plots **$A_{1,2}$** show the maximum NaCN induced increase in tSN burst amplitude during inspiration before (**$A_1$**) and after (**$A_2$**) systemic administration of Vehicle or NLX-101 (10nM or 100nM). In the same manner, plots **$B_{1,2}$** and **$C_{1,2}$** show greatest NaCN induced changes in tSN burst amplitudes during post-inspiratory phase, and the second phase of expiration (E2), respectively. Plots **$D_{1,2}$** - **$F_{1,2}$**, show the greatest NaCN induced increases in tSN trough values during inspiration (**$D_{1,2}$**), during Post-I (**$E_{1,2}$**), and during E2 (**$F_{1,2}$**). Plots **$G_{1,2}$** show the maximum NaCN induced increase in tSN area under the curve during inspiration, normalized to inspiratory phase duration in seconds. respiratory phase duration in seconds. Similarly, plots **$H_{1,2}$** and **$I_{1,2}$** show normalised area under the curve for tSN activity during Post-I (**$H_{1,2}$**,) and during E2 (**$I_{1,2}$**). Values are mean ± SEM. 2-WAY Repeated Measures ANOVA with Sidak correction for comparisons of NLX-101 groups (10nM or 100nM) vs. vehicle control yielded no results. Statistical analysis is performed separately for each NaCN (25 μL, 50 μL, or 75μL) response. Mean values of pre-treatment baseline vs. maximum NaCN-elicited sympathetic activities, and statistical comparisons thereof, are reported in **Supplementary Tables S5A/B** (See appendix).

**Table 3-9A** Means for maximum tSN response to intra-arterial NaCN pre- and post-treatment with NLX-101 (10nM or 100nM) or vehicle.

Values are mean **±** SEM per treatment group. NLX-101 (10nM or 100nM) group means are not significantly different from Vehicle group means. Table is continued on next page (**Table 3-9B**).

| | | pre-treatment | | | post-treatment | | |
|---|---|---|---|---|---|---|---|
| **tSN parameter** | **NaCN dose** | **Vehicle** | **NLX-101 (10nM)** | **NLX-101 (10nM)** | **Vehicle** | **NLX-101 (10nM)** | **NLX-101 (10nM)** |
| **Δ amplitude I (μV)** | **25 μL** | 2.15 ±0.47 | 1.39 ±0.33 | 1.50 ±0.61 | 1.56 ±1.13 | 1.61 ±0.66 | 3.55 ±0.88 |
| | **50 μL** | 2.33 ±0.36 | 1.83 ±0.66 | 4.02 ±0.92 | 2.68 ±0.50 | 2.04 ±0.61 | 4.07 ±1.05 |
| | **75 μL** | 2.46 ±0.48 | 1.88 ±0.46 | 5.01 ±1.26 | 3.06 ±0.76 | 2.10 ±0.53 | 4.22 ±1.11 |
| **Δ amplitude PI (μV)** | **25 μL** | 2.20 ±0.47 | 2.28 ±0.46 | 1.74 ±0.61 | 2.33 ±1.16 | 2.31 ±0.68 | 4.82 ±1.15 |
| | **50 μL** | 3.60 ±0.69 | 2.63 ±0.45 | 5.32 ±1.59 | 4.15 ±0.76 | 2.55 ±0.43 | 4.74 ±1.17 |
| | **75 μL** | 3.25 ±0.66 | 2.84 ±0.55 | 5.47 ±1.46 | 3.99 ±0.76 | 2.55 ±0.43 | 4.74 ±1.17 |
| **Δ amplitude E2 (μV)** | **25 μL** | 1.68 ±0.46 | 1.42 ±0.28 | 0.73 ±0.24 | 1.13 ±0.90 | 1.47 ±0.36 | 3.57 ±0.92 |
| | **50 μL** | 2.79 ±0.81 | 2.12 ±0.49 | 4.05 ±1.47 | 3.25 ±0.70 | 2.60 ±0.51 | 3.53 ±0.92 |
| | **75 μL** | 2.60 ±0.71 | 2.30 ±0.34 | 2.84 ±0.77 | 3.64 ±0.83 | 2.21 ±0.39 | 3.92 ±0.89 |
| **Δ trough I (μV)** | **25 μL** | 0.70 ±0.31 | 0.46 ±0.11 | 0.37 ±0.12 | 0.82 ±0.45 | 0.82 ±0.17 | 0.85 ±0.27 |
| | **50 μL** | 1.19 ±0.44 | 1.09 ±0.29 | 0.80 ±0.19 | 1.66 ±0.41 | 1.52 ±0.35 | 1.82 ±0.42 |
| | **75 μL** | 1.77 ±0.46 | 1.09 ±0.25 | 1.24 ±0.37 | 2.02 ±0.43 | 1.20 ±0.22 | 2.36 ±0.51 |
| **Δ trough PI (μV)** | **25 μL** | 1.58 ±0.39 | 1.92 ±0.44 | 0.81 ±0.26 | 1.83 ±0.81 | 2.04 ±0.38 | 2.75 ±0.74 |
| | **50 μL** | 2.59 ±0.61 | 2.06 ±0.34 | 3.14 ±0.66 | 3.63 ±0.69 | 2.88 ±0.51 | 3.57 ±0.83 |
| | **75 μL** | 2.73 ±0.72 | 2.54 ±0.47 | 3.55 ±1.00 | 3.96 ±0.83 | 2.98 ±0.54 | 3.34 ±0.78 |
| **Δ trough E2 (μV)** | **25 μL** | 1.61 ±0.62 | 1.23 ±0.33 | 0.45 ±0.12 | 1.68 ±0.90 | 2.05 ±0.56 | 2.98 ±0.96 |
| | **50 μL** | 2.56 ±0.70 | 1.75 ±0.43 | 2.28 ±0.70 | 3.43 ±0.87 | 2.83 ±0.62 | 3.70 ±0.93 |
| | **75 μL** | 2.36 ±0.76 | 2.40 ±0.48 | 2.43 ±0.69 | 3.86 ±1.06 | 3.28 ±0.60 | 4.08 ±0.94 |

**Table 3-9B** Means for maximum tSN response to intra-arterial NaCN pre- and post-treatment with NLX-101 (10nM or 100nM) or vehicle.

Continuation of **Table 3-9A**. Values are mean **±** SEM per treatment group. NLX-101 (10nM or 100nM) group means are not significantly different from Vehicle group means.

| | | pre-treatment | | | post-treatment | | |
|---|---|---|---|---|---|---|---|
| **tSN parameter** | **NaCN dose** | **Vehicle** | **NLX-101 (10nM)** | **NLX-101 (10nM)** | **Vehicle** | **NLX-101 (10nM)** | **NLX-101 (10nM)** |
| **Δ normalised AUC I** | **25 µL** | 1.27 ±0.41 | 0.76 ±0.18 | 0.50 ±0.17 | 0.76 ±1.02 | 1.05 ±0.25 | 2.23 ±0.66 |
| | **50 µL** | 1.76 ±0.46 | 1.41 ±0.31 | 1.89 ±0.41 | 2.11 ±0.47 | 1.75 ±0.45 | 3.03 ±0.73 |
| | **75 µL** | 2.23 ±0.55 | 1.55 ±0.22 | 3.08 ±0.80 | 2.56 ±0.54 | 1.79 ±0.37 | 3.64 ±0.79 |
| **Δ normalised AUC PI** | **25 µL** | 3.55 ±0.99 | 4.18 ±0.74 | 2.76 ±0.85 | 2.74 ±1.42 | 4.04 ±0.68 | 4.82 ±1.04 |
| | **50 µL** | 3.73 ±0.68 | 3.49 ±0.26 | 7.03 ±0.99 | 5.62 ±1.12 | 5.09 ±0.84 | 7.89 ±1.74 |
| | **75 µL** | 4.84 ±0.84 | 5.21 ±0.80 | 6.86 ±1.37 | 6.32 ±1.60 | 4.75 ±0.71 | 10.58 ±2.62 |
| **Δ normalised AUC E2** | **25 µL** | 5.90 ±2.51 | 6.75 ±1.53 | 4.54 ±1.26 | 3.06 ±1.64 | 6.81 ±1.39 | 6.62 ±1.53 |
| | **50 µL** | 5.27 ±1.55 | 5.16 ±0.71 | 10.74 ±1.77 | 7.31 ±2.07 | 8.39 ±2.50 | 10.87 ±2.38 |
| | **75 µL** | 6.27 ±1.39 | 11.27 ±2.41 | 9.95 ±2.46 | 8.65 ±2.99 | 6.49 ±0.89 | 12.53 ±3.07 |

## 3.4 CHAPTER DISCUSSION

### *3.4.1 Summary of results in the light of aims and hypotheses*

The aim of the present chapter was to assess the effects of systemic administration of selective 5-$HT_{1A}$ receptor agonist NLX-101 on restful respiratory activity (recorded at PN, HN, cVN, and AbN) in the *in situ* WHBP of juvenile rats. Further, we aimed to establish the respiratory response, as well as respiratory modulation of sympathetic activity (recorded at PN, cVN, AbN, and at the thoracic sympathetic chain), upon hypercapnia and upon peripheral chemoreceptor stimulation in the *in situ* WHBP.

The work presented in this chapter provides unique contributions to our understanding of 5-$HT_{1A}$ transmission in respiratory control. Experiments in section 3.3.1 provide the first comprehensive assessment of effects of selective 5-$HT_{1A}$R agonism on eupnoeic respiratory motor output from the intact and unanaesthetised respiratory network. In addition, experiments in this chapter provide the first comprehensive assessment of effects of selective 5-$HT_{1A}$ agonism on sympatho-respiratory responses to hypercapnia (section 3.3.2) and peripheral chemoreflex activation with NaCN (section 3.3.3) in the intact and unanaesthetised respiratory network.

Systemic administration of 5-$HT_{1A}$R agonist was hypothesised to result in increased respiratory rate, and in augmented amplitudes and burst envelopes of respiratory motor output under resting conditions. Our findings in concentration-response experiments with systemic administration NLX-101 vs. vehicle in in situ WHBP of juvenile rats (see section 3.3.1) are largely in line with this hypothesis. Systemic administration of NLX-101 resulted in concentration-dependent increases in burst amplitudes and normalised burst envelopes of integrated motor outputs of the PN, and AbN compared to vehicle controls.No significant effects of NLX-101 on respiratory pattern were observed in integrated HN and cVN motor outputs **(see Fig. 3-6, Table 3-2)**.

With respect to respiratory rhythm, systemic administration of NLX-101 in *in situ* WHBP of rats resulted in a concentration-dependent increase in respiratory rate. This increased respiratory rate appears to be mediated to a greater extent by shortening of expiratory phase duration than by shortening of inspiratory phase duration. However, shortening of expiratory phase duration was not significant. This is surprising given the large effect sizes observed at higher doses (see PN dur. E (s) at 100µM, 500µM, and 1µM NLX-101 vs. vehicle control in **figure 3-5A$_3$** and **table 3-1)**. The absence of statistical significance of this

effect may be due to the relatively low samples sizes in these experiments (NLX-101 n=7, vehicle n =5). Power analysis (InVivoStat, Bate & Clark (2014)) suggests that, assuming variance and an effect size equal to that observed for PN dur. E (s) at 1µM NLX-101 vs. vehicle in the present thesis, 70-92% power to detect this effect with α =.05 requires sample sizes of 6 to 10 recordings in each treatment group **(see supplementary figure S1A)**. The expiratory phase comprises the Post-I phase, followed by the E2 phase. Post-I phase duration was not significantly shortened. Post-I duty cycle, i.e. the duration of Post-I phase as a fraction of expiratory phase duration, was not significantly affected **(see Fig. 3-5B$_1$)**. This suggests that the relative durations of Post-I and E2 phases were unaltered in the NLX-101 treatment group compared to vehicle controls. The respiratory rhythm remained tri-phasic throughout the full range of the NLX-101 dosing schedule (1nM-1µM).

Non-hypothesised effects on respiratory rhythm in the NLX-101 treatment group vs. vehicle controls included a statistically significant shortening of the latency between onset and peak activity in the ʃHN (HN Tpeak(s)), as well as a concentration-dependent increase in late-E activity in the NLX-101 treatment group vs. vehicle controls. The latter effect is shown in a significant increase in late-E burst amplitude (see **fig. 3-6D$_2$**, and **table 3-2)**. AbN late-E rate (bpm) was not significantly increased in the NLX-101 treatment group compared to vehicle controls. The absence of statistical significance in the effect on late-E rate is surprising, given its large effect size. Average occurrence of AbN late-E (bpm) in the NLX-101 treatment group increased from nearly non-occurring (pre-treatment, M±SEM are 1.65 ± 1.21) to occurring nearly every respiratory cycle (at 1µM NLX-101, M±SEM are 33.08 ± 3.64) **(**see **Fig. 3-5D$_1$**, and **table 3-1)**. In comparison, the mean and SEM late-E rate (bpm) at pre-treatment conditions in the vehicle control group was 7.93 ± 3.98, and increased to 19.80 ± 6.71 bpm at the highest concentration. This suggests that the absence of statistical significance is possibly due to high variability in the control group. Power analysis (InVivoStat, Bate and Clark (2014)) suggests that, assuming variance and an effect size equal to that observed for AbN late-E rate (bpm) at 1µM NLX-101 vs. vehicle in the present thesis, 69-91% power to detect this effect with α =.05 can be achieved with sample sizes from 11 to 19 recordings in each treatment group **(see supplementary figure S1B)**.

The respiratory and sympatho-respiratory hypercapnic response in the *in situ* WHBP of juvenile rats was hypothesised to be unaffected by systemic administration of 5-HT$_{1A}$ agonist NLX-101 (10nM), but to be augmented after systemic administration of 5-HT$_{1A}$ antagonist WAY-100635 (300nM), when compared to vehicle controls. This is because NLX-101 is postulated to be a 5-HT$_{1A}$ hetero-receptor biased agonist, whereas WAY-

100635 is an antagonist of both hetero-receptors and auto-receptors without functional bias. We did not observe any significant changes in sympatho-respiratory hypercapnic response parameters in the NLX-101 treatment group or the WAY-100635 treatment group when compared to vehicle controls (section 3.3.2).

The sympatho-respiratory response to stimulation of peripheral chemoreceptors through intra-arterial bolus injections (25, 50, or 75µL) with NaCN (0.03%) solution in *in situ* WHBP of juvenile rats was hypothesised to be attenuated by systemic administration of NLX-101 (10nM or 100nM) when compared to vehicle controls. However, relative to vehicle controls, NLX-101 treatment groups did not display a significant change in sympatho-respiratory response to NaCN intra-arterial bolus injections, both in magnitude and latency of maximum response.

### *3.4.2 Technical considerations*

*Technical consideration with regard to the use of the in situ working-heart-brainstem preparation*

The use of the *in situ* WHBP has a number of characteristics that make it more suitable for the present thesis' objectives compared to *in vivo* animals or further reduced *in situ* or *in vitro* preparations of the respiratory CPG. However, the *in situ* WHBP also has its limitations which must be acknowledged and/or accounted for in experimental design and in the interpretation of data.

A major advantage of the *in situ* WHBP over more reductive *in* vitro methods, is that the *in situ* WHBP has a near-intact respiratory network. This is important because any excision of network components is likely to affect the network interactions in the remaining circuitry. A further advantage is that the *in situ* WHBP enables simultaneous recordings of multiple peripheral nerves (used in chapter 3), which can be combined with single cell recordings in the brainstem (used in chapter 5). Simultaneous recordings of multiple peripheral nerves provides a comprehensive picture of respiratory network outputs. Such comprehensive assessment of network outputs can be used to optimally capitalize on known CPG network mechanisms to hypothesise the putative changes in the network that underlie the observed responses to experimental manipulations. In the *in situ* WHBP, the liver and kidneys are removed. This abolishes drug elimination and thereby stabilizes the concentration of drug present in the system throughout the duration of the experimental protocol. The preparation is transcardially perfused, which enables control over the metabolic state of the respiratory network through clamping of $CO_2$ and $O_2$ gases in the

perfusate. Transcardiac perfusion also supports selective stimulation of CB chemoreceptors through intra-arterial bolus injections of cyanide salt solutions upstream of the carotid bifurcation.

Despite the above advantages of the *in situ* WHBP, there are a number of compromises to consider. Although the brainstem remains intact, there are two ways in which the respiratory network is reduced in the *in situ* WHBP. First, decerebration eliminates cortical descending inputs to the brainstem respiratory network. In the intact animal, the brainstem respiratory network receives cortical inputs involved in voluntary control of respiratory activity (e.g. during vocalization, mastication, defecation, etc) (Davies and Moores, 2010). Therefore, a decerebrated preparation is technically a reduction of the respiratory system and could be considered less favourable compared to the *in vivo* animal. However, the cortical inputs are irregular, perturbed under anaesthesia, and difficult to control for. Therefore, they could also be considered confounding factors when trying to methodically assess the effect and mechanisms of an experimental manipulation (e.g. drug administration). Also worth considering is that *in vivo* experiments with recordings of respiratory motor outputs typically require the use of opioid and/or barbiturate anaesthetics which are known to suppress respiratory neurones (Lee and Jones, 2018), and thereby introduce a confounding modulation of the respiratory CPG. The decerebrate *in situ* WHBP, on the other hand, allows for recordings and manipulations of the respiratory CPG without the requirement for anaesthetics.

A second way in which the integrity of the respiratory CPG is compromised is trough removal of the lungs and sectioning of the vagal nerve. This eliminates pulmonary mechanoreceptor inputs to the respiratory CPG and constitutes elimination of the Herring-Breuer reflex (HBR) (see section 1.3.3). As a result, the eupnoeic respiratory rate is slightly reduced through elongation of inspiratory phase duration (Paton, 1996a). Loss of HBR feedback through vagotomisation is also reported to promote an increase in activity of inspiratory-to-expiratory phase spanning neurones in the PBc that are involved in the pontine medullary feedback loop (Molkov et al., 2013, Dick et al., 2008, Feldman and Gautier, 1976). It is possible that such increased activity of the pontine feedback loop acts to compensate for the loss of HBR feedback to drive inspiratory to expiratory phase transitioning (see section 1.3.3).

In *in situ* WHBP recordings, perfusion pressure is upregulated with the use of AVP, which binds to V(1A) receptors on vascular smooth muscle cells to induce vasoconstriction

(Henderson and Byron, 2007). However, AVP also acts on V(1A) receptors in brainstem regions such as the area postrema (AP) and ventrolateral medulla, by which it can promote suppression of PN and HN respiratory activity in anaesthetised rats (Chuang et al., 2005, Chuang et al., 2003, Yang et al., 2006). In addition, AVP is thought to modulate sympathetic activity through excitatory influence on NTS barosensitive neurones (Hegarty and Felder, 1997), and through action at AVP V(1A) receptors in the RVLM (Kc et al., 2010). Endogenous AVP circulating in blood plasma does not cross the BBB in physiologically significant amounts (Landgraf, 1992). Therefore, arterial perfusion of AVP is not likely to affect respiratory or sympathetic nerve activity. However, through leakage of aCSF from blood vessels in the opened cranium, brainstem tissue in *in situ* WHBP becomes superfused with aCSF. This can result in diffusion of perfusate components (e.g. AVP) in brainstem tissue in a way that constitutes removal of the blood-brain barrier. Such diffusion of aCSF components is limited to peripheral areas of the brainstem only, and is not likely to affect deeper respiratory regions such as the ventrolateral medulla. We cannot exclude potential effects on respiratory and sympathetic activity as a result of diffusion of AVP in the most peripheral areas of the respiratory network, such as the area postrema or the commissural NTS. That said, the use of AVP in WHBP recordings in the present thesis was kept low (0.5-3 nM, compared to 27.7-461.2 µM microinjected in the NTS by Hegarty and Felder (1997)), and potential effects on the respiratory network are expected to be minimal.

In situ WHBP have reduced temperature (30-32 °C), which is important to maintain preparation viability and stability for the long duration (>1hr) of experiments reported in this thesis. We cannot categorically exclude the possibility that hypothermia influences respiratory function in these preparations compared to *in vivo.* However, the functioning of the *in situ* WHBP brainstem respiratory network at rest, and in response to chronic and acute challenges (e.g. hypoxia, high blood pressure, lung inflation) is comparable to that observed *in vivo* (Braga et al., 2007, Dutschmann et al., 2009a, Zoccal et al., 2009a, Lemes et al., 2016a, Taxini et al., 2017)

Pioneering experiments with *in situ* WHBP used aCSF solutions with high $K^+$ concentrations (6.25mM) to enhance neural excitability in the preparation (Paton, 1996b). It was later found that 6.25mM $K^+$ concentrations are not required for function of the respiratory network in the *in situ* WHBP that is comparable to that observed *in vivo* (Lemes et al., 2016a, Dutschmann et al., 2009a, Taxini et al., 2017). The concentration of potassium in aCSF used in experiments reported here is 5.2 mM, which equates median

physiological concentrations in male Wistar rat serum (Boehm et al., 2007). Therefore, enhanced excitability due to high $K^+$ concentrations is not a factor limiting translation of the present thesis' *in situ* WHBP experiments to *in vivo* animals.

Hyperoxic aCSF (92% or 95% $O_2$) used in the present studies may lead to a reduction in baseline activity of $O_2$ chemoreceptors. We acknowledge that this may result in different baseline respiratory activity compared to freely moving *in vivo* animals. However, freely moving animals do not permit the comprehensive recording of respiratory output from multiple motor nerves. And nerve recordings in anaesthetised animals *in vivo* are performed under similarly hyperoxic conditions, as animals are typically ventilated with 100% $O_2$ gas.

Perhaps the greatest disadvantage of the *in situ* WHBP is that the preparation can deteriorate, for example, through the formation of embolisms induced by transcardiac perfusion. To control for deterioration of the preparation over the course of an experiment, recordings in which the eupnoeic respiratory pattern changes in pre-treatment conditions are excluded from the dataset. Second, temporal controls are incorporated in the experimental design to control for changes in respiratory output over time that are not attributable to experimental manipulations.

*Technical consideration with regard to the use of NLX-101*

NLX-101 is a brain permeable high efficacy agonist with high selectivity (>1000-fold) at 5-$HT_{1A}$ receptors compared to a wide range (>40) of other receptors, ion channels, or monoamine-transporters (Newman-Tancredi et al., 2009). The use of NLX-101 is an important feature of the present studies, notably because its selectivity for 5-$HT_{1A}$R is not achieved by drugs used in previous pharmacological studies on the role of 5-$HT_{1A}$ transmission in respiratory control. NLX-101 is also reported to have biased agonist transmission properties. The consequences of the latter for effects of NLX-101 on distinct neural populations are not yet fully understood. This poses a limitation to the interpretation of our data.

A biased agonist is a GPCR ligand that stabilises a specific active conformation of the receptor, leading to preferential activation of select receptor coupled intracellular pathways (Stott et al., 2016). *In vitro*, NLX-101 is reported to preferentially activate Gαi subunits over Gαo subunits at 5-$HT_{1A}$ receptors (Newman-Tancredi et al., 2009). NLX-101 was also reported to have greater potency in phosphorylation of ERK1/2 relative to measures of other intracellular signaling mechanisms, such as: inhibition of cAMP

accumulation; receptor internalization; and $Ca^{2+}$ mobilization *in vitro* (Newman-Tancredi et al., 2009, Sniecikowska et al., 2019a). The same *in vitro* experiments, revealed that other 5-$HT_{1A}$R ligands (5-HT, buspirone; 8-OH-DPAT; and various 1-(1-benzoylpiperidin-4-yl)methanamine derivates, a family of compounds to which NLX-101 also belongs) indiscriminately activated all signaling cascades. This suggests the results indicative of biased agonism by NLX-101 were not merely the result of differential amplification in the measures selected to represent various intracellular responses.

Differences in host cell environment can determine which G-proteins interact with a G-protein coupled receptor (GPCR). This can result in differential recruitment of intracellular responses in response to GPCR agonism across neural subpopulations (Mannoury la Cour et al., 2006). Based on *In vivo* and *ex vivo* experiments, it has been suggested that the biased agonist signaling properties of NLX-101 translate to differential potency of the drug in different brain regions. Systemic administration of NLX-101 results in phosphorylation of ERK1/2 and c-fos activation preferentially in the frontal cortex compared to raphe regions, as observed *ex vivo* (Newman-Tancredi et al., 2009). Further, microdialysis measurements of 5-HT release in the hippocampus – which is inhibited by auto-receptor activation - and dopamine (DA) release in the medial prefrontal cortex (mPFC) - which is disinhibited by 5-$HT_{1A}$ hetero-receptor mediated suppression of mPFC inhibitory interneurones - showed that systemic administration of NLX-101 affects the latter with greater potency compared to the former in anesthetized rats (Llado-Pelfort et al., 2010). Similarly, extracellular recordings of mPFC pyramidal cells and dorsal raphe neurons in anesthetized rats revealed that systemic administration of NLX-101 results in excitation of mPFC pyramidal cells at low concentrations, whereas higher concentrations were necessary to inhibit raphe neurons (Llado-Pelfort et al., 2010). The above *in vivo* effects were all abolished by prior administration of selective 5-$HT_{1A}$ antagonist (WAY-100635). The above findings have been interpreted by some to suggest preferential inhibition by NLX-101 of neurones with 5-$HT_{1A}$ hetero-receptors over those with auto-receptors. This notion is supported by a series of pharmacological magnetic resonance imaging (phMRI) and positron emission tomography (PET) studies in cats and rats, which show that systemic administration with NLX-101 exhibits a distinct profile of brain region targeting when compared to other 5-$HT_{1A}$ agonists (befiradol/NLX-112, F13714, and 8-OH-DPAT). Notably, NLX-101 produces anatomical patterns of energy metabolism that indicate activity in cortical regions is affected, whereas activity in dorsal raphe regions is not (Becker et al., 2016, Levigoureux et al., 2019, Vidal et al., 2018, Vidal et al., 2020).

However, the support for the hypothesis that NLX-101 biased agonism translates to preferential inhibition of neurones with hetero-receptors versus those with auto-receptors has its limitations. Notably, the above mentioned *in vivo* and *ex* vivo studies (Llado-Pelfort et al., 2010, Newman-Tancredi et al., 2009) rely on direct comparison of 5-$HT_{1A}$ hetero- versus auto-receptor mediated effects (DA release and neural activity in mPFC pyramidal cells, 5-HT release in the hippocampus, and neural activity in the dorsal raphe) that may be differentially amplified and subject to distinct network interferences. These experiments lack the necessary controls to account for such confounding differential amplification and interference. Therefore, the observed difference in sensitivity of the hetero-receptor versus auto-receptor mediated responses is not necessarily representative of differential potency of NLX-101 at raphe neurone auto-receptors compared to hetero-receptors in the mPFC. Further, at the cellular level, differential responses to NLX-101 in neurones with auto-receptors vs. neurones with hetero-receptors could be mediated by differences in sensitivity or receptor reserve between these cell populations. The relative intrinsic efficacy of NLX-101 and other 5-$HT_{1A}$R agonists at auto- vs. hetero-receptor expressing populations remains to be experimentally established.

I*n vitro* studies indicate that NLX-101 preferably recruits Gαi over Gαo activation, and ERK1/2 pathway activation over other intracellular responses (Newman-Tancredi et al., 2009, Sniecikowska et al., 2019a). It has been suggested that differential engagement of G protein subunits and intracellular signaling pathways in different neurone populations results in a translation of the above biased agonism to preferential inhibition of hetero-receptor expressing neurons compared to auto-receptor expressing raphe neurones. This notion is supported by the above mentioned PET and phMRI studies which show that NLX-101 produces anatomical patterns of energy metabolism that indicate activity in cortical regions is affected, whereas activity in dorsal raphe regions is not (Becker et al., 2016, Levigoureux et al., 2019, Vidal et al., 2018, Vidal et al., 2020).However, at present, the above notion is not established beyond reasonable doubt. Some key questions remain to be answered. First, do 5-$HT_{1A}$ R differentially couple with Gαi or Gαo subunits at auto receptors in raphe serotonergic neurones versus hetero-receptors elsewhere in the respiratory network? Second, what is the relative intrinsic efficacy of NLX-101 and other 5-$HT_{1A}$R agonists at auto- vs. hetero-receptor expressing respiratory populations? The lack of clarity regarding the potential for differential potency of NLX-101 at raphe serotonergic

neurones with 5-$HT_{1A}$ auto-receptors versus other populations in the respiratory network with hetero-receptors poses a limitation for the interpretation of our data.

*Technical considerations with regard to experimental design*

The dataset of peripheral chemoreflex experiments shows, for some parameters, significant differences between treatment group means in pre-treatment conditions. The presence of pre-treatment differences in treatment group means indicates presence of confounding group differences not related to the experimental manipulation. This could potentially be due to a flaw in the experimental design applied for this experiment. That is, animals from different batches were not distributed across drug vs. vehicle treatment groups evenly. However, the significant pre-treatment differences did not occur in groups that showed significant post-treatment differences; and vehicle responses remained consistent pre- and post-treatment. Therefore, significant effects observed are likely to be real. On the other hand, it is possible that some effects existed that were not found to be significant because they were masked by pre-treatment group differences.

Optimal support for the notion that effects of NLX-101 in the present thesis are mediated by selective 5-$HT_{1A}$R transmission requires experimental evidence that the effects of NLX-101 are challenged by systemic co-administration of 5-$HT_{1A}$R antagonist. In a small set of preliminary and experimental recordings with *in situ* WHBPs, I performed experiments in which systemic administration of NLX-101 was followed by co-administration of WAY-100635. Effects observed in these recordings suggest that 5-$HT_{1A}$R antagonism reverses effects of NLX-101 on respiratory activity (see **figure 3-16**). However, experimental protocols were not identical across these recordings (details on recording protocols are provided in legend to **figure 3-16**), and sample sizes were small (n=4). Therefore, these recordings cannot be used for statistical comparisons to provide categorical evidence that functional effects of NLX-101 observed in the present thesis are mediated selectively by 5-$HT_{1A}$R transmission. I acknowledge that the absence of such categorical evidence poses limitations to the degree of certainty with which I can attribute effects observed after administration of NLX-101 to selective 5-$HT_{1A}$R agonism.

That said, previous studies provide strong experimental support that effects of NLX-101 *in vitro* and *in vivo* are mediated selectively by 5-$HT_{1A}$R agonism.*In* vitro, NLX-101 has >1000-fold selectivity at 5-$HT_{1A}$ receptors compared to a wide range (>40) of other receptors, ion channels, or monoamine-transporters (Newman-Tancredi et al., 2009). Whole cell patch-clamp recordings show that NLX-101 (1μM) bath administration inhibits

dorsal raphe neurones in acute brain slices of rat, and this effect can be blocked with pre-treatment with 5-$HT_{1A}$R antagonist WAY-100635 (1µM) (Levitt et al., 2013). *In vivo*, effects of systemic NLX-101 (i.v.) on the discharge rate of pyramidal neurones in medial prefrontal cortex (mPFC) and on that of dorsal raphe 5-HT neurones were both reversed by the 5-$HT_{1A}$R antagonist WAY-100635 in anaesthetised rats (Llado-Pelfort et al., 2010) (see section 3.4.2, pages 128-129). These findings, together with the *in situ* WHBP recordings reported in **figure 3-16**, suggest that functional effects of NLX-101 as described in this thesis are likely to be mediated selectively by 5-$HT_{1A}$R transmission.

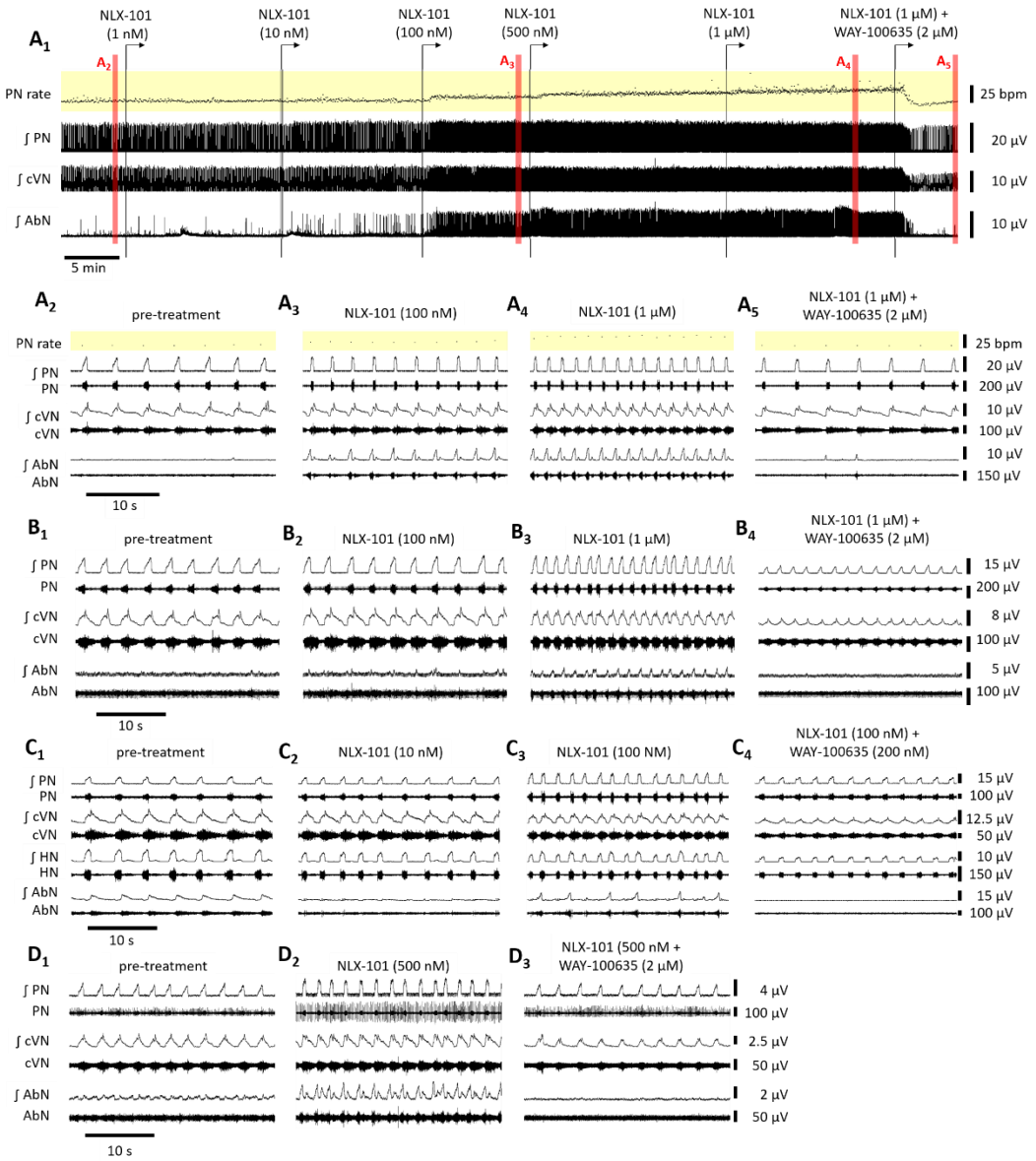


**Figure 3-16:** effects of NLX-101 on respiratory rhythm and pattern can be reversed by co-administration of 5-$HT_{1A}$ R antagonist WAY-100635.

Peripheral nerve recordings of the PN, HN, cVN, and AbN in two *in situ* WHBP illustrate the effects of systemic NLX-101 on respiratory rhythm and pattern, and the full or partial reversal of these effects after subsequent systemic administration of 5-$HT_{1A}$R antagonist WAY-100635. (**$A_1$**) The full time-course of a concentration response recording with NLX-101 (1nM, 10nM, 100nM, 500nM, and 1µM) and subsequent co-administration of WAY-100635 (2µM). Red annotation indicates 30s sections depicted in more detail below **($A_{2-5}$).**.Figures (**$B_{1-4}$**) show excerpts of another NLX-101 concentration-response recording (1nM, 10nM, 100nM, 600nM, 1µM NLX-101), followed by co-administration of WAY-100635 (2µM). Figures (**$C_{1-4}$**) show excerpts of an NLX-101 concentration-response protocol (1nM, 10nM, 100nM NLX-101), followed by co-administration of WAY-100635 (200nM). In this recording, a two-minute hypercapnic stimulus (7% $CO_2$, $O_2$-balanced) was performed pre-treatment, and after each drug administration (not shown). Excerpts depicted here are sampled after recovery from each hypercapnic stimulus (>5 min after cessation of hypercapnic stimulus). Figures (**$D_{1-3}$**) show excerpts of a recording with a (pre-treatment) hypercapnic stimulus (8% $CO_2$, $O_2$-balanced) (not shown), followed by NLX-101 (500nM), followed by co-administration of WAY-100635 (2µM). The pre-treatment excerpt depicted here is sampled after recovery from the hypercapnic stimulus (>9 min after cessation of hypercapnic stimulus).

### *3.4.3 Interpretation of data*

*Systemic 5-HT$_{1A}$ transmission results in increased respiratory drive in resting conditions.*

The closest resemblance in previous literature to the concentration response experiments of section 3.3.1 is a series of studies on the effects of systemic administration of 5-HT$_{1A/7}$ receptor agonist (8-OH-DPAT) on respiratory rate and minute activity derived from recordings of the PN in *in* situ WHBP of rats. Minute PN activity (mPNA) was defined as the average PN motor burst envelope per minute, and can be considered a surrogate of minute ventilation. Systemic administration 8-OH-DPAT was reported to increase mPNA and significantly increase respiratory rate in *in situ* WHBP of juvenile rats in resting conditions (Corcoran et al., 2013, Manzke et al., 2009, Manzke et al., 2010). Conversely, systemic application 5-HT$_{1A}$antagonist (WAY-100635) resulted in depression of mPNA in *in situ* WHBP of rats (Manzke et al., 2009). Similarly, systemic administration of 8-OH-DPAT (i.v.) resulted in increased respiratory rate and tidal volumes observed through plethysmography recordings in anesthetised rats (Szereda-Przestaszewska and Kaczynska, 2007, Valic et al., 2008, Manzke et al., 2009). These effects, too, were reversible by subsequent administration of 5-HT$_{1A}$ R antagonist (WAY-100635) (Valic et al., 2008, Manzke et al., 2009). Thus, systemic administration of 5-HT$_{1A/7}$ R agonist (8-OH-DPAT) resulted in increased respiratory rate and tidal volume, or physiological substrates thereof, *in vivo* and *in situ*. These findings are in line with the increased respiratory rate and increased PN burst amplitude and envelope observed after systemic administration of NLX-101 in *in situ* WHBP in concentration response experiments of the present chapter. Further, the significant increases in late-E amplitude also correspond to the increased tidal volume observed through plethysmography recordings, as forced expiration decreases lung volume below functional residual capacity so that the inspiratory volume of the subsequent breathing cycle can be increased. Overall, NLX-101 concentration-response experiments revealed similar effects on restful respiratory drive as has previously been reported after administration of 8-OH-DPAT. The NLX-101 concentration-response experiments in the present chapter offer direct experimental support for the hypothesis that network wide selective 5-HT$_{1A}$ agonism promotes increased respiratory drive.

Discrepancies between effects of systemic NLX-101 on restful respiratory activitiy and previous literature on respiratory effects of systemic 5-HT$_{1A}$ transmission.

Although findings from NLX-101 concentration-response experiments in this chapter are consistent with previous work that suggests 5-HT$_{1A}$ transmission results in increased

respiratory drive, the specific 5-$HT_{1A}$R mediated changes in respiratory rhythm and pattern are distinct from findings and modelling hypotheses in the current literature.

One finding regarding pattern changes in restful respiratory activity in response to NLX-101 that is not consistent with previous reports is the lack of an effect on normalised burst envelope and peak amplitudes in integrated HN motor output. Besnard et al. (2007, 2012) reported that central injections (in the $4^{th}$ ventricle) of 8-OH-DPAT promoted a significant increase in tonus of upper airway muscles involved in upper airway dilation and stabilization (genioglossus, geniohyoid, and digastric muscles) observed through electromyography recordings in anesthetised rats. The genioglossus and geniohyoid muscles are innervated by the HN, whereas the digastric muscle is innervated by the facial nerve (CN 7). Our recordings of the HN, however, did not reveal any changes in pattern (normalised burst envelope or peak amplitude) under resting conditions in response to systemic administration of NLX-101. It is currently not clear what could explain the discrepancy between these findings and the results observed in the present thesis. Differences between these studies include a difference in drug administration (injection in $4^{th}$ ventricle vs. arterial perfusion), which could result in differential spread of 5-$HT_{1A}$R agonist across the regions of the respiratory CPG. Further, the selectivity of the drugs used is different (5-$HT_{1A/7}$R agonist 8-OH-DPAT vs. selective 5-$HT_{1A}$R agonis NLX-101). Effects of 5-$HT_7$ transmission on respiratory network interactions are plausible as 73.9% of glycinergic ($GlyT_2$ positive) cells in the pre-BötC are also 5-$HT_7$ positive (Manzke et al., 2009). Ultimately, the use of anaesthesia (urethane) could affect respiratory responses to the pharmacological manipulation. Although the anaesthetic used (urethane) affects cardiovascular and respiratory systems in rodents to a lesser extent than barbiturates and opioids (Lee and Jones, 2018) effect on respiratory function are still present, and urethane is reported to affect multiple neurotransmitter gated ion channels at approximately anaesthetic 50% effective concentration (Hara and Harris, 2002). Therefore, confounding effects of anaesthesia cannot be excluded.

There are also some notable differences between our experimental findings and previous literature regarding respiratory rhythm changes in response to systemic 5-$HT_{1A}$R transmission. Single cell recordings of expiratory neurones combined with PN recordings in anesthetised cats revealed that systemic administration of 8-OH-DPAT resulted in changes of the activity pattern of Post-I neurones (Manzke et al., 2009). Specifically, a low dose of 8-OH-DPAT (10 $\mu g/kg^{-1}$) resulted in the receding of onset of bursting activity from the Post-I phase into the I phase. At a high dose of 8-OH-DPAT, Post-I neurone activity

became suppressed throughout most of the respiratory cycle via hyperpolarizing currents. Inspired by these recordings, a computational model was developed that described hypothetical 5-$HT_{1A}$R mediated changes in interactions among expiratory and inspiratory neurone populations in the BötC and pre-BötC, respectively (Shevtsova et al., 2011). The specific putative effects of 5-$HT_{1A}$ R transmission at BötC and pre-BötC neurones, and how these are suggested to affect VRC network interactions, are beyond the scope of the present chapter but will be addressed in detail in chapter 5. Relevant with regard to the findings in the present chapter, however, is that both Manzke et al. (2009) and the subsequent modelling hypothesis (Shevtsova et al., 2011) assumed that the change in activity pattern observed in Post-I neurones can be extrapolated to the network level, and that systemic administration of a 5-$HT_{1A}$ agonist would result in a shift and, at higher concentrations, in suppression, of cVN Post-I activity. This was suggested to transform the tri-phasic eupnoeic respiratory rhythm to a two-phased oscillation between inspiratory and expiratory activity (without the Post-I phase). Although the NLX-101 concentration-response experiment revealed a non-significant trend of shortening of cVN Post-I activity, we did not observe a phase shift, nor a loss of cVN Post-I activity. At all stages in the NLX-101 concentration response curve, the tri-phasic rhythm remained intact. A number of factors could explain the discrepancy between our findings and the experimental findings by Manzke et al. (2009) and modelling hypothesis based thereon (Shevtsova et al., 2011). Manzke et al. (2009) used a non-selective 5-$HT_{1A/7}$ R agonist (8-OH-DPAT), and single cell recordings of respiratory neurones are performed in pentobarbital anesthetised cats. One cannot exclude confounding effects of 5-$HT_7$ transmission and/or barbiturate anaesthesia on the respiratory network. Further, the assumption that systemic stimulation of 5-$HT_{1A}$ transmission resulted in the complete loss of Post-I activity at the network level was never experimentally verified. This assumption was based on extrapolation of the responses to systemic administration of 8-OH-DPAT observed in 4 Post-I neurones, to the subpopulation of Post-I neurones at large. The limited sample size of these recordings does not permit such inference with confidence. Ultimately, the computational model by Shevtsova et al. (2011) relied on assumptions not experimentally verified with regard to the neuroanatomical and biochemical properties of specific VRC respiratory functional subpopulations (e.g. Post-I neurones, Early-I neurones, etc), this topic will be addressed in more detail in chapter 5 (section 5.1.1).

Interpretation of putative mechanisms underlying effects of systemic NLX-101 inspired by lessons from the broader respiratory control literature.

The effects of NLX-101 on resting state respiratory rhythm show interesting parallels with respiratory behaviours in health and disease that may contribute to a better understanding of how 5-$HT_{1A}$ affects the respiratory CPG.

One such parallel can be found in research on the mechanism and treatment of respiratory dysrhythmia in Rett Syndrome (RTT). As addressed in the General Introduction (section 1.8.2), RTT is a neurological disorder most often caused by loss of function of transcriptional regulator MeCP2 (Chahrour et al., 2008, Percy, 2016, Young et al., 2005). Common features of disordered breathing in RTT include spontaneous central apnoea, active breath holding, and valsalva maneuvers (Ramirez et al., 2013, Bissonnette and Knopp, 2006, Weese-Mayer et al., 2006). These behaviours have been associated with overactivity of the laryngeal adductors that control expiratory airflow via closure of the glottis, and with overactivity of expiratory neural populations that ultimately drive these muscles (Abdala et al., 2014a, Ramirez et al., 2013). The respiratory phenotype of RTT syndrome is mimicked in MeCP2 deficient mice, which display respiratory rhythm variability and high incidence of spontaneous central apnoeas (Abdala et al., 2010, Levitt et al., 2013, Samaco et al., 2013, Schmid et al., 2012, Chao et al., 2007). In *in situ* WHBP of rats and mice, central apnoeas are characterized by enhanced activity and duration of Post-I activity in the cVN (Stettner et al., 2007, Abdala et al., 2010). Thus, exacerbated expiratory (Post-I) activity is a prominent feature of respiratory dysrhythmia in mouse models of RTT.

Systemic administration of 5-$HT_{1A/7}$R agonist (8-OH-DPAT) or 5-$HT_{1A}$R agonist and D2 R antagonist (Sarizotan) can depress respiratory apnoea in unanaesthetised MeCP2 deficient mice *in vivo* (Abdala et al., 2010), as well as in *in situ* WHBP of MeCP2 deficient mice (Abdala et al., 2010). Systemic administration of NLX-101 was found to reduce apnoea and improve breath irregularity in unanaesthetised MeCP2 deficient mice *in vivo* in a dose dependent manner (Levitt et al., 2013). Conversely, systemic administration 5-$HT_{1A}$R antagonist WAY-100635 induces periodic apnoeas in *in situ* WHBP of healthy WT mice (Dhingra et al., 2016). It is suggested that 5-$HT_{1A}$ transmission alleviates dysrhythmia in MeCP2 deficient mice through suppression of Post-I activity (Abdala et al., 2014a, Wittman et al., 2019).

In the present chapter, we observed that the increase in resting state respiratory rate after systemic administration of NLX-101 appears to be mediated predominantly through shortening of expiratory phase duration (PN TE(s)) (see **Fig. 3-5A$_3$** and **Table 3-1**), that appears mediated to equal extent by shortening of Post-I and E2 phase durations (see **Fig. 3-5B$_{1,2}$** and **Table 3-1**). Although not statistically significant, the reduction in PN TE(s) had a large effect size. To conclude, findings in the present thesis suggest that the increased respiratory rate is mediated chiefly by shortening of expiratory phase duration. This is consistent with suppression of Post-I activity in response to systemic 5-HT$_{1A}$ agonism in MeCP2 deficient mice. It is conceivable that the stabilization of respiratory dysrhythmia in mouse models of RTT syndrome, and the increase in respiratory rate in *in situ* WHBP of rats in response to systemic 5-HT$_{1A}$ transmission are mediated by a shared mechanism. Further exploration of this notion benefits from data presented in subsequent chapters of the present thesis, and will therefore be addressed in the general discussion.

Another interesting parallel that may help to elucidate putative mechanisms underlying the effect of systemic NLX-101 can be found in the similarities between the response to NLX-101 and the hypercapnic respiratory response. In *in situ* WHBP, the hypercapnic respiratory response was described as increased respiratory rate and pattern, combined with the emergence of late-E activity (Abdala et al., 2009, Marina et al., 2010). *In vivo*, a similar response was observed: increased tidal volume along with forced expiration through abdominal contraction (late-E) (Huckstepp et al., 2015, Falquetto et al., 2018). The network response to systemic administration of NLX-101 resembled the hypercapnic response: i.e. an increase in respiratory drive that included enhanced respiratory rate, increased pattern in PN and AbN respiratory motor outputs, and a (non-significant) increase in the incidence of late-E bursts. One noteworthy distinction is that late-E activity in response to hypercapnia is described as an all or nothing event, with similar amplitudes observed in all AbN late-E bursts (Abdala et al., 2009), whereas Late-E bursts in response to NLX-101 were a graded phenomenon, with dose-dependent increases in burst amplitude (see **fig. 3-6D$_2$**). Under hypercapnic conditions, the increase in respiratory rate and pattern is thought to be mediated by enhanced excitatory drive from $CO_2$ chemoreceptors to respiratory neurones in the VRC, notably to inspiratory neurones in the pre-BötC (Bochorishvili et al., 2012, Mulkey et al., 2004, Guyenet et al., 2016) (see section 1.4.1). Similarly, the emergence of late-E activity under hypercapnic conditions was suggested to be mediated by enhanced excitatory chemoreceptor drive to late-E neurones of the expiratory oscillator in the pFRG (Marina et al., 2010, Abbott et al., 2011)

(see section 1.4.4). Systemic NLX-101 and WAY-100635 did not affect the respiratory and sympathetic responses to hypercapnia or peripheral chemoreflex activation. Therefore, it is unlikely that systemic administration of NLX-101 or WAY-100635 resulted in increased chemoreceptor drive. An alternative mechanism via which systemic NLX-101 administration could putatively promote the respiratory responses also observed under hypercapnic responses, is through disinhibition of mechanisms downstream of central chemoreceptors. Disinhibition of pFRG expiratory oscillator through focal co-administration of $GABA_AR$ antagonist (bicuculline) and glycine receptor antagonist (strychnine) was reported to promote late-E activity in anesthetised rats (Huckstepp et al., 2015, Silva et al., 2019). Therefore, it is conceivable that systemic administration of NLX-101 promoted late-E activity through suppression of inhibitory afferents to the pFRG (i.e. disinhibition of the pFRG). Similarly, disinhibition of inspiratory VRC populations downstream of chemoreceptors could contribute to the observed increases in respiratory rate and pattern.

Further discussion of putative mechanisms underlying the effects of systemic administration of NLX-101 on restful respiratory activity, as well as an interpretation of the absence of an effect on respiratory and sympatho-respiratory responses to hypercapnia and peripheral chemoreceptor activation, benefits from data presented in chapters 4 and 5. To this end, the general discussion will provide a comprehensive interpretation of the data presented across chapters of this thesis in the context of the relevant literature on respiratory behaviour in health and disease (e.g. the hypercapnic response, RTT syndrome, μOR-induced depression of respiratory activity). Topics addressed further in the general discussion include: putative mechanisms underlying [1] the increased respiratory rate and shortening of expiratory phase duration; [2] the emergence of late-E activity [3] the potentiation of respiratory pattern in some, but not all respiratory motor outputs; and [4] an interpretation of the absence of effects of NLX-101 on chemoreflex responses.

# Chapter 4: 5-$HT_{1A}$ Receptor RNA Distribution Across Brainstem Regions of Respiratory Control.

## 4.1 Chapter Introduction

### *4.1.1 Identification of putative mechanisms underlying effects of 5-$HT_{1A}$ transmission requires an understanding of 5-$HT_{1A}$R distribution among key regions of respiratory control.*

Chapter three provides a comprehensive account of the effects of selective 5-$HT_{1A}$ receptor agonism on the eupnoeic respiratory rhythm and pattern, and on the respiratory and sympathetic responses to peripheral and central chemoreflex activation. Previous experimental and modelling studies have suggested that 5-$HT_{1A}$ receptor agonism induces changes in respiratory rhythm and pattern chiefly due to inhibition of subpopulations of inhibitory respiratory interneurones in the VRC (Manzke et al., 2009, Manzke et al., 2010, Shevtsova et al., 2011) (see section 1.7.3). To determine whether differential anatomical distribution of 5-$HT_{1A}$R could partly explain the agonism functional effects, I investigated the distribution of 5-$HT_{1A}$R RNA transcripts over inhibitory and non-inhibitory neurones in key brainstem regions of respiratory control.

There are multiple brainstem regions at which 5-$HT_{1A}$ transmission could hypothetically modulate respiratory network activity. The BötC and pre-BötC contain concentrations of respiratory neurones important for expiratory and inspiratory rhythm generation, respectively. Inhibitory interneurons in these regions are thought to be involved in the coordination of multiphase respiratory activity (Smith et al., 2013) (see section 1.2.3).The RVRG is thought to contain concentrations of respiratory neurons that contribute to respiratory pattern formation and relay rhythmic respiratory drives to (pre-)motor regions (Ezure et al., 1988, Alheid and McCrimmon, 2008) (see section 1.2.3). 5-$HT_{1A}$R expression in motor neurones could suppress respiratory pattern, whereas 5-$HT_{1A}$R expression in inhibitory pre-motor neurones could disinhibit motor neurones. Regions of the parabrachial complex are thought to contribute to inspiratory-to-expiratory phase transitioning (Alheid et al., 2004, Dutschmann and Dick, 2012) (see section 1.3). The NTS (Alheid et al., 2011) and the RTN (Guyenet et al., 2019) contain neurone populations involved in the respiratory and sympathetic peripheral and central chemoreflex responses (see sections 1.4.1, 1.5.2, and 1.6.2). Ultimately, the raphe nuclei contain serotonergic

neurones which modulate respiratory activity through 5-HT release, and of which subpopulations are reported to be involved the central chemoreflex responses (Brust et al., 2014, Hennessy et al., 2017) (see sections 1.4.2, 1.7.2, and 1.7.3).

### *4.1.2 Current understanding of 5-HT$_{1A}$R distribution in the respiratory CPG*

Histological-, *in situ* hybridization-, and PCR experiments indicate that 5-HT$_{1A}$R are expressed in the BötC and pre-BötC (Manzke et al., 2009, Manzke et al., 2010), the NTS (Vantrease et al., 2015), and in the dorsal and median raphe nuclei (Sotelo et al., 1990) of rats. Single cell recordings of neurones of the dorsal raphe in acute brain slices of mice suggested GIRK channel activation by NLX-101 (Levitt et al. 2013), which is consistent with the above histological evidence of 5-HT$_{1A}$R in this region. Microdialysis of 5-HT$_{1A/7}$R agonist (8-OH-DPAT) suggest that 5-HT$_{1A}$ receptors are also present in the raphe magnus and raphe pallidus (Li et al., 2006) (see section 1.7.3). Further, RT-PCR studies revealed presence of 5-HT$_{1A}$R RNA in glomus cells isolated from carotid bodies of rat (Yokoyama et al., 2015). Thus, there is conclusive evidence for 5-HT$_{1a}$ R expression in the CB, BötC, pre-BötC, NTS, and raphe nuclei of the pons (dorsal and median raphe), and there is pharmacological data that suggests there may be 5-HT$_{1A}$R expression in caudal raphe nuclei (raphe magnus, raphe pallidus).

A comprehensive mapping of 5-TH$_{1A}$ R expression throughout key regions of the respiratory CPG is still lacking. Furthermore, expression of 5-HT$_{1A}$ specifically in inhibitory (GlyT2 positive) neurones has, as yet, only been reported for the pre-BötC and not compared to other regions (Manzke et al., 2009, Manzke et al., 2010). Given the relatively well described and important role of inhibitory interneurons in respiratory rhythm and pattern formation, and their differential functional-anatomical distribution in the respiratory network, this study aimed to map and compare expression of 5-HT$_{1A}$R transcripts in inhibitory neurone populations located in brainstem respiratory nuclei.

### *4.1.3 Chapter aims and hypotheses*

**Chapter Aim:** The aim this chapter is to establish the distribution of 5-HT$_{1A}$R RNA throughout key regions of the brainstem respiratory network, particularly in inhibitory neurone populations.

**Methodological approach:** GABAergic and Glycinergic neurones were identified by expression of vesicular inhibitory amino-acid transporter (SLC32A1) RNA. Fluorescence *in situ* hybridization (FISH) of 5-HT$_{1A}$ RNA and SLC32A1 RNA was performed in key brainstem regions of respiratory control. Analyzed regions of the VRC are the BötC; the pre-BötC;

and the RVRG. Analyzed regions with (pre-)motor neurones are the nucleus ambiguus compactus (N. Amb. C., which contains hypoglossal and vagal (pre-)motor neurones (McGovern and Mazzone, 2010, Ezure, 1990)); the dorsal motor nucleus of the vagus (N10); the hypoglossal motor nucleus (N12); and a region dorsomedial to the N. Abm. C. that contains hypoglossal pre-motor neurones (XII pre-motor region) (Koizumi et al., 2008). Analyzed regions of the PBc are the medial parabrachial nucleus (MPB); the internal, central, and external parts of the lateral parabrachial nucleus (LPBI, LBPC, and LPBE, respectively); and the Kölliker Fuse nucleus (KF). The ventral parafacial region where RTN neurones are located ($pF_V$/RTN) and the commissural part of the NTS (NTScomm) are analyzed, both of which are important regions for chemoreceptor feedback mechanisms in respiratory control. And last, brainstem raphe nuclei are analyzed: raphe magnus (RMg); raphe obscurus (ROb); raphe pallidus (RPa), and the dorsal raphe nucleus. FISH was performed in fixed brain sections of adult rats.

**Hypotheses:** Based on previous functional studies, I expected to find 5-$HT_{1A}$R RNA in the NTS, median raphe, BötC , pre-BötC. I expected to find 5-$HT_{1A}$ R and Solute Carrier Family 32 Member 1 (SLC32A1, a marker of glycinergic and GABAergic neurones) RNA (co-)expression in the pre-BötC. For other regions, the mapping of 5-$HT_{1A}$ R and SLC32A1 (co-)expression is an exploratory effort.

## 4.2 CHAPTER METHODS

### *4.2.1 Method description and justification*

To establish distribution of 5-$HT_{1A}$ R in various respiratory regions, and further identify the phenotype of 5-$HT_{1A}$R expressing neurones, I used commercial fluorescence *in situ* hybridization (FISH) probes for labelling of rat $5HT_{1A}$ receptor mRNA, Solute Carrier Family 32 Member 1 mRNA (SLC32A1), and Peptidylprolyl Isomerase B mRNA (PPIB, an abundant housekeeping gene targeted as a positive control) with RNAscope® Fluorescent Multiplex assay (Advanced Cell Diagnostics Inc., Newark, USA). FISH enabled single molecule visualization of target mRNA in individual cells, while preserving tissue context. RNAscope® has improved selectivity and signal-to-noise ratio relative to conventional ISH methods (Wang et al., 2012). Furthermore, this proprietary platform facilitated simultaneous detection of multiple target mRNA's (Wang et al., 2012). The method utilizes dual probes which bind to contiguous sequences of target RNA. Each probe consists of a (18-25 base) sequence complementary to a sequence of the target RNA, a spacer sequence, and a (14 base) tail sequence. This probe design is conceptualised as a 'Z-probe'. Of the two Z-probes binding to contiguous sequences of target RNA (double Z), the two 'tail' sequences are different, and together form a single (28-base) hybridization site for pre-amplifier molecules. Each pre-amplifier contains 20 binding sites for amplifier molecules, and each amplifier contains 20 binding sites to specific fluorescent label probes (for a schematic of this design, see **figure 4-1**). This design ensures minimal background noise because the 14-base tail sequence of a single z-probe will not bind the pre-amplifier with sufficient strength to result in successful signal amplification, and it is highly unlikely that a non-specific hybridization event will juxtapose a pair of z-probes along an off-target mRNA molecule to form the 'double-z' 28-base hybridization site for the preamplifier. Multiple distinct RNA sequences can be targeted simultaneously using distinct Z-probe pairs, each dual Z sequence targeted by a cognate set of pre-amplifiers, amplifiers, and fluorescent label probes.

The strong and selective signal amplification with RNAscope® FISH means that individual hybridized RNA molecules are discernible as punctate dots with confocal imaging. Consequently, when FISH is combined with Nissl nucleic acid staining (labelling ribosomal RNA, and other accumulations of nucleic acid in the neurone), neural soma outlines can be established, and FISH labeled RNA (co-expression) levels can be counted per cell in a given neuro-anatomical structure. Additional DAPI staining was used for anatomical

referencing throughout the brainstem. Thus, FISH with RNAscope® Fluorescent Multiplex assay, combined with Nissl and DAPI staining, was used to perform a detailed analysis of 5-$HT_{1A}$ receptor and SLC32A1 mRNA (co-)expression levels in individual neurones throughout key brainstem structures in respiratory control.

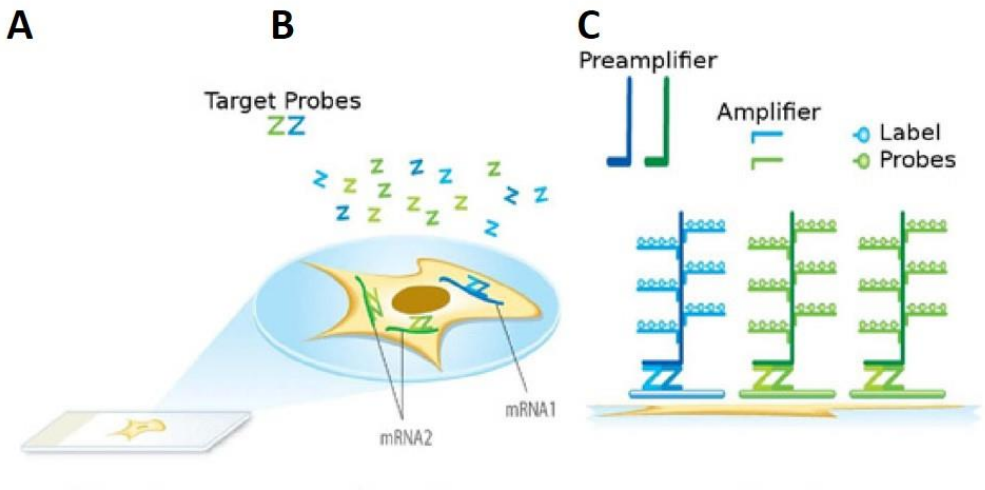


**Figure 4-1:** Schematic representation of RNAscope® Fluorescent Multiplex assay design.

RNAscope® Fluorescent Multiplex assay (Advanced Cell Diagnostics Inc., Newark, USA) enables single molecule visualization of target mRNA in individual cells, while preserving tissue context in PFA fixated brain slices (**A**). Multiple RNA sequences can be labelled simultaneously. For each targeted RNA, a distinct pair of 'z-probes' is designed to hybridize with contiguous sequences of that RNA, and form a 'double-z' probe pair (**B**). The combined tail sequences of the 'double- z' probe pair hybridize exclusively with cognate pre-amplifier molecules, to which exclusively cognate amplifiers and fluorescent label probes can bind (**C**). This ensures highly selective, yet powerfully amplified fluorescent labelling of the target RNA. Schematic is adapted from Wang et al. (2012).

### *4.2.2 Preparation of fixed brain sections for ISH labelling or Neutral red stain*

Brain section for RNAscope® ISH was acquired from four adult (~200g) male Wistar rats that were anesthetised with isoflurane until loss of hind paw pinch reflex, and subsequently euthanised with i.p. injection (10mL/kg) of Euthatal (200 mg/mL sodium pentobarbital; Merial, Harlow, United Kindgom). After euthanasia, the rat was transcardially perfused with 50mL 1x PBS, immediately followed by perfusion with 100mL 4% PFA in 1x PBS. The brain was then carefully collected and stored in 4% PFA solution in 1x PBS overnight at 4°C for postfixation. The brain was then transferred to 20% sucrose in 1x PBS solution, and left in sucrose solution for 24 hours at 4°C for cryoprotection. Blocks of pontine and medullary brainstem tissue were then prepared and suspended in O.C.T. embedding media (Cellpath, Newtown, United Kingdom) and stored airtight at -80°C for a duration of up to two days until cryostat sectioning. 15 Micrometer coronal sections of

the pons and sagittal sections of the lateral and medial medulla were prepared with a cryostat and mounted on Superfrost Plus slides (Thermo Scientific, Waltham, U.S.A.). When cutting and mounting sections, all slides were numbered in order of sectioning, and every fifth section was set aside for Neutral Red (1% in $H_2O$) lysosomal staining for anatomical reference. The remaining sections were stored airtight at -80°C to be used for FISH labelling within 2 months from the day of euthanasia and PFA perfusion. The neutral red stained sections were evaluated for anatomical landmarks, based on which sections cut from immediately adjacent brain tissue were selected for FISH labelling. Except for O.C.T. embedding media, all solutions and materials in contact with brain tissue during this process were rendered RNAse free.

### *4.2.3 Selection of sections for FISH labelling, and selection of anatomical structures for confocal imaging and image analysis*

From each of the four rat brains fixed and sectioned (see section 4.2.2), three sections were selected for FISH analysis of $5HT_{1A}R$ RNA and SLC32A1 RNA (co-)expression in various brain regions of respiratory control. This selection of sections was guided by Paxinos and Watson (2007), and based on the presence of brainstem regions involved in respiratory control. A sagittal section of the lateral medulla (~ 2.1mm lateral from midline) was obtained from three out of four rats (in one of four rats I failed to obtain such a section). These sagittal lateral medulla sections were used for analysis of $5HT_{1A}R$ and SLC32A1 (co-)expression in the following brainstem regions: the ventral parafacial region, where RTN neurones are situated ($pF_V$/RTN); the Bötzinger Complex (BötC); the pre-Bötzinger Complex (pre-BötC); the Rostroventral Respiratory Group (RVRG); Nucleus Ambiguus Compactus (N. Abm. C.); and a region with XII premotor neurones. Additionally, from each of the four rats, a sagittal section of the medial medulla (~ 0.1mm lateral from midline) was obtained for analysis of $5HT_{1A}$ and SLC32A1 (co-)expression in: raphe Magnus (RMg); raphe Pallidus (RPa); raphe Obscurus (ROb); Dorsal Nucleus of the Vagus Nerve (N10); the hypoglossal motor nucleus (N12); and the commissural part of the Nucleus Tractus Solitarius (NTScomm). Finally, from each of the four rats, a coronal section was obtained of the pons (~8.88mm caudal from bregma) was obtained for analysis of $5HT_{1A}$ and SLC32A1 (co-)expression in: the dorsal raphe, caudal part; the Medial Parabrachial Nucleus (MPB, bilaterally); the internal part of the Lateral Parabrachial Nucleus (LPBI, bilaterally); the central part of the Lateral Parabrachial Nucleus (LPBC, bilaterally); the external part of the Lateral Parabrachial Nucleus (LPBE, bilaterally); and the Kölliker Fuse Nucleus (KF, bilaterally).

To select the right sections for FISH, neutral red stained sections obtained during cryostat sectioning (see section 4.2.2) were imaged with a bright-field microscope, and evaluated relative to figures and images in the rat brain atlas by Paxinos and Watson (2007). Based on evaluation of anatomical landmarks in neutral red stained sections, and utilizing a numbering system applied when cryostat sectioning (see section 4.2.2), the appropriate sections were selected for FISH. Key anatomical landmarks for selection of lateral medulla sections were the presence of the facial nucleus, the nucleus ambiguous compactus, and the lateral reticular nucleus. Key anatomical landmarks for selection of the medial medulla sections were the principle-, medial-, and dorsal nuclei of the inferior olive, the hypoglossal nucleus, and the central canal. Key anatomical landmarks for selection of the pontine section were the shape of the fourth ventricle and the superior cerebellar peduncles. **Figure 4-2** provides images of neutral red stained sections of the lateral medulla (sagittal) the medial medulla (sagittal), and the pons (coronal), each annotated with the key landmarks and brainstem regions selected for imaging and analysis of $5HT_{1A}$ R and SLC32A1 (co-)expression.

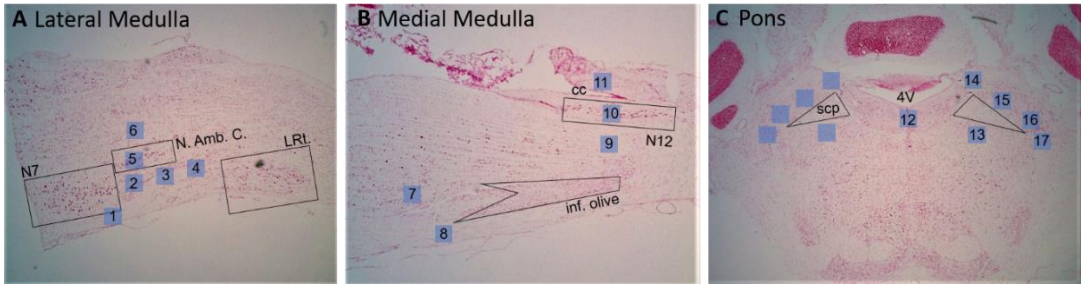


**Figure 4-2:** Sections of medulla and pons with annotation of brain regions in which FISH is quantified and analysed.

Brightfield images of sagittal sections of the lateral meduula (~2.10 mm lateral from midline), (**A**) and medial medulla (~0.10 mm lateral from midline) (**B**), and a coronal section of the pons (~8.88mm caudal from bregma) (**C**). Sections were counterstained with neutral red stain for anatomical reference. Numbered blue boxes correspond to the regions in FISH treated sections that are imaged with a confocal microscope for subsequent RNA transcript counting and analysis. Pontine regions labelled with numbers 13 to 17 are imaged bilaterally. The numbers correspond to the following regions: 1 = ventral parafacial region ($pF_V$) / retrotapezoid nucleus (RTN); 2 = Bötzinger Complex; 3 = pre-Bötzinger Complex; 4 = Rostroventral Respiratory Group; 5 = Nucleus Ambiguus Compactus; 6 = region with XII premotor neurones; 7 = raphe Magnus; 8 = raphe Pallidus; 9 = raphe Obscurus; 10 = Dorsal Nucleus of the Vagus Nerve; 11 = Nucleus Tractus Solitarius, commissural part; 12 = dorsal raphe, caudal part; 13 = Medial Parabrachial Nucleus; 14 = Lateral Parabrachial Nucleus, internal part; 15 = Lateral Parabrachial Nucleus, central part; 16 = Lateral Parabrachial Nucleus, external part; 17 = Kölliker Fuse Nucleus. Abbreviations: N7 = facial nucleus; N. Amb. C. = nucleus ambiguus compactus; LRt = lateral reticular nucleus; inf. olive = inferior olive; N12 = hypoglossal nucleus; cc = central canal; 4V = fourth ventricle; scp = superior cerebellar peduncle.

### 4.2.4 Protocol for fluorescence *in situ* hybridization with DAPI and Nissl counterstaining

The RNAscope® Fluorescent Multiplex assay (Advanced Cell Diagnostics Inc., Hayward, USA) protocol was performed as per manufacturer's instructions, with additional NISSL and Dapi counterstaining for anatomical reference. This section provides a description and justification of the steps taken throughout the two-day protocol. The protocol was performed in a designated RNAse free zone, and all solutions and materials used were rendered RNAse free.

Post fixation and dehydration of sections

Upon collection from storage at -80°C, slides with selected sections were rinsed in PBS and placed in cold 4% PFA in PBS solution for 30 minutes for post fixation. Slides were then rinsed again with PBS and sections were dehydrated through three consecutive 5-minute immersions in 50% EtOH, 75% EtOH, and 100% EtOH. This was followed by drying and baking the sections at 60°C for 30min. The baking step, along with subsequent warm (40°C) hybridization steps were performed with the use of a HybEZ hybridization oven (Advanced Cell Diagnostics Inc., Hayward, USA).

Permeabilization and target retrieval

Permeabilization of sections was performed by application of hydrogen peroxide (10 min at room temperature), and subsequently rinsed with distilled water ($dH_2O$). A second permeabilization procedure performed was heat induced target retrieval (HITR), which facilitates target access and increases detection sensitivity of subsequent RNA hybridization steps through reversal of cross linking caused by PFA fixation. For HITR, slides were submerged in RNAscope® target retrieval reagent (provided in the RNAscope® Fluorescent Multiplex assay kit) for 2 minutes at 98-102 °C, and subsequently rinsed with $dH_2O$ and dehydrated through submersion in 100% EtOH for 3 minutes.

Hybridization of z-probes to RNA

Preceding RNA hybridization, amplification, and fluorophore binding steps, a hydrophobic barrier (0.75" * 0.75") surrounding the section was drawn on each slide with a PAP hydrophobic barrier pen. To remove protein surrounding RNA strands, RNAscope®protease III solution (provided in the RNAscope® Fluorescent Multiplex assay kit) was applied to cover the section and allowed to incubate at 40°C for 15 minutes in a humified chamber, and subsequently removed and washed off with $dH_2O$. For multiplex RNA hybridization, a mix of ISH probes targeting 5-$HT_{1A}$ R RNA (Rn-Htr1a, Advanced Cell

Diagnostics product code: 404801), PPIB RNA (Rn-Ppib, Advanced Cell Diagnostics product code: 320891), and SLC32A1 RNA (Rn-Slc32a1, Advanced Cell Diagnostics product code: 424551-C3) was prepared as per manufacturer's instructions. 120µL Probe mix was pipetted on each section and allowed to incubate at 40°C for 2 hours in a humified chamber. After hybridization, sections were washed in wash buffer (provided in the RNAscope® Fluorescent Multiplex assay kit) and stored overnight at room temperature in 5x SSC (Sigma-Aldrich, Steinham, Germany) to resume with amplification and fluorophore binding steps the next day.

Hybridization and amplification

Hybridization of pre-amplifiers was performed with three distinct types of pre-amplifier, each type binding exclusively to one of the three RNA-binding probes. A solution containing a mix of all three pre-amplifiers (AMP1 solution, provided in the RNAscope® Fluorescent Multiplex assay kit) was applied on the sections and was left to incubate at 40°C for 30 minutes in a humified chamber. This was followed with application and incubation (30 minutes at 40°C in a humidified chamber) of a mix of 3 amplifiers (AMP2 solution, provided in the RNAscope® Fluorescent Multiplex assay kit), each binding exclusively to their cognate pre-amplifiers. Ultimately, a binding stabilizer (AMP3 Solution, provided in the RNAscope® Fluorescent Multiplex assay kit) for the newly formed probe-pre-amplifier-amplifier complexes was applied and incubated at 40°C for 15 min in a humidified chamber. Each of the three amplification steps (hybridization of pre-amplifiers, hybridization of amplifiers, and application of binding stabilizer) was preceded by washing with wash buffer.

Hybridization of fluorescent label probes to amplifiers

For Fluorescence signal development at hybridized target RNA's, the RNAscope® Fluorescent Multiplex assay utilizes Tyramide Signal Amplification Plus (TSA Plus®) fluorophores (Perkin Elmer, Waltham, USA). TSA Plus® utilizes fluorescently labelled tyramide that can be converted to highly reactive free radicals that form covalent bonds with tyrosine residues near a probe. This conversion is catalysed by horseradish peroxidase (HRP). The TSA free radicals have a very short half-life and will form dimers that are subsequently washed away if they do not encounter a tyrosine residue. RNAscope® Multiplex assay signal development is performed through sequential fluorescent labelling of each of the three distinct amplifiers. The exact labelling design is undisclosed, but it involves incubation on the section (15 min at 40°C in a humidified chamber) of a reagent solution (HRP_C1 solution) that likely contains HRP conjugated to

tyrosine rich probes which bind selectively to one of the three distinct amplifier types (HRP_C2 solution and HRP_C3 solution could be used to selectively target each of the remaining two amplifier types, all HRP solutions were provided in the RNAscope® Fluorescent Multiplex assay kit). Subsequent incubation (30 minutes at 40°C in a humidified chamber) of TSA fluorophores will result in HRP-mediated deposition of fluorescently labelled tyramide at the probes bound to the target amplifier. An HRP blocker (RNAscope® Multiplex FLv2 HRP blocker, provided in the RNAscope® Fluorescent Multiplex assay kit) was applied (15 minutes at 40°C in a humidified chamber) to quench remaining HRP activity after TSA fluorescent probe deposition. All incubations were preceded and followed by washing steps with wash buffer. This fluorescent labelling sequence was first performed to bind TSA Plus Fluorescein dye (1:750 in TSA buffer, 150µL) at amplifiers targeting 5-$HT_{1A}$ mRNA (using HRP_C1 solution), followed by TSA Plus Cyanine 3 dye (Cy3, 1:1500 in TSA buffer, 150µL) at amplifiers targeting PPIB mRNA (using HRP_C2 solution), and TSA Plus Cyanine 5 dye (Cy5 ,1:1500 in TSA buffer, 150µL) at amplifiers targeting SLC32A1 mRNA (using HRP_C3 solution).

Nissl and DAPI counterstaining

After completion of RNAscope® Multiplex assay signal development, sections were counterstained with fluorescent Nissl stain and DAPI. Sections were submerged in PBS with 0.1% Triton X-100 (10 min at room temperature), subsequently washed with PBS. Sections were covered with Neurotrace™ Blue Nissl stain (Invitrogen™, Carlsbad, U.S.A.) solution (1:50 dilution in PBS) which was left to incubate (20 minutes at room temperature), followed by a wash (10 min at room temperature) with PBS with 0.1% Triton X-100. After additional washing steps with PBS (2x 5 minutes, 1x 2 hours at room temperature), DAPI was applied to each section and left to incubate for 1 minute at room temperature. Sections were washed with PBS for a final time (2x 2 minutes), and coverslipped with Prolong Gold Antifade Mounting medium.

The concentrations of TSA Plus fluorescent dye solution, and optimization of Nissl and DAPI counterstaining were established through trial experiments with the use of a set of 3-plex positive control probes which target RNA of genes expressed in all rat cells to varying degrees (RNAscope® 3-plex Positive Control Probe- Rn, Advanced Cell Diagnostics, product code: 320891). These positive control probes target RNA Polymerase II Subunit A (Polr2a) RNA (high expression), PPIB RNA (moderate-high expression), and Ubiquitin C (UBC) RNA (moderate-low expression).

### *4.2.5 Confocal Imaging*

Confocal images of brainstem regions involved in respiratory control were obtained with a Leica SP5-Acousto Optical Beam Splitter confocal laser scanning microscope, and with the use of Leica Application Suite AF image acquisition software (Leica, Newcastle Upon Tyne, UK). The imaging setup was equipped with a 50 mW diode laser (405nm), a 100 mW Argon laser (used for 488nm light), a 10 mW yellow laser (561 nm), and a 10 mW Red He/Ne laser (633 nm). Of each brainstem area, z-stack images (z-axis range = 10µm, step-size = 2µm, 6 steps) of the fluorescein signal (FISH labelled $5HT_{1a}$ R RNA), the Cy3 signal (FISH labelled PPIB RNA), the Cy5 signal (FISH labelled SLC32A1 RNA), and the DAPI signal pooled with the Neurotrace Blue signal (Nissl bodies and DNA for anatomical reference) were sequentially obtained with a 40x oil immersion lens (Leica HCX PL APO 40x/1.25). For clarity in future reference, the fluorescein, Cy3, and Cy5 signals will be referred as the 5-$HT_{1A}$R-, PPIB-, and SLC32A1 signals, respectively. The signal for DAPI pooled with Neurotrace Blue will be referred to as the 'DAPI+Nissl' signal. Imaging resolution was 1046 x 1024 pixels, Airy Unit (A.U.) was set at 1, and images were obtained from a line average of 5 scans. Prior to obtaining each image, gain and laser power settings for each laser were optimized so that the pixel intensity extremes fitted just within the spectrum of image saturation according to the quick look up table (QLUT) image view. **Table 4-1** displays details of excitation and emission wavelengths applied during imaging. Images were exported as .TIFF files for post-hoc image analysis.

**Table 4-1:** Confocal imaging emission and excitation wavelengths.
The table lists the targets labelled with fluorophores, the peak emission ($\lambda_{em}$) and excitation ($\lambda_{ex}$) wavelengths of fluorophores, and the wavelength used to excite fluorophores during imaging, and the wavelength filter settings for capturing light emitted by fluorophores during imaging. The Neutotrace Blue and DAPI signals were pooled and obtained simultaneously, as they served the same purpose (anatomical reference).

| **target** | **fluorophore** | **fluorophore peak $\lambda_{ex}$** | **fluorophore peak $\lambda_{em}$** | **imaging $\lambda_{ex}$** | **imaging $\lambda_{filter}$** |
|---|---|---|---|---|---|
| $5HT_{1a}$ R RNA | Fluorescein | 494 | 521 | 488 | 498-535 |
| PPIB RNA | Cyanine 3 | 554 | 568 | 561 | 571-622 |
| SLC32A1 RNA | Cyanine 5 | 649 | 666 | 633 | 643-720 |
| Nissl bodies | Neurotrace Blue | 405 | 455 | 405 | 415-485 |
| DNA | DAPI | 358 | 461 | 405 | 415-485 |

### *4.2.6 Post-Hoc image processing and analysis*

Post-hoc image analysis was performed with Volocity 6.3 imaging analysis software (Perkin Elmer, Waltham, USA). For each image, z-stacks were merged with a brightest point merge. Contrast settings were optimized with an automated contrast enhancement function. An automated protocol was set up to find objects in the DAPI+Nissl signal that represented cell somata. To avoid the identification of cell nuclei (labelled with DAPI) as cell somata, the minimum object size was set at 25µm$^2$ and an object size guide parameter was set at 150µm$^2$. A medium filter was applied to remove noise from identified objects. Touching objects were separated and holes in objects were filled. Subsequently, regions of interest (ROI's) were defined from the objects found in the DAPI+Nissl signal. FISH labelled RNA molecules were visible in the images as high contrast puncta. A Volocity function designed for the detection of high contrast spots was utilized to identify these puncta in 5-HT$_{1A}$R-, PPIB-, and SLC32A1 signals separately. Ultimately, for each ROI (cell soma) in the image, the count of puncta (FISH labelled RNA) was calculated per signal (5-HT$_{1A}$R, PPIB, SLC32A1). To avoid experimenter bias, determining ROI's and counting puncta per signal per ROI was done through an automated procedure and was applied with identical parameter settings to all images. For clarity, an ROI derived from the DAPI+Nissl signal will henceforth be referred to as a 'cell', and the puncta count of an ROI will henceforth be referred to as its 'transcript count'.

Cells were assigned to phenotypes and expression level categories based on their transcript count observed in each imaging signal (5-HT$_{1A}$R, PPIB, and SLC32A1). The expression level categories are: 0; 1 to 40 in bins of 2; and >40 transcripts per cell. Any cell with >0 transcripts observed in the 5-HT$_{1A}$R, PPIB, or SLC32A1 signal was classified as 5-HT$_{1A}$R-, PPIB-, or SLC32A1-positive, respectively. Additionally, the population of cells that is 5-HT$_{1A}$R positive (>0 transcripts per cell observed in the 5-HT$_{1A}$R signal), is broken down into a subpopulation of cells that co-express 5HT$_{1A}$R and SLC32A1 transcripts (5HT1aR$^+$SLC32A1$^+$) and a subpopulation of cells that are 5HT$_{1A}$R positive and SLC32A1 negative (5HT1AR$^+$SLC32A1$^-$). Similarly, the population of cells that is SLC32A1 positive (>0 transcripts per cell observed in the SLC32A1 signal), is subdivided into a SLC32A1 and 5-HT$_{1A}$R transcript co-expressing subpopulation (SLC32A1$^+$5HT1aR$^+$) and a subpopulation of cells that are SLC32A1 positive and 5-HT$_{1A}$R negative (SLC32A1$^+$5HT1AR$^-$). Note that 5HT1aR$^+$SLC32A1$^+$ and SLC32A1$^+$5HT1aR$^+$ describe the same population of 5-HT1AR and SLC32A1 co-expressing cells. The difference between these two definitions is that in the former group, each co-expressing cell is assigned to an expression level category based

on its 5HT1AR transcript count, whereas in the latter group each co-expressing cell is assigned to an expression level category based on its SLC32A1 transcript count. This allows for evaluation of the distribution of cells in the co-expressing population over various 5-$HT_{1A}$R expression levels, as well as over SLC32A1 expression levels.

For each image of each brainstem region, the relative amount of PPIB-positive, 5-$HT_{1A}$R positive (including subpopulations $5HT1aR^{+}SLC32A1^{+}$ and $5HT1aR^{+}SLC32A1^{-}$), and SLC32A1-positive (including subpopulations $SLC32A1^{+}5HT1AR^{+}$ and $SLC32A1^{+}5HT1AR^{-}$) cells per expression level category (1 to 40 in bins of 2; and >40 transcripts per cell) was expressed as the percentage of all cells in the image. Cumulative percentages in order of ascending expression level category (with exclusion of cells with zero transcripts) were also calculated for each phenotype. For brainstem regions imaged from lateral medulla sections (listed in **figure 4.2A**), the frequency (%) and cumulative frequency (%) values per expression level category were obtained from 4 images of sections from 4 different rats. The same applies for images of the dorsal raphe obtained from pontine sections (see **figure 4.2C**). For brainstem regions imaged on medial medulla sections (listed in **figure 4.2B**), the frequency (%) and cumulative frequency (%) values per expression level category were obtained from 3 images of sections from 3 different rats. Brain regions of the parabrachial complex in pontine sections from 4 different rats were imaged bilaterally, resulting in 8 images for each region (See **figure 4.2C**). For every brainstem region, averages and standard deviations were calculated of the frequency (%) and cumulative frequency (%) of cells assigned to each expression level category (1 to 40 in bins of 2; and >40 transcripts per cell) per phenotype ($PPIB^{+}$, 5-$HT1A^{+}$, $5HT1aR^{+}SLC32A1^{+}$ $5HT1aR^{+}SLC32A^{-}$, $PPIB^{+}$, $SLC32A1^{+}$, $SLC32A1^{+}5HT1aR^{+}$, and $SLC32A1^{+}5HT1AR^{-}$). For each brain region, figures plotted expression level categories against the average frequencies (%) and average cumulative frequencies (%) of cells of a certain phenotype assigned to each expression level category. These figures give an indication of the prevalence of various phenotypes in each brain region (i.e., the cumulative frequency of a phenotype at >40 transcripts per cell), but also of the distribution of cells with a certain RNA phenotype over various RNA expression levels within that region. Plots were made with GraphPad Prism (GraphPad Software Inc., La Jolla, USA).

## 4.3 CHAPTER RESULTS

By multiplex FISH, and subsequent automated quantification of hybridized transcripts per cell, I determined the distribution of 5-$HT_{1A}$ receptor RNA (5HT1AR), vesicular inhibitory amino acid transporter RNA (SLC32A1), and housekeeping gene Cyclophylin B RNA (PPIB) transcripts in a series of brainstem nuclei involved in respiratory control. The brainstem regions in which FISH and quantification was performed are listed on annotated sections of the pons and medulla in (see section 4.2.3, **figure 4.2)**. **Figures 4-3 to 4-20** display representative images and plots that illustrate the average frequency (%) of cells categorised by their quantity of PPIB, 5HT1AR, and SLC32A1 transcripts in each of the brainstem regions. The make-up of figures 4-3 to 4-20 is identical, and to reduce repetition, it is described in a general legend in **textbox 1**. A summary of FISH quantification results is provided in **table 4-2**.

**Textbox 1**: general legend for figures 4-3 to 4-20.

**Figures 4-3 to 4-20** show representative images and plots that illustrate fluorescence *in situ* hybridization (FISH) data, each figure describes a different brain region. RNA Transcripts labelled with FISH are 5-HT1a receptor RNA (5HT1AR), vesicular inhibitory amino acid transporter RNA (SLC32A1), and Cyclophilin B (PPIB) RNA. PPIB is a housekeeping gene and serves as a positive control. A combination of DAPI and Nissl counterstain (DAPI+Nissl) is used to determine cell outlines through automated analysis. **($A_1$)** Shows a representative image of the relevant brain region with 5HT1AR, SLC32A1, PPIB, and DAPI+Nissl labelling. Individual FISH labelled transcripts show as punctate dots. White arrows, if present, mark examples of cells that contain both 5HT1AR and SLC32A1 RNA transcripts. **($A_2$)** Shows the same image with only 5HT1AR labelling in view. Dotted white lines mark the cell outlines derived from the DAPI+Nissl signal. **($A_3$)** Is similar to $A_2$ but shows SLC32A1 labelling and cell outlines. **(B)** Within each cell outline, hybridized transcripts are counted, and for each transcript type (PPIB, 5HT1AR, SLC32A1) cells are assigned to categories based on their transcript count (categories are: 0; 1 to 40 in bins of 2; and >40 transcripts/cell). In figure **($B_1$)**, the various transcript count categories (excluding the category of cells with zero transcripts) are plotted against the cumulative frequency (% of all analysed cells in image) of cells that fit each category. **Figure $B_2$** is as figure $B_1$ but plots the transcript count categories against the (non-cumulative) frequency (%) of cells that fit these categories. Combined, the plots **$B_1$** and **$B_2$** give an indication of the prevalence of 5HT1AR, SLC32A1, or PPIB RNA transcript expressing cells (i.e. the cumulative frequency at >40 transcripts per cell, annotated to the right of each curve), but also of the distribution of transcript expressing cells over various expression levels (i.e. the frequency at any given transcript count category). **Figure (C)** shows the cumulative frequencies (%) **($C_1$)**, and frequencies (%) (**$C_2$**) of cells that fit the various transcript count categories for PPIB and 5HT1AR, and for subpopulations of 5HT1AR positive cells that do ($5HT1AR^+SLC32A1^+$) or do not ($5HT1aR^+SLC32A1^-$) co-express SLC32A1. **Figure D** shows the cumulative frequencies (%) (**$D_1$**) and frequencies (%) (**$D_2$**) of cells that fit the various transcript count categories for PPIB and SLC32A1, and for subpopulations of SLC32A1 positive cells that do ($SLC32A1^+5HT1AR^+$) or do not ($SLC32A1^+5HT1AR^-$) co-express 5HT1AR. Note that, although the $5HT1AR^+SLC32A1^+$ population in figures $C_{1,2}$ and the $SLC32A1^+5HT1AR^+$ population in figures $D_{1,2}$ are in effect the same population of cells, $C_{1,2}$ and $D_{1,2}$ differ in the way in which the cells of that population are distributed over various transcript-count categories. In $C_{1,2}$, 5HT1AR+SLC32A1+ cells are assigned to transcript count categories by their 5HT1AR count. In $D_{1,2}$, $SLC32A1^+5HT1AR^+$ cells are assigned to transcript count categories by their SLC32A1 count. Plotted values are averages of 4 images from 4 rats, unless stated otherwise in the individual figure legends. Error bars are SD.

### *4.3.1 Distribution of 5-HT$_{1A}$ receptor RNA and vesicular inhibitory amino acid transporter RNA in the ventral respiratory column: BötC, pre-BötC, and RVRG.*

**Figures 4-3, 4-4 and 4-5** describe the frequency and distribution of cells with PPIB, 5HT1AR, and SLC32A1 transcripts in the BötC, pre- BötC, and RVRG, respectively. All values described in these figures are averages derived from 3 images from 3 rats for each region.

In the BötC images, the average cumulative frequency of cells in which any transcripts are observed is 98.9% for PPIB transcripts, 42.6% for 5HT1AR transcripts, and 37% for SLC32A1 transcripts (**figure 4-3B$_1$**). **Figure 4-3B$_2$** shows that the 5HT1AR or SLC32A1 transcripts presented mostly with lower transcript counts relative to the transcript counts for PPIB RNA. **Figure 4-3C$_1$** breaks down the population of 5HT1AR cells into 5HT1AR expressing cells that do (5HT1AR$^+$SLC32A1$^+$) or do not (5HT1AR$^+$SLC32A1$^-$) co-express SLC32A1. On average, 26.2% of the analysed cells in the BötC were 5HT1AR$^+$SLC32A1$^+$, whereas 16.3% were 5HT1AR$^+$SLC32A1$^-$. **Figure 4-3D$_2$** shows that 10.7% of all cells in the BötC samples were SLC32A1$^+$5HT1AR$^-$. This means that 61.5% of 5HT1AR positive cells co-expressed SLC32A1, and 70.8% of SLC32A1 positive cells co-expressed 5HT1AR. The average number of cells analysed in the BötC was 243.3 ± 11.6.

In the pre-BötC images, the average cumulative frequency of cells in which any count of transcripts was observed is 98.7% for PPIB transcripts, 46.6% for 5HT1AR transcripts, and 46.4% for SLC32A1 transcripts (**figure 4-4B$_1$**). On average, 32.7% of the analysed cells in the pre-BötC images were 5HT1AR$^+$SLC32A1$^+$, whereas 13.9% of the total amount of cells in the pre-BötC images were 5HT1AR$^+$SLC32A1$^-$ **(figure 4-4C$_1$)**. 13.7% of analysed cells in the pre-BötC were SLC32A1$^+$5HT1AR$^-$ **(figure 4-4D$_1$)**. As such, in the pre-BötC, 70.2% of 5HT1AR positive cells co-expressed SLC32A1, and 70.5% of SLC32A1 positive cells co-expressed 5HT1AR. The average total cell count in the pre-BötC images used for these plots was 252.7± 8.1.

In the RVRG **(figure 4-5)**, the average cumulative frequency of cells in which transcripts are observed is 99.1% for PPIB transcripts, 34.9% for 5HT1AR transcripts, and 31.8% for SLC32A1 transcripts (**figure 4-5B$_1$**). On average, 19.4% of analysed cells in the RVRG were 5HT1AR$^+$SLC32A1$^+$, and 15.5% of analysed cells in the pre-RVRG were 5HT1AR$^+$SLC32A1$^-$ **(figure 4-5C$_1$)**. 12.5% of analysed cells in the RVRG samples were SLC32A1$^+$5HT1AR$^-$ **(figure 4-5D$_1$)**. Of all 5HT1AR positive cells in the RVRG, 55.6% co-expressed SLC32A1, and

61% of SLC32A1 positive cells co-expressed 5HT1AR. The average analysed cell count in the RVRG images used for these plots was 231.7 ± 16.1.

Comparison of BötC, pre- BötC, and RVRG averages shows that cells that express 5HT1AR, SLC32A1, or both are present in all three regions. The frequency of cells with 5HT1AR transcripts was highest in the pre- BötC images (pre-BötC 46.6%; BötC 42.6%; RVRG 34.9%). The same is true for the frequency of cells with SLC32A1 transcripts (pre-BötC 46.4%; BötC 37%; RVRG 31.8%), and for cells with both 5HT1AR and SLC32A1 transcripts (pre- BötC 32.7%; BötC 26.2%; RVRG 19.4%). These findings are consistent with the notion that observed functional effects of systemic NLX-101 on respiratory rhythm and pattern may be mediated by modulation of activity of inspiratory and/or expiratory rhythmogenic populations in the BotC and pre-BotC, and of respiratory neurones in VRC transmission circuits.

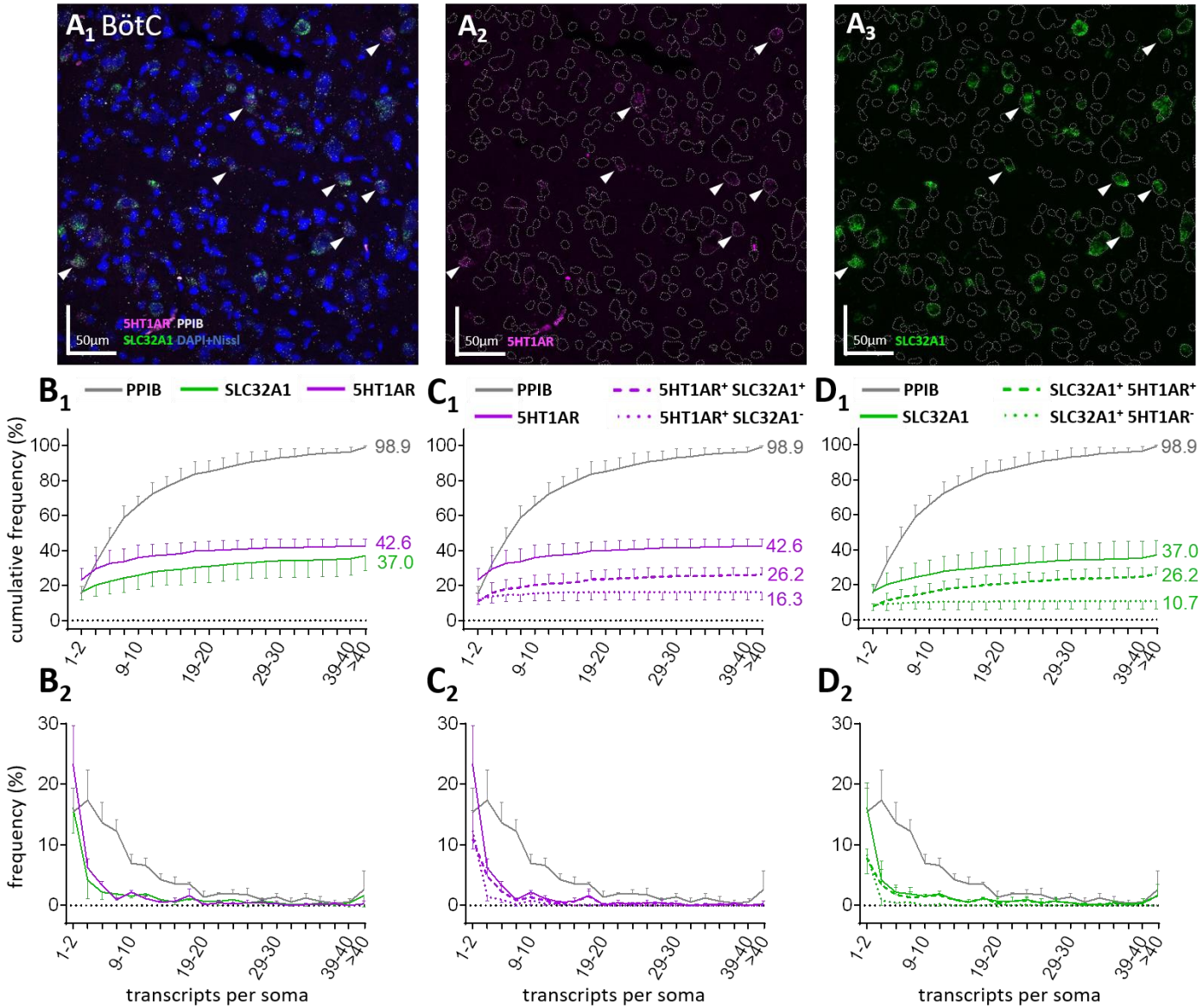


**Figure 4-3:** Fluorescence *in situ* hybridization (FISH) of 5-HT1a receptor RNA (5HT1AR), vesicular inhibitory amino acid transporter RNA (SLC32A1), and cyclophilin B RNA (PPIB) in the Bötzinger Complex (BötC).

($A_{1,2,3}$) Representative image of the BötC region. Individual FISH labelled transcripts show as punctate dots, a combination of DAPI and Nissl counterstain (DAPI+Nissl) was used to determine cell outlines (dotted lines). White arrows mark examples of $5HT1AR^{+}SLC32A1^{+}$ cells. ($B_{1,2}$ $C_{1,2}$ $D_{1,2}$) Cells that expressed PPIB, 5HT1AR, and/or SLC32A1 were categorized by their transcript count. Plots show the frequencies (%), and cumulative frequencies (%) of cells assigned to each transcript count category. Cells with 0 transcripts are excluded from plots. All values are averages of 3 images from 3 rats. Error bars are SD. See textbox 1 for a detailed description of figures.

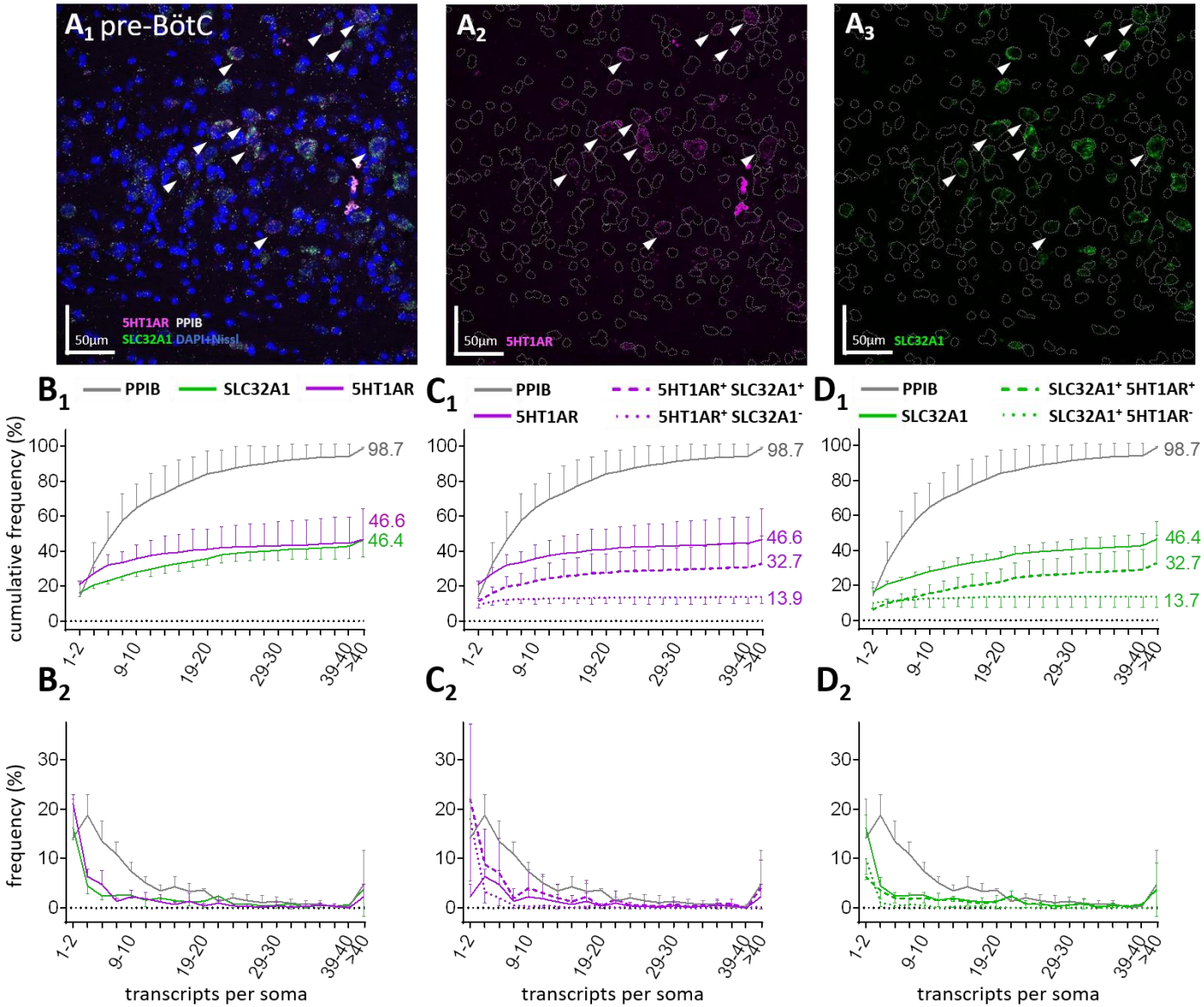


**Figure 4-4:** Fluorescence in situ hybridization (FISH) of 5-HT1a receptor RNA (5HT1AR), vesicular inhibitory amino acid transporter RNA (SLC32A1), and cyclophilin B RNA (PPIB) in the pre-Bötzinger Complex (pre-BötC).

($A_{1,2,3}$) Representative image of the pre-BötC region. Individual FISH labelled transcripts show as punctate dots, a combination of DAPI and Nissl counterstain (DAPI+Nissl) was used to determine cell outlines (dotted lines). White arrows mark examples of 5HT1AR+SLC32A1+ cells. ($B_{1,2}$ $C_{1,2}$ $D_{1,2}$) Cells that express PPIB, 5HT1AR, and/or SLC32A1 are categorized by their transcript count. Plots show the frequencies (%), and cumulative frequencies (%) of cells assigned to each transcript count category. Cells with 0 transcripts are excluded from plots. All values are averages of 3 images from 3 rats. Error bars are SD. See textbox 1 for a detailed description of figures.

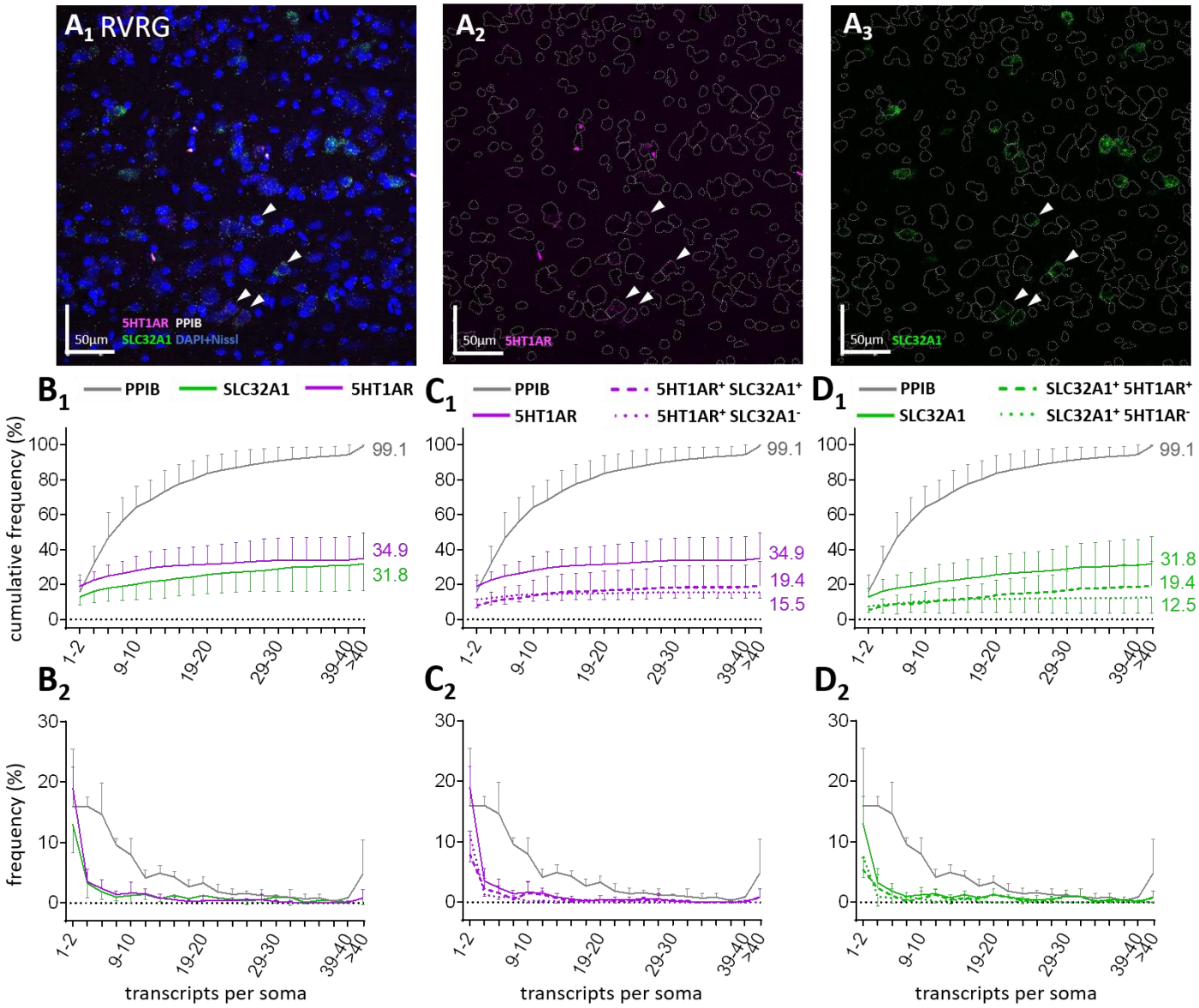


**Figure 4-5:** Fluorescence in situ hybridization (FISH) of 5-HT1a receptor RNA (5HT1AR), vesicular inhibitory amino acid transporter RNA (SLC32A1), and cyclophilin B RNA (PPIB) in the Rostroventral Respiratory Group (RVRG).

($A_{1,2,3}$) Representative image of the RVRG region. Individual FISH labelled transcripts show as punctate dots, a combination of DAPI and Nissl counterstain (DAPI+Nissl) was used to determine cell outlines (dotted lines). White arrows mark examples of 5HT1AR+SLC32A1+ cells. ($B_{1,2}$ $C_{1,2}$ $D_{1,2}$) Cells that express PPIB, 5HT1AR, and/or SLC32A1 are categorized by their transcript count. Plots show the frequencies (%), and cumulative frequencies (%) of cells assigned to each transcript count category. Cells with 0 transcripts are excluded from plots. All values are averages of 3 images from 3 rats. Error bars are SD. See textbox 1 for a detailed description of figures.

### *4.3.2 Distribution of 5-HT$_{1A}$ receptor RNA and vesicular inhibitory amino acid transporter RNA in respiratory motor and pre-motor nuclei: Nucleus Ambiguus Compactus, N10, N12, and XII premotor neurones.*

Figures 4-6, 4-7, 4-8, and 4-9 describe the frequency and distribution of cells with PPIB, 5HT1AR, and SLC32A1 transcripts in the Nucleus Ambiguus Compactus (N. Amb. C.), the Dorsal Nucleus of the Vagus Nerve (N10), the Hypoglossal Nucleus (N12), and a region with Hypoglossal premotor neurones (XII premotor), respectively. All values in plots describing N. Amb. C. (**figure 4-6**), N10 (**figure 4-7**), and XII premotor neurones (**figure 4-9**) are averages derived from 3 images from 3 rats. Values in plots describing N12 (**figure 4-8**) are averages derived from 4 images from 4 rats.

In the N. Amb. C., the average cumulative frequency of cells in which any transcripts were present is 98.5% for PPIB transcripts, 38.3% for 5HT1AR transcripts, and 38.4% for SLC32A1 transcripts (**figure 4-6B$_1$**). 20% Of the total amount of analysed cells in the N. Amb. C. images were 5HT1AR$^+$SLC32A1$^+$ (**figure 4-6C$_1$)**. This means that for both the population of cells with 5HT1AR transcripts and the population with SLC32A1 transcripts, approximately half of the cells were co-expressing. 18.3% Of the analysed cells in the N. Amb. C. were 5HT1AR$^+$SLC32A1$^-$ (**figure 4-6C$_1$)**. **Figure 4-6D$_1$** shows that 18.4% of all cells in the N. Amb. C. region were SLC32A1$^+$5HT1AR$^-$ The average total cell count in the N. Amb. C. images used for these plots was 115.7 ±11.9.

In the N10 images, the average ultimate cumulative frequency of cells in which any count of transcripts was observed is 98.7% for PPIB transcripts, 29.6% for 5HT1AR transcripts, and 47.2% for SLC32A1 transcripts (**figure 4-7B$_1$**). On average, 21.7% of the analysed cells in the N10 region were 5HT1AR$^+$SLC32A1$^+$. Relatively few cells in the N10, 7.9% of the analysed cells in the region, were 5HT1AR$^+$SLC32A1$^-$ **(figure 4-7C$_1$).** 25.5% Of analysed cells in the N10 region were SLC32A1$^+$5HT1AR$^-$ **(figure 4-7D$_1$)**. From the above it follows that, in the N10, 46% of 5HT1AR positive cells co-expressed SLC32A1, and 73.3% of SLC32A1 positive cells co-expressed 5HT1AR. The average total cell count in the N10 images used for these plots was 97 ±46.8.

In the N12 region **(figure 4-8)**, the average cumulative frequency of cells in which transcripts were observed is 99.2% for PPIB transcripts, 30.3% for 5HT1AR transcripts, and 15.8% for SLC32A1 transcripts (**figure 4-8B$_1$**). **Figure 4-8B$_2$** shows that the 5HT1AR or SLC32A1 transcripts were present mostly in cells with low transcript counts. A relatively low amount (8.9%) of analysed cells in the N12 region was 5HT1AR$^+$SLC32A1$^+$, the

remainder of the 5HTAR1 positive population ($5HT1AR^{+}SLC32A1^{-}$ cells) was 21.3% of analysed cells in the N12 images **(figure 4-8$C_1$)**. This means that, in the N12, the population of $5HT1AR^{+}SLC32A1^{+}$ cells comprised of 29.4% of all $5HT1AR^{+}$ cells, and of 56.3% all $SLC32A1^{+}$ cells. 12.5% Of analysed cells in the N12 images were $SLC32A1^{+}$ $5HT1AR^{-}$ **(figure 4-8$D_1$)**. The average total cell count in the RVRG images used for these plots was 200.8 ±41.

In the region with XII premotor neurones, the average ultimate cumulative frequency of cells in which any transcripts were observed is 97.6% for PPIB transcripts, 50.8% for 5HT1AR transcripts, and 55.3% for SLC32A1 transcripts (**figure 4-9$B_{1,2}$**). On average, 35.4% of all analysed cells in the XII premotor images were $5HT1AR^{+}SLC32A1^{+}$, whereas 15.4% of analysed cells in the images was $5HT1AR^{+}SLC32A1^{-}$ (**figure 4-9$C_{1,2}$**). It follows that 69.7% of 5HT1AR positive cells co-express SLC32A1, and 64% of SLC32A1 positive cells co-express 5HT1AR. **Figure 4-9$D_{1,2}$** shows that 19.9% of analysed cells in the XII premotor images were $SLC32A1^{+}5HT1AR^{-}$. The average total cell count in the images used for these plots was 249.3 ±3.1.

When reviewing the analysed respiratory (pre)motor regions together, it is noteworthy that the frequency of cells with 5HT1AR transcripts in the XII premotor region (50.8%) exceeded that in the other (pre)motor nuclei analysed (N. Amb. C. 38.3%, N10 29.6%, and N12 30.3%). The N10 and XII premotor region images showed high frequencies of cells with SLC32A1 transcripts as well (47.2% and 55.3%, respectively). This indicates that some level of local disinhibition may play a role in observed 5-$HT_{1A}$R agonist functional effects on respiratory pattern. Finally, in both N10 and N12, populations with 5HT1AR transcripts consisted largely of cells with a low transcript count. That is, 92% (in N10) 91% (in N12) of $5HT1AR^{+}$ cells had 6 or fewer 5HT1AR transcripts.

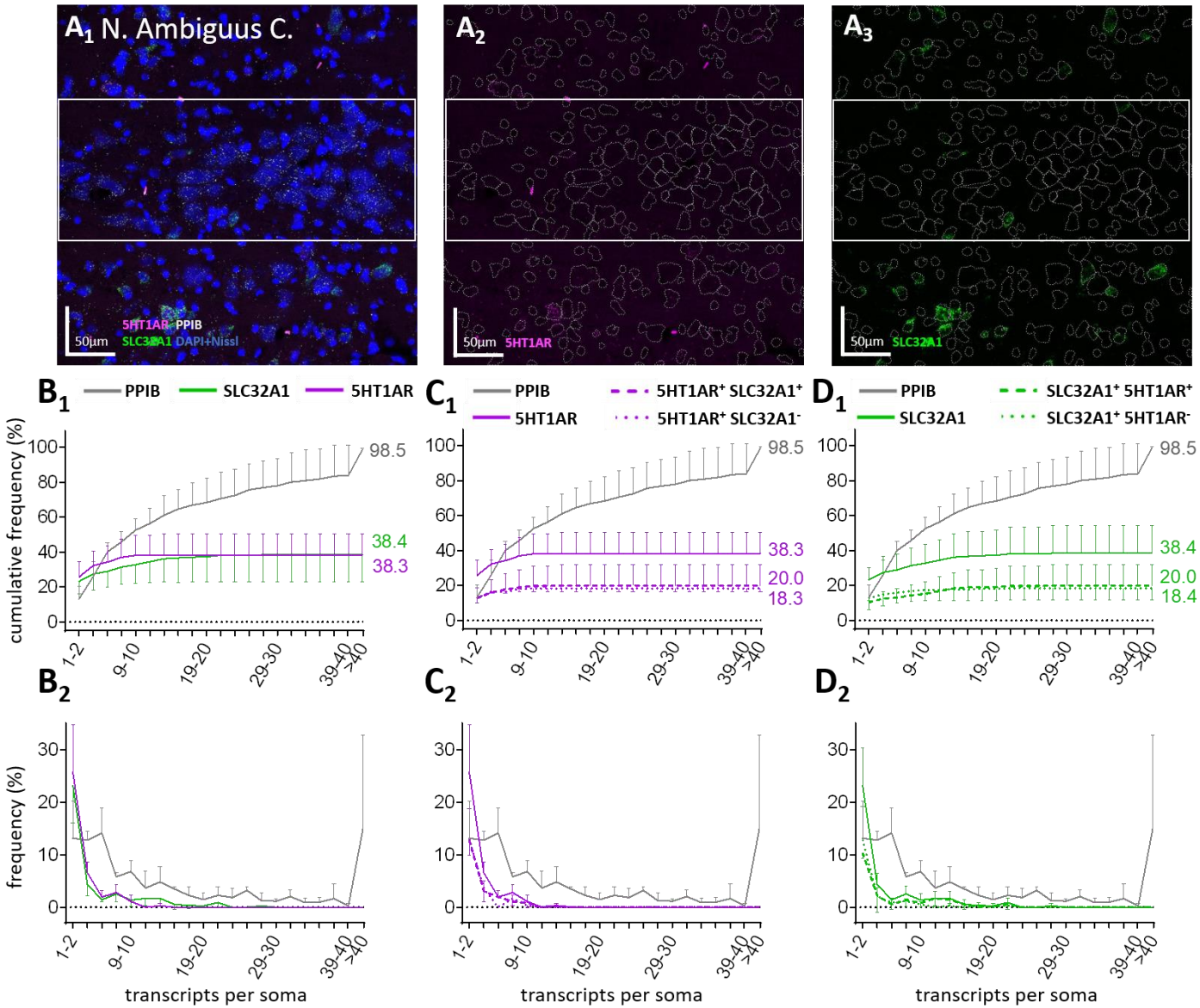


**Figure 4-6:** Fluorescence in situ hybridization (FISH) of 5-HT1a receptor RNA (5HT1AR), vesicular inhibitory amino acid transporter RNA (SLC32A1), and cyclophilin B RNA (PPIB) in the Nucleus Ambiguus Compactus (N. Amb. C.).

($A_{1,2,3}$) Representative image of the N. Amb. C. region. Individual FISH labelled transcripts show as punctate dots, a combination of DAPI and Nissl counterstain (DAPI+Nissl) was used to determine cell outlines (dotted lines). ISH data analysis was restricted to cells within the white box. ($B_{1,2}$ $C_{1,2}$ $D_{1,2}$) Cells that express PPIB, 5HT1AR, and/or SLC32A1 are categorized by their transcript count. Plots show the frequencies (%), and cumulative frequencies (%) of cells assigned to each transcript count category. Cells with 0 transcripts are excluded from plots. All values are averages of 3 images from 3 rats. Error bars are SD. See textbox 1 for a detailed description of figures.

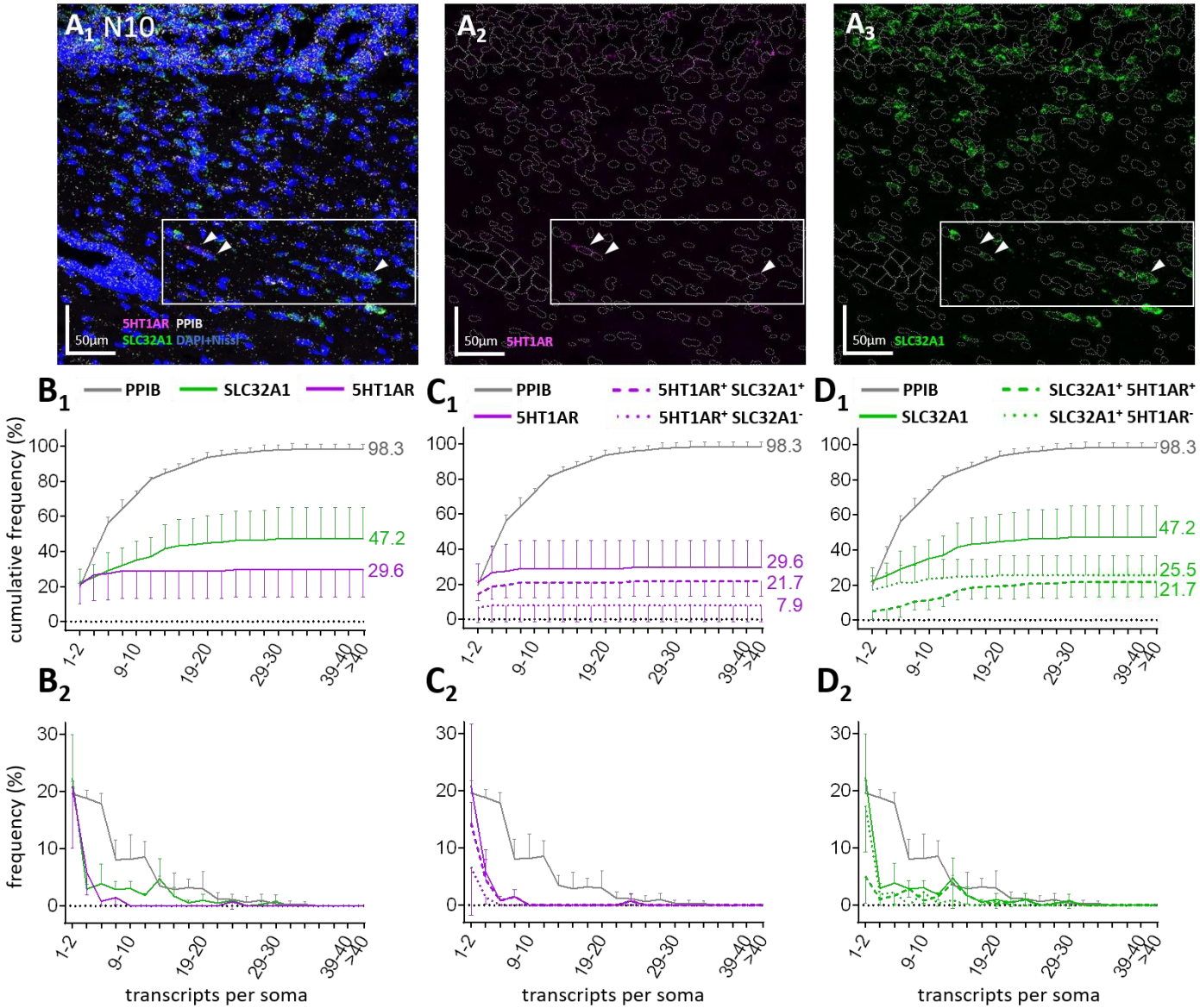


**Figure 4-7:**Fluorescence in situ hybridization (FISH) of 5-HT1a receptor RNA (5HT1AR), vesicular inhibitory amino acid transporter RNA (SLC32A1), and cyclophilin B RNA (PPIB) in the Dorsal Nucleus of the Vagus Nerve (N10).

($A_{1,2,3}$) Representative image of the N10 region. Individual FISH labelled transcripts show as punctate dots, a combination of DAPI and Nissl counterstain (DAPI+Nissl) was used to determine cell outlines (dotted lines). ISH data analysis was restricted to cells within the white box. White arrows mark examples of 5HT1AR+SLC32A1+ cells. ($B_{1,2}$ $C_{1,2}$ $D_{1,2}$) Cells that express PPIB, 5HT1AR, and/or SLC32A1 are categorized by their transcript count. Plots show the frequencies (%), and cumulative frequencies (%) of cells assigned to each transcript count category. Cells with 0 transcripts are excluded from plots. All values are averages of 3 images from 3 rats. Error bars are SD. See textbox 1 for a more detailed figure legend.

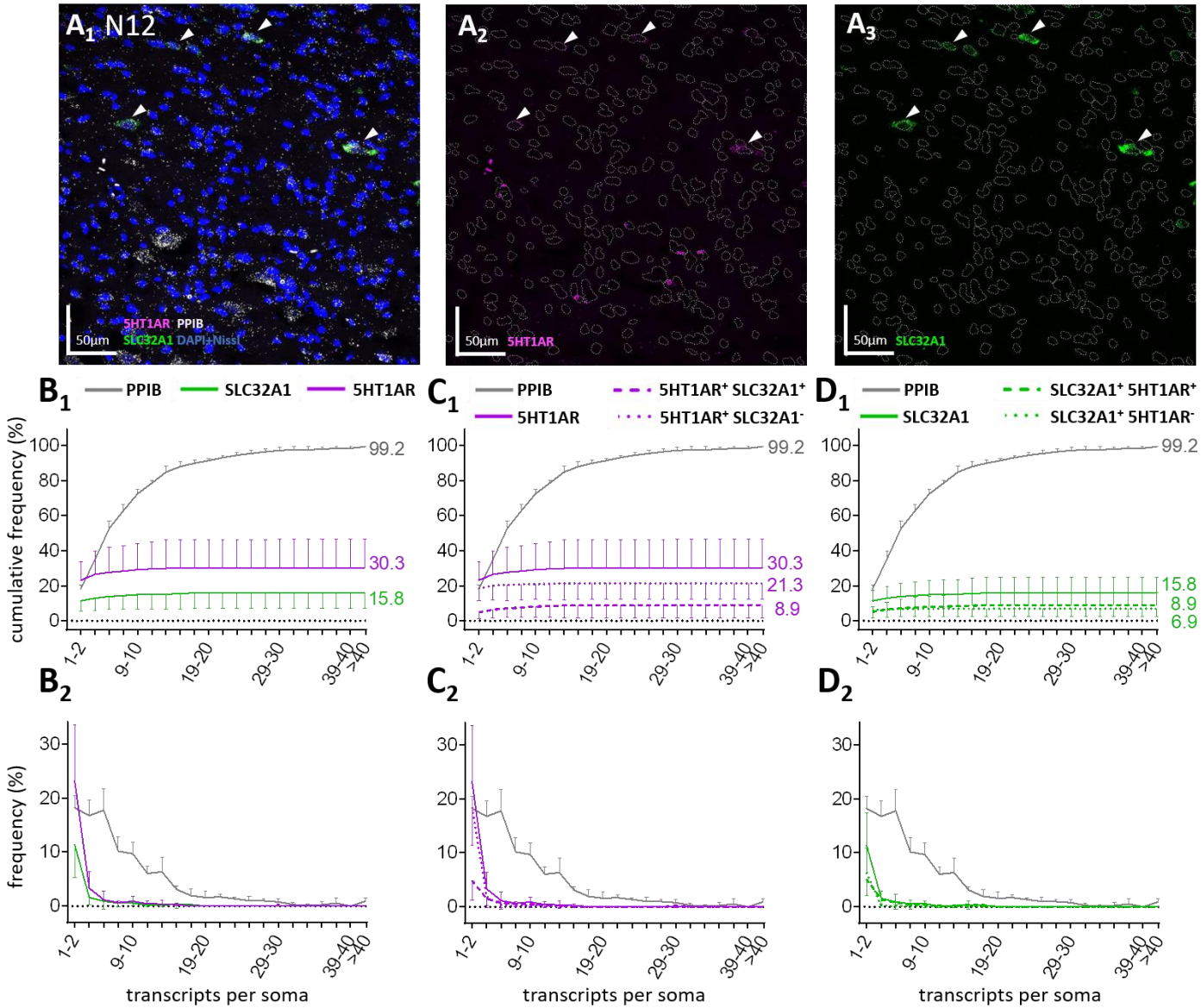


**Figure 4-8:** Fluorescence in situ hybridization (FISH) of 5-HT1a receptor RNA (5HT1AR), vesicular inhibitory amino acid transporter RNA (SLC32A1), and cyclophilin B RNA (PPIB) in the Hypoglossal Nucleus (N12).

($A_{1,2,3}$) Representative image of the N12 region. Individual FISH labelled transcripts show as punctate dots, a combination of DAPI and Nissl counterstain (DAPI+Nissl) was used to determine cell outlines (dotted lines). White arrows mark examples of 5HT1AR+SLC32A1+ cells. ($B_{1,2}$ $C_{1,2}$ $D_{1,2}$) Cells that express PPIB, 5HT1AR, and/or SLC32A1 are categorized by their transcript count. Plots show the frequencies (%), and cumulative frequencies (%) of cells assigned to each transcript count category. Cells with 0 transcripts are excluded from plots. All values are averages of 4 images from 4 rats. Error bars are SD. See textbox 1 for a detailed description of figures.

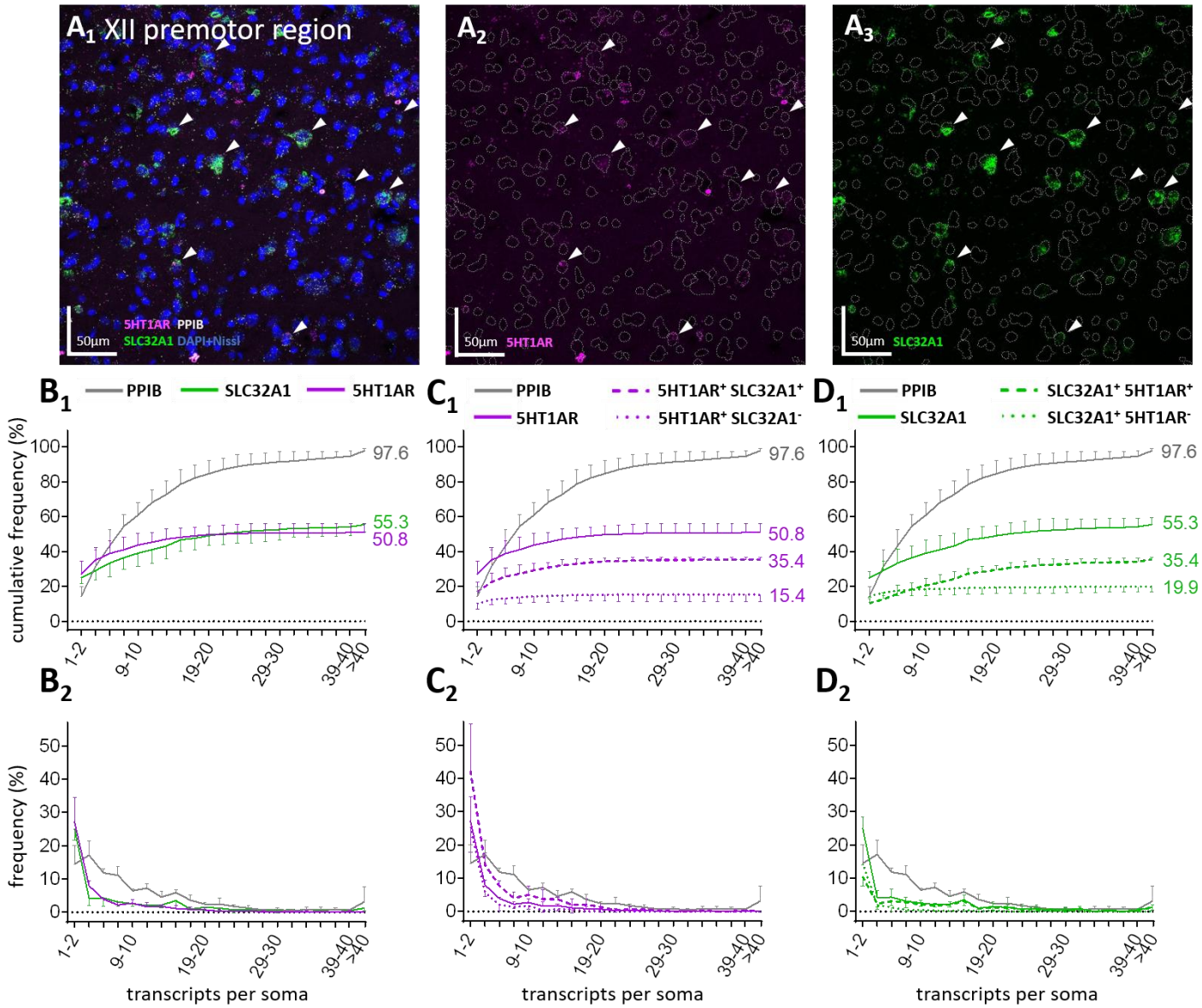


**Figure 4-9:** Fluorescence in situ hybridization (FISH) of 5-HT1a receptor RNA (5HT1AR), vesicular inhibitory amino acid transporter RNA (SLC32A1), and cyclophilin B RNA (PPIB) in XII premotor neurones (XII premotor).

($A_{1,2,3}$) Representative image of the XII premotor region. Individual FISH labelled transcripts show as punctate dots, a combination of DAPI and Nissl counterstain (DAPI+Nissl) was used to determine cell outlines (dotted lines). White arrows mark examples of 5HT1AR+SLC32A1+ cells. ($B_{1,2}$ $C_{1,2}$ $D_{1,2}$) Cells that express PPIB, 5HT1AR, and/or SLC32A1 are categorized by their transcript count. Plots show the frequencies (%), and cumulative frequencies (%) of cells assigned to each transcript count category. Cells with 0 transcripts are excluded from plots. All values are averages of 3 images from 3 rats. Error bars are SD. See textbox 1 for a detailed description of figures.

### *4.3.3 Distribution of 5-HT$_{1A}$ receptor RNA and vesicular inhibitory amino acid transporter RNA in the parabrachial complex.*

The present section describes the frequency and distribution of cells with PPIB, 5HT1AR, and SLC32A1 transcripts in the Kölliker Fuse (KF) (**figure 4-10)**, Medial Parabrachial (MBP) region (**figure 4-11)**, the internal part of the Lateral Parabrachial (LPBI) region (**figure 4-12**), the central part of the Lateral Parabrachial region (LPBC) (**figure 4-13)**, and the external part of the Later Parabrachial region (LPBE) (**figure 4-14**). All values described in figures 4-10 to 4-14 are averages derived from 8 images from 4 rats for each region (regions are imaged bilaterally).

In the KF, the average ultimate cumulative frequency of cells in which any transcripts are present was 99.3% for PPIB transcripts, 43.1% for 5HT1AR transcripts, and 13.8% for SLC32A1 transcripts (**figure 4-10B$_1$**). The average frequency of SLC32A1$^+$5HT1AR$^+$ cells was 7.4% of all analysed cells in images of this region (**figure 4-10C$_1$/D$_1$)**. From these percentages, it follows that these co-expressing cells constitute 17.2% of 5-HT1AR$^+$ cells, and 53.6% of SLC32A1$^+$ cells. (**figure 4-10C$_1$)**. 35.7% Of all analysed cells in the KF was 5HT1AR$^+$SLC32A1$^-$ (**figure 4-10C$_1$)**, and 6.4% of all cells were SLC32A1$^+$5HT1AR$^-$ **(figure 4-10D$_1$)**. The average total cell count in the KF images used for these plots is 266.4 ± 15.6.

In images of the MPB, 48.9% of analysed cells were 5HT1AR positive, 23.3% of cells were SLC32A1 positive, and 98.9% of cells in the MPB images contained transcripts of PPIB (**figure 4-11B$_1$**). On average, 14.2% of the total amount of analysed cells in the MPB was 5HT1AR$^+$SLC32A1$^+$, whereas 34.7% of analysed cells was 5HT1AR$^+$SLC32A1$^-$ **(figure 4-11C$_1$). 9.2**% Of analysed MPB cells were SLC32A1$^+$ 5HT1AR $^-$ **(figure 4-11D$_1$)**. This means that 29% of 5HT1AR positive cells in the MPB also contained SLC32A1, and 60.9% of SLC32A1 positive cells also had 5HT1AR transcripts. The average total cell count in the MPB images used for these plots was 259.5 ± 18.9.

In the LPBI region, the average cumulative frequency of cells in which transcripts were observed is 99.1% for PPIB transcripts, 36.6% for 5HT1AR transcripts, and 22.6% for SLC32A1 transcripts (**figure 4-12B$_1$**). 12.6% Of cells in the LPBI images was 5HT1AR$^+$SLC32A1$^+$, and the remainder of the 5HTAR1 positive population (5HT1AR$^+$SLC32A1$^-$ cells) comprised 21.3% of all cells analysed **(figure 4-12C$_1$)**. Thus, in the LPBI, the population of cells that co-expressed 5HT1AR and SLC32A1 RNA comprised 34.4% of all 5HT1AR positive cells, and 55.8% of all SLC32A1 positive cells. 12.6% Of all

cells in the LPBI images were SLC32A1$^{+}$5HT1AR$^{-}$ **(figure 4-12D$_1$)**. The average total cell count in the images used for these plots is 270.9 ± 25.4.

In the LPBC, cells with PPIB transcripts comprised 99.2% of all cells, 5HT1AR positive cells comprised 41.6% of all cells, and cells with SLC32A1 transcripts comprised 20.5% of all analyzed cells in the images (**figure 4-13B$_1$**). On average, 11.8% of analyzed cells in the LPBC images were 5HT1AR$^{+}$SLC32A1$^{+}$, whereas 29.8% of cells were 5HT1AR$^{+}$SLC32A1$^{-}$ **(figure 4-13C$_1$).** 8.7% Of all analysed cells in the LPBC images were SLC32A1$^{+}$5HT1AR$^{-}$ **(figure 4-13D$_1$)**. It follows that 29% of 5HT1AR positive cells in the LPBC co-expressed SLC32A1, and that this population of co-expressing cells makes up 57.6% of the SLC32A1 positive population. The average total cell count in the images used for these plots is 286 ± 28.6.

The final parabrachial region for which 5HT1AR and SLC32A1 transcripts were quantified, was the LPBE. In this region, the average cumulative frequency of cells in which any transcripts are observed was 98.7% for PPIB transcripts, 31.5% for 5HT1AR transcripts, and 32.5% for SLC32A1 transcripts (**figure 4-14B$_{1,2}$**). The average prevalence of 5HT1AR$^{+}$SLC32A1$^{+}$ cells is 12% of all analysed cells in the LPBE. 19.5% analysed cells was 5HT1AR$^{+}$SLC32A1$^{-}$ (**figure 4-14C$_{1,2}$**). Derived from the above, is that 5HT1AR$^{+}$SLC32A1$^{+}$ cells makes up 38.1% of 5HT1AR positive cells, and 36.9% of SLC32A1 positive cells. **figure 4-14D1,$_2$** shows that 20.5% of all analysed cells in the LPBE regions were SLC32A1+5HT1AR$^{-}$. The average total cell count in the LPBE images used for these plots is 276 ± 26.5.

When comparing the PBc regions, prevalence of cells with 5HT1AR transcripts is highest in the MPB (48.9%), followed by the KF (43.1%), and the LPBC(41.6). In the LPBI and LPBE images, cells that have 5HT1AR transcripts are less prevalent (36.6% and 31.5% of all cells, respectively). The highest prevalence of cells with SLC32A1 transcripts was observed in the LPBE images (32.5%). In the KF, MPB, LPBI, and LPBC regions, prevalence of cells with SLC32A1 transcripts ranged from 13.8% to 23.3%. In all analysed regions of the parabrachial complex, prevalence of cells with both 5HT1AR and SLC32A1 transcripts was relatively low, ranging from 7.4% (KF) to 14.2% (LPBI). Regions of the parabrachial complex are thought to contribute to inspiratory-to-expiratory phase transitioning by providing excitatory drive to Post-I neurones (Alheid 2004; Dutschman & Dick 2012); Abdala et al. 2016; Barnett et al. 2018) (see section 1.3). The present FISH findings are consistent with the possibility that 5-HT$_{1A}$ transmission in excitatory respiratory neurones

of the PBc may contribute to changes in respiratory rhythm observed after systemic 5-$HT_{1A}$R agonist (see section 3.3.1)

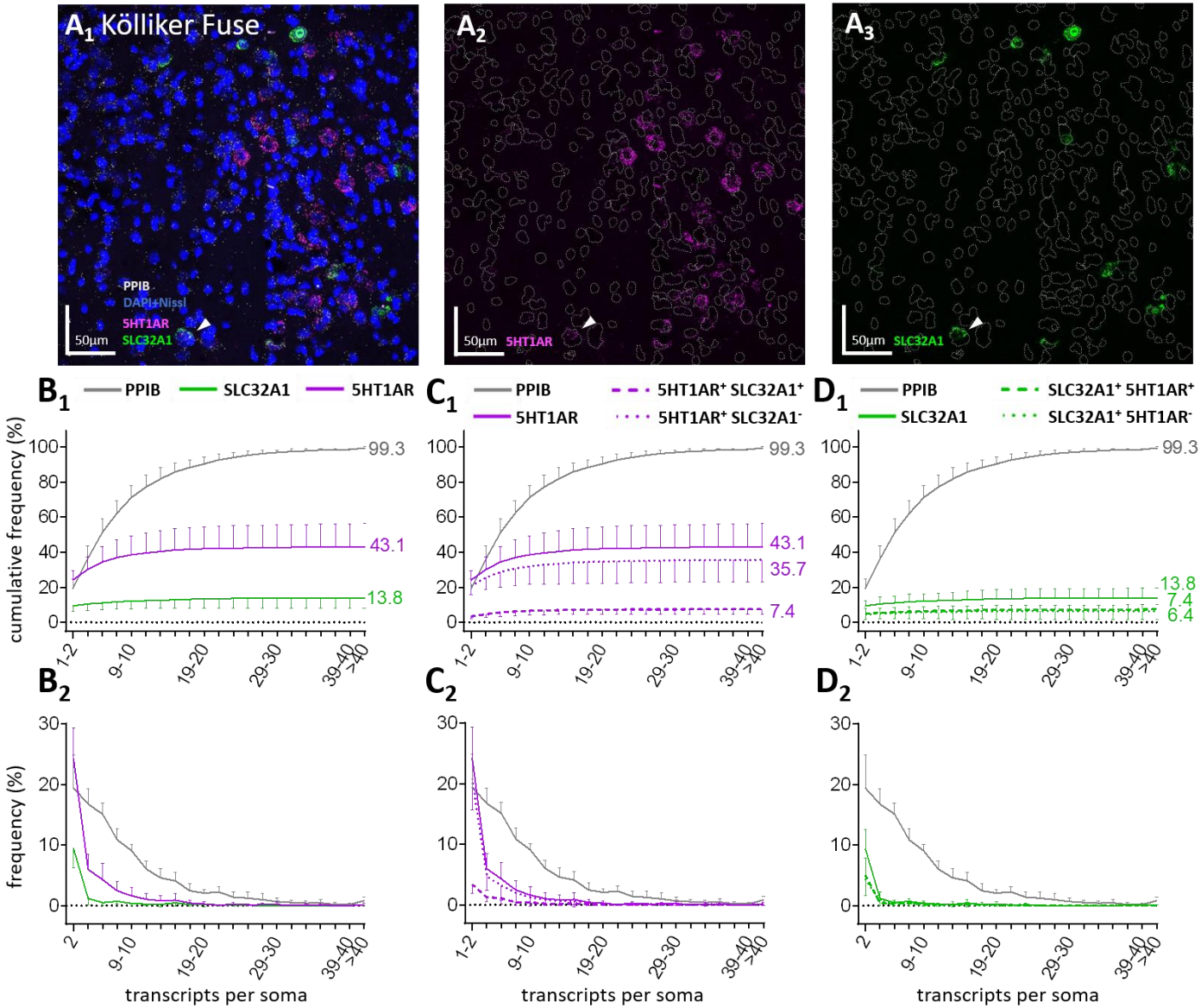


**Figure 4-10:** Fluorescence in situ hybridization (FISH) of 5-HT1a receptor RNA (5HT1AR), vesicular inhibitory amino acid transporter RNA (SLC32A1), and cyclophilin B RNA (PPIB) in the Kölliker Fuse (KF**)**

($A_{1,2,3}$) Representative image of the KF region. Individual FISH labelled transcripts show as punctate dots, a combination of DAPI and Nissl counterstain (DAPI+Nissl) was used to determine cell outlines (dotted lines). White arrow marks an example 5HT1AR+SLC32A1+ cell. ($B_{1,2}$ $C_{1,2}$ $D_{1,2}$) Cells that express PPIB, 5HT1AR, and/or SLC32A1 are categorized by their transcript count. Plots show the frequencies (%), and cumulative frequencies (%) of cells assigned to each transcript count category. Cells with 0 transcripts are excluded from plots. All values are averages of 8 images from 4 rats. Error bars are SD. See textbox 1 for a detailed description of figures.

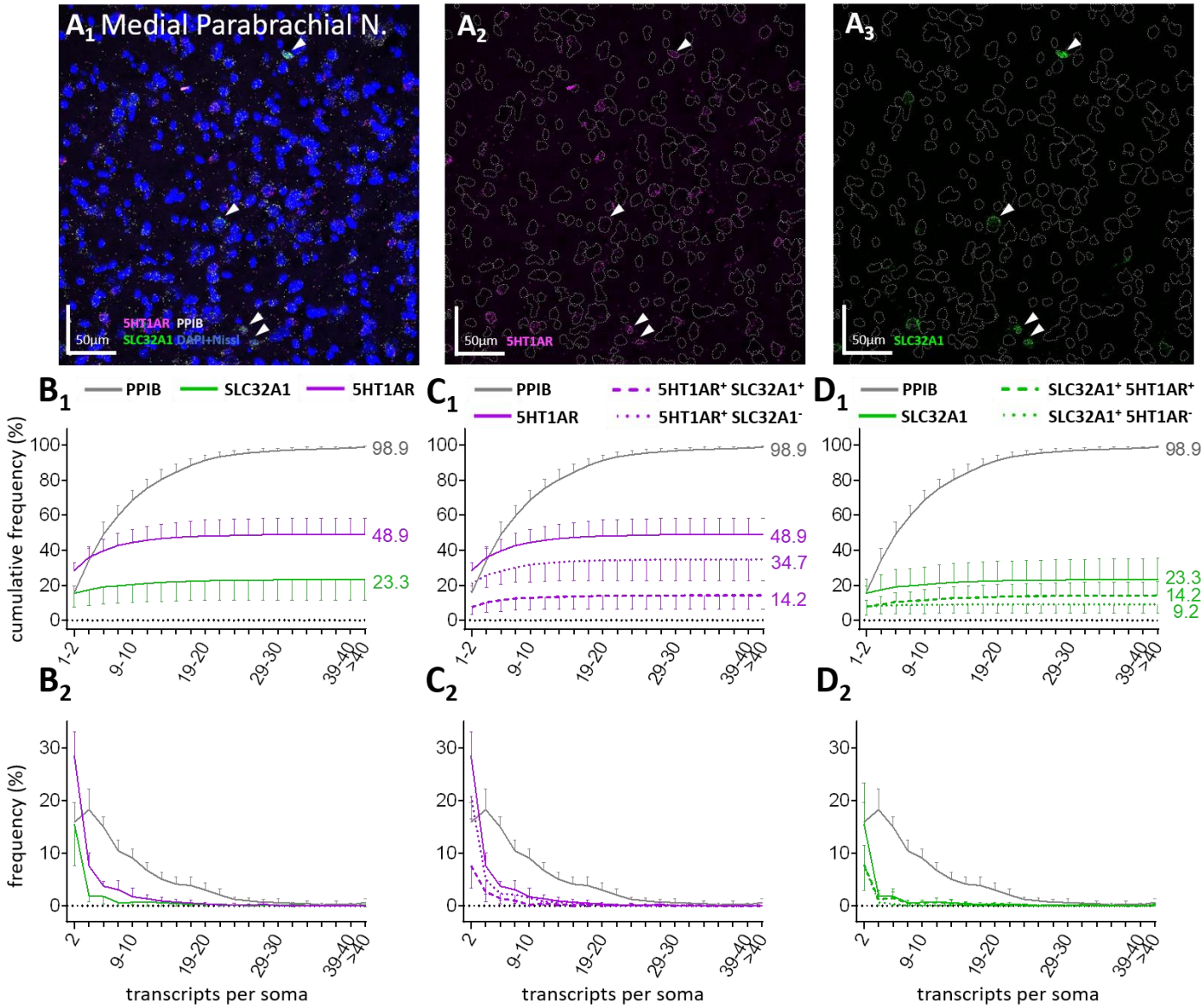


**Figure 4-11:** Fluorescence in situ hybridization (FISH) of 5-HT1a receptor RNA (5HT1AR), vesicular inhibitory amino acid transporter RNA (SLC32A1), and cyclophilin B RNA (PPIB) in the Medial Parabrachial (MPB) region.

($A_{1,2,3}$) Representative image of the MPB region. Individual FISH labelled transcripts show as punctate dots, a combination of DAPI and Nissl counterstain (DAPI+Nissl) was used to determine cell outlines (dotted lines). White arrows mark examples of 5HT1AR+SLC32A1+ cells. ($B_{1,2}$ $C_{1,2}$ $D_{1,2}$) Cells that express PPIB, 5HT1AR, and/or SLC32A1 are categorized by their transcript count. Plots show the frequencies (%), and cumulative frequencies (%) of cells assigned to each transcript count category. Cells with 0 transcripts are excluded from plots. All values are averages of 8 images from 4 rats. Error bars are SD. See textbox 1 for a detailed description of figures.

v

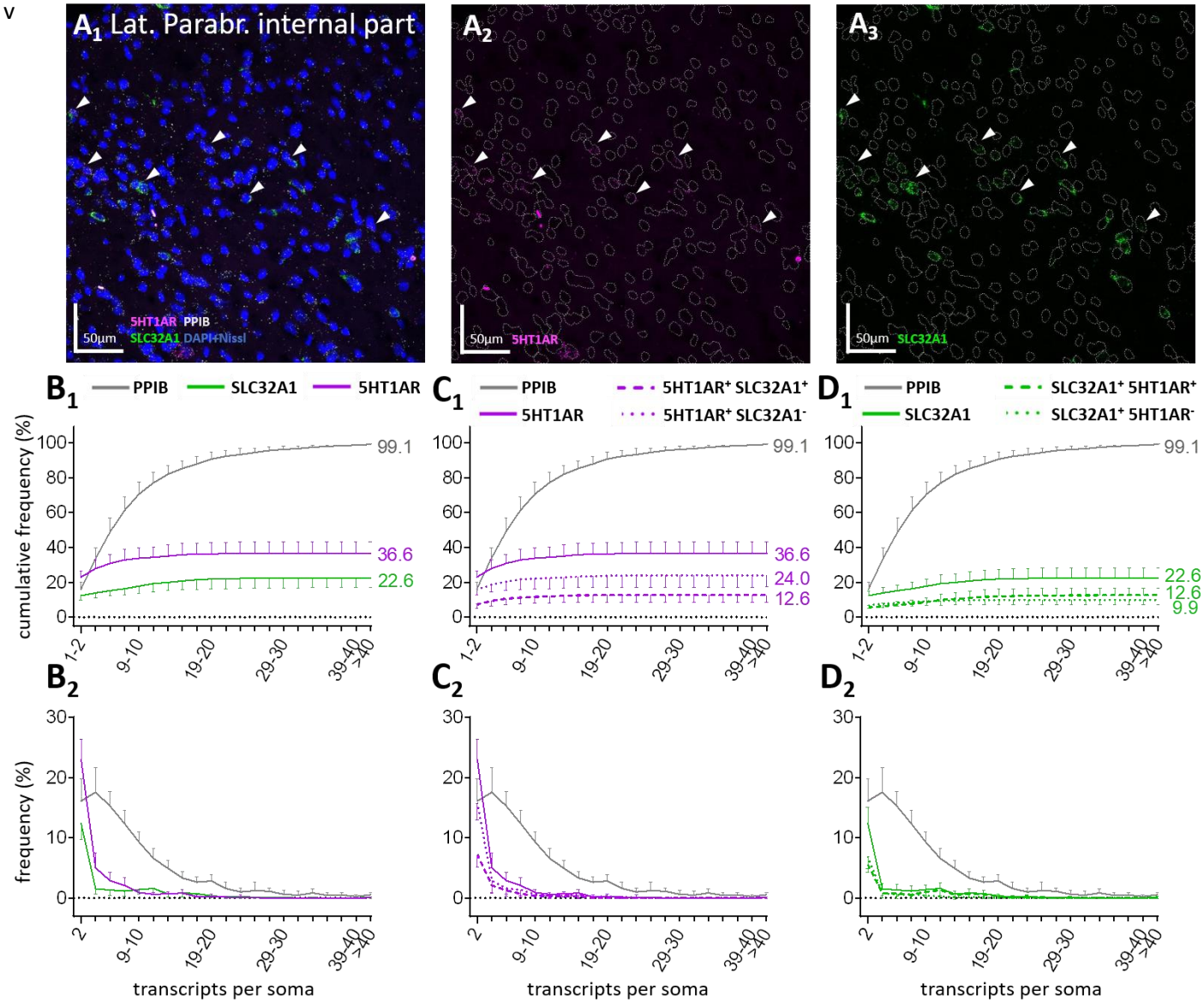


**Figure 4-12:** Fluorescence in situ hybridization (FISH) of 5-HT1a receptor RNA (5HT1AR), vesicular inhibitory amino acid transporter RNA (SLC32A1), and cyclophilin B RNA (PPIB) in the internal part of the Lateral Parabrachial (LPBI) region.

($A_{1,2,3}$) Representative image of the LPBI region. Individual FISH labelled transcripts show as punctate dots, a combination of DAPI and Nissl counterstain (DAPI+Nissl) was used to determine cell outlines (dotted lines). ($B_{1,2}$ $C_{1,2}$ $D_{1,2}$) Cells that express PPIB, 5HT1AR, and/or SLC32A1 are categorized by their transcript count. Plots show the frequencies (%), and cumulative frequencies (%) of cells assigned to each transcript count category. Cells with 0 transcripts are excluded from plots. All values are averages of 8 images from 4 rats. Error bars are SD. See textbox 1 for a detailed description of figures.

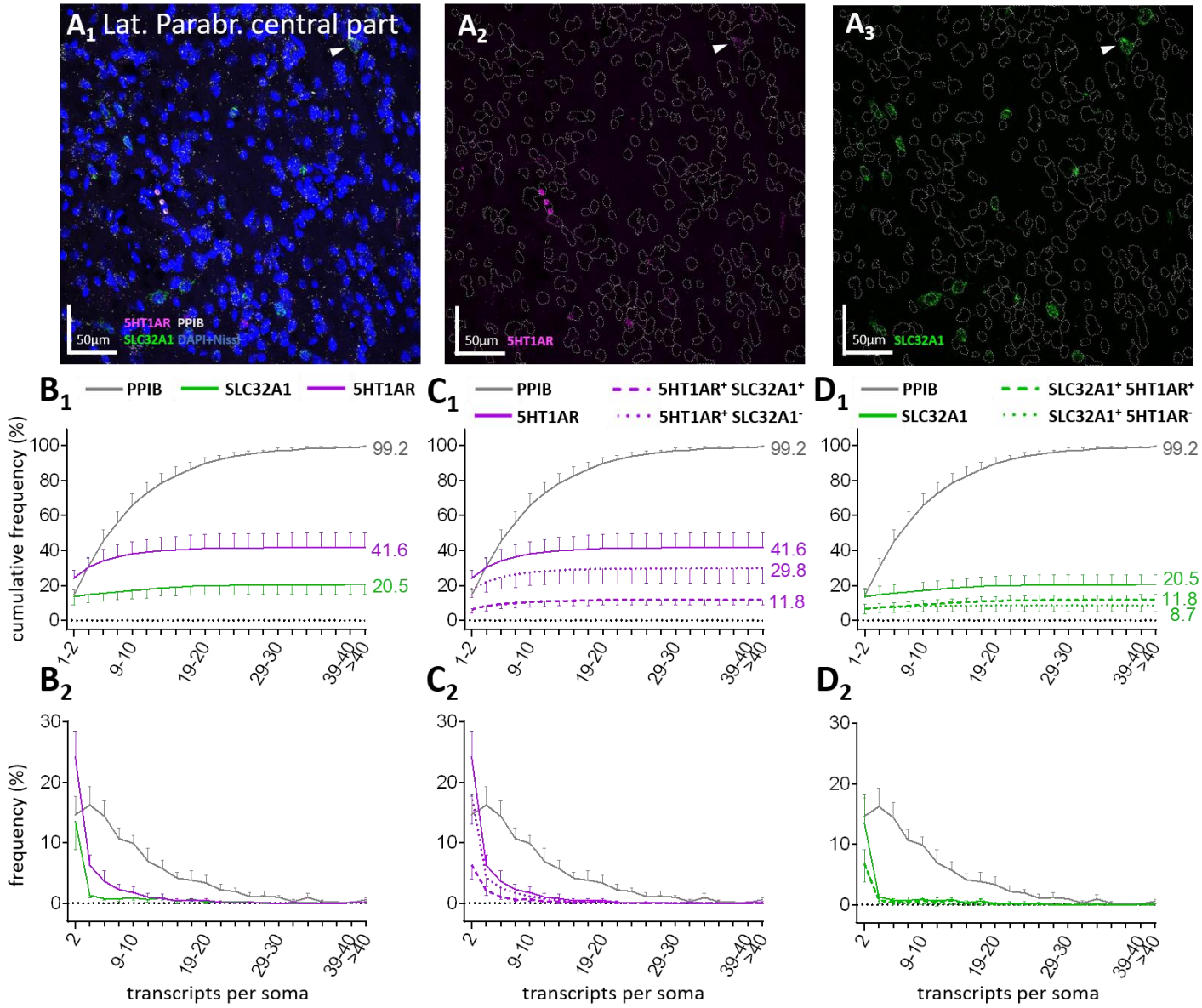


**Figure 4-13:** Fluorenscence in situ hybridization (FISH) of 5-HT1a receptor RNA (5HT1AR), vesicular inhibitory amino acid transporter RNA (SLC32A1), and cyclophilin B RNA (PPIB) in the central part of the Lateral Parabrachial (LPBC) region.

($A_{1,2,3}$) Representative image of the LPBC region. Individual FISH labelled transcripts show as punctate dots, a combination of DAPI and Nissl counterstain (DAPI+Nissl) was used to determine cell outlines (dotted lines). ($B_{1,2}$ $C_{1,2}$ $D_{1,2}$) Cells that express PPIB, 5HT1AR, and/or SLC32A1 are categorized by their transcript count. Plots show the frequencies (%), and cumulative frequencies (%) of cells assigned to each transcript count category. Cells with 0 transcripts are excluded from plots. All values are averages of 8 images from 4 rats. Error bars are SD. See textbox 1 for a detailed description of figures.

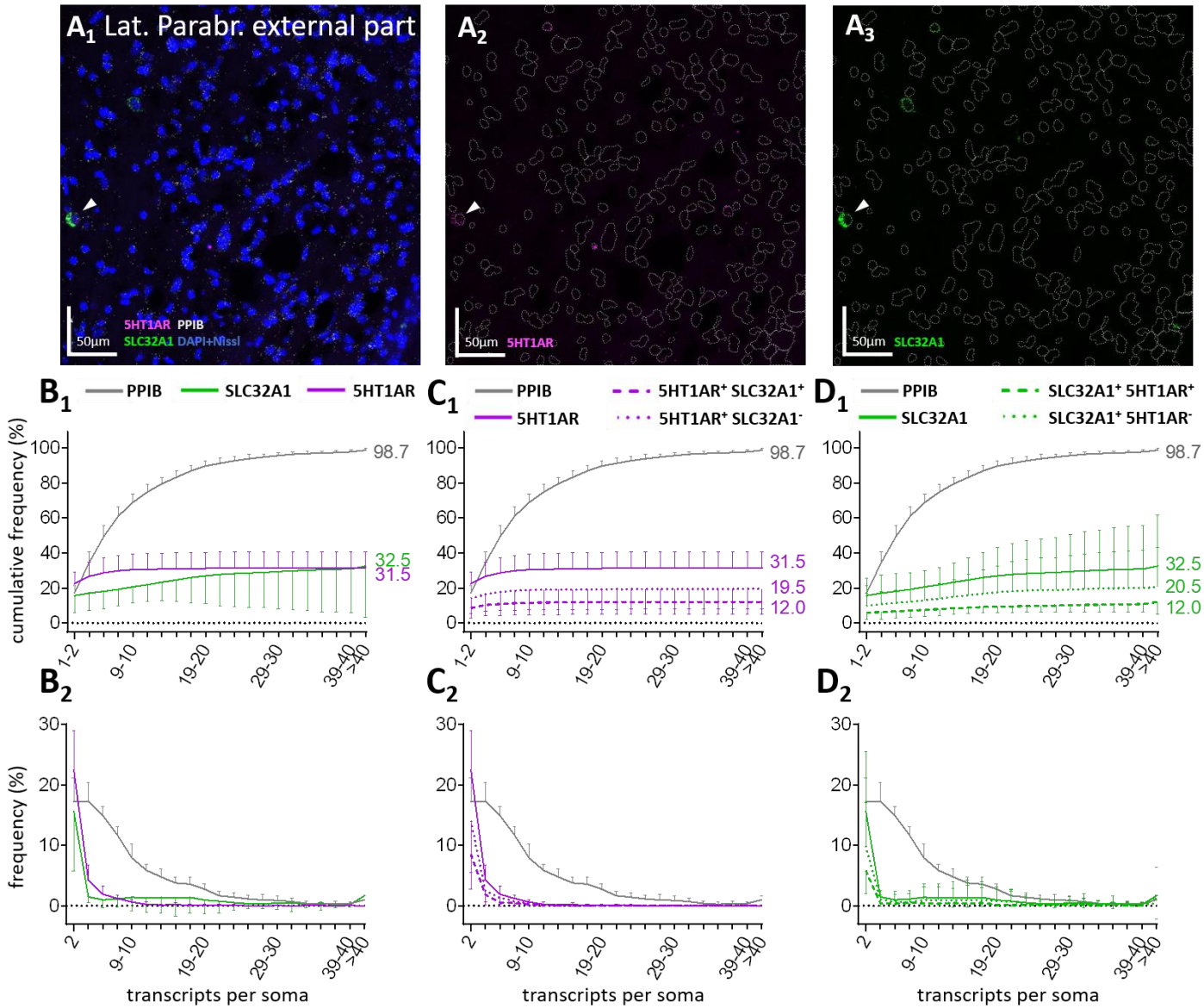


**Figure 4-14:** Fluorescence in situ hybridization (FISH) of 5-HT1a receptor RNA (5HT1AR), vesicular inhibitory amino acid transporter RNA (SLC32A1), and cyclophilin B RNA (PPIB) in the external part of the Lateral Parabrachial (LPBE) region.

($A_{1,2,3}$) Representative image of the LPBE region. Individual FISH labelled transcripts show as punctate dots, a combination of DAPI and Nissl counterstain (DAPI+Nissl) was used to determine cell outlines (dotted lines). White arrow marks an exemplary 5HT1AR+SLC32A1+ cell. ($B_{1,2}$ $C_{1,2}$ $D_{1,2}$) Cells that express PPIB, 5HT1AR, and/or SLC32A1 are categorized by their transcript count. Plots show the frequencies (%), and cumulative frequencies (%) of cells assigned to each transcript count category. Cells with 0 transcripts are excluded from plots. All values are averages of 8 images from 4 rats. Error bars are SD. See textbox 1 for a detailed description of figures.

### *4.3.4 Distribution of 5-HT$_{1A}$ receptor RNA and vesicular inhibitory amino acid transporter RNA in the commissural part of the Nucleus Tractus Solitarius, and in the Retrotrapezoid Nucleus region.*

**Figure 4-15** describes the frequency and distribution of cells with PPIB, 5HT1AR, and SLC32A1 transcripts in the commissural part of the Nucleus Tractus Solitarius (NTScomm). Similarly, **figure 4-16** describes the ventral parafacial region where RTN neurones are located. (pF$_V$/RTN). All values in the plots describing the NTScomm are averages derived from 4 images of 4 rats. All values in the plots describing the pF$_V$/RTN region are averages derived from 3 images of 3 rats.

In the NTScomm, a population of cells with 5HT1AR transcripts was observed that comprised 55.9% of all analysed cells in the image. The population of cells with SLC32A1 transcripts comprised 44.5% of analysed cells, and 98.7% of cells in the NTS images contained transcripts of PPIB (**figure 4-15B$_1$**). On average, 28.3% of the total amount of cells in the NTS images was 5HT1AR$^+$SLC32A1$^+$, whereas 27.6% of the total amount of cells was 5HT1AR$^+$SLC32A1$^-$ **(figure 4-15C$_1$).** 16.2% Of all cells in the NTScomm were SLC32A1$^+$5HT1AR$^-$ **(figure 4-15D$_1$)**. Thus, 50.6% of 5HT1AR positive cells in the NTScomm also contained SLC32A1, and 63.6% of SLC32A1 positive cells also have 5HT1AR transcripts. The average total cell count in the NTScomm images used for these plots is 159.5 ± 34.5.

In the pF$_V$/RTN region, the average cumulative frequency of cells in which transcripts were observed is 99.4% for PPIB transcripts, 19.4% for 5HT1AR transcripts, and 17.3% for SLC32A1 transcripts (**figure 4-16B$_1$**). 9.1% Of analysed cells in the pF$_V$/RTN images were 5HT1AR$^+$SLC32A1$^+$ and the remainder of the 5HTAR1 positive population (5HT1AR$^+$SLC32A1$^-$ cells) comprised 10.2% of all cells analysed **(figure 4-16C$_1$)**. This means that, in the pF$_V$/RTN, the population of 5HT1AR$^+$SLC32A1$^-$ cells comprised 46.9% of all 5HT1AR positive cells, and 52.6% of all SLC32A1 positive cells. 8.2% Of analysed cells were SLC32A1$^+$5HT1AR$^-$ **(figure 4-16D$_1$)**. The average total cell count in the images used for these plots is 276 ± 26.5. Compared to other regions analysed in this chapter, there are relatively few 5HT1AR$^+$ (19.4%) cells in the pF$_V$/RTN (see **table 4-2**). This, combined with the absence of an effect of systemic 5-HT$_{1A}$R agonist (NLX-101) or antagonist (WAY-100635) on the central chemoreflex response (see section 3.3.2), suggests that 5-HT$_{1A}$ transmission may not affect central chemoreceptor activity.

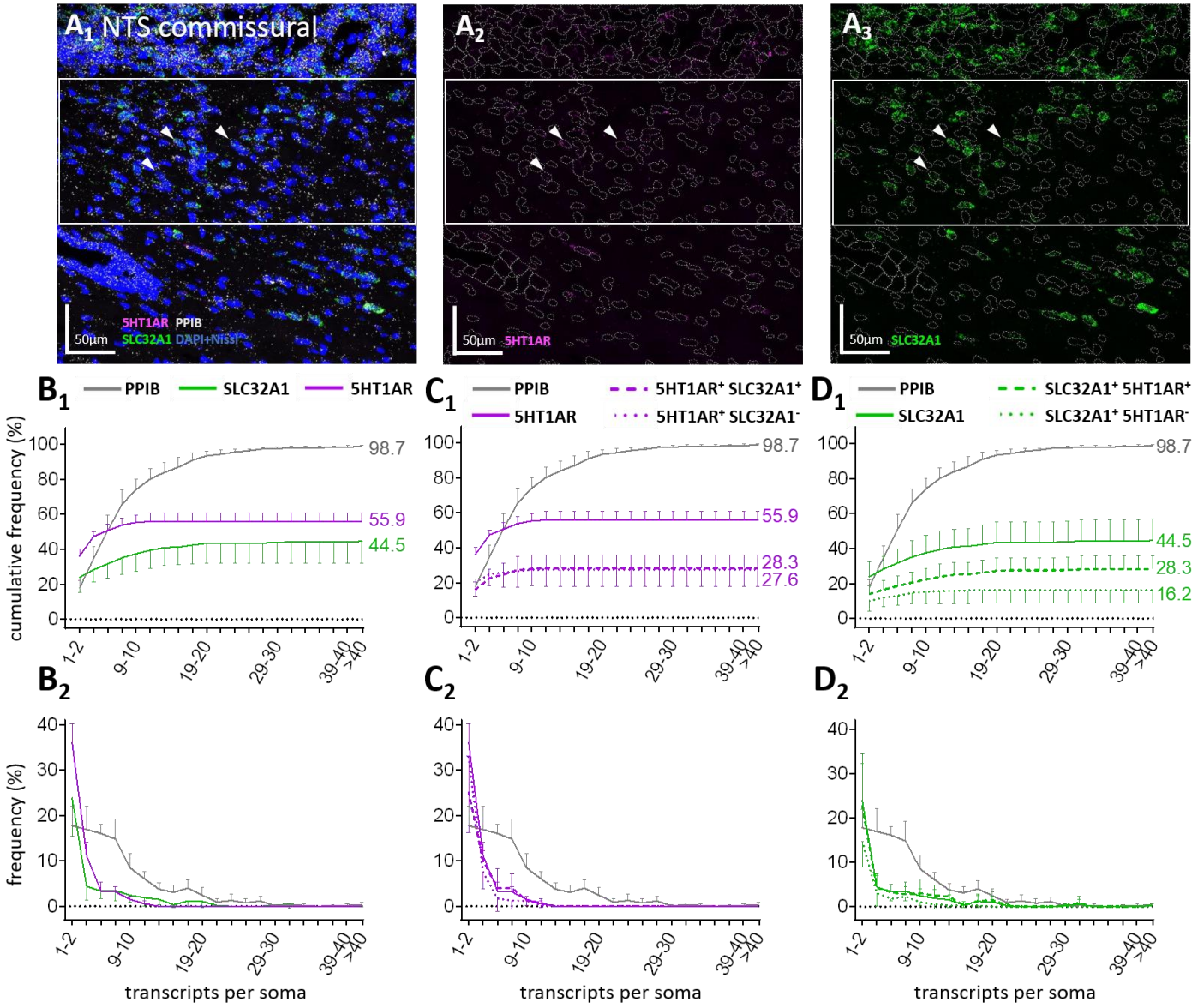


**Figure 4-15:** Fluorescence in situ hybridization (FISH) of 5-HT1a receptor RNA (5HT1AR), vesicular inhibitory amino acid transporter RNA (SLC32A1), and cyclophilin B RNA (PPIB) in the commissural part of the Nucleus Tractus Solitarius (NTS-comm).

($A_{1,2,3}$) Representative image of the NTS-comm region. Individual FISH labelled transcripts show as punctate dots, a combination of DAPI and Nissl counterstain (DAPI+Nissl) was used to determine cell outlines (dotted lines). ISH data analysis was restricted to cells within the white box. White arrows mark examples of 5HT1AR+SLC32A1+ cells. ($B_{1,2}$ $C_{1,2}$ $D_{1,2}$) Cells that express PPIB, 5HT1AR, and/or SLC32A1 are categorized by their transcript count. Plots show the frequencies (%), and cumulative frequencies (%) of cells assigned to each transcript count category. Cells with 0 transcripts are excluded from plots. All values are averages of 4 images from 4 rats. Error bars are SD. See textbox 1 for a detailed description of figures.

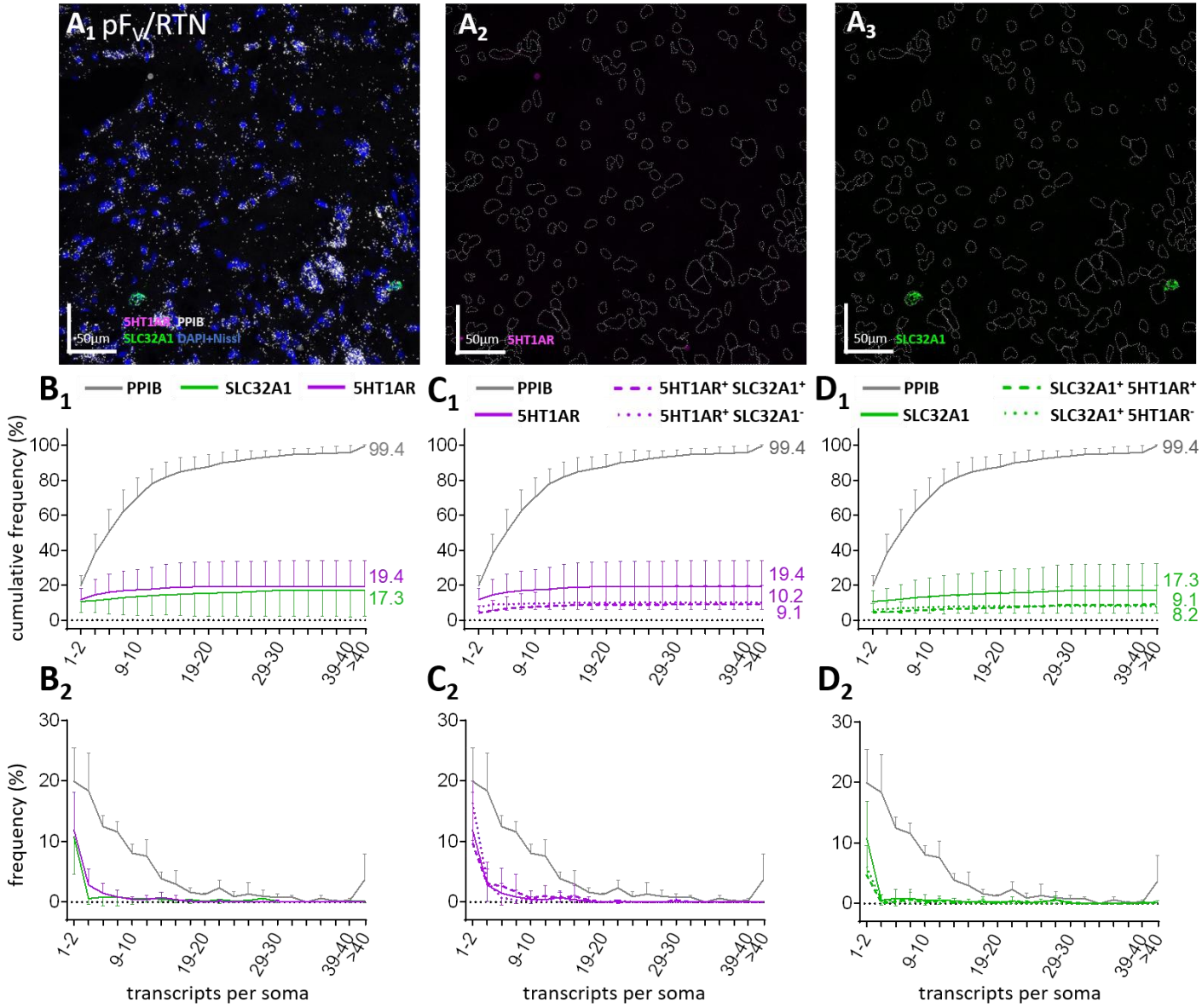


**Figure 4-16:** Fluorescence in situ hybridization (FISH) of 5-HT1a receptor RNA (5HT1AR), vesicular inhibitory amino acid transporter RNA (SLC32A1), and cyclophilin B RNA (PPIB) in the ventral parafacial region ($pF_V$) where retrotrapezoid nucleus (RTN) neurones are located**.**

($A_{1,2,3}$) Representative image of the $pF_V$/RTN. Individual FISH labelled transcripts show as punctate dots, a combination of DAPI and Nissl counterstain (DAPI+Nissl) was used to determine cell outlines (dotted lines). ($B_{1,2}$ $C_{1,2}$ $D_{1,2}$) Cells that express PPIB, 5HT1AR, and/or SLC32A1 are categorized by their transcript count. Plots show the frequencies (%), and cumulative frequencies (%) of cells assigned to each transcript count category. Cells with 0 transcripts are excluded from plots. All values are averages of 3 images from 3 rats. Error bars are SD. See textbox 1 for a detailed description of figures.

### *4.3.5 Distribution of 5-HT$_{1A}$ receptor RNA and vesicular inhibitory amino acid transporter RNA in raphe nuclei: raphe Magnus, raphe Obscurus, raphe Pallidus, and the caudal part of the dorsal raphe.*

**Figures 4-17, 4-18, 4-19, and 4-20** describe the frequency and distribution of cells with PPIB, 5HT1AR, and SLC32A1 transcripts in the raphe Magnus (RMg) region, raphe Obscurus (Rob) region, the raphe Pallidus (RPa) region, and the dorsal raphe (DR), respectively. All values in plots that describe the RMg, ROb, and RPa are averages derived from 4 images from 4 rats. Plots that describe the DR are made with averages derived from 2 images from 2 rats.

In the RMg region, the average cumulative frequency of cells in which transcripts are observed is 99% for PPIB transcripts, 54% for 5HT1AR transcripts, and 44.6% for SLC32A1 transcripts (**figure 4-17B$_1$**). 31.4% Of all analysed cells in the RMg images were 5HT1AR$^+$SLC32A1$^+$, and the remainder of the 5HTAR1 positive population (5HT1AR$^+$SLC32A1$^-$ cells) comprised 22.5% of analysed cells **(figure 4-17C$_1$)**. From this one can derive that, in the RMg images, the population of 5HT1AR$^+$SLC32A1$^-$ co-expressing cells comprises 58.1% of all 5HT1AR positive cells, and 70.4% of all SLC32A1 positive cells. 13.2% Of all cells in the RMg images were SLC32A1$^+$5HT1AR$^-$ **(figure 4-17D$_1$)**. The population of 5HT1AR$^+$SLC32A1$^-$ cells and the population of SLC32A1$^+$5HT1AR$^-$ were both largely comprised of cells with low transcript counts for 5HT1AR and SLC32A1, respectively. The average total cell count in the images used for these plots is 261 ± 25.2.

In the ROb, cells with PPIB transcripts comprised 98.3% of all analysed cells, 5HT1AR positive cells comprised 48% of all cells, and cells with SLC32A1 transcripts comprised 23.1% of analysed cells in the images (**figure 4-18B$_1$**). On average, 17.2% of cells in the ROb images were 5HT1AR$^+$SLC32A1$^+$, whereas 30.8% of the cells were 5HT1AR$^+$SLC32A1$^-$ **(figure 4-18C$_1$).** 5.9% Of all analysed cells in the ROb images were SLC32A1$^+$5HT1AR$^-$ **(figure 4-18D$_1$)**. It follows that 35.8% of 5HT1AR positive cells in the RMg region co-expressed SLC32A1, and that this population of co-expressing cells comprises 74.5% of the SLC32A1 positive population. The population of SLC32A1$^+$5HT1AR$^-$ cells is largely comprised of cells with low transcript counts. The average total cell count in the images used for these plots is 247 ± 30.1.

In the RPa, a population of cells with 5HT1AR transcripts was observed that comprised 41.1% of all analysed cells in the image. The population of cells with SLC32A1 transcripts comprised 39.8% of all cells, and 99.1% of all analysed cells in the RPa images contained transcripts of PPIB (**figure 4-19B$_1$**). On average, 20.8% of cells in the RPa images were 5HT1AR$^+$SLC32A1$^+$, whereas 20.3% of the total amount of cells were 5HT1AR$^+$SLC32A1$^-$ **(figure 4-19C$_1$).** 19% Of analysed cells in the RPa were SLC32A1$^+$5HT1AR$^-$ **(figure 4-19D$_1$)**. This means that 50.6% of 5HT1AR positive cells in the RPa also contained SLC32A1, and 52.3% of SLC32A1 positive cells also had 5HT1AR transcripts. The average total cell count in the MPB images used for these plots is 185 ± 102.2.

The final raphe nucleus for which 5HT1AR and SLC32A1 transcripts were quantified, is the dorsal raphe (DR) (**figure 4-201)**. In this region, the average cumulative frequency of cells in which any transcripts are observed was 99.6% for PPIB transcripts, 73.6% for 5HT1AR transcripts, and 45.6% for SLC32A1 transcripts (**figure 4-20B$_{1,2}$**). On average, 35.1% of the total amount of analysed cells in the DR images were 5HT1AR$^+$SLC32A1$^+$, whereas 38.5% of the total amount of cells were 5HT1AR$^+$SLC32A1$^-$ (**figure 4-20C$_{1,2}$**). From these numbers, it follows that 5HT1AR$^+$SLC32A1$^+$ cells made up 47.7% of 5HT1AR positive cells, and 77% of SLC32A1 positive cells. **Figure 4-20D1,$_2$** shows that 10.5% of all analysed cells in the DR regions were SLC32A1$^+$5HT1AR$^-$. The average total cell count in the DR images is 120 ± 11.3.

Comparison of the analysed raphe nuclei reveals that the relative size of the 5HT1AR positive cell population was largest in the DR (73.6%), followed by the RMg (54%), then the ROb (48%), and ultimately the RPa (41.1%). The same order was observed when comparing the populations of 5HT1AR and SLC32A1 co-expressing cells. In the DR, 35.1% of all analysed cells were co-expressing (5HT1AR$^+$SLC32A1$^+$), followed by the RMg (31.4%), and then the RPa and ROb (20.8% and 17.2%, respectively). The SLC32A1 positive population, too, was most prevalent in the DR (45.8%). This was closely followed by the SLC32A1 positive population in RMg (44.6%), then that in the RPa (39.8), and last that in the ROb (23.1%). These findings indicate that 5-HT$_{1A}$R expression is highly prevalent in GABAergic and/or glycinergic, and other raphe neurones.

**Table 4-2**: Overview of the brainstem regions in which FISH is quantified, and the corresponding average percentages of cells that meet various 5HT1AR and SLC32A1 expression profiles.

Summary of FISH data presented in **figures 4-3 to 4-20**. For each of the brainstem regions of which images after FISH are analysed, the average prevalence (% of all analysed cells in image) is provided of cells that meet one of the 4 possible 5HT1AR and SLC32A1 expression profiles. The 5HT1AR and SLC32A1 expression profiles are: 5HT1AR positive and SLC32A1 negative ($5HT1aR^{+}SLC32A1^{-}$); 5HT1AR positive and SLC32A1 positive ($5HT1AR^{+}SLC32A1^{+}$); 5HT1AR negative and SLC32A1 positive ($5HT1AR^{-}SLC32A1^{+}$); and 5HT1AR negative and SLC32A1 negative ($5HT1AR^{-}SLC32A1^{-}$).

| | **$5HT1AR^{+}$** | **$5HT1AR^{+}$ $SLC32A1^{-}$** | **$5HT1AR^{+}$ $SLC32A1^{+}$** | **$SLC32A1^{+}$** | **$5HT1AR^{-}$ $SLC32A1^{+}$** | **$5HT1AR^{-}$ $SLC32A1^{-}$** |
|---|---|---|---|---|---|---|
| **BötC** | 42.6 | 16.3 | 26.2 | 37 | 10.7 | 46.8 |
| **pre-BötC** | 46.6 | 13.9 | 32.7 | 46.4 | 13.7 | 39.7 |
| **RVRG** | 34.9 | 15.5 | 19.4 | 31.8 | 12.5 | 52.6 |
| **N. Amb. C.** | 38.3 | 18.3 | 20 | 38.4 | 18.4 | 43.3 |
| **N10** | 29.6 | 7.9 | 21.7 | 47.2 | 25.5 | 44.9 |
| **N12** | 30.3 | 21.3 | 8.9 | 15.8 | 6.9 | 62.9 |
| **XII premotor** | 50.8 | 15.4 | 35.4 | 55.3 | 19.9 | 29.3 |
| **KF** | 43.1 | 35.7 | 7.4 | 13.8 | 6.4 | 50.5 |
| **MPB** | 48.9 | 34.7 | 14.2 | 23.3 | 9.2 | 41.9 |
| **LPBI** | 36.6 | 24 | 12.6 | 22.5 | 9.9 | 53.5 |
| **LPBC** | 41.6 | 29.8 | 11.8 | 20.5 | 8.7 | 49.7 |
| **LPBE** | 31.5 | 19.5 | 12 | 32.5 | 20.5 | 48 |
| **NTScomm** | 55.9 | 27.6 | 28.3 | 44.5 | 16.2 | 27.9 |
| **pFv/RTN** | 19.3 | 10.2 | 9.1 | 17.3 | 8.2 | 72.5 |
| **RMg** | 54 | 22.5 | 31.4 | 44.6 | 13.2 | 32.9 |
| **ROb** | 48 | 30.8 | 17.2 | 23.1 | 5.9 | 46.1 |
| **RPa** | 41.1 | 20.3 | 20.8 | 39.8 | 19 | 39.9 |
| **dorsal raphe** | 73.6 | 38.5 | 35.1 | 45.6 | 10.5 | 15.9 |

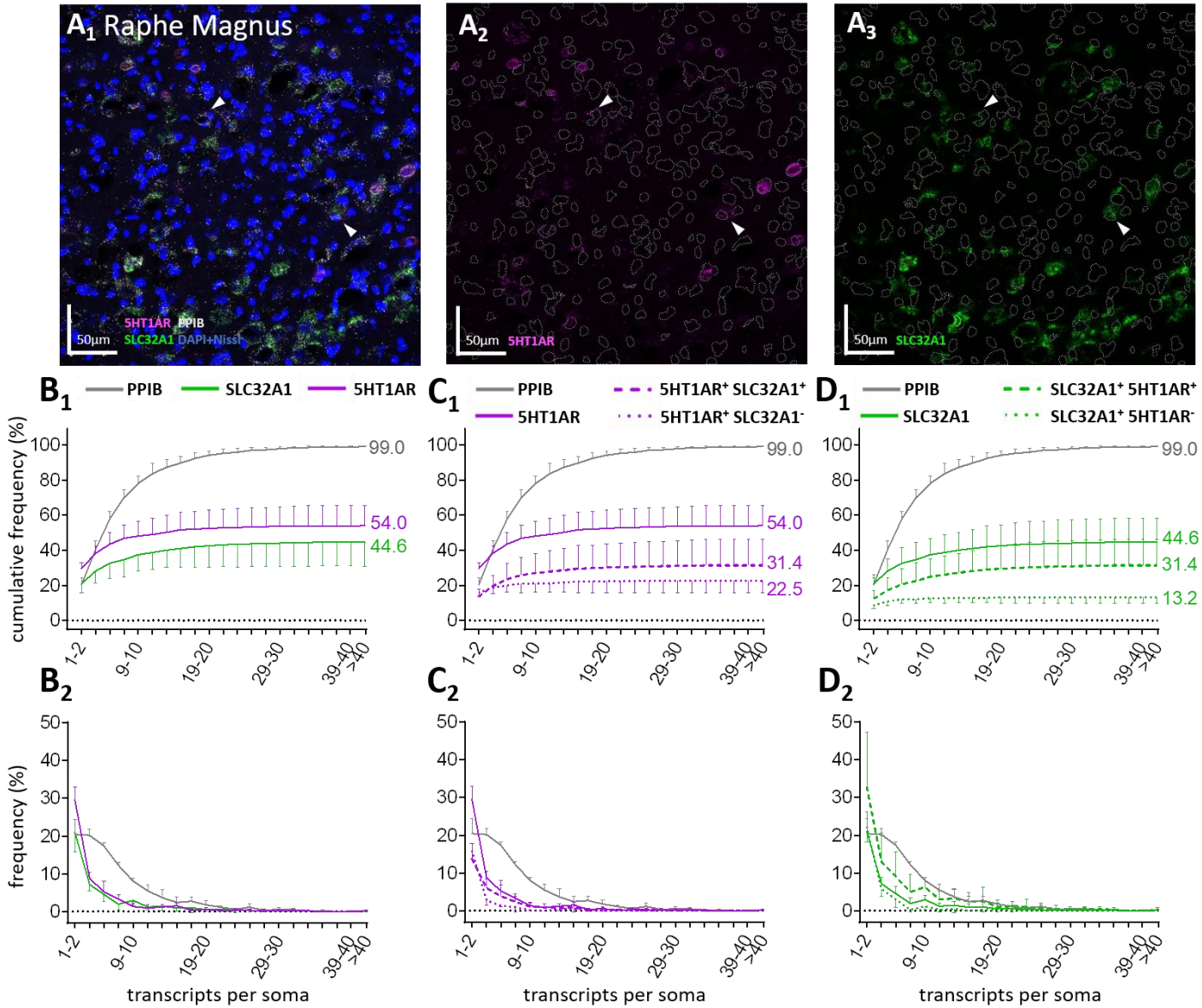


**Figure 4-17:** Fluorescence in situ hybridization (FISH) of 5-HT1a receptor RNA (5HT1AR), vesicular inhibitory amino acid transporter RNA (SLC32A1), and cyclophilin B RNA (PPIB) in the raphe Magnus (RMg). ($A_{1,2,3}$). Representative image of the RMg region. Individual FISH labelled transcripts show as punctate dots, a combination of DAPI and Nissl counterstain (DAPI+Nissl) was used to determine cell outlines (dotted lines). White arrows mark examples of $5HT1AR^{+}SLC32A1^{+}$ cells. ($B_{1,2}$ $C_{1,2}$ $D_{1,2}$) Cells that express PPIB, 5HT1AR, and/or SLC32A1 are categorized by their transcript count. Plots show the frequencies (%), and cumulative frequencies (%) of cells assigned to each transcript count category. Cells with 0 transcripts are excluded from plots. All values are averages of 4 images from 4 rats. Error bars are SD. See textbox 1 for a detailed description of figures.

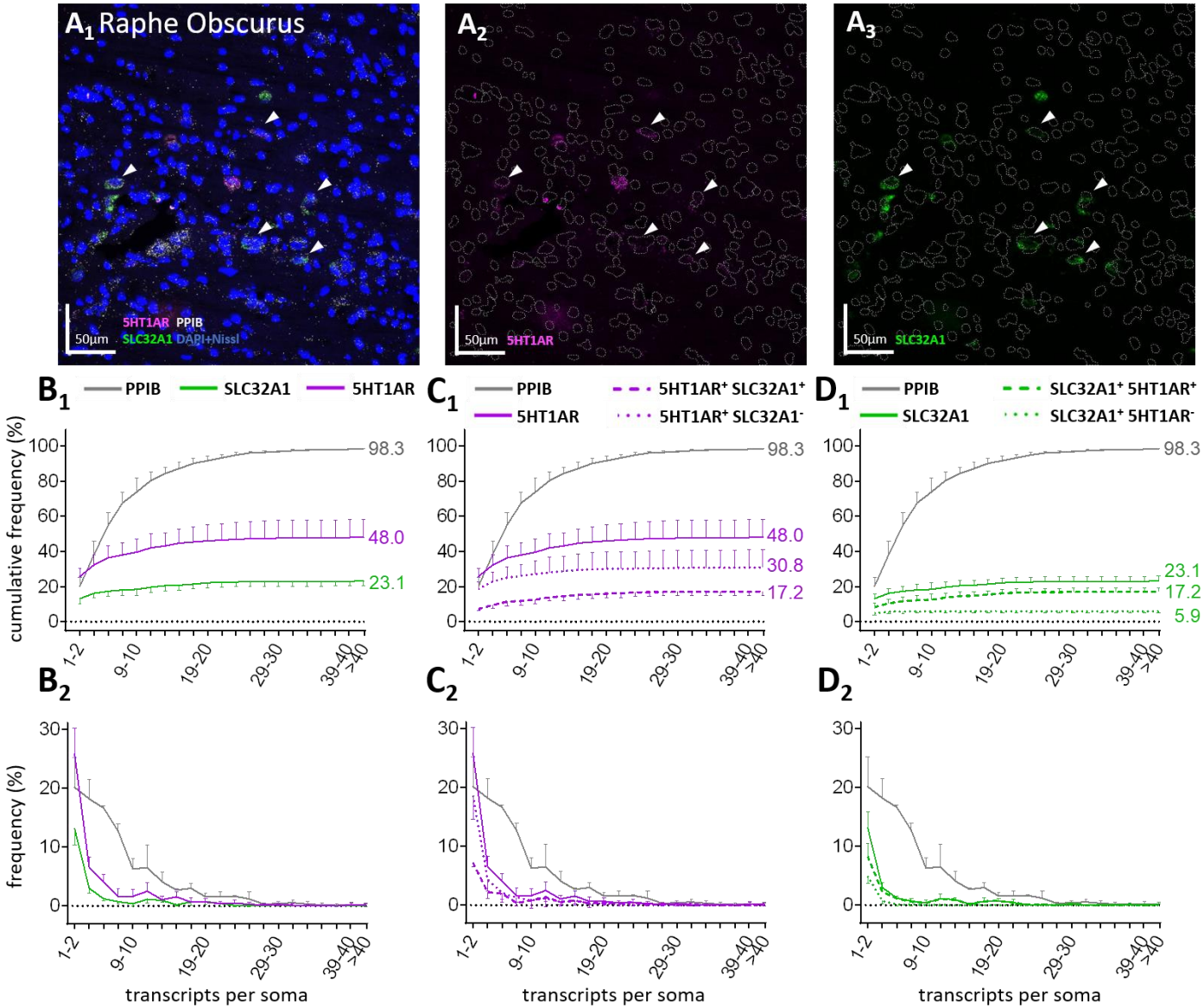


**Figure 4-18:** Fluorescence in situ hybridization (FISH) of 5-HT1a receptor RNA (5HT1AR), vesicular inhibitory amino acid transporter RNA (SLC32A1), and cyclophilin B RNA (PPIB) in the raphe Obscurus (ROb).

($A_{1,2,3}$) Representative image of the RMg region. Individual FISH labelled transcripts show as punctate dots, a combination of DAPI and Nissl counterstain (DAPI+Nissl) was used to determine cell outlines (dotted lines). White arrows mark examples of $5HT1AR^{+}SLC32A1^{+}$ cells. ($B_{1,2}$ $C_{1,2}$ $D_{1,2}$) Cells that express PPIB, 5HT1AR, and/or SLC32A1 are categorized by their transcript count. Plots show the frequencies (%), and cumulative frequencies (%) of cells assigned to each transcript count category. Cells with 0 transcripts are excluded from plots. All values are averages of 4 images from 4 rats. Error bars are SD. See textbox 1 for a detailed description of figures.

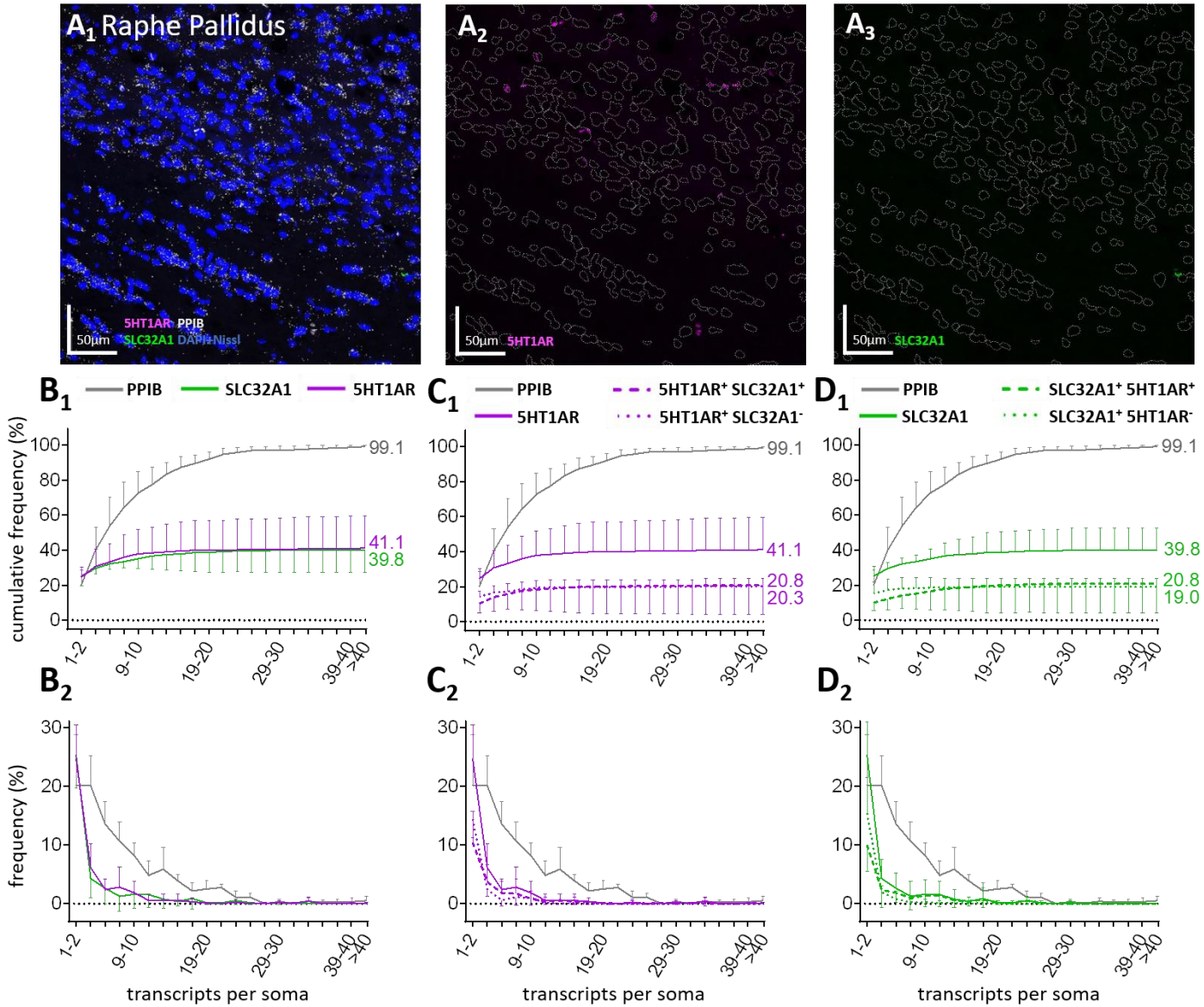


**Figure 4-19:** Fluorescence in situ hybridization (FISH) of 5-HT1a receptor RNA (5HT1AR), vesicular inhibi-tory amino acid trans- porter RNA (SLC32A1), and cyclophilin B RNA (PPIB) in the Raphe Pallidus (RPa).

($A_{1,2,3}$) Representative image of the RPa region. Individual FISH labelled transcripts show as punctate dots, a combination of DAPI and Nissl counterstain (DAPI+Nissl) was used to determine cell outlines (dotted lines). ($B_{1,2}$ $C_{1,2}$ $D_{1,2}$) Cells that express PPIB, 5HT1AR, and/or SLC32A1 are categorized by their transcript count. Plots show the frequencies (%), and cumulative frequencies (%) of cells assigned to each transcript count category. Cells with 0 transcripts are excluded from plots. All values are averages of 4 images from 4 rats. Error bars are SD. See textbox 1 for a detailed description of figures.

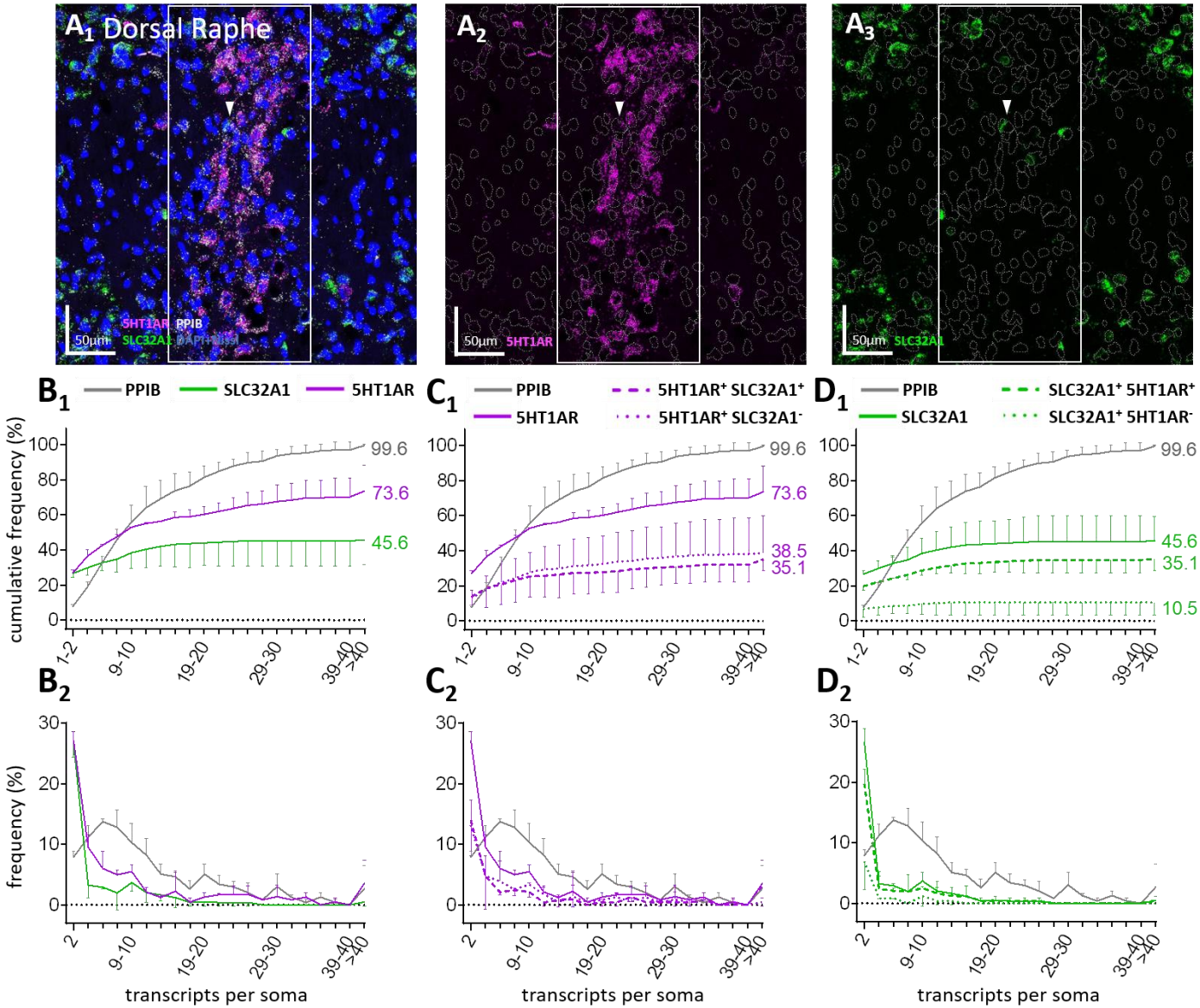


**Figure 4-20:** Fluorescence in situ hybridization (FISH) of 5-HT1a receptor RNA (5HT1AR), vesicular inhibi-tory amino acid trans- porter RNA (SLC32A1), and cyclophilin B RNA (PPIB) in the caudal part of the Dorsal Raphe (DR).

($A_{1,2,3}$) Representative image of the DR region. Individual FISH labelled transcripts show as punctate dots, a combination of DAPI and Nissl counterstain (DAPI+Nissl) was used to determine cell outlines (dotted lines). ISH data analysis was restricted to cells within the white box. White arrow marks an exemplary $5HT1AR^{+}SLC32A1^{+}$ cell. ($B_{1,2}$ $C_{1,2}$ $D_{1,2}$) Cells that express PPIB, 5HT1AR, and/or SLC32A1 are categorized by their transcript count. Plots show the frequencies (%), and cumulative frequencies (%) of cells assigned to each transcript count category. Cells with 0 transcripts are excluded from plots. All values are averages of 2 images from 2 rats. Error bars are SD. See textbox 1 for a detailed description of figures.

## 4.4 CHAPTER DISCUSSION

### *4.4.1 Summary of results in light of aims and hypotheses*

Because the existing literature does not provide a comprehensive description of 5-$HT_{1A}$R expression in the brainstem respiratory CPG network, and because little is known about the chemical phenotype of 5-$HT_{1A}$R expressing brainstem neurones, I mapped the distribution of 5-$HT_{1A}$R RNA as well as SLC32A1 RNA in key brainstem regions of respiratory control. Previous histological-, *in situ* hybridization-, and PCR experiments indicated that 5-$HT_{1A}$R are expressed in the BötC and pre-BötC (Manzke et al., 2009, Manzke et al., 2010), the NTS (Vantrease et al., 2015); the carotid bodies (Yokoyama et al. 2015); and in the dorsal and median raphe nuclei (Sotelo et al., 1990) of rats. Data in the present chapter expands knowledge of 5-$HT_{1A}$R distribution in the respiratory CPG through classification of cells by their 5-$HT_{1A}$R RNA and/or SLC32A1 RNA expression profile, as well as through quantification of the amount of 5-$HT_{1A}$R RNA and/or SLC32A1 RNA transcripts present per cell, in each of the following regions: respiratory regions of the VRC (BotC, pre-BotC, and RVRG), respiratory (pre-)motor regions (N. Ambiguus Compactus, XII pre-motor neurones, N10, N12), pontine respiratory nuclei of the PB complex (KF, LBPI, LPBC, LBPE, MBP), the $pF_V$/RTN region, the commissural part of the NTS, and brainstem raphe nuclei (raphe Magnus, raphe Obscurus, raphe Pallidus, and the caudal part of the dorsal raphe). Tissue morphology in coronal and sagittal brainstem sections was maintained, and RNA expression levels were quantified per individual neurone in each of the brainstem regions listed above. As such, the present studies provide the first comprehensive and high-resolution mapping of 5-$HT_{1A}$R RNA expression combined with mapping of SLC32A1 RNA co-expression throughout key brainstem regions of respiratory control.

Final paragraphs of results subsections in this chapter provide brief written summaries of 5-$HT_{1A}$R RNA and SLC32A1 RNA distribution in the VRC (section 4.3.1), the PB complex (section 4.3.2), in (pre-)motor regions (section 4.3.3), and in raphe nuclei (section 4.3.5). Additionally, table 4-2 provides a summary of the relative amounts of cells of all possible 5-$HT_{1A}$ R and SLC32A1 RNA expression profiles within each analyzed brainstem region. A selection of notable findings is discussed here.

5-$HT_{1A}$ R RNA was observed in both SLC32A1 positive (glycinergic and/or GABAergic) cells and SLC32A1 negative cells in all imaged brainstem regions involved in respiratory control.

Among these regions, the highest prevalence of cells with 5-$HT_{1A}$R RNA was observed in the following areas: the BötC (on average, 42.6% of all analyzed cells in BötC images contained 5-$HT_{1A}$R RNA) and the pre-BötC (46.6%) in the VRC; the KF (43.1%), MPB (48.9%), and LPBC (41.6%) in the PB complex; a region with XII pre-motor neurons dorsal to the nucleus ambiguus (50.8%); the commissural part of the NTS (55.9%); and raphe nuclei. Among raphe nuclei, the percentage of cells with 5-$HT_{1A}$R RNA was highest in the dorsal raphe (73.6%), followed by the RMg (54%), the ROb (48%), and the RPa (41.1%). Lowest relative amounts of 5-$HT_{1a}$R RNA positive cells (19.3%) were observed in images of the $pF_V$/RTN. The highest percentages of 5-$HT_{1A}$R RNA and SLC32A1 RNA co-expressing cells per region were observed in the pre-BotC (32.7%), the NTS commissural (28.3%), in XII premotor region (35.4%), the RMg (31.4%), and the dorsal raphe (35.1%). Also noteworthy, the prevalence of cells with co-expression was low in regions of the PBc (KF (7.4%), MPB (25.3%), LBPI (12.6%) , LPBC (11.8%), LPBE (12%). Finally, 5-$HT_{1A}$R positive populations in the N10 and N12 regions consisted primarily of cells with a low 5-$HT_{1A}$R RNA transcript count. That is, 92% of 5-$HT_{1A}$R RNA positive cells in images of N10, and 91% of 5-$HT_{1a}$ R RNA positive cells in images of N12, have 6 or fewer 5HT1AR transcripts.

### *4.4.2 Technical considerations*

Considerations regarding the use of the Nissl+DAPI signal for determining cell outlines

5-$HT_{1A}$R-, SLC32A1-, and PPIB RNA sequences were fluorescently labeled with the use of RNAscope® fluorescence *in situ* hybridization (FISH). This labelling technique was described in detail in section 4.2.1. The main advantages of the use of this technique are: [1] improved selectivity and signal-to-noise ratio relative to conventional ISH methods; [2] simultaneous detection of multiple target mRNA's; and [3] high signal amplification results in individually discernible hybridized RNA molecules (Wang et al., 2012). In the present study, RNAscope® FISH was combined with Nissl and DAPI staining for anatomical reference and visualisation of outlines of cell somata. As a result, hybridized RNA strands could be counted per cell soma in any given neuro-anatomical structure. This allowed for quantification of both the number of cells with 5-$HT_{1A}$ R RNA and/or SLC32A1 RNA per anatomical region, as well as the RNA counts within each cell. Despite these advantages, the use of RNAscope® in combination with Nissl and DAPI staining does have its limitations.

First, there are limitations to the selectivity of structures in which RNA is counted in the present analysis. In neurones, RNA translation does not exclusively occur in cell bodies, RNA can also be found in dendrites (Middleton et al., 2019) and axons (Piper and Holt, 2004). Further, expression of VIAAT RNA (Echigo and Moriyama, 2004) and 5-$HT_{1a}$R RNA (Miyazaki et al., 2013) also occurs in glial cells. Similarly, Nissl bodies are most abundant in neural soma, but are also present in neural dendrites and synaptic terminals, and glial cells (Garcia-Cabezas et al., 2016). I used NeuroTrace™ Nissl dye in low concentrations (1:50 dilution), consistent with manufacturer instructions for selective neuronal labelling. However, I cannot exclude the possibility that Nissl+DAPI staining labels structures other than neural soma.

As described in section 4.3.2, an automated analysis protocol was set up to find objects in the DAPI+Nissl signal that represented cell soma. In this protocol, the minimum object size was set at 25$\mu m^2$ and an object size guide parameter was set at 150$\mu m^2$. This size cut-off prevents identification of cell nuclei (labelled with DAPI) as cell soma, but also serves to prevent Nissl+DAPI staining of fibres and synaptic terminals to be misrepresented as cell soma. However, this method does not exclude from count RNA in fibres overlapping Nissl+DAPI stained soma, nor does it allow to distinguish neurones from glial cells. I acknowledge that limitations to the ability to distinguish neurones from glial cells in the present chapter limits interpretation of this data. To ensure optimal selectivity of neural soma versus glial cells in FISH data analysis, follow up studies could include an RNAScope® FISH probe for a neurone-selective marker such as NeuN (neuronal nuclei) RNA (Rn-Rbfox3n, Advanced Cell Diagnostics product code: 436351). Although a select subset of neurone populations is known to be NeuN negative (for an overview of NeuN negative neurones, see: Wolf et al. (1996); Mullen et al. (1992)), these populations are not present in the regions analysed in this chapter. Because all neurones (but not other cell types) in regions analysed in this chapter express NeuN, co-labelling of NeuN RNA with 5HT1AR and SLC32A1 RNA would enable analysis of the distribution of the latter two selectively in neurones.

A Second limitation to the use of RNAscope® in combination with Nissl and DAPI staining, is that the DAPI+Nissl signal provides an approximation of the outlines of soma, but not an exact outline. Visual inspection revealed that the far extremities of soma were sometimes inadequately labelled. This could result in an underestimation of the size of neural soma, and consequently, in a failure to include labelled RNA strands in the peripheries of cell somas. Further, small 'gaps' or other imperfections in the labelling

could result in an overestimation of the number of cell soma. That is, in image processing, suboptimal Nissl+DAPI labelling could occasionally result in the identification of two or more objects to represent what is in fact a single soma. Here too, the use of a minimum object size (25µm$^2$) as well as an object size guide parameter (150µm$^2$) helped to reduce the occurrence of false positives and to improve the signal-to-noise ratio. Despite the above limitations, misrepresentations of RNA counts can be expected to be minimal. Furthermore, since experimental conditions and quantification methods were automated procedures, it can be inferred that the error rate in RNA counts is similar for neurones across all imaged regions. Therefore, the image analysis produced quantification of RNA count with adequate accuracy for comparisons of relative RNA expression levels across the imaged regions.

Positive and negative controls for RNA hybridization with RNAscope™

In separate experiments with sections from the ventrolateral medulla, I used probes targeting DapB RNA of Bacillus subtilis bacteria (RNAscope® 3-plex Negative Control Probe, Advanced Cell Diagnostics product code: 320871) as negative controls, and observed absence of labelling (data not shown). This indicates absence of non-selective RNA hybridization and fluorescent label binding in the assay. I used PPIB (housekeeping gene) RNA as a positive control. Across all analysed regions, PPIB was observed in nearly all cells, distributed over a wide range of expression levels categories. This indicates that RNA scope protocol was able to label RNA with high sensitivity. The broad distribution across expression level categories can be expected with variability in size of analysed cell soma. High levels of 5HT1AR RNA labelling in the dorsal raphe (73.6% of all analysed soma) is consistent with previous ISH experiments that report high 5-HT$_{1A}$R RNA levels in this region in rat (Zhang et al., 2000). Similarly, high levels of SLC32A1 RNA labelling in the pre-BötC (46.4% of all analysed soma) is consistent with previous reports that approximately half of pre-BötC neurones are immunoreactive for glycinergic and/or GABA-ergic markers (most are glycinergic) (Winter et al., 2009, Koizumi et al., 2013, Manzke et al., 2009). These findings suggest high sensitivity of the 5HT1AR and SLC32A1 ISH probes, and suggests that findings of low expression elsewhere are valid.

Considerations regarding the anatomical locations of imaged regions.

Anatomical regions were imaged from sections on a single anatomical plane. Caudal raphe regions (RMg, RPa, ROb) and N10, N12, and NTScomm were imaged on sagittal sections of the medial medulla, at the lateral edge of the central canal. Therefore, the medial most anatomical structures (RMg, RPa, ROb, NTScomm), images were obtained at their lateral

edge, and more lateral structures (N12, N10) were imaged at their medial edge. Of the regions imaged from sagittal sections of the lateral medulla (BotC, pre-BotC, RVRG, N Amb., XII premotor neurons, $pF_V$/RTN), it should be noted that images of region with XII premotor neurones show the lateral edge of the anatomical region where XII premotor neurons are located. Further, the $pF_V$/RTN region shows a caudal, ventromedial part of the parafacial region. This means the $pF_V$/RTN images cover the anatomical regions where RTN neurons are located, but not the region where the pFRG expiratory oscillator has been most recently located; i.e. at the rostro-lateral edge of the facial nucleus (Huckstepp et al., 2015, Zoccal et al., 2018). Further, regarding the RTN it should be noted that this structure consists of a small population of neurons interspersed in the region imaged, and it is primarily defined by phenotype (see section 1.4.1 for the exact phenotype definition of RTN neurones). Therefore, the distribution of 5-$HT_{1A}$R and SLC32A1 RNA in images of the $pF_V$/RTN region should be considered as descriptive of the region in which RTN neurons are located, rather than as descriptive of RTN neurones exclusively. This is reflected in the presence of some SLC32A1 RNA positive neurons in the imaged region, whereas RTN neurons have been described as lacking in markers of GABAergic and glycinergic neurons (Guyenet et al., 2019).

### *4.4.3 Interpretation of findings*

Systemic 5-$HT_{1A}$ R transmission appears to induce specific effects on respiratory control that are suggestive of inhibitory action or disinhibition at select brainstem regions and mechanisms. Therefore, one would expect the selectivity of functional effects is reflected in the distribution of 5-$HT_{1A}$R RNA over key brainstem regions in respiratory control. Considering this, it is suprising to see that none of the imaged respiratory regions were exempt of 5-$HT_{1A}$R-expressing neurones. The presence of 5-$HT_{1A}$R RNA positive cells in all imaged regions precludes exclusion of any regions and mechanisms as candidate contributors to the nett respiratory effects of 5-$HT_{1A}$ agonism. Therefore, the dissection of the neural mechanisms underlying the effects of systemic 5-$HT_{1A}$ transmission on respiratory function cannot be guided simply by the distribution of 5-$HT_{1A}$R. Further knowledge of the phenotype, connectivity, and function in respiratory control of 5-$HT_{1A}$ R expressing cells is required to understand the mechanisms underlying effects of 5-$HT_{1A}$ transmission in respiratory control.

Despite the above, some regional differences in levels of (co-)expression of 5-$HT_{1A}$R and SLC32A1 RNA provide cues for hypothetical mechanisms underlying the network effect of systemic 5-$HT_{1A}$R transmission. The FISH data in the present chapter will be incorporated in a discussion of putative mechanisms that could underlie the observed effects of systemic administration of NLX-101 on respiratory rhythm and pattern in restful breathing and in the respiratory and sympatho-respiratory responses to hypercapnia and peripheral chemoreceptor activation. Because this discussion is based on converging evidence presented across chapters of this thesis, as well as in the literature, it will be presented in the general discussion (chapter 6).

# Chapter 5: 5-$HT_{1A}$ Receptor Distribution Across Functional Subpopulations of Respiratory Neurones in the Ventral Respiratory Column

## 5.1 Chapter Introduction

To help identify the mechanism underlying the effects of systemic administration of selective 5-$HT_{1A}$R agonist (NLX-101) on respiratory control (see Chapter 3), I established the distribution of 5-$HT_{1A}$R and SLC32A1 RNA in key regions of the respiratory CPG (see Chapter 4). In addition to biochemical phenotype, anatomical location, and connectivity, neurones of the respiratory CPG can be described in terms of their functional phenotype (i.e. activity pattern relative to the respiratory cycle). The functional phenotypes of respiratory neurones ultimately shape network activity of the respiratory CPG, yet the distinct functional phenotypes of respiratory neurones are rarely exclusively associated with a biochemical marker. To further aid identification of mechanisms underlying the effects of 5-$HT_{1A}$ transmission on respiratory control, I investigated the distribution of 5-$HT_{1A}$ receptors in specific functional subpopulations of CPG respiratory neurones.

### *5.1.1 Current understanding of 5-$HT_{1A}$R distribution among CPG respiratory neurone functional subpopulations*

Pioneering studies aimed at identifying the effect of 5-$HT_{1A}$R transmission at the level of functional subpopulations of respiratory neurones have reported hyperpolarization of expiratory (Aug-E) neurones after systemic application or iontophoresis application at the individual neurones in the VRC of anesthetised cats (Richter et al., 1997, Lalley et al., 1994). In these studies, respiratory neurones were recorded intracellularly under voltage or current clamp, and their functional subtype was identified by their discharge pattern relative to PN motor output. Later, using a similar approach, Manzke et al. (2009) recorded 4 Post-I/Dec-E neurones in which, after systemic administration of low doses of 8-OH-DPAT, they registered a release from Early-I inhibitory input. The loss of early-I inhibitory input caused the recorded Post-I neurones to advance onset of their bursting activity into the inspiratory phase. At higher concentrations (8-OH-DPAT 10-50 μg-$kg^{-1}$), this effect was combined with a hyperpolarizing $K^+$ current which resulted in a silencing of the Post-I neurones throughout most of the respiratory cycle (with only brief bursting activity during late inspiration). At the network level, the authors observed an increase in respiratory rate due to a shortening of inspiratory and expiratory phase durations

recorded from the PN. From the shortening of expiratory phase duration, along with the loss of bursting activity during the Post-I phase recorded from (what under control conditions were) Post-I neurones, the authors inferred that systemic administration of 8-OH-DPAT resulted in a complete loss of post-I activity at the network level, and a transition from a tri-phasic respiratory pattern (I, Post-I, E2) to a bi-phasic respiratory pattern (I, E2) (see section 1.7.3).

Ways in which 5-$HT_{1A}$R transmission can affect target cells include: inhibition of intracellular mechanisms mediated by the CA-cAMP-PKA pathway; GIRK channel activation; and activation of voltage gated $Ca^{2+}$ channels (Richter et al., 2003) (see section 1.7.3, **Figure 1-9**). 5-$HT_{1A}$R transmission is also to reported have neuromodulatory effects, as it augmented glycine-activated inhibitory $Cl^-$ currents in HEK293 cells co-expressing 5-$HT_{1A}$R and $Gly_{\alpha 3}$ receptors (Manzke et al., 2010). In *in situ* WHBP of juvenile rats, the augmented PN rate in response to 8-OH-DPAT was abolished when glycine receptors were blocked by systemic application of strychnine before or after administration of 8-OH-DPAT (Manzke et al., 2010, Manzke et al., 2009). Furthermore, IHC labelling showed that $Gly_{\alpha 3}$R was expressed in glycinergic neurones in both the BötC and pre-BötC, and 5-$HT_{1A}$R expression was observed on glycinergic neurones of the pre-BötC (Manzke et al., 2010, Manzke et al., 2009). On the basis of these findings, it has been suggested that network effects of systemic 8-OH-DPAT administration may be shaped not only by 5-$HT_{1A}$R activated inhibitory $K^+$ channels, but to a large extend by 5-$HT_{1A}$R mediated modulation of $Gly_{\alpha 3}$ receptors, resulting in potentiation of glycine activated inhibitory chloride currents in select populations of respiratory neurones in the VRC (Manzke et al., 2009, Manzke et al., 2010, Shevtsova et al., 2011).

Computational modelling simulations (Shevtsova et al., 2011) suggested that the effect of systemic 8-OH-DPAT administration on respiratory control is largely mediated by 5-$HT_{1A}$R-dependent potentiation of glycinergic currents in Early-I neurones and Aug-E neurones at low doses, in combination with hyperpolarizing $K^+$ currents in Early-I and Post-I neurones due to activation of GIRK channels at higher doses. The augmented glycinergic inhibition at glycinergic Early-I neurones was suggested to result in a loss of inspiratory post-synaptic inhibition at Post-I neurones, resulting in the advanced onset of bursting activity in Post-I neurones. The augmented glycinergic inhibition at Early-I neurones, as well as augmented glycinergic inhibition at GABAergic and glycinergic Aug-E neurones was suggested to underlie a shortening of I and E2 phases, respectively. This model was able to reproduce the effects of systemic administration of 8-OH-DPAT on Post-I neurones and at network

level as observed in the experimental single cell and PN recordings by Manzke et al. (2009). The model was also able to reproduce the previously reported hyperpolarization and inhibition of a VRC Aug-E neurones after systemic administration of 8-OH-DPAT in anesthetised cats (Lalley et al., 1994). Furthermore, the model predicted 5-$HT_{1A}$R-induced loss of Post-I activity at the network level, an effect inferred from the loss of activity recorded in Post-I neurones by Manzke et al. (2009).

*Gaps in understanding of the effect of 5-$HT_{1A}$R agonism on the VRC respiratory network*

The above model provided the most comprehensive working hypothesis currently available to describe putative mechanisms underlying the effect of systemic 5-$HT_{1A}$ receptor agonism on respiratory control. However, it relied on several assumptions not supported by experimental verification, some of which have already been pointed out in the discussion of chapter 3 (section 3.4.3). First, the model attributed effects of 5-$HT_{1A/7}$R agonism exclusively to mechanisms mediated by 5-$HT_{1A}$ R. Second, effects of anaesthesia in the experimental findings on which the model was based (Manzke et al., 2009) cannot be excluded. Third, the model extrapolated the effects of systemic 8-OH-DPAT administration experimentally observed in a small set of single cell recordings of VRC Post-I neurones (n = 4 neurones) (Manzke et al., 2009) to network level responses (i.e. changes in cVN Post-I activity). (Manzke et al., 2009). The limited sample size of Post-I neurone recordings does not permit such inference with confidence. In fact, experimental findings presented in Chapter 3 of this thesis do not support a phase shift or abolition of Post-I activity at the network level in response to systemic administration of a selective 5$HT_{1A}$R agonist (NLX-101) (see section 3.4.3).

It is possible that the discrepancy between experimental observations at the network level, and observations at the level of individual neurones is due to a certain degree of heterogeneity in the response to systemic 5-$HT_{1A}$R agonism among the population of neurones with a Post-I discharge pattern. This could be due to heterogeneity of 5-$HT_{1A}$R and/or $Gly_{\alpha 3}$R (co-)expression in the population of Post-I neurones themselves, but also due to heterogeneity within populations of neurones that project to Post-I neurones (notably, Early-I neurones). This remains to be verified experimentally.

The fourth point is that the model made assumptions with regard to the distribution of 5-$HT_{1A}$ R, as well as $Gly_{\alpha 3}$R (co-)expression over functionally distinct subpopulations of respiratory neurones in the VRC (e.g. Aug-E neurones, Post-I neurones, Early-I neurones, etc). Although co-expression of both receptor types is anatomically confirmed in VRC

respiratory regions in which the relevant neurone populations are concentrated (i.e. the BötC and pre-BötC), experimental data on 5-$HT_{1A}$ expression at specific functional subtypes of respiratory neurones is limited to a small number of expiratory (Post-I/Dec-E and Aug-E) neurones. Furthermore, in only one of these recordings 8-OH-DPAT was administered juxta-cellularly to (Aug-E) neurone via iontophoresis (reported in Lalley et al. (1994)). In all other recordings, 8-OH-DPAT was administered systemically, and one cannot exclude that effects on the recorded neurone were induced by indirect network interactions rather than by direct effects at 5-$HT_{1A}$R of the recorded cell.

### *5.1.2 Chapter Aims and Hypotheses*

**Chapter aim:** The aim of this chapter is to establish which functionally defined subpopulations of respiratory neurones respond to 5-$HT_{1A}$R agonist, allowing inference of 5-$HT_{1A}$R expression. Functional phenotypes of respiratory neurones are defined by their discharge pattern relative to the respiratory cycle. Previous literature, along with the results presented in chapters 3 and 4 of this thesis, suggest that 5-$HT_{1A}$ transmission likely affects respiratory control at multiple sites in the respiratory network (e.g. the VRC and the PBc). However, the theoretical framework for network interactions that shape the respiratory rhythm, and the putative mechanisms by which 5-$HT_{1A}$ transmission may affect these interactions, is best developed for the VRC. Therefore, to capitalize on the currently existing body of knowledge, I focused on VRC respiratory neurones.

**Experiment**: To infer 5-$HT_{1A}$R expression at functionally defined respiratory neurones of the VRC, I performed extracellular single unit recordings combined with juxta-cellular pico-ejections of 5-$HT_{1A}$R selective agonist NLX-101, combined with recordings of the PN in *in* situ WHBP of juvenile rats.

**Hypothesis:** Based on previous literature, I expect 5-$HT_{1A}$R expression predominantly in VRC respiratory neurones with an Early-I discharge pattern, as well as in VRC neurones with an Aug-E discharge pattern. Experimental findings also suggest presence of 5-$HT_{1A}$ receptors in Post-I neurones.

## 5.2 CHAPTER METHODS.

### *5.2.1 Description and justification of extracellular recordings combined with juxta-cellular pico-ejection of drugs*

Extracellular single unit recordings in the *in situ* WHBP allow for the identification of respiratory neurone functional subtypes through evaluation of the recorded neurones burst pattern and its phase relation with simultaneously recorded PN activity. With the use of a multi-barrel microelectrode, extracellular single unit recordings can be combined with juxtacellular drug pico-ejections. This enables us to infer receptor expression at individual functionally identified neurones in the *in situ* WHBP. I can exclude wider network effects induced by drug pico-ejection through monitoring peripheral nerve respiratory output. While I cannot exclude possible effect on neighbouring cells, a high multi-barrel micro-electrode tip resistance (15-20MΩ) ensures volumes of drug pico-ejected from the pipette are almost insignificant, and diffusion is minimal. I know from experience that if any sizable volume of drug solution is ejected, the recorded cell dies or is pushed away. Therefore, the stability of the recording during pico-ejection can be used as a control to ensure minimal volumes of drug solution are pico-ejected and possible effects on neighbouring cells are unlikely. Pico-ejection of GABA or Glutamate can be used as a positive control to verify effective drug delivery. Because I use i*n situ* WHBP, there is no need for the use of anaesthetics, and their potential confounding effects can be excluded. Thus, peripheral nerve recordings in the *in situ* WHBP, combined with extracellular single unit recordings and juxtacellular pico-ejectons of 5-$HT_{1A}$ agonist (NLX-101), GABA, or glutamate enable us to establish expression of 5-$HT_{1A}$ receptors in functionally identified respiratory neurone subtypes.

### *5.2.2 Additional surgical procedures for extracellular recordings in in situ WHBP*

In situ WHBP were prepared as described in the General Methods (section 2.2.2), only the PN was exposed and cut for nerve recordings. Additional surgical procedures were performed to enable a dorsal approach of the brainstem with multi-barrel electrodes for extracellular recordings combined with juxtacellular pico-ejection. For exposing the dorsal surface of the medulla, all muscle and connective tissue surrounding dorsal and lateral regions of the atlanto-occipital joint were removed. The exoccipital bones and atlanto-occipital membrane were carefully cut, and the occipital bone was removed to expose the dorsal surface of the brainstem and cerebellum. Subsequently, the meninges covering the cerebellum were removed and the cerebellar peduncles were cut, after which, the

cerebellum was lifted and removed. This enabled unobstructed access to the dorsal surface of the medulla. The preparation was placed in prone position in the recording chamber with head fixed in ear bars and an incisor bar, set up so that the medulla was oriented horizontally. Prior to each descend with multi-barrel electrodes into the medullary tissue, the pia was carefully punctured and removed from the site of entrance. This prevented the breaking of electrode tips upon descending into medullary brain tissue.

### *5.2.3 Multibarrel electrodes for extracellular recording and drug pico-ejection*

Multibarrel micro-electrodes for combined extracellular single unit recordings combined with juxtacellular drug pico-ejection were custom made by fastening together 3 borosilicate glass capillaries (GC150-F10, Harvard Apparatus, Kent, United Kingdom). These were twisted to conjoin under heat and pulled to a single tip with a pipette puller (PE-2 8405, Narisighe, Tokyo, Japan). One of three barrels of the multibarrel electrodes was filled with NLX-101 solution (1mM, pH 7.3), and a second barrel was filled with GABA solution (500mM, pH 7.3), Glycine solution (10Nm, pH 7.3), or Glutamic acid solution (10mM, pH 7.3). Positive air pressure for pico-ejection was applied to each barrel independently from a pico-pressure device (Picospritzer III, Intracel Ltd., Shepreth, United Kingdom). The third barrel of the multibarrel electrode was filled with NaCl (3M, pH 7.3) solution and fitted a recording electrode for extracellular recordings. The multibarrel electrode tip was broken to obtain a resistance of 15-20 MΩ. A reference electrode was suspended in the perfusate filled cranial cavity of the decerebrated preparation, in proximity of the brainstem. The multibarrel electrode was mounted on a hydraulic micromanipulator (MO-10, Narishige International LTD, London, United Kingdom) which was placed on a 3D mechanical micromanipulator (SM-11 11020, Narishige International LTD, London, United Kingdom)

### *5.2.4 Solutions and Pharmacological Agents*

NLX-101 fumarate (Neurolixis Inc. Dana Point, USA) solution (1mM) for pico-ejections was made up with aCSF (Harvard Apparatus, Holliston, U.S.A.). Glycine solution (10mM) (ab120050, Abcam, Cambridge, UK) for pico-ejection was made up with aCSF. GABA (A-5835, Merck & Co, Kenilworth, U.S.A.) solution (500mM) for pico-ejections was made up with saline (0.9%). L-Glutamic Acid solution (10mM) (G-1626, Merck & Co, Kenilworth, U.S.A.) for pico-ejections was made up with saline (0.9%). pH Recording electrodes were

filled with saline (3M). All solutions were adjusted to pH 7.3 with NaOH and HCl solution in $H_2O$.

### *5.2.5* Experimental protocols, data acquisition, processing, and analysis

Experimental protocols

For extracellular single unit recordings of medullary respiratory neurones, combined with drug (NLX-101, GABA, or glutamate) pico-ejections, combined with PN recordings, *in situ* WHBP of juvenile (50-90g) male rats were made as described in General Methods (section 1.2.2) with additional surgical procedures as described in section 4.1.2. When an eupnoeic ramping pattern was established of the PN, a multi-barrel electrode was slowly descended vertically and unilaterally into the medullary VRC region into the medulla (coordinates from Obex Callimus Scriptorius: AP = + 0.6 - 1.8mm; L = ± 1.4−2.0 mm; V = -1.8-2.7mm) (Fong and Potts, 2006). Once an extracellular recording of a VRC respiratory neurone was obtained, the cell was exposed to pico-ejection of NLX-101 (1mM). Pico-ejection pressure started at 5-PSI, and was sequentially increased to maximally 45 PSI in 10 PSI increments, whereby each incremental step had a duration of three to five respiratory cycles. If, at any step during this pico-ejection sequence, a notable change of action potential (AP) frequency was observed by the experimenter, pico-ejection was stopped after completion of that ejection step. If no change of AP frequency during pico-ejection was observed, pico-ejection was stopped after the final step of the sequence, at maximum pico-ejection pressure (50 PSI). Recovery from any response to drug pico-ejection was near instantaneous, suggesting that only the minimally required volume of drug was ejected juxta-cellular to the recorded neurone to elicit a response. After a brief interval, this pico-ejection sequence was repeated with GABA (500mM), Glycine (10mM), or Glutamate (10mM) pico-ejection as a positive control.

*Data acquisition*

Data acquisition parameters and the hardware and software used for PN recordings are described in the General Methods (section 2.2.4). Single unit electrophysiological recordings were amplified (20K) and bandpass filtered (60 Hz to 3 kHz) (Model 1800 Microelectrode AC amplifier, A-M systems, Sequim, USA). 50 Hz Electrical interference was eliminated with the use of a Humbug noise eliminator (AM-systems, Sequim, USA). A-D conversion was performed using a Micro 1401 data-acquisition unit (Cambridge Electronic Design Ltd, Cambridge, UK) and Spike2 data acquisition and analysis software (Cambridge Electronic Design Ltd., Cambridge, UK).

*Data processing and analysis*

From the PN recording, timepoints of onset of each respiratory cycle, and respiratory cycle durations were obtained with a custom script (Abdala Sheikh, 2020) in Spike2 data analysis software (Cambridge Electronic Design Ltd., Cambridge, UK). In the extracellular single unit recording, a waveform analysis function built in Spike2 was applied to enhance the action potential (AP) signal-to-noise ratio. That is, representative AP waveforms were manually selected to construct an AP waveform template, which was then used to automatically search the extracellular recording for matching waveforms. The resulting selection of AP waveforms was manually checked. AP waveforms and match inclusion parameters were such that AP's should remain detectable if the AP signal were slightly depressed due to mechanical displacement during pico-ejection. On the other hand, waveforms of a different shape (e.g. ECG or other noise) would not match the AP template waveform.

The timepoint of onset of each selected AP waveform was marked to establish the normalised burst rate per respiratory cycle of the recorded neurone (AP-count per respiratory cycle: respiratory cycle duration (s)). Additionally, burst pattern histograms were made with AP count per 0.05s bin (AP/.05s). AP/.05s histogram data relative to PN activity was used to categorise the respiratory neurone among known functional subtypes. These functional subtypes are: neurones with a pre-inspiratory and inspiratory phase spanning ramping burst pattern (Pre-I/I); Early-inspiratory (early-I) neurones with a decrementing burst patter spanning the inspiratory phase; neurones with an incrementing (ramping) burst pattern spanning the inspiratory phase (Ramp-I); Neurones with a decrementing burst pattern spanning the expiratory (Dec-E neurones) or post-inspiratory phase (Post-I neurones); and neurones that have an incrementing (augmenting) burst pattern occurring during the expiratory phase, with termination at onset of the inspiratory phase (Aug-E). Both Post-I and Dec-E neurones are most found in BötC, presenting with a decrementing burst pattern through expiration, and both are important for inspiratory to expiratory phase transitioning. Depending on physiological conditions, the activity pattern of these two functional subtypes of respiratory neurones can overlap, and they cannot conclusively be distinguished by their burst pattern relative to PN activity. Therefore, Post-I and Dec-E neurones were pooled (Post-I/Dec-E) in the classifications applied here.

For each drug pico-ejection, a sample of five consecutive respiratory cycles immediately preceding that pico-ejection was selected, and their firing frequencies (AP/s) per

respiratory cycle were used to establish firing frequency baseline averages and standard deviation (SD) values. Firing frequency (AP/s) values of two respiratory cycles during pico-ejection at the final and highest pico-ejection pressure were selected to calculate the average firing frequency (AP/s) during drug exposure. Any change in activity of the recorded cell during drug pico-ejection was expressed as the percentage change in average firing frequency during pico-ejection relative to the baseline average firing frequency (ΔAP/s % = ((pico-ejection average AP/s - baseline average AP/s)/baseline average AP/s )*100). Cells were classified as responsive to NLX-101, GABA, or Glycine if the reduction in average firing frequency (AP/s) during pico-ejection was equal to or greater than two times the SD of the average firing frequency (AP/s) of the baseline sample. Similarly, cells were classified as responsive to glutamate if the increase in average firing frequency (AP/s) during pico-ejection was equal to or greater than two times the SD of the average firing frequency (AP/s) of the baseline sample. There were two single unit recordings for which sample sizes are different than described above. The first is a Pre-I/I neurone recording (NLX-101 pico ejection: baseline = 2 respiratory cycles, pico-ejection = 1 respiratory cycle. Glutamate pico-ejection: baseline = 3 respiratory cycles; pico-ejection = 1 respiratory cycle), and the second is a Post-I/Dec-E neurone recording (NLX-101 pico ejection: baseline = 5 respiratory cycles, pico-ejection = 2 respiratory cycles. GABA pico-ejection: baseline = 2 respiratory cycles; pico-ejection =2 respiratory cycles).

Extracellular recordings were excluded from the dataset if cells were classified non-responsive to NLX-101 pico-ejection, as well as non-responsive to pico-ejection of Glutamate, GABA, or Glycine. The lack of response to positive control pico-ejections indicated a likely failure of drug administration (e.g. electrode tip was too far from the cell). Cells were also excluded if pico-ejection resulted in a significant loss of AP amplitude. This suggested that the pico-ejection volume was too high due to a damaged micro-electrode tip. If this was observed, the electrode was retracted and replaced. These criteria resulted in exclusion of 3 recordings from analysis (two Post-I/Dec-E recordings, and one Aug-E recording).

## 5.3 CHAPTER RESULTS

I performed PN recordings, combined with single unit extracellular recordings of respiratory neurones of the ventral respiratory column, combined with juxtacellular pico-ejection of NLX-101 solution (1mM in aCSF, pH 7.3) and pico-ejection of GABA (500mM in saline, pH = 7.3), Glycine (10mM in aCSF, pH = 7.3), or glutamic acid (10mM in saline (0.9%), pH = 7.3) in the *in situ* WHBP of juvenile rats. Via this approach I identified functional subtypes of respiratory neurones in the VRC that were responsive to the selective 5-$HT_{1A}$R agonist, NLX-101 (i.e. functional subtypes that express 5-$HT_{1A}$ receptors).

### *5.3.1 Overall responsiveness of respiratory neurones to juxtacellular pico-ejection of NLX-101*

**Figure 5-1A** shows the relative and absolute quantities of neurones that are classified as responsive to juxtacellular pico-ejection of NLX-101. In total, 46 single unit recordings of VRC neurones were included in analysis, of which 25 (54%) neurones were inhibited by NLX-101.

### *5.3.2 Responsiveness of Ramp-I respiratory neurones to juxtacellular pico-ejection of NLX-101*

Ramp-I neurons were identified by their incrementing inspiratory burst pattern (see **figure 5-2A** for representative traces of a Ramp-I neurone and simultaneously recorded PN activity). **Figure 5-2A$_1$** shows the response of that neurone to pico-ejection of NLX-101, whereas **Figure 5-2A$_2$** shows the response of that same neurone to subsequent GABA pico-ejection. Twenty-two Ramp-I neurones were identified in recordings from in *situ* WHBP of 11 different rats. In 21 of these recordings, NLX-101 pico-ejections were paired with a subsequent pico-ejection of inhibitory amino acid (GABA or glycine). The remaining Ramp-I recording did not have a positive control but was inhibited by NLX-101. Fifteen out of the 22 (67%) recorded Ramp-I respiratory neurones of the VRC were inhibited by NLX-101. (see **figure 5-1A**). **Figure 5-1B** shows the average effect sizes of inhibition in response to juxtacellular pico-ejection of NLX-101 inhibition (or lack thereof), as well as the average effect sizes of inhibition in response to juxta-cellular pico-ejection of GABA or Glycine (pooled) for the recorded samples of NLX-101 responsive, and non-responsive Ramp-I neurones. Of the 15 NLX-101 responsive Ramp-I neurons, the average firing frequency (AP/s) was reduced by 63% upon juxtacellular NLX-101 pico-ejection. In the subset of this population of cells in which juxtacellular pico ejection of GABA or glycine was performed,

this resulted in a reduction of the average firing frequency (AP/s) by 94% (**Figure 5-1B**). Of the 7 Ramp-I neurons classified as NLX-101 non-responsive, the average firing frequency (AP/s) was increased by 4% upon juxtacellular NLX-101 pico-ejection. In the same population of cells, juxtacellular pico ejection of GABA or Glycine resulted in a reduction of the average firing frequency (AP/s) by 81% (**Figure 5-1B**).

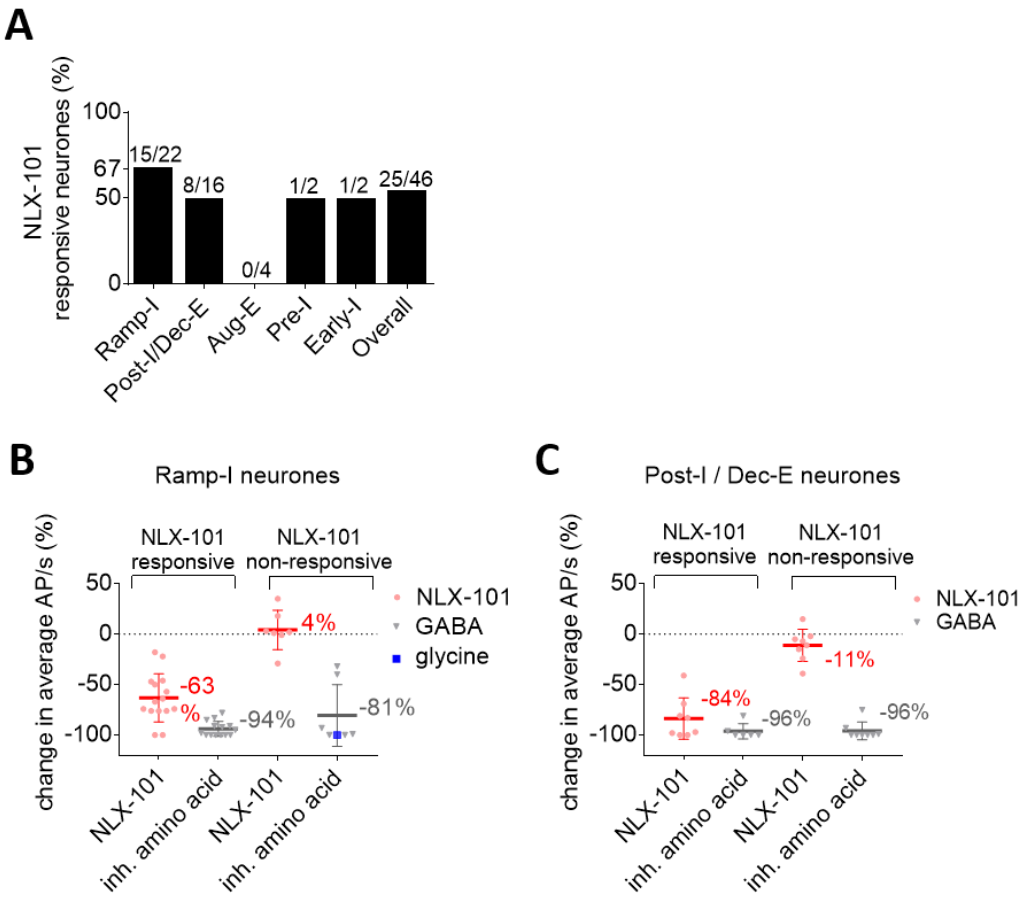


**Figure 5-1:** Responses of functional subpopulations of VRC respiratory neurones to juxta-cellular pico-ejection of NLX-101

Figure **A** shows, for each functionally identified group of respiratory neurones, percentages and counts of neurones that are inhibited by NLX-101. Neurones were classified as NLX-101 responsive if change from baseline in AP/s during NLX-101 pico-ejection was greater than twice the SD of the baseline sample. **(B)** Percentage change in average firing frequency (AP/s) during NLX-101 and inhibitory amino-acid pico-ejection relative to baseline average firing frequencies (AP/s) for all NLX-101 responsive and non-responsive Ramp-I neurones. n = 22 neurones from 11 rats. One of the plotted neurones did not have a positive control (GABA,glycine,or L-glutamic acid) pico-ejection, but was inhibited by NLX-101. **(C)** Percentage change in average firing frequency (AP/s) during NLX-101 and inhibitory amino-acid pico-ejection relative to baseline average firing frequencies (AP/s) for all NLX-101 responsive and non-responsive Post-I/Dec-E neurones. n = 16 neurones from 11 rats. In one recording NLX-101 pico-ejection was paired with subsequent pico-ejection of L-Glutamic acid (not shown). One of the plotted Post-I/Dec-E recordings did not have a positive control but was inhibited by NLX-101.

### *5.3.3 Responsiveness of Post-I/Dec-E respiratory neurones to juxtacellular pico-ejection of NLX-101*

Post-Inspiratory and decrementing expiratory (Post-I/Dec-E) neurons were identified by their decrementing burst pattern during expiration, with onset immediately after termination of the inspiratory phase. **Figure 5-2B** shows representative traces of a Post-I/Dec-E neurone and simultaneously recorded PN activity. **Figure 5-2B$_1$** shows the response of that neurone to pico-ejection of NLX-101, whereas **figure 5-2B$_2$** shows the response of the same neurone to subsequent GABA pico-ejection. 16 Recordings of Post-I or Dec-E neurones were obtained from 11 rats. In 14 of these recordings, NLX-101 pico-ejections were paired with a subsequent pico-ejection of GABA. In one recording NLX-101 pico-ejection was paired with subsequent pico-ejection of L-Glutamic acid. The remaining Post-I/Dec-E recording did not have a positive control but was inhibited by NLX-101. Eight of the 16 (50%) recorded Post-I/Dec-E respiratory neurones of the VRC were inhibited by NLX-101 (see **figure 5-1A**). **Figure 5-1C** shows the average effect sizes of inhibition (or lack thereof) in response to juxtacellular pico-ejection of NLX-101, as well as the average effect sizes of inhibition in response to juxtacellular pico-ejection of GABA (if obtained) for the recorded samples of NLX-101 responsive, and NLX-101 non-responsive Post-I/Dec-E neurones. Of the 8 NLX-101 responsive Post-I/Dec-E neurons, the average firing frequency (AP/s) was reduced by 84% upon juxta-cellular NLX-101 pico-ejection. In the subset of this population of cells in which juxta-cellular pico ejection of GABA was performed, this resulted in a reduction of the average firing frequency (AP/s) by 96% (**figure 5-1C**). Of the 8 Post-I/Dec-E neurones classified as NLX-101 non-responsive, the average firing frequency (AP/s) was decreased by 11% upon juxta-cellular NLX-101 pico-ejection. In the subset of this population of cells in which juxta-cellular pico ejection of GABA was performed, this resulted in a reduction of the average firing frequency (AP/s) by 96% (**figure 5-1C**).

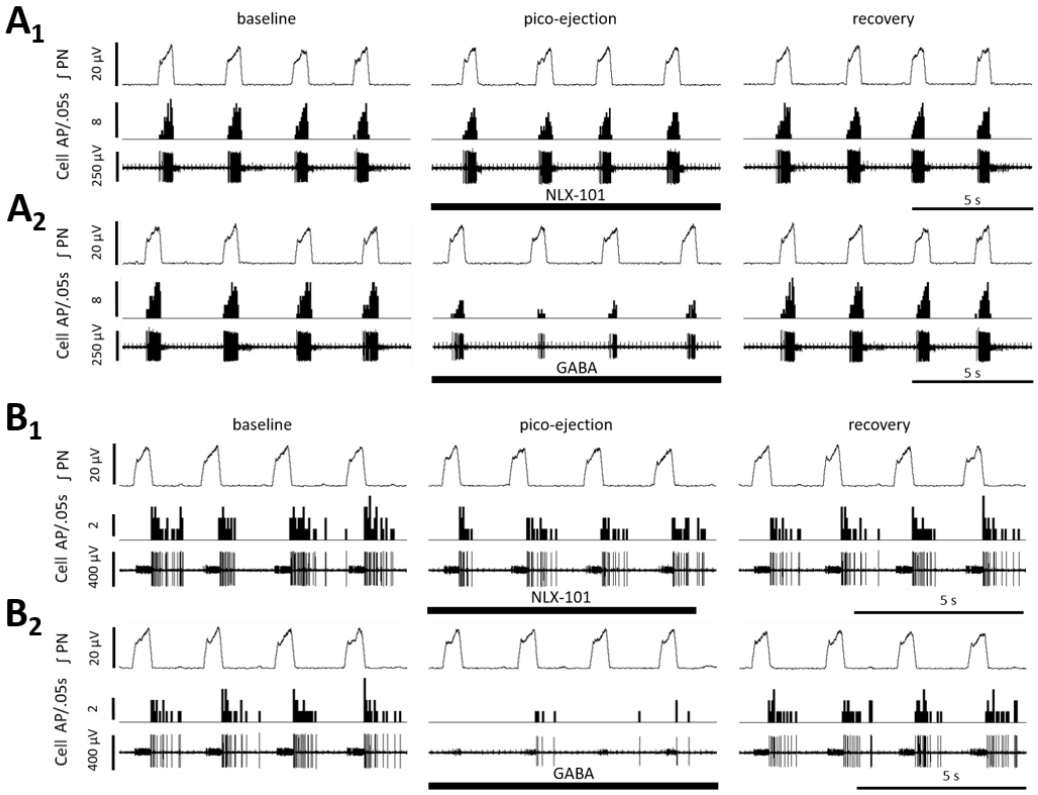


**Figure 5-2:** Representative traces of extracellular recordings of a Ramp-I, and a Post-I/Dec-E neurone with pico-ejections of NLX-101 and GABA.

**A** Shows representative traces of extracellular recordings (Cell), histograms with extracellularly recorded action potentials per 0.05s bin (AP/.05s), and integrated phrenic nerve activity (∫PN). **$A_1$** Shows activity of a Ramp-I neurone during baseline, pico-ejection of NLX-101 (22% reduction in average firing frequency (AP/s) relative to baseline), and recovery. **$A_2$** shows the activity of the same cell in response to GABA pico-ejection (83% reduction in average firing frequency (AP/s) relative to baseline). **$B_1$** and **$B_2$** are representative traces from a Post-I/Dec-E neurone in the same way as $A_1$ and $A_2$. During pico-ejection of NLX-101 and GABA, reduction of firing frequencies (AP/s) compared to the corresponding baseline averages is 41% and 81%, respectively. Both neurones shown in $A_{1,2}$ and $B_{1,2}$ are classified as NLX-101 responsive.

### *5.3.4 Responsiveness of Aug-E respiratory neurones to juxtacellular pico-ejection of NLX-101*

Augmenting expiratory (Aug-E) neurons were identified by their augmenting burst pattern with onset during the expiratory phase and termination of burst activity at the onset of the inspiratory phase. **Figure 5-3C** shows representative traces of an Aug-E neurone and simultaneously recorded PN activity**. Figure 5-3C$_1$** shows the response of that neurone to pico-ejection of NLX-101, whereas **figure 5-3C$_2$** shows the response of the same neurone to subsequent GABA pico-ejection. Four Recordings of Aug-E neurones were obtained from *in situ* WHBP of 4 rats. None of these recorded neurones were classified as responsive to juxta-cellular NLX-101 pico-ejections (see **figure 5-1A**), while all were responsive to a subsequent pico-ejection of GABA.

### *5.3.5 Responsiveness of Pre-I/I respiratory neurones to juxtacellular pico-ejection of NLX-101*

Pre-inspiratory and inspiratory (Pre-I/I) neurones were identified by their incrementing burst pattern during inspiration, with onset slightly prior to onset of the inspiratory phase. **Figure 5-3A** shows representative traces of a Pre-I/I neurone and simultaneously recorded PN activity. **Figure 5-3A$_1$** shows the response of a Pre-I/I neurone to pico-ejection of NLX-101, whereas **figure 5-3A$_2$** shows the response of that same neurone to subsequent L-glutamic acid pico-ejection. Two recordings of Pre-I/I neurones were obtained from *in situ* WHBP of two rats. One of the two recordings was responsive to juxtacellular pico-ejection of NLX-101 (see **figure 5.1A**), which was paired with a subsequent pico-ejection of L-glutamate (see **figure 5-3A**). In the other recording NLX-101 pico-ejection was paired with subsequent pico-ejection of glycine.

### *5.3.6 Responsiveness of Early-I respiratory neurones to juxtacellular pico-ejection of NLX-101*

Early inspiratory (Early-I) neurones were identified by their decrementing burst pattern during inspiration. See f**igure 5-3B** for representative traces of an Early-I neurone and simultaneously recorded PN activity. **Figure 5-3B$_1$** shows the (lack of) response of an Early-I neurone to pico-ejection of NLX-101, whereas **figure 5-3B$_2$** shows the response of that same neurone to subsequent juxtacellular pico-ejection of GABA. Two recordings of Early-I neurones were obtained from *in situ* WHBP of two rats. One of the two recordings was responsive to juxtacellular pico-ejection of NLX-101 (see **figure 5-1A**). The other recording

was not responsive to juxtacellular pico-ejection of NLX-101, but was inhibited by subsequent pico-ejection of GABA.

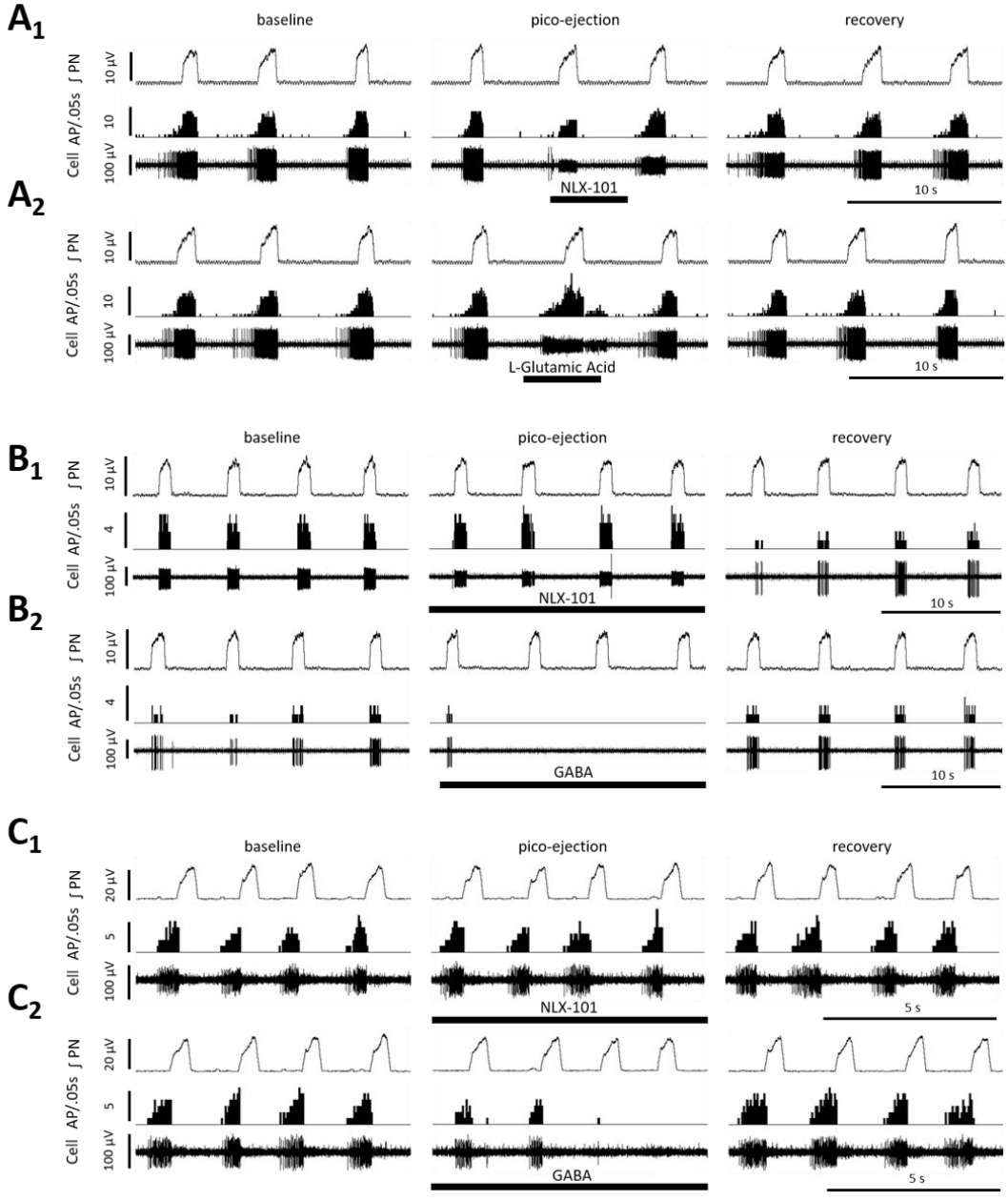


**Figure 5-3:** Representative traces of extracellular recordings of a Pre-I, an Early-I, and an Aug-E VRC neurone with pico-ejections of NLX-101, L-glutamic acid, and GABA.

Representative traces of extracellular recordings (Cell), histograms with extracellularly recorded action potentials per 0.05s bin (AP/.05s), and integrated phrenic nerve activity (∫PN).Figure caption is continued on the next page.

## 5.4 CHAPTER DISCUSSION

### *5.4.1 Summary and review of results in light of aims and hypotheses*

To help identify mechanisms underlying the effects of systemic 5-$HT_{1A}$ transmission on respiratory control, the present chapter presents an exploratory investigation of 5-$HT_{1A}$R expression (inferred from agonist-mediated inhibition) at functionally identified individual respiratory neurones in the intact, unanaesthetised respiratory network in *in situ* WHBP of rat. Fluorescence ISH evidence of 5-$HT_{1A}$R RNA and SLC32A1 RNA in the BötC, pre-BötC, and RVRG (chapter 4) as well as IHC evidence of 5-$HT_{1A}$R and GlyT2 expression in the pre-BötC (Manzke et al., 2009, Manzke et al., 2010) suggest that 5-$HT_{1A}$R are present in inhibitory neurones of the VRC. Previously published experiments with iontophoresis of 5-$HT_{1A/7}$R agonist (8-OH-DPAT) and single cell recordings at individual VRC neurones in anesthetised cats suggested that 5-$HT_{1A}$R are expressed in Aug-E neurones of cats (Richter et al., 1997, Lalley et al., 1994). Other experimental evidence with systemic administration of 8-OH-DPAT and single cell recordings of Post-I neurones in the VRC of anesthetised cats suggest that 5-$HT_{1A}$ may also be expressed in inhibitory inspiratory neurones that project to Post-I neurones, as well as in Post-I neurones themselves (Manzke et al., 2009).

**Figure 5-3, caption continued from previous page:** Representative traces of extracellular recordings (Cell), histograms with extracellularly recorded action potentials per 0.05s bin (AP/.05s), and integrated phrenic nerve activity (∫PN). **$A_1$** Shows activity of one of two recorded Pre-I/I neurones during baseline, pico-ejection of NLX-101 (39% reduction in average firing frequency (AP/s) relative to the baseline average), and recovery. **$A_2$** shows the activity of the same cell in response to pico-ejection of L-glutamic acid (44% increase in average firing frequency (AP/s) relative to the baseline average). In the same fashion, **$B_{1,2}$** shows representative traces from one of two recorded Early-I neurones. **$B_1$**, shows a 4% increase in average firing frequency (AP/s) relative to the baseline average. **$B_2$** Shows full inhibition in response to GABA pico-ejection in the same cell. This cell is classified as an NLX-101 non-responsive neurone. **$C_{1,2}$** Shows representative traces from one of four recorded Aug-E neurones. **$C_1$**, shows a 13% reduction in average firing frequency during (AP/s) NLX-101 pico-ejection relative to the baseline average. **$C_2$** Shows strong inhibition (95% reduction in average firing frequency (AP/s)relative to the baseline average) in response to GABA pico-ejection in the same cell. This cell is classified as an NLX-101 non-responsive neurone.

The present study is the first to establish 5-$HT_{1A}$ transmission at functionally identified individual respiratory neurones of the VRC in rat, and the first to do so in an unanaesthetised intact respiratory CPG network. In total 46 respiratory neurones were recorded, distributed across 5 distinct functional subtypes defined by their discharge pattern relative to the respiratory cycle. Prior to the present experiments, 5-$HT_{1A}$R transmission was established in a single Aug-E neurone recording combined with juxtacellular iontophoresis of 8-OH-DPAT in anesthetised cat (Lalley et al., 1994). As such, the present work offers a substantial expansion of the existing knowledge of 5-$HT_{1A}$R distribution across functional phenotypes of respiratory neurones in the VRC.

Recordings of the PN, combined with extracellular recordings of VRC respiratory neurones, and with juxtacellular pico-ejection of NLX-101 in the *in situ* WHBP, revealed that 5-$HT_{1A}$R are expressed in subsets of the following functional subpopulations: Ramp-I neurones (15 out of 22 neurones were inhibited by NLX-101); Post-I/Dec-E neurones (8 out of 16 neurones inhibited); Pre-I/I neurones (1 out of 2 neurones inhibited); and Early-I neurones (1 out of 2 neurones inhibited). An additional four augmenting expiratory neurones (Aug-E) were recorded that were all non-responsive to juxtacellular pico-ejection of NLX-101. All respiratory neurones that were non-responsive to pico-ejection of NLX-101, were responsive to pico-ejection of glycine, GABA, and/or glutamic acid. This suggests that the absence of a response to NLX-101 pico-ejection is likely not due to failure of drug delivery, but rather absence of 5-$HT_{1A}$R at the recorded neurone.

To summarize, data in the present chapter demonstrate that: [1] 5-$HT_{1A}$R presence is established among Ramp-I, Post-I/Dec-E, Pre-I, and Early-I respiratory neurones in the VRC; and [2] functional subpopulations of respiratory neurones as defined per discharge pattern appear heterogeneous regarding 5-$HT_{1A}$R expression. I hypothesised that 5-HT1A R were predominantly expressed in Early-I, Post-I and Aug-E neurones (see section 5.1). Although our findings indicate presence of 5-$HT_{1A}$ R expression in Early-I, Post-I and Aug-E neurones, 5-$HT_{1A}$ R are not exclusively present in these subpopulations, and there is thus far no indication of increased 5-$HT_{1A}$ R expression in any specific functional phenotype relative to others in the VRC.

### *5.4.2 Technical considerations*

Potential indirect effects of drug pico-ejection on the recorded neurones.

An important consideration in the present chapter's experiments is the question whether the pharmacological manipulations are selective of the recorded neurone, or whether neighbouring cells may also be exposed to pico-ejection of drugs. The latter could result in confounding indirect manipulations of the recorded neurone via network interactions. Drug pico-ejection on neighbouring cells cannot be excluded, but they are unlikely to occur. The volumes that come out of the pipette are almost insignificant and diffusion would be minimal. This is reflected in the near-immediate cessation of any drug induced effect on the recorded cell when turning off the positive air pressure on the ejection pipette, as well as in the absence of systemic effects. I know from experience that if any sizable volume comes out, the cell being recorded dies or is pushed away. I use the stability of the recording during pico-ejection as a control. Wider network effects can be excluded through monitoring of PN activity during pico-ejections.

Limitations to the classification of respiratory neurone functional subtypes by discharge pattern relative to PN activity.

Discharge pattern relative to the respiratory cycle is a valuable classification by which to assess the distribution of 5-$HT_{1A}$R across subpopulations of respiratory neurones, in part because no biochemical markers are known by which functional phenotypes of VRC respiratory neurones could be identified. Nevertheless, the interpretation of the present chapter's findings is limited by the restrictions to what can be said about a respiratory neurone, and its physiological function, based on its discharge pattern alone.

First, because only PN recordings were performed for reference to the network respiratory output, Post-I neurons and Dec-E neurons (both described in section 1.2.1) could not be reliably distinguished as there is no accurate cVN/RLN recording to determine the duration of the Post-I phase.

Second neurones of the same functional phenotype likely have shared or similar afferent projections but may differ in their efferent projections. Additional information on projection targets of recorded neurones can help to classify recorded neurones in more detail, and potentially reveal distinctions among subpopulations with shared discharge patterns. One way to attain information on efferent projections of a recorded neurone is by performing electrical stimulations at potential projection sites of VRC neurones, combined with action potential collision tests at the recorded neurone. In a collision test

(Lipski, 1981), constant latency action potentials in response to electrical stimulation are occluded when the stimulus was delivered within a critical interval following a spontaneous spike. Such occlusion suggests that axons of the recorded neurones travel to or through the site of electrical stimulation, as orthodromic synaptic action potentials appear to have collided with antidromic spikes along the axon.

In respiratory research, spike collision tests have been used to identify bulbospinal pre-motor (Richter et al., 1991, Schwarzacher et al., 1991, Moraes et al., 2014b, Zheng et al., 1991, Fortuna et al., 2008) or pre-sympathetic (Moraes et al., 2013) neurones through stimulation of contralateral segments of the spinal cord. Cranial motor neurones can be identified through antidromic stimulations of various cranial nerves (e.g. the hypoglossal nerve, glossopharyngeal nerve, facial nerve, and pharyngeal and laryngeal branches of the vagal nerve) (Bianchi et al., 1995, Song et al., 2015, Schwarzacher et al., 1991, Moraes et al., 2014b, Zheng et al., 1991, Moraes and Machado, 2015). If antidromic stimulation is applied comprehensively at each of these sites, absence of an antidromic response in the recorded neurone suggests that it is propriobulbar. If propriobulbar neurones have contralateral projections, these could be identified by contralateral stimulations in brainstem regions (Guyenet and Wang, 2001, Saether et al., 1987). However, opportunities for identification of propriobulbar projection sites are limited as low stimulation intensity will recruit axons in only a limited range from the stimulation site, whereas stronger stimulation intensities can lesion parts of the CPG. Further, the insertion of an additional (stimulating) electrode in the respiratory CPG could result in mechanical damage of the CPG and could therefore only be performed at regions distal from the site of the recording electrode (i.e. not elsewhere in the ipsilateral VRC). Therefore, antidromic stimulation can be applied only in a limited set of regions to which recorded neurones could project. Further, one cannot exclude the possibility that a recorded neurone with a positive collision test has axons passing through, but not terminating at, the site of electrical stimulation.

Third, for many functional phenotypes, it remains unknown whether the recorded neurones are inhibitory or excitatory. One possible approach to discern inhibitory from excitatory neurones among recorded VRC neurones is to inject viral vectors for excitatory opsin (e.g. ChR2) transgene expression under a VGLUT1 (to target glutamatergic neurones, (Zhang et al., 2011a), GAD67 (to target GABAergic neurones (Rasmussen et al., 2007)) or GlyT2 (to target glycinergic neurones (Moraes et al., 2014a) promoter in VRC regions of rat. Recordings and pico-ejections as described in the present chapter could be

followed up by light stimulation after systemic administration of pharmacological synaptic blockers (e.g. CNQX, AP5, strychnine, and bicuculline). If a recorded neurone responds to light stimulation under conditions of synaptic blockade, this suggests presence of ChR2 in that neurone from which one can infer whether it is glutamatergic, glycinergic or GABAergic (depending on the promoter used to drive ChR2 expression). Disadvantages of this approach include the possibility of less than perfect efficacy and selectivity of viral vector mediated opsin expression. Additional histological experiments would have to be performed to verify efficacy and selectivity of transgene expression with the viral vectors used. Further, after systemic administration of synaptic blockers, a preparation would no longer be usable for recordings of other respiratory neurones or network activity. Histological control experiments would have to be performed to verify efficacy and selectivity of the promoters used.

The above limitations likely underlie the observed heterogeneity of 5-$HT_{1A}$R phenotypes within neurone populations of a similar discharge pattern. Antidromic mapping strategies and/or optogenetic excitation could provide additional information on the connectivity and phenotype of recorded neurones that could help to classify neurones of a similar discharge pattern in more detail. However, these experimental approaches have their limitations (addressed above), are technically challenging, and would come at the expense of reduction of animal use and/or numbers of recorded neurones.

### *5.4.3 Interpretation of data*

Effects of systemic 5-$HT_{1A}$R transmission on respiration likely emerge as a network effect from multiple distinct respiratory neurone populations in the respiratory CPG.

In the present chapter, neurones with an Aug-E discharge pattern were the only functional subpopulations in which no response to NLX-101 pico-ejection was observed. All other known functional subpopulations of VRC respiratory neurones contained cells responsive to NLX-101 pico-ejection (Pre-I, Early-I, Ramp-I, Post-I/Dec-E). One previously reported study with juxtacellular administration of 5-$HT_{1A}$R agonist (8-OH-DPAT) suggests that 5-$HT_{1A}$R expression can occur in Aug-E neurones also (Lalley et al. 1994). Thus, collectively, experiments with single cell recordings combined with juxtacellular pico-ejection of 5-$HT_{1A}$R agonist indicate that 5-$HT_{1A}$R are expressed across VRC neurone populations of all functional phenotypes. Further, data from the present thesis, combined with that of Lalley et al. (1994), give no indication of greater 5-$HT_{1A}$R expression in any specific functional phenotype relative to others in the VRC. Regarding the latter, it should be

noted that sample sizes are small, and patterns in the distribution may yet emerge with greater sample sizes.

One noteworthy finding in the present thesis is the high prevalence of NLX-101 mediated inhibition of Ramp-I neurones. Ramp-I neurones are thought to be excitatory bulbospinal pre-motor neurones that project to spinal PN motor neurones innervating the diaphragm (Smith et al., 2013, Alheid and McCrimmon, 2008). Therefore, 5-$HT_{1A}$R mediated inhibition of Ramp-I neurones appears contradictory to the increase in pattern parameters (increased amplitude and normalised burst envelopes) observed in integrated PN output after systemic NLX-101 administration in *in situ* WHBP (see section 3.3.1). Two factors may contribute to this discrepancy.

First, recorded Ramp-I neurones were heterogenous with regard to 5-$HT_{1A}$R expression. The majority of recorded Ramp-I neurones (15 out of 22) was NLX-101 responsive. However, there are limitations to the certainty with which one can extrapolate the relative distribution of NLX-101 responsive and non-responsive neurones observed among the sampled Ramp-I neurones to the population of Ramp-I neurones at large. This is in part a result of the limited sample size in the present chapter. In addition, there may be a sampling bias for larger cells in extracellular single cell recordings. Larger neurones have greater field potentials relative to smaller cells and can therefore be recorded from a greater distance. Smaller cells are more likely to incur damage when an electrode comes in close enough proximity to record. As a result, I cannot exclude the possibility that smaller neurones are underrepresented in the present dataset of single unit recordings.

Second, given the broad expression of 5-$HT_{1A}$R across key regions of the respiratory CPG (see Chapter 4), as well as among respiratory neurone functional subtypes in the VRC (present chapter), multiple candidate mechanisms could contribute to the network effect of systemic 5-$HT_{1A}$R agonism with NLX-101. Therefore, direct 5-$HT_{1A}$R mediated inhibition of Ramp-I neurones may be overcome by disinhibition and enhanced excitatory network inputs to these neurones as a result of 5-$HT_{1A}$R agonism elsewhere (a topic explored further in Chapter 6).

To conclude, the current understanding of distribution of 5-$HT_{1A}$R among VRC neural populations with distinct discharge patterns does not, by itself, suggest a predominant role of 5-$HT_{1A}$R agonism at any specific subsets of VRC populations in the network response to systemic 5-$HT_{1A}$R agonism. No VRC functional subpopulations can be excluded as putative contributors to the effects of systemic 5-$HT_{1A}$ transmission on respiratory

control. Therefore, it is likely that that effects of systemic 5-$HT_{1A}$R activation on respiratory motor output (see chapter 3) emerged as a network effect from multiple distinct respiratory neurone populations in the respiratory CPG.

Distinct biochemical characteristics of 5-$HT_{1A}$R expressing respiratory neurones may mediate differential contributions of neural subpopulations to the respiratory CPG network response to systemic 5-$HT_{1A}$R agonism.

The specific functional effects of systemic 5-$HT_{1A}$ agonist (chapter 3) appear not reflected in a selective distribution of 5-$HT_{1A}$ R across anatomical regions (chapter 4), nor in a selective distribution of 5-$HT_{1A}$ R across functional subpopulations of respiratory neurones (present chapter). An additional level of organization by which broad 5-$HT_{1A}$R expression in the respiratory network could underlie selective responses to systemic 5-$HT_{1A}$ transmission, is through differential recruitment of intracellular and neuromodulatory mechanisms across subpopulations of 5-$HT_{1A}$R expressing respiratory neurones.

One such intracellular mechanism that may contribute to differentiation of respiratory neurons by their responses to 5-$HT_{1A}$R agonism is activation of G-protein coupled inward rectifying potassium (GIRK) channels. GIRK activation hyperpolarizes neurones and inhibits neuronal firing. (Clarke et al., 1987). GIRK channel activation in response to 5-$HT_{1A}$R agonism is mediated by G protein βγ subunits (Richter et al., 2003, Polter and Li, 2010, Clarke et al., 1987). Voltage clamp recordings revealed that Post-I neurones demonstrated hyperpolarizing currents consistent with GIRK channel activation after systemic administration of 8-OH-DPAT in anesthetized cats (Manzke et al., 2009). It is plausible that the response to 5-$HT_{1A}$R activation at respiratory neurones can differ across respiratory neurone populations, depending on co-expression levels of GIRK channels. Differential responses to 5-$HT_{1A}$R agonism on the basis of distinct 5-$HT_{1A}$R and GIRK channel co-expression profiles between respiratory subpopulations is a feature of multiple computational modelling studies that explore potential mechanisms underlying the network responses to systemic 5-$HT_{1A}$ (Shevtsova et al., 2011, Wittman et al., 2019). However, the distribution of 5-$HT_{1A}$R and GIRK channels across neurons of distinct functional subpopulations is yet to be experimentally established.

A second mechanism that may contribute to differential responses to 5-$HT_{1A}$R agonism across respiratory subpopulations is potentiation of $Gly_{\alpha 3}$R inhibitory currents. 5-$HT_{1A}$ agonism is reported to augment glycine-activated inhibitory $Cl^-$ currents in HEK293 cells co-expressing 5-$HT_{1A}$R and $Gly_{\alpha 3}$ receptors (Manzke et al., 2010). Pharmacological

evidence for the involvement of glycinergic transmission in the respiratory response to 5-$HT_{1A}$ transmission (Manzke et al., 2009, Manzke et al., 2010), as well as histological evidence for the presence of $Gly_{\alpha 3}R$ in the VRC (Manzke et al., 2009, Manzke et al., 2010) has been addressed in the introduction to this chapter (section 5.1.1). It is plausible that neuromodulatory effects of 5-$HT_{1A}R$ transmission can result in enhanced glycinergic inhibition at select respiratory subpopulations, depending on 5-$HT_{1A}R$ and $Gly_{\alpha 3}R$ co-expression and the nature of afferent glycinergic innervation. The pattern of enhanced inhibition in response to 5-$HT_{1A}R$ agonism would be dependent on the pattern of glycine release from afferent projections to the co-expressing neurons. Differential responses to 5-$HT_{1A}R$ agonism based on distinct 5-$HT_{1A}R$ and $Gly_{\alpha 3}R$ channel co-expression profiles, as well as distinct patterns of glycinergic afferent input, has previously been suggested as an important mediator of inhibition of select respiratory subpopulations in response to systemic 5-$HT_{1A}R$ agonism (Shevtsova et al., 2011). However, the distribution of 5-$HT_{1A}R$ and $Gly_{\alpha 3}R$ co-expression across respiratory subpopulations, as well as the pattern of pre-synaptic glycine release in co-expressing neurons, is yet to be experimentally established.

The third mechanism involves 5-$HT_{1A}R$ mediated modulation of voltage gated $Ca^{2+}$ currents, thereby modulating a neurone's discharge properties. Influx of $Ca^{2+}$ can depolarize the neurone and promote burst activity. However, $Ca^{2+}$ also influences multiple calcium-dependent intracellular processes, and elevated internal concentration of $Ca^{2+}$ triggers second messenger cascades that act as a negative feedback loop and promote reduction of $Ca^{2+}$ influx, $Ca^{2+}$ efflux, and $Ca^{2+}$ buffering. The consequent decline in intracellular $Ca^{2+}$ concentrations promotes a periodic refractory cessation of burst activity (Catterall, 2011). 5-$HT_{1A}R$ transmission can inhibit voltage gated $Ca^{2+}$ channel activity mediated by G protein βγ subunit (Bayliss et al., 1997b, Chen and Penington, 1996). In hypoglossal motorneurones in acute brainstem slices of neonatal mice, activation of $5HT_{1A}$ receptors with 8-OH-DPAT substantially down-regulated voltage evoked $Ca^{2+}$ signals without a significant impact on basal $Ca^{2+}$ concentrations (Ladewig et al., 2004).

High-voltage activated $Ca^{2+}$ and $Ca^{2+}$ dependent $K^+$ currents are suggested to be important mediators of intrinsic adaptive properties (incrementing and decrementing burst patterns) of respiratory neurones in the VRC, notably the Aug-E, Post-I and Early-I subpopulations (Molkov et al., 2010, Rubin et al., 2009, Rybak et al., 2007, Smith et al., 2007). It is conceivable that 5-$HT_{1A}R$ mediated inhibition of voltage gated calcium currents can affect adaptive properties of respiratory neurones, likely promoting neural excitation at small currents, followed by cessation of activity (i.e. shortening of burst duration) at

larger currents. 5-$HT_{1A}$R transmission may evoke $Ca^{2+}$ responses and corresponding changes in excitability that are different across subpopulations of respiratory neurones, as a function of differential co-expression levels of 5-$HT_{1A}$R and voltage gated $Ca^{2+}$ channels across subpopulations. Additionally, emergent network drives can result in differential susceptibility to 5-$HT_{1A}$R mediated changes in $Ca^{2+}$ signalling between neurone subpopulations. For example, in some populations, early suppression of burst activity by inhibitory input can pre-empt potential effects of $Ca^{2+}$ signalling, whereas populations with longer burst durations may be more susceptible to changes in excitability due to effects of 5-$HT_{1A}$R transmission on $Ca^{2+}$ signalling.

To conclude, differential recruitment of each of the three mechanisms discussed above can potentially differentiate respiratory neurone subpopulations and their responses to 5-$HT_{1A}$R agonism in ways not reflected by 5-$HT_{1A}$R distribution alone. To the best of my knowledge, the potential for differentiation of respiratory subpopulations by distinct recruitment of each of the above mechanisms in response to 5-$HT_{1A}$ agonism remains to be experimentally explored.

# Chapter 6: General Discussion

## 6.1 Overarching Thesis aims, Hypotheses, and Results

### 6.1.1 Thesis aims and hypotheses

The overarching aim of this thesis is to establish the effects of systemic administration of selective 5-$HT_{1A}$R agonist (NLX-101) on eupnoeic respiratory activity, as well as on modulation of respiratory and sympathetic activity in response to activation of homeostatic respiratory reflexes, as established in the intact respiratory CPG network in *in* situ WHBP of juvenile rats. In addition, this thesis aims to contribute to establishing the network interactions that underlie the respiratory and sympathetic responses to systemic administration of 5-$HT_{1A}$R agonist NLX-101. The overarching hypothesis was that systemic administration of selective 5-$HT_{1A}$R agonist would result in net enhanced respiratory drives that are determinant of ventilation. The homeostatic respiratory reflexes investigated were the responses to hypercapnia, as well as the responses to peripheral chemoreceptor activation by intra-arterial bolus administration of NaCN solution. Although systemic 5-$HT_{1A}$R agonism was thought to attenuate the hypercapnic response, respiratory and sympathetic hypercapnic responses were hypothesised to be unaffected by systemic administration of NLX-101. This was because the attenuation of the hypercapnic response was thought to be mediated by 5-$HT_{1A}$R auto-receptor transmission, and NLX-101 is thought to exert functional bias for hetero-receptors (see section 1.3.2). Systemic 5-$HT_{1A}$R antagonist WAY-100635 was hypothesised to potentiate the respiratory and sympathetic hypercapnic responses. Respiratory and sympathetic responses to activation of peripheral chemoreceptors were hypothesised to be attenuated by systemic administration of NLX-101. Descriptive mapping of the distribution of 5-$HT_{1A}$ R RNA and SLC32A1 RNA (co-)expression was performed throughout key regions of the respiratory CPG. In addition, responsiveness to juxtacellular pico-ejection of NLX-101 was established at the level of individual neurones to explore the distribution of 5-$HT_{1A}$R across functionally defined subpopulations of respiratory neurones in the VRC.

### 6.1.2 Thesis results

Data presented in this thesis revealed that systemic administration of 5-$HT_{1A}$R agonist NLX-101 in *in situ* WHBP of rats resulted in a significant increase in respiratory rate, chiefly due to a shortening to equal extent of Post-I and E2 phase durations. This effect

on respiratory rhythm can be interpreted as reduced activity of expiratory-, relative to inspiratory rhythmogenic neurone populations. In addition, systemic NLX-101 promoted enhanced late-E activity under eucapnic normoxic conditions, reflected in a significant increase in AbN late-E amplitude (μV).

Respiratory pattern parameters (normalised burst envelopes and peak amplitudes of integrated activity) were significantly increased in motor output obtained from the PN and AbN, but not in cVN and HN motor output. Respiratory and sympathetic responses to hypercapnia were unaffected by systemic administration of NLX-101 or 5-$HT_{1A}$R antagonist WAY-100635 compared to vehicle controls. Similarly, respiratory, and sympathetic responses to peripheral chemoreceptor activation were unaffected by systemic administration of NLX-101 compared to vehicle controls.

Anatomical mapping of 5-$HT_{1A}$R RNA and SLC32A1 RNA in key brainstem regions of respiratory control in rat revealed that 5-$HT_{1A}$R expression occured in both SLC32A1 RNA positive (i.e. glycinergic and/or GABAergic) and SLC32A1 negative neurones across all imaged respiratory regions of the brainstem. Extracellular recordings of functionally identified respiratory neurones of the VRC, combined with juxtacellular pico-ejection of NLX-101 indicated that most of the recorded respiratory subpopulations contained 5-$HT_{1A}$R expressing neurones. Specifically, NLX-101 responsive neurones were observed among VRC populations with Ramp-I, Post-I/Dec-E, Pre-I/I, and Early-I discharge patterns. Four Aug-E neurones were recorded of which none were responsive to NLX-101 pico-ejection. However previous studies with anesthetised cats had shown that juxtacellular electrophoresis of 5-$HT_{1A/7}$ agonist 8-OH-DPAT in anesthetised cats resulted in inhibition of these neurones too (Lalley et al., 1994). Therefore, 5-$HT_{1A}$R expression is likely not selective to neurones of any specific functional phenotypes as identified by discharge pattern relative to the respiratory cycle.

## 6.2 Putative mechanisms contributing to network effects of systemic 5-$HT_{1A}$R agonism

The present section will present hypotheses, along with further considerations, regarding mechanisms putatively contributing to the network response to systemic 5-$HT_{1A}$R transmission.

### *6.2.1 General considerations regarding mechanisms contributing to the network response to systemic 5-HT$_{1A}$R transmission.*

When considering candidate mechanisms that could underlie the net effect of systemic 5-HT$_{1A}$ transmission on respiratory control, there are a few things one must keep in mind. First, respiratory subpopulations of the CPG are thought to be interconnected in the fashion of a half-centre oscillator, with reciprocal inhibitory functional relationships between neural populations associated to each respiratory phase (see section 1.2.3) (Rybak et al., 2007, Smith et al., 2007, Rubin et al., 2009, Molkov et al., 2010). Enhanced inspiratory activity is paired with suppression of Post-I and Aug-E activity, and vice versa. Therefore, a relative reduction of expiratory activity, as observed in the present thesis, could be mediated by both excitation or disinhibition of inspiratory neurones (an indirect effect of 5-HT$_{1A}$R agonism), as well as by inhibition or reduced excitation of expiratory neurones (a direct effect of 5-HT$_{1A}$ transmission). Second, at the cellular level, the effect of 5-HT$_{1A}$R activation on neural excitability can differ among distinct populations, depending on the extent to which various intracellular mechanisms are recruited upon receptor activation. The (co-)expression levels of 5-HT$_{1A}$R with GIRK channels, with voltage gated $Ca^{2+}$ channels, and with Glyα3R are notable factors by which the cellular response to 5-HT$_{1A}$R agonism may differ among various neurone populations (see section 5.4.3). Third, given the broad expression of 5-HT$_{1A}$R across key regions of the respiratory CPG, as well as among respiratory neurone functional subtypes in the VRC, multiple candidate mechanisms could contribute to the network effect of systemic 5-HT$_{1A}$R agonism with NLX-101. The observed network effect of systemic administration of NLX-101 is likely mediated by simultaneous recruitment of multiple mechanisms that have both direct and indirect effects within the network. The multitude of possible effects at the cellular level, as well as at the circuit level, underscores the value of exploring and refining hypotheses in the network context through computational modelling simulations. Therefore, hypotheses presented in the subsequent sections could be evaluated and refined in the more comprehensive network context of the inhibitory ring model in future collaborative *in silico* studies.

### *6.2.2 Putative mechanisms contributing to augmented respiratory rate through shortening of expiratory phase duration.*

Increased respiratory rate combined with a trend of reduced expiratory phase duration suggests a reduction in activity of expiratory VRC neurone populations (concentrated in the BötC) relative to inspiratory VRC neurone populations (concentrated in the pre-BötC).

Absence of changes in cVN Post-I duty cycle indicates that the shortening of expiratory phase duration is mediated by shortening of Post-I and E2 phase durations to roughly equal extent. Under the half-centre oscillator paradigm (see section 1.2), this corresponds to a reduction in activity of Post-I and Aug-E neurones relative to inspiratory neurones. Although inspiratory and expiratory rhythmogenic neurone populations are thought to be concentrated in the BötC and pre-BötC of the VRC, they are (often reciprocally) connected with respiratory neurones in other brainstem regions. Important sources of inhibitory and excitatory drive to the VRC include neurones in the PBc, the pFRG expiratory oscillator, central chemoreceptors (in the RTN and raphe nuclei), and peripheral chemoreceptors (relayed via the NTS) (see sections 1.2 -1.5) (Koizumi et al., 2013, Smith et al., 2007). Thus, the balance between expiratory and inspiratory activity is shaped by VRC microcircuitry interactions, but also by inputs from other populations in the CPG to the VRC. The present section proposes two mechanisms that may contribute to changes in drive to VRC subpopulations in a manner consistent with the increased respiratory rate and shortening of expiratory phase durations observed in response to systemic 5-$HT_{1A}$R transmission.

Enhanced respiratory drive through disinhibition of inspiratory populations

The first mechanism suggested to contribute to an enhanced respiratory rate and a shortening of expiratory phase duration in response to systemic 5-$HT_{1A}$ transmission involves disinhibition of inspiratory neurones in the pre-BötC that receive central chemoreceptor drive. As addressed in the discussion of chapter 3 (section 3.4.3), the respiratory behaviour in response to systemic NLX-101 resembles respiratory activity under hypercapnic conditions. The similarities include the increase in respiratory rate and pattern, along with the emergence of late-E (Abdala et al., 2009, Marina et al., 2010). In the hypercapnic response, increased respiratory rate and pattern is thought to be mediated by enhanced excitatory drive from RTN chemoreceptor neurones to inspiratory neurones in the pre-BötC (Yang et al., 2020, Huckstepp et al., 2015, Zoccal et al., 2018, Ikeda et al., 2019, Guyenet et al., 2019). NLX-101 does not affect the hypercapnic response. Therefore, increase in rate and pattern in restful respiratory activity observed after systemic administration is likely not mediated by modulation of chemoreceptor neurones. However, it is possible that NLX-101 promotes increased respiratory rate and pattern through disinhibition of pre-BötC inspiratory neurones downstream of central chemoreceptors. This scenario would be consistent with the resemblance of the response to NLX-101 to the hypercapnic response in the absence of changes in chemoreceptor output. Given the relative reduction of expiratory activity observed in the present thesis,

along with the high levels of 5-$HT_{1A}$ RNA and SLC32A1 RNA co-expressing neurones in the BötC (26.2% of analysed neurones in region) and pre-BötC (32.7%), I propose that 5-$HT_{1A}$R mediated suppression of expiratory populations in the VRC is a plausible contributor to disinhibition of inspiratory neurones downstream from chemoreceptors. Whether systemic administration of 5-$HT_{1A}$R agonist does indeed promote disinhibition of inspiratory neurones downstream of central chemoreceptors, and whether this is mediated by inhibition of GABAergic and/or glycinergic expiratory populations, remains to be experimentally verified.

The notion of enhanced respiratory drive through inhibition of expiratory activity is also consistent with the finding that 5-$HT_{1A}$ transmission can counteract opioid induced respiratory depression. Systemic administration of opioids can result in suppression of respiratory activity (Dahan et al., 2018). (see section 1.8.1). This respiratory suppression is thought to be mediated by μ-opioid receptor (μOR) mediated inhibition of inspiratory neurone populations in the pre-BötC (Gray et al., 1999, Montandon et al., 2011, Manzke et al., 2003, Varga et al., 2020) (Gray 1999, Montandon 2011, Manzke 2003, Varga 2020) and the KF (Levitt, 2020, Levitt et al., 2015, Varga et al., 2020). 5-$HT_{1A}$R agonism is observed to rescue respiratory activity that was suppressed by μOR agonism in rats (Manzke et al., 2009, Shevtsova et al., 2011, Guenther et al., 2012, Ren et al., 2015). This suggests that 5-$HT_{1A}$ can restore the balance between inspiratory- and expiratory activity after initial suppression of inspiratory activity. Given that in our experiments, the increase in respiratory rate appears largely mediated by a shortening of expiratory phase duration, it is possible that inhibition of expiratory populations contributes to disinhibition of inspiratory populations and thereby counteracts μOR induced respiratory depression. Thus, 5-$HT_{1A}$R mediated recovery from μOR induced respiratory depression is consistent with the notion of 5-$HT_{1A}$ mediated increases in respiratory drive through inhibition of expiratory activity, and consequent disinhibition of inspiratory activity.

<u>Inhibition of BötC Post-I neurones through 5-$HT_{1a}$ mediated suppression of KF neurones.</u>

A second hypothetical mechanism that could contribute to increased respiratory rate through shortening of expiratory phase durations in response to systemic 5-$HT_{1A}$R agonism involves reduction of excitatory drive from KF neurones to glycinergic BötC Post-I neurones.

Periodic apnoeas In Rett syndrome are associated with exacerbation of Post-I activity (Stettner et al., 2007, Abdala et al., 2010). Systemic administration of 5-$HT_{1A}$R agonists can

alleviate respiratory dysrhythmia in MeCP2 deficient mouse models of Rett syndrome, and it has been suggested to do so through corrective suppression of Post-I activity (Abdala et al., 2014a, Wittman et al., 2019) (see sections 1.8.2 and 3.4.3). In the discussion of Chapter 3 (section 3.4.3), it was suggested that the increased respiratory rate through shortening of expiratory phase duration after systemic administration of NLX-101 may be in part mediated by 5-$HT_{1A}$R-mediated suppression of Post-I activity. Post-I activity is thought to depend on excitatory drive from the KF to BötC Post-I neurones (Song et al., 2015, Molkov et al., 2013) (see section 1.3.2). Post-I activity can be prolonged through pharmacological excitation or disinhibition of neurones in the KF (Abdala et al., 2016, Barnett et al., 2018, Bonis et al., 2013, Dutschmann and Herbert, 2006) and suppressed through pharmacological inhibition of the KF (Dutschmann and Herbert, 2006, Jenkin et al., 2017, Levitt et al., 2015). Exacerbated Post-I activity in RTT syndrome has been suggested to be caused, at least in part, by deficits in synaptic inhibition in the KF (Abdala et al., 2016). Indeed, focal administration of 5-$HT_{1A}$R agonist in the KF (Abdala et al., 2014b) depressed respiratory apnoea in *in* situ WHBP of MeCP2 deficient mice. Conversely, systemic administration of 5-$HT_{1A}$R antagonist (WAY-100635) promoted central apnoeas in *in situ* WHBP of WT mice, and this effect is recapitulated by focal administration of WAY-100635 in the KF (Dhingra et al. 2016). These findings suggest that 5-$HT_{1A}$ transmission in the KF mediates Post-I activity in MeCP2 deficient and WT mice, presumably through attenuation of excitatory drive from the KF to BötC Post-I neurones (Abdala et al., 2014a, Wittman et al., 2019).

In the present thesis, I observed significant increases in respiratory rate, mediated to equal extent by a shortening of Post-I and E2 phase durations, after systemic administration of 5-$HT_{1A}$R agonist NLX-101. Chapter 4 shows relatively high expression of 5-$HT_{1A}$R RNA (43.1% of all analysed neurones) in neurones of the KF, the majority of which are SLC32A1 negative (not GABAergic, nor glycinergic) neurones (35.7% of all analysed neurones, 82.8% of 5-$HT_{1A}$ R RNA positive neurones). These findings are consistent with the notion that 5-$HT_{1A}$R mediated suppression of the KF results in inhibition of Post-I activity. I propose that 5-$HT_{1A}$R mediated suppression of neurones in the KF results in a reduction of excitatory drive from the KF to BötC Post-I neurones, and that this mechanism contributes to the enhancement of respiratory rate through shortening of expiratory phase duration observed after systemic administration of NLX-101.

### *6.2.3 Putative mechanisms contributing to the emergence of late-E*

Systemic administration of 5-$HT_{1A}$R agonist NLX-101 promoted enhanced late-E activity under eucapnic normoxic conditions, reflected in a significant increase in AbN late-E amplitude (μV). Emergence of AbN (and tSN) late-E bursts is driven by a release from inhibition of late-E neurones in the pFRG expiratory oscillator. In hypercapnic conditions, AbN and tSN late-E is thought to emerge as a result of enhanced excitatory chemoreceptor drive to the pFRG, by which pFRG late-E neurones can overcome their inhibitory inputs. Based on the absence of effects on chemoreflex responses, I assume that systemic administration of NLX-101 does not affect chemoreceptor output. The pFRG contains glutamatergic neurons (Onimaru et al., 2008) and lacks inhibitory neurons (Ellenberger, 1999, Stornetta and Guyenet, 1999, Tanaka et al., 2003). Therefore, I propose that the emergence of AbN late-E activity in response to NLX-101 is likely mediated by 5-$HT_{1A}$R mediated suppression of distal inhibitory inputs to the pFRG, rather than through enhanced chemoreceptor drive (see section 3.4.3) or through suppression of local inhibitory interneurons.

Injection of retrograde tracers at the pFRG expiratory oscillator resulted in labelling of GABAergic and 5-HT neurones in the RMg and ROb (Silva et al., 2020). Selective lesioning of 5-HT neurones in the RMg or ROb through local micro-injections with Saporin did not affect the hypercapnic late-E response observed at abdominal EMG ($Abd_{EMG}$) recordings in anesthetised rats. Subsequent focal administration of $GABA_A$ agonist (muscimol) potentiated the amplitude of $Abd_{EMG}$ late-E activity under hypercapnic conditions (Silva et al., 2019). The hypercapnic stimulus applied was strong (9-10% $CO_2$) and resulted in late-E activity at every respiratory cycle, this saturation of the late-E rate meant that potential increases in late-E rate could not be established. Nevertheless, these findings indicate that GABAergic neurones in the RMg and ROb project to the pFRG expiratory oscillator, and that their inhibition results in disinhibition of abdominal late-E activity.

A similar set of experiments revealed that GABAergic neurones in the commissural part of the NTS (NTScomm) also project to the pFRG expiratory oscillator. Inhibition of these neurones resulted in a tonic increase in $Abd_{EMG}$ activity in anesthetised rats (Silva et al., 2019). FISH experiments in the present thesis (Chapter 4) show that 5-$HT_{1A}$R RNA was expressed in SLC32A1 RNA positive (GABAergic and/or glycinergic) neurones of the RMg (22.5% of all analysed RMg neurones), the ROb (30.8%), as well as the NTScomm (27.6%). It is possible that systemic 5-$HT_{1A}$ transmission promoted disinhibition of the pFRG

through inhibition of the RMg, ROb, and/or NTScomm GABAergic neurones described in Silva et al. (2020,2019).

A fourth source of inhibitory drive to the pFRG are glycinergic Post-I neurones in the BötC. Optogenetic inhibition, via selective expression of a light-sensitive inhibitory $Cl^-$ channel (eNpHR3.0) at glycinergic neurones of the BötC, during the post-I phase, evoked generation of late-E abdominal nerve activity in *in situ* WHBP of rats. In contrast, optogenetic excitation of glycinergic BötC neurones via a light-sensitive cation channel (ChETA) during the post-I phase suppressed late-E abdominal nerve activity in hypercapnic conditions (Moraes et al., 2014a). In the same *in situ* preparations, intracellular recordings of pFRG late-E neurones confirmed that inhibitory input during the post-I phase prevents generation of late-E neurone activity under eucapnic conditions (Moraes et al., 2014a). Given the evidence in support of 5-$HT_{1A}$ mediated suppression of Post-I activity (see section 6.2.2), it is possible that systemic administration of NLX-101 promotes suppression of Post-I activity, which in turn results in disinhibition of the pFRG, and thereby promotes emergence of late-E activity.

Going one step further, given the role of 5-$HT_{1A}$ transmission in the KF in the emergence of Post-I activity as evidenced by RTT research (see section 6.2.2), it is plausible that suppression of the KF is one mechanism by which systemic administration of NLX-101 can promote disinhibition of late-E activity. The notion of such interactions between the KF, BötC Post-I neurones, and the-pFRG expiratory oscillator is supported by pharmacological evidence that suppression of the KF promotes both suppression of Post-I activity and emergence of late-E activity (Jenkin et al., 2017). Conversely, pharmacological disinhibition of the KF increases cVN Post-I activity and suppresses the emergence of late-e activity under hypercapnic conditions (Barnett et al., 2018) (see section 1.4.4, figure 1-5). Thus, 5-$HT_{1A}$ mediated suppression of Post-I activity can suppress inhibitory input from glycinergic post-I neurones to the pFRG expiratory oscillator and thereby promote late-E activity. This hypothesis is in line with mechanisms previously suggested to contribute to enhanced respiratory rate through suppression of expiratory (Post-I) activity in response to systemic 5-$HT_{1A}$ transmission (section 6.2.2).

### *6.2.4 Putative mechanisms contributing to augmented respiratory pattern in select motor nerves*

The respiratory pattern was significantly augmented in PN, and AbN motor outputs. Cervical vagus nerve and HN motor output, on the other hand, remained unaffected.

Further, respiratory pattern was increased throughout all respiratory phases, even if phase durations were suppressed. Given that respiratory pattern was augmented in only a subset of motor nerves (PN and AbN) yet throughout all respiratory phases and irrespective of changes in rhythm, the pattern enhancement may be predominantly mediated at the level of PN and AbN pre-motor and motor regions rather than in rhythmogenic circuitry. The mechanism by which Inhibitory 5-$HT_{1A}$ transmission could hypothetically induce augmented pattern in motor outputs would be disinhibition of motor or (excitatory) pre-motor neurones.

To the best of my knowledge, there is presently little evidence to test the notion of 5-$HT_{1A}$ disinhibition of PN or AbN (pre-)motor neurones. However, Silva et al. (2019) revealed that suppression of GABAergic projections from the NTS to the pFRG promoted tonic excitation of AbN output. This is potentially reflective of disinhibition of excitatory AbN pre-motor neurones. FISH experiments in the present thesis (chapter 4) do not exclude the possibility of 5-$HT_{1A}$ mediated disinhibition of (pre-)motor neurones, as there is 5-$HT_{1A}$R RNA and SLC32A1 co-expression throughout all imaged brainstem regions involved in respiratory control (including: (pre-)motor respiratory regions (N10, N12, N. Amb. C., XII premotor neurones); VRC transmission cicuits (RVRG); and the NTS). It must be noted that the distribution of 5-$HT_{1A}$R RNA and SLC32A1 RNA specifically in PN and AbN motor nuclei is, to the best of my knowledge, not yet established. Nonetheless, given that systemic administration of NLX-101 resulted in increased peak amplitudes and burst envelopes in the integrated respiratory motor output of some, but not all nerves, and in a fashion irrespective of respiratory phases, it is conceivable that systemic 5-$HT_{1A}$ transmission promoted enhanced pattern through disinhibition of (pre-)motor activity. Whether this is the case remains to be experimentally verified.

### *6.2.5 Interpretation of absence of effect on chemoreflex responses*

Activity of central chemoreceptors is likely not affected by systemic 5-$HT_{1A}$R agonism.

I did not see an effect of systemic NLX-101 or WAY-100635 on the respiratory and sympathetic response to hypercapnia. These findings contrast with previous studies in which systemic administration of 5-$HT_{1A/7}$R agonist (8-OH-DPAT) results in a loss of the hypercapnic respiratory response in *in situ* WHBP of juvenile rats (Corcoran et al., 2013). Further, focal administration of 8-OH-DPAT in the RPa or RMg attenuated the hypercapnic response in conscious rats (Li et al., 2006), yet focal administration of 5-$HT_{1A}$R antagonist and D4 receptor agonist (WAY-100635) in the LC also attenuated the hypercapnic response in anesthetised rats (de Souza Moreno et al., 2010). The latter studies suggest physiologically antagonistic contributions of 5-$HT_{1A}$R transmission in distinct brainstem regions to the hypercapnic response.

Differences in the animal models and experimental designs used (anesthetised rats *in vivo* vs. unanaesthetised i*n situ WHBP* of rats; focal administration vs. systemic administration; $5HT_{1A/7}$R agonism vs. 5-$HT_{1A}$R agonism) do not permit direct comparisons between the above studies and experiments in the present thesis. I cannot exclude the possibility of simultaneous recruitment of physiologically antagonistic mechanisms that cancel out potential effects of 5-$HT_{1A}$R transmission on the hypercapnic network response. However, compensatory effects downstream of central chemoreceptor effects can be expected to selectively modulate certain hypercapnic response activities and leave others unaffected. In light of this, the absence of effects after systemic selective 5-$HT_{1A}$R agonist (NLX-101) as well as after systemic 5-$HT_{1A}$R antagonist (WAY-100635), observed in all analysed hypercapnic respiratory and sympathetic activities of unanaesthetised *in situ* WHPB of rats, suggests that output of central chemoreceptors is not affected by systemic 5-$HT_{1A}$ transmission.

Absence of effect of NLX on the hypercapnic response can be attributed to biased agonism, and/or to absence of 5-$HT_{1A}$R at central chemoreceptors.

Previous studies suggest that raphe serotonergic neurons with intrinsic $CO_2$ chemosensitivity are exclusively expressed in Erg2-Pet1 neurones from rhombomeric lineage r3 and r5, the anatomical location of these populations corresponds to the caudal part of the dorsal raphe, and the caudal parts of raphe magnus and raphe pallidus nuclei (Brust et al., 2014). A population of (presumed not intrinsically) $CO_2$ chemosensitive 5-HT neurons that also contributes to hypercapnic respiratory response was identified in the Raphe Obscurus (Hennessy et al., 2017) (see section 1.4.2). RTN neurones are also thought

to act as $CO_2$ chemoreceptors (Guyenet et al., 2019) (see section 1.4.1). FISH experiments presented in Chapter 4 show that 5-$HT_{1A}$R RNA positive neurones were present in each of the above anatomical regions (54% of RMg, 48% of RPa, 41.1% of Rob, and 19.3% of $pF_V$/RTN neurons were 5-$HT_{1A}$R RNA positive). The 5-$HT_{1A}$R RNA positive neurones were not functionally or biochemically identified as chemoreceptors, but the possibility of 5-$HT_{1A}$R expression in $CO_2$ chemoreceptor neurones cannot be excluded based on the anatomical distribution of 5-$HT_{1A}$R RNA alone. Of further note, previous studies reported that 5-$HT_{1A}$R RNA is present in cytosol of isolated glomus cells from CB's of rats (Yokoyama et al., 2015). These glomus cells were responsive to reductions in $pO_2$. Given that glomus cells are thought to specialize in either $CO_2$ or $O_2$ sensitivity (Lu et al., 2013) (see section 1.5.1), it is plausible that the 5-$HT_{1A}$ expressing cells reported in this study are not $CO_2$ chemoreceptors.

It is possible that 5-$HT_{1A}$R are present as auto-receptors in raphe chemoreceptor or chemosensitive neurones, but that these are not potently recruited by NLX-101 due to its potential functional bias for hetero-receptors over auto-receptors. One indication that NLX-101 might inhibit raphe serotonergic neurones comes from (Levitt et al., 2013), who report that bath application of NLX-101 (1µM) hyperpolarizes dorsal raphe neurones in a manner consistent with GIRK channel activation as observed through whole cell recordings in acute brain slices of mice. FISH experiments in the present thesis showed that 5-$HT_{1A}$R expressing neurones were highly prevalent in the dorsal raphe (73.6% of all analysed neurones, see section 4.3.5). The phenotype of neurones recorded by Levitt et al. was not verified, but it is possible that the recorded neurones were serotonergic, and that 1µM NLX-101 can indeed hyperpolarize raphe serotonergic neurones via activation of 5-$HT_{1A}$ auto-receptors. However, the dose use by Levitt et al. (2013) was high (1µM), given that NLX-101 is active at nanomolar range *in vitro* (Newman-Tancredi et al., 2009), and the presumed functional hetero-receptor bias of NLX-101 is dependent on concentration (Llado-Pelfort et al., 2010). It is therefore possible that NLX-101 stimulates 5-$HT_{1A}$ auto-receptors at 1µM, but not at the dose applied in hypercapnic response experiments of the present thesis (10nM).

To conclude, absence of effect on the hypercapnic response after systemic NLX-101 could be attributed to absence of expression of 5-$HT_{1A}$R at chemoreceptor populations, in raphe regions as well as in the RTN and CB's and/or to failure of NLX-101 (10nM) to inhibit raphe serotonergic chemoreceptor neurones because of functional hetero-receptor bias. However, either possibility remains to be experimentally verified.

Effects of 5-$HT_{1A}$R transmission on peripheral chemoreflex sympatho-respiratory responses

Based on previous reports of 5-$HT_{1A}$R RNA in cytosol of $O_2$ chemosensitive isolated glomus cells from rats (Yokoyama et al., 2015), I hypothesized that the peripheral chemoreceptor response would be attenuated after systemic administration of NLX-101 in *in situ* WHBP. One explanation for the absence of effect is that the effects of 5-$HT_{1A}$ transmission on intracellular mechanisms in these cells does not substantially change responsiveness to reductions in $pO_2$ in these cells. However, here too, I cannot exclude the possibility that that $O_2$ chemoreceptor responses are indeed affected, but that compensatory mechanisms occur downstream of the glomus cells. For instance, disinhibition of second order chemosensitive neurones of the NTS could theoretically compensate for the reduced activity of CB chemoreceptor neurons. FISH experiments in chapter 4 showed that 55.9% of all analysed cells in the commissural part of the NTS express 5-$HT_{1A}$R, indicating that inhibition of second order peripheral chemoreceptor neurones in the NTS is a possibility. Effects of 5-$HT_{1A}$R transmission at brainstem respiratory neurones involved in the peripheral chemoreflex responses remain to be experimentally established.

## 6.3 CONCLUSIONS

Based on converging evidence from the present thesis, research on the respiratory hypercapnic response, RTT research, and research on μOR induced respiratory depression, I propose that the network effect of systemic 5-$HT_{1A}$ transmission constitutes a shift in the balance between activity of inspiratory and expiratory neural populations in favour of the former. The broad expression of 5-$HT_{1A}$R across respiratory regions and functional subpopulations of VRC respiratory neurones indicates that the effect of systemic 5-$HT_{1A}$ transmission on respiratory activity is likely not mediated by a single subset of neurones and mechanisms. Rather, the effect is an emergent network effect mediated by action at multiple neurone populations and mechanisms throughout the respiratory network. I propose that the following mechanisms provide key contributions to the effect of systemic 5-$HT_{1A}$ transmission. First, systemic 5-$HT_{1A}$ transmission promotes enhanced respiratory rate and pattern via disinhibition of inspiratory VRC populations downstream of chemoreceptors. Second, systemic 5-$HT_{1A}$ transmission suppresses expiratory activity via attenuation of excitatory drive from the KF to BötC Post-I neurones. Third, systemic 5-$HT_{1A}$ transmission promotes emergence of late-E activity via attenuation of inhibitory drive to the pFRG expiratory oscillator. Ultimately, based on the absence of effect of systemic administration of NLX-101 on chemoreflex responses, I hypothesise that systemic administration of NLX-101 does not affect central and peripheral chemoreceptor function.

## 6.4 FUTURE DIRECTIONS

### *6.4.1 Multilevel computational modelling can aid formulation of hypotheses and determine optimal strategy for future experimental studies.*

The multitude of possible responses to systemic administration of NLX-101 at the cellular level, as well as at the circuit level, illustrates the importance of exploring and refining hypotheses in the network context through computational modelling simulations. Therefore, hypotheses presented in this thesis are best refined and evaluated *in silico* in a context that incorporates possible direct and indirect effects at the cellular and circuit level.

Currently, the most comprehensive theory of respiratory CPG network architecture is presented in the inhibitory ring model. This is a multilevel computational model that incorporates detailed biophysical properties and ion channel kinetics of individual neurones (modelled in Hodgkin-Huxley style) as well as population dynamics (each population represented by 20 to 50 neurones) (Molkov et al., 2010, Rubin et al., 2009, Rybak et al., 2007, Smith et al., 2007). The inhibitory ring model is able to reproduce *in* silico experimental observations of the eupnoeic three-phase respiratory rhythm, respiratory reflex responses, and specific experimental manipulations (e.g. transections and pharmacological manipulations) (Molkov et al., 2010, Rubin et al., 2009, Rybak et al., 2007, Smith et al., 2007, Barnett et al., 2016, Barnett et al., 2018). The major weakness of any computational model is that it relies on assumptions to fill in the gaps of knowledge. I do not know the full connectivity and phenotype characteristics of 5-$HT_{1A}$R expressing neurones, nor do I know whether and how 5-$HT_{1A}$R transmission differentially affects intracellular mechanisms across distinct neural populations. It is likely that multiple configurations of the model can reproduce *in silico* the results of systemic 5-$HT_{1A}$R transmission described in the present thesis. Nonetheless, computational modelling simulations can help to guide the focus for future experimental efforts aimed at experimental verification of such gaps in knowledge.

With the ultimate aim to experimentally establish the key mechanisms underlying network effects of systemic 5-$HT_{1A}$ transmission, the next step will be an *in silico* evaluation of the hypotheses presented in the present thesis in the context of the inhibitory ring model.

### *6.4.1 Experimental strategies for testing of thesis and modelling hypotheses*

Based on the previous literature, one can ascribe specific functional contributions of neurone populations in distinct anatomical brainstem regions to the generation of respiratory activities. For example, expiratory neurone populations (Post-I/Dec-E, Aug-E) are concentrated in the BötC, whereas inspiratory neurones (Pre-I/I, Early-I, Ramp-I) are concentrated in the pre-BötC (see section 1.2.3). Further, activity of auto-rhythmic excitatory neurones in the pFRG drives AbN and tSN late-E activity (Pagliardini et al., 2011, Abdala et al., 2009, Huckstepp et al., 2015). Inhibitory neural populations in the NTS (Silva et al., 2019), the RMg and ROb (Silva et al., 2020), and the BötC (Moraes et al., 2014a) are thought to modulate to late-E activity via projections to the pFRG. Excitatory neurones in the KF region are thought to project to inhibitory Post-I neurones in the BötC, and to indirectly modulate the latter's inhibitory drive to pFRG late-E activity (see section 6.2.3). These findings facilitate experimental strategies to test hypotheses on the contributions of 5-$HT_{1A}$R transmission in specific functional-anatomical regions to the network response to systemic 5-$HT_{1A}$R transmission.

One such experimental strategy is to perform focal micro-injections of 5-$HT_{1A}$R agonist (NLX-101) in specific brainstem regions of respiratory control and monitor respiratory motor outputs via electrophysiological recordings of peripheral nerves and neural populations in *in situ* WHBP of rats. For example, the hypothesis that 5-$HT_{1A}$R mediated inhibition of expiratory BötC neurones promotes enhanced respiratory rate (see section 6.2.2) and late-E activity (see section 6.2.3) could be experimentally tested by focal microinjection of NLX-101 in the BötC while monitoring respiratory motor outputs (e.g. in PN, cVN, and AbN). Similarly, the hypotheses that 5-$HT_{1A}$R agonism at (non-serotonergic) neurones of the RMg and RPa, at neurones in the NTS, and/or at KF neurones contributes to disinhibition of late-E activity can be tested via focal micro-injection of NLX-101 in either of these regions. Such experiments could be performed under normocapnia, or under differing degrees of hypercapnia to gradually increase excitatory chemoreceptor drive to the pFRG and reduce the threshold for putative 5-$HT_{1A}$R mediated disinhibition of late-E activity to become discernible. Effects of these manipulations can be monitored with electrophysiological recordings of PN and AbN respiratory activities, and with local field potential recordings of late-E neurones in the pFRG. To demonstrate that effects of NLX-101 are mediated selectively by 5-$HT_{1A}$R agonism, effects of NLX-101 micro-injections must be reversible by co-administration of 5-$HT_{1A}$R antagonist (WAY-100635).

An alternative experimental approach to assess the contributions of the above functional-anatomical regions to the network response to systemic 5-$HT_{1A}$R agonist (NLX-101) is to compare the network response to systemic NLX-101 to the network response to systemic NLX-101 after focal microinjections of 5-$HT_{1A}$R antagonist (WAY-100635) in one of the above regions. The advantage of this approach compared to micro-injections of 5-$HT_{1A}$R agonist is that contributions of 5-$HT_{1A}$R transmission in specific regions can be evaluated against a background of systemic 5-$HT_{1A}$R agonism. This adds a control for 5-$HT_{1A}$ mediated changes to the wider respiratory network that likely contribute to effects of systemic NLX-101 as observed in the present thesis. In all micro-injection experiments, drugs must be co-injected with dye for post-hoc anatomical verification of injection sites.

# APPENDIX: SUPPLEMENTARY DATA

**Supplementary Table 1:** Means for baseline and hypercapnic respiratory rhythms and patterns.

Values are mean ± SEM for baseline and hypercapnic PN, cVN, and AbN activity. The dataset consists of pooled recordings of the pre-treatment hypercapnic response in all treatment groups (vehicle; NLX-101 10nM; NLX-101 100nM) (see section 3.3.2). Repeated measures t-test indicates that hypercapnic sympathetic responses in **bold red text** are significantly different compared to baseline ($p < .05$). PN n=25; cVN n=13; AbN n=25

| nerve | parameter | baseline | hypercapnia |
|---|---|---|---|
| PN | rate (bpm) | 19.17 ±1.46 | 18.78 ±1.12 |
| | dur. I (s) | 1.08 ±0.34 | **0.75 ±0.03** |
| | dur. E (s) | 2.68 ±0.34 | 2.82 ±0.23 |
| | Tpeak (s) | 0.80 ±0.06 | **0.41 ±0.02** |
| | normalised AUC I | 14.25 ±1.61 | **17.01 ±1.93** |
| | amplitude I (µV) | 17.94 ±2.36 | **20.42 ±2.68** |
| cVN | dur. PI (s) | 2.10 ±0.48 | **1.51 ±0.24** |
| | dur.PI : dur.E (%) | 69.09 ±3.50 | **59.32 ±2.76** |
| | normalised AUC I | 5.53 ±0.47 | **5.98 ±0.55** |
| | normalised AUC PI | 4.17 ±0.34 | 4.38 ±0.37 |
| | amplitude PI (µV) | 6.32 ±0.64 | 6.09 ±0.69 |
| AbN | late-E rate (bpm) | 1.95 ±0.74 | **14.39 ±6.7** |
| | late-E amplitude (µV) | 0.94 ±0.30 | **4.71 ±1.30** |
| | amplitude PI (µV) | 1.67 ±0.60 | **2.09 ±0.58** |

**Supplementary Table 2:** Means for baseline and hypercapnic sympathetic activity.

Values are mean ± SEM for tSN baseline and hypercapnic activity. The dataset consists of pooled recordings of the pre-treatment hypercapnic response in all treatment groups (vehicle; NLX-101 10nM; NLX-101 100nM) (see section 3.3.2). Repeated measures t-test indicates that hypercapnic sympathetic responses in **bold red text** are significantly different compared to baseline ($p < .05$). n=14

| tSN parameter | baseline | hypercapnia |
|---|---|---|
| amplitude I (µV) | 4.03 ±0.53 | **4.72 ±0.59** |
| amplitude PI (µV) | 3.31 ±0.45 | **4.17 ±0.58** |
| amplitude E2 (µV) | 2.68 ±0.38 | **3.37 ±0.45** |
| trough I (µV) | 0.73 ±0.13 | **1.13 ±0.71** |
| trough PI (µV) | 0.31 ±0.07 | 0.14 ±0.06 |
| trough E2 (µV) | 0.46 ±0.08 | 0.60 ±0.11 |
| normalised AUC I | 4.66 ±0.38 | **5.23 ±0.44** |
| normalised AUC PI | 3.82 ±0.29 | **4.20 ±0.35** |
| normalised AUC E2 | 3.87 ±0.28 | **4.22 ±0.33** |

**Supplementary Table 3:** Means for baseline respiratory rhythms and respiratory rhythms elicited by intra-arterial NaCN bolus administration.

Values are mean **±** SEM for PN baseline, and for PN greatest rhythm response to intra-arterial NaCN bolus administrations (25µL, 50µL, 75µL). The dataset consists of pooled recordings of pre-treatment NaCN bolus administrations in all treatment groups (vehicle; NLX-101 10nM; NLX-101 100nM) (see section 3.3.3). Two-way repeated measures ANOVA with Geisser-Greenhouse correction and Sidak's multiple comparisons test indicates that NaCN response values annotated in **bold red text** are significantly different compared to baseline ($p < .05$)**.** n=22

| PN parameter | NaCN dose | Baseline | NaCN greatest response |
|---|---|---|---|
| **Δ rate (bpm)** | **25 µL** | 21.66 ±2.15 | **48.87 ±3.37** |
| | **50 µL** | 23.15 ±2.06 | **56.93 ±2.13** |
| | **75 µL** | 24.10 ±2.33 | **62.00 ±2.10** |
| **Δ dur. I (s)** | **25 µL** | 0.85 ±0.04 | **0.61 ±0.03** |
| | **50 µL** | 0.80 ±0.03 | **0.51 ±0.02** |
| | **75 µL** | 0.76 ±0.03 | **0.49 ±0.01** |
| **Δ dur. E (s)** | **25 µL** | 2.47 ±0.31 | **0.71 ±0.12** |
| | **50 µL** | 2.19 ±0.25 | **0.50 ±0.04** |
| | **75 µL** | 2.23 ±0.28 | **0.42 ±0.04** |
| **Δ Tpeak (s)** | **25 µL** | 0.60 ±0.04 | **0.34 ±0.04** |
| | **50 µL** | 0.55 0.03± | **0.21 0.02±** |
| | **75 µL** | 0.52 ±0.03 | **0.15 ±0.02** |

| nerve | parameter | NaCN dose | baseline | NaCN greatest response |
|---|---|---|---|---|
| PN | amplitude I (µV) | 25 µL | 15.25 ±2.58 | 17.00 ±2.83 |
| | | 50 µL | 15.43 ±2.63 | 18.20 ±3.00 |
| | | 75 µL | 15.90 ±2.82 | 19.95 ±3.37 |
| | normalised AUC I | 25 µL | 12.15 ±1.70 | 13.94 ±2.01 |
| | | 50 µL | 12.36 ±1.78 | 15.41 ±2.23 |
| | | 75 µL | 12.64 ±1.87 | 16.65 2.51± |
| AbN | ampltitude PI (µV) | 25 µL | 2.62 ±0.57 | 9.60 ±2.53 |
| | | 50 µL | 2.89 ±0.57 | 13.95 ±2.29 |
| | | 75 µL | 3.16 ±0.58 | 15.85 ±2.13 |
| | ampltitude E2 (µV) | 25 µL | 2.19 ±0.45 | 7.64 ±1.58 |
| | | 50 µL | 2.28 ±0.40 | 11.76 ±1.68 |
| | | 75 µL | 2.82 ±0.48 | 13.83 ±1.79 |
| cVN | normalised AUC I | 25 µL | 6.10 ±0.37 | 7.01 ±0.38 |
| | | 50 µL | 6.00 ±0.35 | 7.49 ±0.43 |
| | | 75 µL | 5.88 ±0.32 | 7.72 ±0.54 |
| | amplitude PI (µV) | 25 µL | 8.49 ±0.93 | 10.63 ±1.37 |
| | | 50 µL | 8.24 ±0.86 | 10.45 ±0.97 |
| | | 75 µL | 7.83 ±0.75 | 10.38 ±1.00 |
| | trough (µV) | 25 µL | 0.10 ±.01 | 0.30 ±.05 |
| | | 50 µL | 0.07 ±0.04 | 0.55 ±0.20 |
| | | 75 µL | 0.06 ±0.06 | 0.87 ±0.24 |

**Supplementary Table 4:** Means for baseline respiratory patterns and respiratory patterns elicited by intra-arterial NaCN bolus administration.

Values are mean ± SEM for PN, AbN, and cVN baseline patterns, and for PN, AbN, and cVN greatest pattern response to intra-arterial NaCN bolus administrations (25µL, 50µL, 75µL). The dataset consists of pooled recordings of pre-treatment NaCN bolus administrations in all treatment groups (vehicle; NLX-101 10nM; NLX-101 100nM) (see section 3.3.3). Two-way repeated measures ANOVA with Geisser-Greenhouse correction and Sidak's multiple comparisons test indicates that NaCN response values annotated in **bold red text** are significantly different compared to baseline ($p < .05$). PN n=22; AbN n=21; cVN n=21

.

| tSN parameter | NaCN dose | Baseline | NaCN greatest response |
|---|---|---|---|
| **amplitude I (µV)** | **25 µL** | 3.32 ±0.51 | **4.99 ±0.70** |
| | **50 µL** | 3.48 ±0.49 | **6.27 ±0.83** |
| | **75 µL** | 3.63 ±0.47 | **6.83 ±0.86** |
| **amplitude PI (µV)** | **25 µL** | 3.06 ±0.43 | **5.11 ±0.62** |
| | **50 µL** | 3.14 ±0.40 | **7.06 ±0.95** |
| | **75 µL** | 3.28 ±0.37 | **7.20 ±0.92** |
| **amplitude E2 (µV)** | **25 µL** | 2.16 ±0.33 | **3.4 ±0.44** |
| | **50 µL** | 2.25 ±0.31 | **5.28 ±0.82** |
| | **75 µL** | 2.35 ±0.30 | **4.94 ±0.59** |
| **trough I (µV)** | **25 µL** | 0.60 ±0.12 | **1.09 ±0.19** |
| | **50 µL** | 0.63 ±0.11 | **1.64 ±0.25** |
| | **75 µL** | 0.69 ±0.11 | **2.06 ±0.30** |
| **trough PI (µV)** | **25 µL** | 0.22 ±0.05 | **1.63 ±0.25** |
| | **50 µL** | 0.26 ±0.05 | **2.88 ±0.35** |
| | **75 µL** | 0.30 ±0.07 | **3.26 ±0.47** |
| **trough E2 (µV)** | **25 µL** | 0.35 ±0.06 | **1.42 ±0.28** |
| | **50 µL** | 0.39 ±0.06 | **2.59 ±0.39** |
| | **75 µL** | 0.43 ±0.08 | **2.83 ±0.41** |

**Supplementary Table 5A:** Means for baseline sympathetic activity and sympathetic activity elicited by intra-arterial NaCN bolus administration.

Values are mean **±** SEM for tSN baseline activity, and for tSN greatest response to intra-arterial NaCN bolus administrations (25µL, 50µL, 75µL). The dataset consists of pooled recordings of pre-treatment NaCN bolus administrations in all treatment groups (vehicle; NLX-101 10nM; NLX-101 100nM) (see section 3.3.3). Two-way repeated measures ANOVA with Geisser-Greenhouse correction and Sidak's multiple comparisons test indicates that NaCN response values annotated in **bold red text** are significantly different compared to baseline ($p < .05$)**.** tSN n=22. Table is continued on next page (**Supplementary Table 5B**).

**Supplementary Table 6B:** Means for baseline sympathetic activity and sympathetic activity elicited by intra-arterial NaCN bolus administration.

Continuation of **Supplementary Table 5A.** Values are mean **±** SEM for tSN baseline activity, and for tSN greatest response to intra-arterial NaCN bolus administrations (25µL, 50µL, 75µL). The dataset consists of pooled recordings of pre-treatment NaCN bolus administrations in all treatment groups (vehicle; NLX-101 10nM; NLX-101 100nM) (see section 3.3.3). Two-way repeated measures ANOVA with Geisser-Greenhouse correction and Sidak's multiple comparisons test indicates that NaCN response values annotated in **bold red text** are significantly different compared to baseline ($p < .05$)**.** tSN n=22.

| tSN parameter | NaCN dose | baseline | NaCN greatest response |
|---|---|---|---|
| **normalised AUC I** | **25 µL** | 4.40 ±0.43 | **5.23 ±0.52** |
| | **50 µL** | 4.50 ±0.42 | **6.19 ±0.58** |
| | **75 µL** | 4.60 ±0.40 | **6.93 ±0.69** |
| **normalised AUC PI** | **25 µL** | 3.75 ±0.31 | **7.21 ±0.68** |
| | **50 µL** | 3.87 ±0.30 | **8.72 ±0.78** |
| | **75 µL** | 3.90 ±0.30 | **9.59 ±0.82** |
| **normalised AUC E2** | **25 µL** | 3.85 ±0.32 | **9.53 ±1.19** |
| | **50 µL** | 3.97 ±0.32 | **11.20 ±1.21** |
| | **75 µL** | 4.02 ±0.32 | **13.22 ±1.42** |

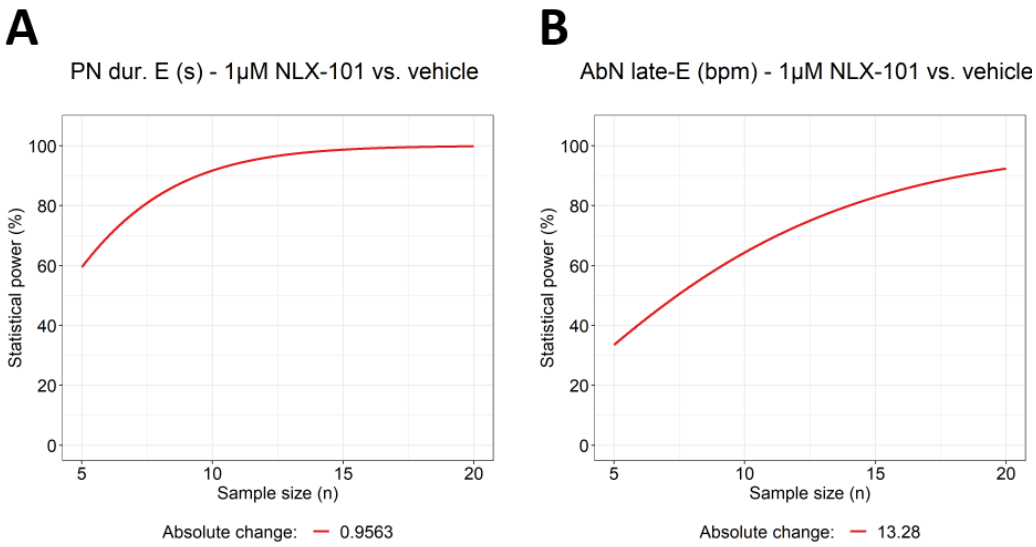


**Supplementary Figure S1::** Power analyses.

Power analysis plots for comparison of means based on respiratory responses to 1µM NLX-101 (n=7) vs. vehicle controls (n=5) as observed in the present thesis (see section 3.3.1). (**A**) The absolute change in PN dur. E (s) at 1µM NLX-101 vs. vehicle controls was a shortening of expiratory phase duration by 0.9563 s. Assuming α = .05, and variance equal to that observed in the present thesis, 70-92% power to detect an absolute change of 0.9563 requires sample sizes of 6 to 10 recordings in each treatment group. (**B**) The absolute change in AbN late-E rate (bpm) at 1µM NLX-101 vs. vehicle controls was an increase in late-E rate by 13.28 bpm. Assuming α = .05, and variance equal to that observed in the present thesis, 69-91% power to detect an absolute change of 13.28 requires sample sizes of 11 to 19 recordings in each treatment group.

## REFERENCES

ABBOTT, S. B., COATES, M. B., STORNETTA, R. L. & GUYENET, P. G. 2013. Optogenetic stimulation of c1 and retrotrapezoid nucleus neurons causes sleep state-dependent cardiorespiratory stimulation and arousal in rats. *Hypertension,* 61**,** 835-41.

ABBOTT, S. B., STORNETTA, R. L., COATES, M. B. & GUYENET, P. G. 2011. Phox2b-expressing neurons of the parafacial region regulate breathing rate, inspiration, and expiration in conscious rats. *J Neurosci,* 31**,** 16410-22.

ABBOTT, S. B., STORNETTA, R. L., FORTUNA, M. G., DEPUY, S. D., WEST, G. H., HARRIS, T. E. & GUYENET, P. G. 2009. Photostimulation of retrotrapezoid nucleus phox2b-expressing neurons in vivo produces long-lasting activation of breathing in rats. *J Neurosci,* 29**,** 5806-19.

ABDALA, A. P., BISSONNETTE, J. M. & NEWMAN-TANCREDI, A. 2014a. Pinpointing brainstem mechanisms responsible for autonomic dysfunction in Rett syndrome: therapeutic perspectives for 5-HT1A agonists. *Front Physiol,* 5**,** 205.

ABDALA, A. P., DUTSCHMANN, M., BISSONNETTE, J. M. & PATON, J. F. 2010. Correction of respiratory disorders in a mouse model of Rett syndrome. *Proc Natl Acad Sci U S A,* 107**,** 18208-13.

ABDALA, A. P., LIOY, D. T., GARG, S. K., KNOPP, S. J., PATON, J. F. & BISSONNETTE, J. M. 2014b. Effect of Sarizotan, a 5-HT1a and D2-like receptor agonist, on respiration in three mouse models of Rett syndrome. *Am J Respir Cell Mol Biol,* 50**,** 1031-9.

ABDALA, A. P., RYBAK, I. A., SMITH, J. C. & PATON, J. F. 2009. Abdominal expiratory activity in the rat brainstem-spinal cord in situ: patterns, origins and implications for respiratory rhythm generation. *J Physiol,* 587**,** 3539-59.

ABDALA, A. P., TOWARD, M. A., DUTSCHMANN, M., BISSONNETTE, J. M. & PATON, J. F. 2016. Deficiency of GABAergic synaptic inhibition in the Kolliker-Fuse area underlies respiratory dysrhythmia in a mouse model of Rett syndrome. *J Physiol,* 594**,** 223-37.

ABDALA SHEIKH, A. P. 2020. Algorithm for analysis of respiratory and sympathetic nerve activities in rodents. V3 ed. figshare.

ALHEID, G. F., JIAO, W. & MCCRIMMON, D. R. 2011. Caudal nuclei of the rat nucleus of the solitary tract differentially innervate respiratory compartments within the ventrolateral medulla. *Neuroscience,* 190**,** 207-27.

ALHEID, G. F. & MCCRIMMON, D. R. 2008. The chemical neuroanatomy of breathing. *Respir Physiol Neurobiol,* 164**,** 3-11.

ALHEID, G. F., MILSOM, W. K. & MCCRIMMON, D. R. 2004. Pontine influences on breathing: an overview. *Respir Physiol Neurobiol,* 143**,** 105-14.

ALSAHAFI, Z., DICKSON, C. T. & PAGLIARDINI, S. 2015. Optogenetic excitation of preBotzinger complex neurons potently drives inspiratory activity in vivo. *J Physiol,* 593**,** 3673-92.

ANDERSON, T. M., GARCIA, A. J., 3RD, BAERTSCH, N. A., POLLAK, J., BLOOM, J. C., WEI, A. D., RAI, K. G. & RAMIREZ, J. M. 2016. A novel excitatory network for the control of breathing. *Nature,* 536**,** 76-80.

ANDERSON, T. M. & RAMIREZ, J. M. 2017. Respiratory rhythm generation: triple oscillator hypothesis. *F1000Res,* 6**,** 139.

AUSBORN, J., KOIZUMI, H., BARNETT, W. H., JOHN, T. T., ZHANG, R., MOLKOV, Y. I., SMITH, J. C. & RYBAK, I. A. 2018. Organization of the core respiratory network: Insights from optogenetic and modeling studies. *PLoS Comput Biol,* 14**,** e1006148.

BAEKEY, D. M., DICK, T. E. & PATON, J. F. 2008. Pontomedullary transection attenuates central respiratory modulation of sympathetic discharge, heart rate and the baroreceptor reflex in the in situ rat preparation. *Exp Physiol,* 93**,** 803-16.

BAEKEY, D. M., MOLKOV, Y. I., PATON, J. F., RYBAK, I. A. & DICK, T. E. 2010. Effect of baroreceptor stimulation on the respiratory pattern: insights into respiratory-sympathetic interactions. *Respir Physiol Neurobiol,* 174**,** 135-45.

BAILEY, E. F. 2011. Activities of human genioglossus motor units. *Respiratory Physiology & Neurobiology,* 179**,** 14-22.

BARNETT, W. H., ABDALA, A. P., PATON, J. F., RYBAK, I. A., ZOCCAL, D. B. & MOLKOV, Y. I. 2016. Chemoreception and neuroplasticity in respiratory circuits. *Exp Neurol*.

BARNETT, W. H., ABDALA, A. P., PATON, J. F., RYBAK, I. A., ZOCCAL, D. B. & MOLKOV, Y. I. 2017. Chemoreception and neuroplasticity in respiratory circuits. *Exp Neurol,* 287**,** 153-164.

BARNETT, W. H., JENKIN, S. E. M., MILSOM, W. K., PATON, J. F. R., ABDALA, A. P., MOLKOV, Y. I. & ZOCCAL, D. B. 2018. The Kolliker-Fuse nucleus orchestrates the timing of expiratory abdominal nerve bursting. *J Neurophysiol,* 119**,** 401-412.

BASTING, T. M., BURKE, P. G., KANBAR, R., VIAR, K. E., STORNETTA, D. S., STORNETTA, R. L. & GUYENET, P. G. 2015. Hypoxia silences retrotrapezoid nucleus respiratory chemoreceptors via alkalosis. *J Neurosci,* 35**,** 527-43.

BATE, S. T. & CLARK, R. A. 2014. *The Design and Statistical Analysis of Animal Experiments*, Cambridge University Press.

BAYLISS, D. A., LI, Y. W. & TALLEY, E. M. 1997a. Effects of serotonin on caudal raphe neurons: activation of an inwardly rectifying potassium conductance. *J Neurophysiol,* 77**,** 1349-61.

BAYLISS, D. A., LI, Y. W. & TALLEY, E. M. 1997b. Effects of serotonin on caudal raphe neurons: inhibition of N- and P/Q-type calcium channels and the afterhyperpolarization. *J Neurophysiol,* 77**,** 1362-74.

BAZILIO, D. S., BONAGAMBA, L. G. H., MORAES, D. J. A. & MACHADO, B. H. 2019. Cardiovascular and respiratory profiles during the sleep-wake cycle of rats previously submitted to chronic intermittent hypoxia. *Exp Physiol*.

BEAUDOIN-GOBERT, M. & SGAMBATO-FAURE, V. 2014. Serotonergic pharmacology in animal models: from behavioral disorders to dyskinesia. *Neuropharmacology,* 81**,** 15-30.

BECKER, G., BOLBOS, R., COSTES, N., REDOUTE, J., NEWMAN-TANCREDI, A. & ZIMMER, L. 2016. Selective serotonin 5-HT1A receptor biased agonists elicitdistinct brain activation patterns: a pharmacoMRI study. *Sci Rep,* 6**,** 26633.

BELTRAN-CASTILLO, S., OLIVARES, M. J., CONTRERAS, R. A., ZUNIGA, G., LLONA, I., VON BERNHARDI, R. & EUGENIN, J. L. 2017. D-serine released by astrocytes in brainstem regulates breathing response to CO2 levels. *Nat Commun,* 8**,** 838.

BESNARD, S., DENISE, P., CAPPELIN, B., DUTSCHMANN, M. & GESTREAU, C. 2009. Stimulation of the rat medullary raphe nuclei induces differential responses in respiratory muscle activity. *Respir Physiol Neurobiol,* 165**,** 208-14.

BESNARD, S., KHEMIRI, H., MASSE, F., DENISE, P., VERDAGUER, M. & GESTREAU, C. 2012. Differential respiratory control of the upper airway and diaphragm muscles induced by 5-HT1A receptor ligands. *Sleep Breath,* 16**,** 135-47.

BESNARD, S., MASSE, F., VERDAGUER, M., CAPPELIN, B., MEURICE, J. C. & GESTREAU, C. 2007. Time- and dose-related effects of three 5-HT receptor ligands on the genioglossus activity in anesthetized and conscious rats. *Sleep Breath,* 11**,** 275-84.

BIANCHI, A. L., DENAVIT-SAUBIE, M. & CHAMPAGNAT, J. 1995. Central control of breathing in mammals: neuronal circuitry, membrane properties, and neurotransmitters. *Physiol Rev,* 75**,** 1-45.

BISSONNETTE, J. M. & KNOPP, S. J. 2006. Separate respiratory phenotypes in methyl-CpG-binding protein 2 (Mecp2) deficient mice. *Pediatr Res,* 59**,** 513-8.

BISSONNETTE, J. M., SCHAEVITZ, L. R., KNOPP, S. J. & ZHOU, Z. 2014. Respiratory phenotypes are distinctly affected in mice with common Rett syndrome mutations MeCP2 T158A and R168X. *Neuroscience,* 267**,** 166-76.

BOCHORISHVILI, G., STORNETTA, R. L., COATES, M. B. & GUYENET, P. G. 2012. Pre-Botzinger complex receives glutamatergic innervation from galaninergic and other retrotrapezoid nucleus neurons. *J Comp Neurol,* 520**,** 1047-61.

BOEHM, O., ZUR, B., KOCH, A., TRAN, N., FREYENHAGEN, R., HARTMANN, M. & ZACHAROWSKI, K. 2007. Clinical chemistry reference database for Wistar rats and C57/BL6 mice. *Biol Chem,* 388**,** 547-54.

BONGIANNI, F., MUTOLO, D., CINELLI, E. & PANTALEO, T. 2010. Respiratory responses induced by blockades of GABA and glycine receptors within the Botzinger complex and the pre-Botzinger complex of the rabbit. *Brain Res,* 1344**,** 134-47.

BONIS, J. M., NEUMUELLER, S. E., KRAUSE, K. L., PAN, L. G., HODGES, M. R. & FORSTER, H. V. 2013. Contributions of the Kolliker-Fuse nucleus to coordination of breathing and swallowing. *Respir Physiol Neurobiol,* 189**,** 10-21.

BOUVIER, J., THOBY-BRISSON, M., RENIER, N., DUBREUIL, V., ERICSON, J., CHAMPAGNAT, J., PIERANI, A., CHEDOTAL, A. & FORTIN, G. 2010. Hindbrain interneurons and axon guidance signaling critical for breathing. *Nat Neurosci,* 13**,** 1066-74.

BRAGA, V. A., SORIANO, R. N., BRACCIALLI, A. L., DE PAULA, P. M., BONAGAMBA, L. G., PATON, J. F. & MACHADO, B. H. 2007. Involvement of L-glutamate and ATP in the neurotransmission of the sympathoexcitatory component of the chemoreflex in the commissural nucleus tractus solitarii of awake rats and in the working heart-brainstem preparation. *J Physiol,* 581**,** 1129-45.

BROWN, T. G. 1911. The intrinsic factors in the act of progression in the mammal. *Proceedings of the Royal Society B: Biological Sciences,* 84**,** 308-319.

BRUST, R. D., CORCORAN, A. E., RICHERSON, G. B., NATTIE, E. & DYMECKI, S. M. 2014. Functional and developmental identification of a molecular subtype of brain serotonergic neuron specialized to regulate breathing dynamics. *Cell Rep,* 9**,** 2152-65.

BUCHER, D., HASPEL, G., GOLOWASCH, J. & NADIM, F. 2015. Central Pattern Generators. *eLS*.

BURKE, P. G., ABBOTT, S. B., COATES, M. B., VIAR, K. E., STORNETTA, R. L. & GUYENET, P. G. 2014. Optogenetic stimulation of adrenergic C1 neurons causes sleep state-dependent cardiorespiratory stimulation and arousal with sighs in rats. *Am J Respir Crit Care Med,* 190**,** 1301-10.

BURKE, P. G., ABBOTT, S. B., MCMULLAN, S., GOODCHILD, A. K. & PILOWSKY, P. M. 2010. Somatostatin selectively ablates post-inspiratory activity after injection into the Botzinger complex. *Neuroscience,* 167**,** 528-39.

BURKE, P. G., KANBAR, R., BASTING, T. M., HODGES, W. M., VIAR, K. E., STORNETTA, R. L. & GUYENET, P. G. 2015. State-dependent control of breathing by the retrotrapezoid nucleus. *J Physiol,* 593**,** 2909-26.

CAO, W. H. & MORRISON, S. F. 2001. Differential chemoreceptor reflex responses of adrenal preganglionic neurons. *Am J Physiol Regul Integr Comp Physiol,* 281**,** R1825-32.

CARRIVE, P. & KUWAKI, T. 2017. Orexin and Central Modulation of Cardiovascular and Respiratory Function. *Curr Top Behav Neurosci,* 33**,** 157-196.

CATTERALL, W. A. 2011. Voltage-gated calcium channels. *Cold Spring Harb Perspect Biol,* 3**,** a003947.

CERPA, V. J., WU, Y., BRAVO, E., TERAN, F. A., FLYNN, R. S. & RICHERSON, G. B. 2017. Medullary 5-HT neurons: Switch from tonic respiratory drive to chemoreception during postnatal development. *Neuroscience,* 344**,** 1-14.

CHAHROUR, M., JUNG, S. Y., SHAW, C., ZHOU, X., WONG, S. T., QIN, J. & ZOGHBI, H. Y. 2008. MeCP2, a key contributor to neurological disease, activates and represses transcription. *Science,* 320**,** 1224-9.

CHAHROUR, M. & ZOGHBI, H. Y. 2007. The story of Rett syndrome: from clinic to neurobiology. *Neuron,* 56**,** 422-37.

CHALMERS, J. P., KORNER, P. I. & WHITE, S. W. 1967. The relative roles of the aortic and carotid sinus nerves in the rabbit in the control of respiration and circulation during arterial hypoxia and hypercapnia. *J Physiol,* 188**,** 435-50.

CHAO, H. T., ZOGHBI, H. Y. & ROSENMUND, C. 2007. MeCP2 controls excitatory synaptic strength by regulating glutamatergic synapse number. *Neuron,* 56**,** 58-65.

CHEMEL, B. R., ROTH, B. L., ARMBRUSTER, B., WATTS, V. J. & NICHOLS, D. E. 2006. WAY-100635 is a potent dopamine D4 receptor agonist. *Psychopharmacology (Berl),* 188**,** 244-51.

CHEN, Y. & PENINGTON, N. J. 1996. Differential effects of protein kinase C activation on 5-HT1A receptor coupling to Ca2+ and K+ currents in rat serotonergic neurones. *J Physiol,* 496 ( Pt 1)**,** 129-37.

CHENG, L., CHEN, C. L., LUO, P., TAN, M., QIU, M., JOHNSON, R. & MA, Q. 2003. Lmx1b, Pet-1, and Nkx2.2 coordinately specify serotonergic neurotransmitter phenotype. *J Neurosci,* 23**,** 9961-7.

CHILMONCZYK, Z., BOJARSKI, A. J., PILC, A. & SYLTE, I. 2015. Functional Selectivity and Antidepressant Activity of Serotonin 1A Receptor Ligands. *Int J Mol Sci,* 16**,** 18474-506.

CHUANG, C. W., CHENG, M. T., LIN, J. T., HSIEN, H. Y., HUNG, H. Y. & HWANG, J. C. 2003. Arginine vasopressin produces inhibition upon respiration without pressor effect in the rat. *Chin J Physiol,* 46**,** 71-81.

CHUANG, C. W., CHENG, M. T., YANG, S. J. & HWANG, J. C. 2005. Activation of ventrolateral medulla neurons by arginine vasopressin via V1A receptors produces inhibition on respiratory-related hypoglossal nerve discharge in the rat. *Chin J Physiol,* 48**,** 144-54.

CLARK, F. J. & VON EULER, C. 1972. On the regulation of depth and rate of breathing. *J Physiol,* 222**,** 267-95.

CLARKE, W. P., DE VIVO, M., BECK, S. G., MAAYANI, S. & GOLDFARB, J. 1987. Serotonin decreases population spike amplitude in hippocampal cells through a pertussis toxin substrate. *Brain Res,* 410**,** 357-61.

COMER, A. M., GIBBONS, H. M., QI, J., KAWAI, Y., WIN, J. & LIPSKI, J. 1999. Detection of mRNA species in bulbospinal neurons isolated from the rostral ventrolateral medulla using single-cell RT-PCR. *Brain Res Brain Res Protoc,* 4**,** 367-77.

COOPER, D. M. & LONDOS, C. 1982. GTP-dependent stimulation and inhibition of adenylate cyclase. *Horiz Biochem Biophys,* 6**,** 309-33.

CORCORAN, A. E., COMMONS, K. G., WU, Y., SMITH, J. C., HARRIS, M. B. & RICHERSON, G. B. 2014. Dual effects of 5-HT(1a) receptor activation on breathing in neonatal mice. *J Neurosci,* 34**,** 51-9.

CORCORAN, A. E., RICHERSON, G. B. & HARRIS, M. B. 2013. Serotonergic mechanisms are necessary for central respiratory chemoresponsiveness in situ. *Respir Physiol Neurobiol,* 186**,** 214-20.

COSTA-SILVA, J. H., ZOCCAL, D. B. & MACHADO, B. H. 2010. Glutamatergic antagonism in the NTS decreases post-inspiratory drive and changes phrenic and sympathetic coupling during chemoreflex activation. *J Neurophysiol,* 103**,** 2095-106.

COSTA, K. M., ACCORSI-MENDONCA, D., MORAES, D. J. & MACHADO, B. H. 2014. Evolution and physiology of neural oxygen sensing. *Front Physiol,* 5**,** 302.

CUMMINGS, K. J. & HODGES, M. R. 2019. The serotonergic system and the control of breathing during development. *Respir Physiol Neurobiol,* 270**,** 103255.

DAHAN, A., VAN DER SCHRIER, R., SMITH, T., AARTS, L., VAN VELZEN, M. & NIESTERS, M. 2018. Averting Opioid-induced Respiratory Depression without Affecting Analgesia. *Anesthesiology,* 128**,** 1027-1037.

DAMASCENO, R. S., TAKAKURA, A. C. & MOREIRA, T. S. 2014. Regulation of the chemosensory control of breathing by Kolliker-Fuse neurons. *Am J Physiol Regul Integr Comp Physiol,* 307**,** R57-67.

DAMASCENO, R. S., TAKAKURA, A. C. & MOREIRA, T. S. 2015. Respiratory and sympathetic chemoreflex regulation by Kolliker-Fuse neurons in rats. *Pflugers Arch,* 467**,** 231-9.

DAMPNEY, R. A. 1981. Brain stem mechanisms in the control of arterial pressure. *Clin Exp Hypertens,* 3**,** 379-91.

DAMPNEY, R. A. 1994a. Functional organization of central pathways regulating the cardiovascular system. *Physiol Rev,* 74**,** 323-64.

DAMPNEY, R. A. 1994b. The subretrofacial vasomotor nucleus: anatomical, chemical and pharmacological properties and role in cardiovascular regulation. *Prog Neurobiol,* 42**,** 197-227.

DAMPNEY, R. A., GOODCHILD, A. K., ROBERTSON, L. G. & MONTGOMERY, W. 1982. Role of ventrolateral medulla in vasomotor regulation: a correlative anatomical and physiological study. *Brain Res,* 249**,** 223-35.

DAVIES, A. & MOORES, C. 2010. *The respiratory system : basic science and clinical conditions,* Edinburgh ; New York, Churchill Livingstone.

DE BRITTO, A. A. & MORAES, D. J. 2017. Non-chemosensitive parafacial neurons simultaneously regulate active expiration and airway patency under hypercapnia in rats. *J Physiol,* 595**,** 2043-2064.

DE SOUZA MORENO, V., BICEGO, K. C., SZAWKA, R. E., ANSELMO-FRANCI, J. A. & GARGAGLIONI, L. H. 2010. Serotonergic mechanisms on breathing modulation in the rat locus coeruleus. *Pflugers Arch,* 459**,** 357-68.

DEL NEGRO, C. A., FUNK, G. D. & FELDMAN, J. L. 2018. Breathing matters. *Nat Rev Neurosci,* 19**,** 351-367.

DEL NEGRO, C. A., HAYES, J. A., PACE, R. W., BRUSH, B. R., TERUYAMA, R. & FELDMAN, J. L. 2010. Synaptically activated burst-generating conductances may underlie a group-pacemaker mechanism for respiratory rhythm generation in mammals. *Prog Brain Res,* 187**,** 111-36.

DEMPSEY, J. A., SHEEL, A. W., ST CROIX, C. M. & MORGAN, B. J. 2002. Respiratory influences on sympathetic vasomotor outflow in humans. *Respir Physiol Neurobiol,* 130**,** 3-20.

DEPUY, S. D., KANBAR, R., COATES, M. B., STORNETTA, R. L. & GUYENET, P. G. 2011. Control of breathing by raphe obscurus serotonergic neurons in mice. *J Neurosci,* 31**,** 1981-90.

DHINGRA, R. R., DICK, T. E., FURUYA, W. I., GALAN, R. F. & DUTSCHMANN, M. 2020. Volumetric mapping of the functional neuroanatomy of the respiratory network in the perfused brainstem preparation of rats. *J Physiol*.

DHINGRA, R. R., DUTSCHMANN, M. & DICK, T. E. 2016. Blockade of dorsolateral pontine 5HT1A receptors destabilizes the respiratory rhythm in C57BL6/J wild-type mice. *Respir Physiol Neurobiol,* 226**,** 110-4.

DHINGRA, R. R., FURUYA, W. I., BAUTISTA, T. G., DICK, T. E., GALAN, R. F. & DUTSCHMANN, M. 2019. Increasing Local Excitability of Brainstem Respiratory Nuclei Reveals a Distributed Network Underlying Respiratory Motor Pattern Formation. *Front Physiol,* 10**,** 887.

DIBONA, G. F. & KOPP, U. C. 1997. Neural control of renal function. *Physiol Rev,* 77**,** 75-197.

DICK, T. E., HSIEH, Y. H., DHINGRA, R. R., BAEKEY, D. M., GALAN, R. F., WEHRWEIN, E. & MORRIS, K. F. 2014. Cardiorespiratory coupling: common rhythms in cardiac, sympathetic, and respiratory activities. *Prog Brain Res,* 209**,** 191-205.

DICK, T. E., HSIEH, Y. H., MORRISON, S., COLES, S. K. & PRABHAKAR, N. 2004. Entrainment pattern between sympathetic and phrenic nerve activities in the Sprague-Dawley rat: hypoxia-evoked sympathetic activity during expiration. *Am J Physiol Regul Integr Comp Physiol,* 286**,** R1121-8.

DICK, T. E., SHANNON, R., LINDSEY, B. G., NUDING, S. C., SEGERS, L. S., BAEKEY, D. M. & MORRIS, K. F. 2008. Pontine respiratory-modulated activity before and after vagotomy in decerebrate cats. *J Physiol,* 586**,** 4265-82.

DOLCE, A., BEN-ZEEV, B., NAIDU, S. & KOSSOFF, E. H. 2013. Rett syndrome and epilepsy: an update for child neurologists. *Pediatr Neurol,* 48**,** 337-45.

DONG, L., KREWSON, E. A. & YANG, L. V. 2017. Acidosis Activates Endoplasmic Reticulum Stress Pathways through GPR4 in Human Vascular Endothelial Cells. *Int J Mol Sci,* 18.

DUALE, H., WAKI, H., HOWORTH, P., KASPAROV, S., TESCHEMACHER, A. G. & PATON, J. F. 2007. Restraining influence of A2 neurons in chronic control of arterial pressure in spontaneously hypertensive rats. *Cardiovasc Res,* 76**,** 184-93.

DUTSCHMANN, M., BAUTISTA, T. G., MORSCHEL, M. & DICK, T. E. 2014a. Learning to breathe: habituation of Hering-Breuer inflation reflex emerges with postnatal brainstem maturation. *Respir Physiol Neurobiol,* 195**,** 44-9.

DUTSCHMANN, M. & DICK, T. E. 2012. Pontine mechanisms of respiratory control. *Compr Physiol,* 2**,** 2443-69.

DUTSCHMANN, M. & HERBERT, H. 2006. The Kolliker-Fuse nucleus gates the postinspiratory phase of the respiratory cycle to control inspiratory off-switch and upper airway resistance in rat. *Eur J Neurosci,* 24**,** 1071-84.

DUTSCHMANN, M., JONES, S. E., SUBRAMANIAN, H. H., STANIC, D. & BAUTISTA, T. G. 2014b. The physiological significance of postinspiration in respiratory control. *Prog Brain Res,* 212**,** 113-30.

DUTSCHMANN, M., MORSCHEL, M., RYBAK, I. A. & DICK, T. E. 2009a. Learning to breathe: control of the inspiratory-expiratory phase transition shifts from sensory- to central-dominated during postnatal development in rats. *J Physiol,* 587**,** 4931-48.

DUTSCHMANN, M., WAKI, H., MANZKE, T., SIMMS, A. E., PICKERING, A. E., RICHTER, D. W. & PATON, J. F. 2009b. The potency of different serotonergic agonists in counteracting opioid evoked cardiorespiratory disturbances. *Philos Trans R Soc Lond B Biol Sci,* 364**,** 2611-23.

DUTSCHMANN, M., WILSON, R. J. & PATON, J. F. 2000. Respiratory activity in neonatal rats. *Auton Neurosci,* 84**,** 19-29.

EASTON, J. & HOWE, A. 1983. The distribution of thoracic glomus tissue (aortic bodies) in the rat. *Cell Tissue Res,* 232**,** 349-56.

ECHIGO, N. & MORIYAMA, Y. 2004. Vesicular inhibitory amino acid transporter is expressed in gamma-aminobutyric acid (GABA)-containing astrocytes in rat pineal glands. *Neurosci Lett,* 367**,** 79-84.

ELLENBERGER, H. H. 1999. Distribution of bulbospinal gamma-aminobutyric acid-synthesizing neurons of the ventral respiratory group of the rat. *J Comp Neurol,* 411**,** 130-44.

ERICKSON, J. T. & MILLHORN, D. E. 1991. Fos-like protein is induced in neurons of the medulla oblongata after stimulation of the carotid sinus nerve in awake and anesthetized rats. *Brain Res,* 567**,** 11-24.

ERICKSON, J. T. & MILLHORN, D. E. 1994. Hypoxia and electrical stimulation of the carotid sinus nerve induce Fos-like immunoreactivity within catecholaminergic and serotoninergic neurons of the rat brainstem. *J Comp Neurol,* 348**,** 161-82.

ERICKSON, J. T., SHAFER, G., ROSSETTI, M. D., WILSON, C. G. & DENERIS, E. S. 2007. Arrest of 5HT neuron differentiation delays respiratory maturation and impairs neonatal homeostatic responses to environmental challenges. *Respir Physiol Neurobiol,* 159**,** 85-101.

EZURE, K. 1990. Synaptic connections between medullary respiratory neurons and considerations on the genesis of respiratory rhythm. *Prog Neurobiol,* 35**,** 429-50.

EZURE, K., MANABE, M. & YAMADA, H. 1988. Distribution of medullary respiratory neurons in the rat. *Brain Res,* 455**,** 262-70.

EZURE, K. & TANAKA, I. 2006. Distribution and medullary projection of respiratory neurons in the dorsolateral pons of the rat. *Neuroscience,* 141**,** 1011-1023.

EZURE, K., TANAKA, I. & KONDO, M. 2003. Glycine is used as a transmitter by decrementing expiratory neurons of the ventrolateral medulla in the rat. *J Neurosci,* 23**,** 8941-8.

FALQUETTO, B., OLIVEIRA, L. M., TAKAKURA, A. C., MULKEY, D. K. & MOREIRA, T. S. 2018. Inhibition of the hypercapnic ventilatory response by adenosine in the retrotrapezoid nucleus in awake rats. *Neuropharmacology,* 138**,** 47-56.

FELDMAN, J. L. & GAUTIER, H. 1976. Interaction of pulmonary afferents and pneumotaxic center in control of respiratory pattern in cats. *J Neurophysiol,* 39**,** 31-44.

FELDMAN, J. L. & KAM, K. 2015. Facing the challenge of mammalian neural microcircuits: taking a few breaths may help. *J Physiol,* 593**,** 3-23.

FLOR, K. C., BARNETT, W. H., KARLEN-AMARANTE, M., MOLKOV, Y. I. & ZOCCAL, D. B. 2020. Inhibitory control of active expiration by the Botzinger complex in rats. *J Physiol*.

FONG, A. Y. & POTTS, J. T. 2006. Neurokinin-1 receptor activation in Botzinger complex evokes bradypnoea. *J Physiol,* 575**,** 869-85.

FORTUNA, M. G., WEST, G. H., STORNETTA, R. L. & GUYENET, P. G. 2008. Botzinger expiratory-augmenting neurons and the parafacial respiratory group. *J Neurosci,* 28**,** 2506-15.

GANDINI, L. G., JR., MARTINS, R. P., DE OLIVEIRA, C. A., ABDALA, A. & BUSCHANG, P. H. 2009. Midsymphyseal distraction osteogenesis: a new alternative for the treatment of dental crowding. *Am J Orthod Dentofacial Orthop,* 135**,** 530-5.

GARCIA-CABEZAS, M. A., JOHN, Y. J., BARBAS, H. & ZIKOPOULOS, B. 2016. Distinction of Neurons, Glia and Endothelial Cells in the Cerebral Cortex: An Algorithm Based on Cytological Features. *Front Neuroanat,* 10**,** 107.

GEERLING, J. C., YOKOTA, S., RUKHADZE, I., ROE, D. & CHAMBERLIN, N. L. 2017. Kolliker-Fuse GABAergic and glutamatergic neurons project to distinct targets. *J Comp Neurol,* 525**,** 1844-1860.

GESTREAU, C., HEITZMANN, D., THOMAS, J., DUBREUIL, V., BANDULIK, S., REICHOLD, M., BENDAHHOU, S., PIERSON, P., STERNER, C., PEYRONNET-ROUX, J., BENFRIHA, C., TEGTMEIER, I., EHNES, H., GEORGIEFF, M., LESAGE, F., BRUNET, J. F., GORIDIS, C., WARTH, R. & BARHANIN, J. 2010. Task2 potassium channels set central respiratory CO2 and O2 sensitivity. *Proc Natl Acad Sci U S A,* 107**,** 2325-30.

GOETZ, C. G., DAMIER, P., HICKING, C., LASKA, E., MULLER, T., OLANOW, C. W., RASCOL, O. & RUSS, H. 2007. Sarizotan as a treatment for dyskinesias in Parkinson's disease: a double-blind placebo-controlled trial. *Mov Disord,* 22**,** 179-86.

GRAY, P. A., HAYES, J. A., LING, G. Y., LLONA, I., TUPAL, S., PICARDO, M. C., ROSS, S. E., HIRATA, T., CORBIN, J. G., EUGENIN, J. & DEL NEGRO, C. A. 2010. Developmental origin of preBotzinger complex respiratory neurons. *J Neurosci,* 30**,** 14883-95.

GRAY, P. A., REKLING, J. C., BOCCHIARO, C. M. & FELDMAN, J. L. 1999. Modulation of respiratory frequency by peptidergic input to rhythmogenic neurons in the preBotzinger complex. *Science,* 286**,** 1566-8.

GUENTHER, U., MANZKE, T., WRIGGE, H., DUTSCHMANN, M., ZINSERLING, J., PUTENSEN, C. & HOEFT, A. 2009. The counteraction of opioid-induced ventilatory depression by the serotonin 1A-agonist 8-OH-DPAT does not antagonize antinociception in rats in situ and in vivo. *Anesth Analg,* 108**,** 1169-76.

GUENTHER, U., THEUERKAUF, N. U., HUSE, D., BOETTCHER, M. F., WENSING, G., PUTENSEN, C. & HOEFT, A. 2012. Selective 5-HT(1A)-R-agonist repinotan prevents remifentanil-induced ventilatory depression and prolongs antinociception. *Anesthesiology,* 116**,** 56-64.

GUYENET, P. G. 2006. The sympathetic control of blood pressure. *Nat Rev Neurosci,* 7**,** 335-46.

GUYENET, P. G. 2014. Regulation of breathing and autonomic outflows by chemoreceptors. *Compr Physiol,* 4**,** 1511-62.

GUYENET, P. G. & BAYLISS, D. A. 2015. Neural Control of Breathing and CO2 Homeostasis. *Neuron,* 87**,** 946-61.

GUYENET, P. G., BAYLISS, D. A., STORNETTA, R. L., KANBAR, R., SHI, Y., HOLLOWAY, B. B., SOUZA, G., BASTING, T. M., ABBOTT, S. B. G. & WENKER, I. C. 2018. Interdependent feedback regulation of breathing by the carotid bodies and the retrotrapezoid nucleus. *J Physiol,* 596**,** 3029-3042.

GUYENET, P. G., BAYLISS, D. A., STORNETTA, R. L., LUDWIG, M. G., KUMAR, N. N., SHI, Y., BURKE, P. G., KANBAR, R., BASTING, T. M., HOLLOWAY, B. B. & WENKER, I. C. 2016. Proton detection and breathing regulation by the retrotrapezoid nucleus. *J Physiol,* 594**,** 1529-51.

GUYENET, P. G., DARNALL, R. A. & RILEY, T. A. 1990. Rostral ventrolateral medulla and sympathorespiratory integration in rats. *Am J Physiol,* 259**,** R1063-74.

GUYENET, P. G., STORNETTA, R. L., BOCHORISHVILI, G., DEPUY, S. D., BURKE, P. G. & ABBOTT, S. B. 2013. C1 neurons: the body's EMTs. *Am J Physiol Regul Integr Comp Physiol,* 305**,** R187-204.

GUYENET, P. G., STORNETTA, R. L., SOUZA, G., ABBOTT, S. B. G., SHI, Y. & BAYLISS, D. A. 2019. The Retrotrapezoid Nucleus: Central Chemoreceptor and Regulator of Breathing Automaticity. *Trends Neurosci,* 42**,** 807-824.

GUYENET, P. G. & WANG, H. 2001. Pre-Botzinger neurons with preinspiratory discharges "in vivo" express NK1 receptors in the rat. *J Neurophysiol,* 86**,** 438-46.

HALBACH, N. S., SMEETS, E. E., BIERAU, J., KEULARTS, I. M., PLASQUI, G., JULU, P. O., ENGERSTROM, I. W., BAKKER, J. A. & CURFS, L. M. 2012. Altered carbon dioxide metabolism and creatine abnormalities in rett syndrome. *JIMD Rep,* 3**,** 117-24.

HANNON, J. & HOYER, D. 2008. Molecular biology of 5-HT receptors. *Behav Brain Res,* 195**,** 198-213.

HARA, K. & HARRIS, R. A. 2002. The anesthetic mechanism of urethane: the effects on neurotransmitter-gated ion channels. *Anesth Analg,* 94**,** 313-8, table of contents.

HARDING, A., PAXINOS, G. & HALLIDAY, G. 2004. The Serotonin and Tachykinin Systems. *The Rat Nervous system.* Third Edition ed.: Academic Press.

HASELTON, J. R. & GUYENET, P. G. 1989. Central respiratory modulation of medullary sympathoexcitatory neurons in rat. *Am J Physiol,* 256**,** R739-50.

HEDLUND, P. B., KELLY, L., MAZUR, C., LOVENBERG, T., SUTCLIFFE, J. G. & BONAVENTURE, P. 2004. 8-OH-DPAT acts on both 5-HT1A and 5-HT7 receptors to induce hypothermia in rodents. *Eur J Pharmacol,* 487**,** 125-32.

HEGARTY, A. A. & FELDER, R. B. 1997. Vasopressin and V1-receptor antagonists modulate the activity of NTS neurons receiving baroreceptor input. *Am J Physiol,* 273**,** R143-52.

HENDERSON, K. K. & BYRON, K. L. 2007. Vasopressin-induced vasoconstriction: two concentration-dependent signaling pathways. *J Appl Physiol (1985),* 102**,** 1402-9.

HENDRICKS, T. J., FYODOROV, D. V., WEGMAN, L. J., LELUTIU, N. B., PEHEK, E. A., YAMAMOTO, B., SILVER, J., WEEBER, E. J., SWEATT, J. D. & DENERIS, E. S. 2003. Pet-1 ETS gene plays a critical role in 5-HT neuron development and is required for normal anxiety-like and aggressive behavior. *Neuron,* 37**,** 233-47.

HENNESSY, M. L., CORCORAN, A. E., BRUST, R. D., CHANG, Y., NATTIE, E. E. & DYMECKI, S. M. 2017. Activity of Tachykinin1-Expressing Pet1 Raphe Neurons Modulates the Respiratory Chemoreflex. *J Neurosci,* 37**,** 1807-1819.

HERBERT, H., MOGA, M. M. & SAPER, C. B. 1990. Connections of the parabrachial nucleus with the nucleus of the solitary tract and the medullary reticular formation in the rat. *J Comp Neurol,* 293**,** 540-80.

HODGES, M. R., OPANSKY, C., QIAN, B., DAVIS, S., BONIS, J. M., KRAUSE, K., PAN, L. G. & FORSTER, H. V. 2005. Carotid body denervation alters ventilatory responses to ibotenic acid injections or focal acidosis in the medullary raphe. *J Appl Physiol (1985),* 98**,** 1234-42.

HODGES, M. R. & RICHERSON, G. B. 2008. Contributions of 5-HT neurons to respiratory control: neuromodulatory and trophic effects. *Respir Physiol Neurobiol,* 164**,** 222-32.

HODGES, M. R., TATTERSALL, G. J., HARRIS, M. B., MCEVOY, S. D., RICHERSON, D. N., DENERIS, E. S., JOHNSON, R. L., CHEN, Z. F. & RICHERSON, G. B. 2008. Defects in breathing and thermoregulation in mice with near-complete absence of central serotonin neurons. *J Neurosci,* 28**,** 2495-505.

HODGES, M. R., WEHNER, M., AUNGST, J., SMITH, J. C. & RICHERSON, G. B. 2009. Transgenic mice lacking serotonin neurons have severe apnea and high mortality during development. *J Neurosci,* 29**,** 10341-9.

HOSFORD, P. S., MOSIENKO, V., KISHI, K., JURISIC, G., SEUWEN, K., KINZEL, B., LUDWIG, M. G., WELLS, J. A., CHRISTIE, I. N., KOOLEN, L., ABDALA, A. P., LIU, B. H., GOURINE, A. V., TESCHEMACHER, A. G. & KASPAROV, S. 2018. CNS distribution, signalling properties and central effects of G-protein coupled receptor 4. *Neuropharmacology,* 138**,** 381-392.

HOWARTH, C., SUTHERLAND, B., CHOI, H. B., MARTIN, C., LIND, B. L., KHENNOUF, L., LEDUE, J. M., PAKAN, J. M., KO, R. W., ELLIS-DAVIES, G., LAURITZEN, M., SIBSON, N. R., BUCHAN, A. M. & MACVICAR, B. A. 2017. A Critical Role for Astrocytes in Hypercapnic Vasodilation in Brain. *J Neurosci,* 37**,** 2403-2414.

HUCKSTEPP, R. T., CARDOZA, K. P., HENDERSON, L. E. & FELDMAN, J. L. 2015. Role of parafacial nuclei in control of breathing in adult rats. *J Neurosci,* 35**,** 1052-67.

HWANG, D. Y., CARLEZON, W. A., JR., ISACSON, O. & KIM, K. S. 2001. A high-efficiency synthetic promoter that drives transgene expression selectively in noradrenergic neurons. *Hum Gene Ther,* 12**,** 1731-40.

ICEMAN, K. E., RICHERSON, G. B. & HARRIS, M. B. 2013. Medullary serotonin neurons are CO2 sensitive in situ. *J Neurophysiol,* 110**,** 2536-44.

IDE, S., ITOH, M. & GOTO, Y. 2005. Defect in normal developmental increase of the brain biogenic amine concentrations in the mecp2-null mouse. *Neurosci Lett,* 386**,** 14-7.

IKEDA, K., IGARASHI, H., YAWO, H., KOBAYASHI, K., ARATA, S., KAWAKAMI, K., IZUMIZAKI, M. & ONIMARU, H. 2019. Optogenetic analysis of respiratory neuronal networks in the ventral medulla of neonatal rats producing channelrhodopsin in Phox2b-positive cells. *Pflugers Arch*.

JANCZEWSKI, W. A., TASHIMA, A., HSU, P., CUI, Y. & FELDMAN, J. L. 2013. Role of inhibition in respiratory pattern generation. *J Neurosci,* 33**,** 5454-65.

JANIG, W. & HABLER, H. J. 2003. Neurophysiological analysis of target-related sympathetic pathways--from animal to human: similarities and differences. *Acta Physiol Scand,* 177**,** 255-74.

JENKIN, S. E., MILSOM, W. K. & ZOCCAL, D. B. 2017. The Kolliker-Fuse nucleus acts as a timekeeper for late-expiratory abdominal activity. *Neuroscience,* 348**,** 63-72.

JENKINS, T. A., NGUYEN, J. C., POLGLAZE, K. E. & BERTRAND, P. P. 2016. Influence of Tryptophan and Serotonin on Mood and Cognition with a Possible Role of the Gut-Brain Axis. *Nutrients,* 8.

JIANG, C., CUI, N., ZHONG, W., JOHNSON, C. M. & WU, Y. 2017. Breathing abnormalities in animal models of Rett syndrome a female neurogenetic disorder. *Respir Physiol Neurobiol,* 245**,** 45-52.

KAM, K., WORRELL, J. W., JANCZEWSKI, W. A., CUI, Y. & FELDMAN, J. L. 2013a. Distinct inspiratory rhythm and pattern generating mechanisms in the preBotzinger complex. *J Neurosci,* 33**,** 9235-45.

KAM, K., WORRELL, J. W., VENTALON, C., EMILIANI, V. & FELDMAN, J. L. 2013b. Emergence of population bursts from simultaneous activation of small subsets of preBotzinger complex inspiratory neurons. *J Neurosci,* 33**,** 3332-8.

KANBAR, R., STORNETTA, R. L., CASH, D. R., LEWIS, S. J. & GUYENET, P. G. 2010. Photostimulation of Phox2b medullary neurons activates cardiorespiratory function in conscious rats. *Am J Respir Crit Care Med,* 182**,** 1184-94.

KAUR, S., PEDERSEN, N. P., YOKOTA, S., HUR, E. E., FULLER, P. M., LAZARUS, M., CHAMBERLIN, N. L. & SAPER, C. B. 2013. Glutamatergic signaling from the parabrachial nucleus plays a critical role in hypercapnic arousal. *J Neurosci,* 33**,** 7627-40.

KC, P., BALAN, K. V., TJOE, S. S., MARTIN, R. J., LAMANNA, J. C., HAXHIU, M. A. & DICK, T. E. 2010. Increased vasopressin transmission from the paraventricular nucleus to the rostral medulla augments cardiorespiratory outflow in chronic intermittent hypoxia-conditioned rats. *J Physiol,* 588**,** 725-40.

KOIZUMI, H., KOSHIYA, N., CHIA, J. X., CAO, F., NUGENT, J., ZHANG, R. & SMITH, J. C. 2013. Structural-functional properties of identified excitatory and inhibitory interneurons within pre-Botzinger complex respiratory microcircuits. *J Neurosci,* 33**,** 2994-3009.

KOIZUMI, H., WILSON, C. G., WONG, S., YAMANISHI, T., KOSHIYA, N. & SMITH, J. C. 2008. Functional imaging, spatial reconstruction, and biophysical analysis of a respiratory motor circuit isolated in vitro. *J Neurosci,* 28**,** 2353-65.

KOSHIYA, N. & GUYENET, P. G. 1996. NTS neurons with carotid chemoreceptor inputs arborize in the rostral ventrolateral medulla. *Am J Physiol,* 270**,** R1273-8.

KOSHIYA, N., HUANGFU, D. & GUYENET, P. G. 1993. Ventrolateral medulla and sympathetic chemoreflex in the rat. *Brain Res,* 609**,** 174-84.

KUBIN, L., ALHEID, G. F., ZUPERKU, E. J. & MCCRIMMON, D. R. 2006. Central pathways of pulmonary and lower airway vagal afferents. *J Appl Physiol (1985),* 101**,** 618-27.

KUMAR, N. N., VELIC, A., SOLIZ, J., SHI, Y., LI, K., WANG, S., WEAVER, J. L., SEN, J., ABBOTT, S. B., LAZARENKO, R. M., LUDWIG, M. G., PEREZ-REYES, E., MOHEBBI, N., BETTONI, C., GASSMANN, M., SUPLY, T., SEUWEN, K., GUYENET, P. G., WAGNER, C. A. & BAYLISS, D. A. 2015. PHYSIOLOGY. Regulation of breathing by CO(2) requires the proton-activated receptor GPR4 in retrotrapezoid nucleus neurons. *Science,* 348**,** 1255-60.

KUMAR, P. & PRABHAKAR, N. R. 2012. Peripheral chemoreceptors: function and plasticity of the carotid body. *Compr Physiol,* 2**,** 141-219.

KUWANA, S., TSUNEKAWA, N., YANAGAWA, Y., OKADA, Y., KURIBAYASHI, J. & OBATA, K. 2006. Electrophysiological and morphological characteristics of GABAergic respiratory neurons in the mouse pre-Botzinger complex. *Eur J Neurosci,* 23**,** 667-74.

LADEWIG, T., LALLEY, P. M. & KELLER, B. U. 2004. Serotonergic modulation of intracellular calcium dynamics in neonatal hypoglossal motoneurons from mouse. *Brain Res,* 1001**,** 1-12.

LAHIRI, S., ROY, A., BABY, S. M., HOSHI, T., SEMENZA, G. L. & PRABHAKAR, N. R. 2006. Oxygen sensing in the body. *Prog Biophys Mol Biol,* 91**,** 249-86.

LALLEY, P. M., BISCHOFF, A. M. & RICHTER, D. W. 1994. 5-HT-1A receptor-mediated modulation of medullary expiratory neurones in the cat. *J Physiol,* 476**,** 117-30.

LANDGRAF, R. 1992. Chapter 6: Central release of vasopressin: stimuli, dynamics, consequences. *Progress in Brain Research.* Elsevier.

LEAVESLEY, H. B., LI, L., PRABHAKARAN, K., BOROWITZ, J. L. & ISOM, G. E. 2008. Interaction of cyanide and nitric oxide with cytochrome c oxidase: implications for acute cyanide toxicity. *Toxicol Sci,* 101**,** 101-11.

LEE, C. & JONES, T. A. 2018. Effects of Ketamine Compared with Urethane Anesthesia on Vestibular Sensory Evoked Potentials and Systemic Physiology in Mice. *J Am Assoc Lab Anim Sci*.

LEMES, E. V., AIKO, S., ORBEM, C. B., FORMENTIN, C., BASSI, M., COLOMBARI, E. & ZOCCAL, D. B. 2016a. Long-term facilitation of expiratory and sympathetic activities following acute intermittent hypoxia in rats. *Acta Physiol (Oxf)*.

LEMES, E. V., COLOMBARI, E. & ZOCCAL, D. B. 2016b. Generation of active expiration by serotoninergic mechanisms of the ventral medulla of rats. *J Appl Physiol (1985)***,** jap 00470 2016.

LEVIGOUREUX, E., VIDAL, B., FIEUX, S., BOUILLOT, C., EMERY, S., NEWMAN-TANCREDI, A. & ZIMMER, L. 2019. Serotonin 5-HT1A Receptor Biased Agonists Induce Different Cerebral Metabolic Responses: A [(18)F]-Fluorodesoxyglucose Positron Emission Tomography Study in Conscious and Anesthetized Rats. *ACS Chem Neurosci,* 10**,** 3108-3119.

LEVITT, E. S. 2020. Pontine mechanisms of opioid-induced respiratory depression. *Control of Breathing Seminar Series.* University of Florida.

LEVITT, E. S., ABDALA, A. P., PATON, J. F., BISSONNETTE, J. M. & WILLIAMS, J. T. 2015. mu opioid receptor activation hyperpolarizes respiratory-controlling Kolliker-Fuse neurons and suppresses post-inspiratory drive. *J Physiol,* 593**,** 4453-69.

LEVITT, E. S., HUNNICUTT, B. J., KNOPP, S. J., WILLIAMS, J. T. & BISSONNETTE, J. M. 2013. A selective 5-HT1a receptor agonist improves respiration in a mouse model of Rett syndrome. *J Appl Physiol (1985),* 115**,** 1626-33.

LI, A., ZHOU, S. & NATTIE, E. 2006. Simultaneous inhibition of caudal medullary raphe and retrotrapezoid nucleus decreases breathing and the CO2 response in conscious rats. *J Physiol,* 577**,** 307-18.

LINDSEY, B. G., NUDING, S. C., SEGERS, L. S. & MORRIS, K. F. 2018. Carotid Bodies and the Integrated Cardiorespiratory Response to Hypoxia. *Physiology (Bethesda),* 33**,** 281-297.

LIPSKI, J. 1981. Antidromic activation of neurones as an analytic tool in the study of the central nervous system. *J Neurosci Methods,* 4**,** 1-32.

LLADO-PELFORT, L., ASSIE, M. B., NEWMAN-TANCREDI, A., ARTIGAS, F. & CELADA, P. 2010. Preferential in vivo action of F15599, a novel 5-HT(1A) receptor agonist, at postsynaptic 5-HT(1A) receptors. *Br J Pharmacol,* 160**,** 1929-40.

LOPEZ-BARNEO, J., ORTEGA-SAENZ, P., GONZALEZ-RODRIGUEZ, P., FERNANDEZ-AGUERA, M. C., MACIAS, D., PARDAL, R. & GAO, L. 2016. Oxygen-sensing by arterial chemoreceptors: Mechanisms and medical translation. *Mol Aspects Med,* 47-48**,** 90-108.

LU, Y., WHITEIS, C. A., SLUKA, K. A., CHAPLEAU, M. W. & ABBOUD, F. M. 2013. Responses of glomus cells to hypoxia and acidosis are uncoupled, reciprocal and linked to ASIC3 expression: selectivity of chemosensory transduction. *J Physiol,* 591**,** 919-32.

LUCK, J. C. 1970. Afferent vagal fibres with an expiratory discharge in the rabbit. *J Physiol,* 211**,** 63-71.

MACHADO, B. H., ZOCCAL, D. B. & MORAES, D. J. A. 2017. Neurogenic hypertension and the secrets of respiration. *Am J Physiol Regul Integr Comp Physiol,* 312**,** R864-R872.

MALPAS, S. C. 1998. The rhythmicity of sympathetic nerve activity. *Prog Neurobiol,* 56**,** 65-96.

MALPAS, S. C. 2010. Sympathetic nervous system overactivity and its role in the development of cardiovascular disease. *Physiol Rev,* 90**,** 513-57.

MANABE, M. & EZURE, K. 1988. Decrementing expiratory neurons of the Botzinger complex. I. Response to lung inflation and axonal projection. *Exp Brain Res,* 72**,** 150-8.

MANDEL, D. A. & SCHREIHOFER, A. M. 2006. Central respiratory modulation of barosensitive neurones in rat caudal ventrolateral medulla. *J Physiol,* 572**,** 881-96.

MANDEL, D. A. & SCHREIHOFER, A. M. 2009. Modulation of the sympathetic response to acute hypoxia by the caudal ventrolateral medulla in rats. *J Physiol,* 587**,** 461-75.

MANNOURY LA COUR, C., EL MESTIKAWY, S., HANOUN, N., HAMON, M. & LANFUMEY, L. 2006. Regional differences in the coupling of 5-hydroxytryptamine-1A receptors to G proteins in the rat brain. *Mol Pharmacol,* 70**,** 1013-21.

MANZKE, T., DUTSCHMANN, M., SCHLAF, G., MORSCHEL, M., KOCH, U. R., PONIMASKIN, E., BIDON, O., LALLEY, P. M. & RICHTER, D. W. 2009. Serotonin targets inhibitory synapses to induce modulation of network functions. *Philos Trans R Soc Lond B Biol Sci,* 364**,** 2589-602.

MANZKE, T., GUENTHER, U., PONIMASKIN, E. G., HALLER, M., DUTSCHMANN, M., SCHWARZACHER, S. & RICHTER, D. W. 2003. 5-HT4(a) receptors avert opioid-induced breathing depression without loss of analgesia. *Science,* 301**,** 226-9.

MANZKE, T., NIEBERT, M., KOCH, U. R., CALEY, A., VOGELGESANG, S., HULSMANN, S., PONIMASKIN, E., MULLER, U., SMART, T. G., HARVEY, R. J. & RICHTER, D. W. 2010. Serotonin receptor 1A-modulated phosphorylation of glycine receptor alpha3 controls breathing in mice. *J Clin Invest,* 120**,** 4118-28.

MARCHENKO, V., KOIZUMI, H., MOSHER, B., KOSHIYA, N., TARIQ, M. F., BEZDUDNAYA, T. G., ZHANG, R., MOLKOV, Y. I., RYBAK, I. A. & SMITH, J. C. 2016. Perturbations of Respiratory Rhythm and Pattern by Disrupting Synaptic Inhibition within Pre-Botzinger and Botzinger Complexes. *eNeuro,* 3.

MARDER, E. & BUCHER, D. 2001. Central pattern generators and the control of rhythmic movements. *Curr Biol,* 11**,** R986-96.

MARINA, N., ABDALA, A. P., KORSAK, A., SIMMS, A. E., ALLEN, A. M., PATON, J. F. & GOURINE, A. V. 2011. Control of sympathetic vasomotor tone by catecholaminergic C1 neurones of the rostral ventrolateral medulla oblongata. *Cardiovasc Res,* 91**,** 703-10.

MARINA, N., ABDALA, A. P., TRAPP, S., LI, A., NATTIE, E. E., HEWINSON, J., SMITH, J. C., PATON, J. F. & GOURINE, A. V. 2010. Essential role of Phox2b-expressing ventrolateral brainstem neurons in the chemosensory control of inspiration and expiration. *J Neurosci,* 30**,** 12466-73.

MARTEL, J. C., LEDUC, N., ORMIERE, A. M., FAUCILLON, V., DANTY, N., CULIE, C., CUSSAC, D. & NEWMAN-TANCREDI, A. 2007. WAY-100635 has high selectivity for serotonin 5-HT(1A) versus dopamine D(4) receptors. *Eur J Pharmacol,* 574**,** 15-9.

MCGOVERN, A. E. & MAZZONE, S. B. 2010. Characterization of the vagal motor neurons projecting to the Guinea pig airways and esophagus. *Front Neurol,* 1**,** 153.

MENUET, C., SEVIGNY, C. P., CONNELLY, A. A., BASSI, J. K., JANCOVSKI, N., WILLIAMS, D. A., ANDERSON, C. R., LLEWELLYN-SMITH, I. J., FONG, A. Y. & ALLEN, A. M. 2014. Catecholaminergic C3 neurons are sympathoexcitatory and involved in glucose homeostasis. *J Neurosci,* 34**,** 15110-22.

MIDDLETON, S. A., EBERWINE, J. & KIM, J. 2019. Comprehensive catalog of dendritically localized mRNA isoforms from sub-cellular sequencing of single mouse neurons. *BMC Biol,* 17**,** 5.

MIFFLIN, S. W. 1992. Arterial chemoreceptor input to nucleus tractus solitarius. *Am J Physiol,* 263**,** R368-75.

MIYAZAKI, I., ASANUMA, M., MURAKAMI, S., TAKESHIMA, M., TORIGOE, N., KITAMURA, Y. & MIYOSHI, K. 2013. Targeting 5-HT(1A) receptors in astrocytes to protect dopaminergic neurons in Parkinsonian models. *Neurobiol Dis,* 59**,** 244-56.

MOLKOV, Y. I., ABDALA, A. P., BACAK, B. J., SMITH, J. C., PATON, J. F. & RYBAK, I. A. 2010. Late-expiratory activity: emergence and interactions with the respiratory CpG. *J Neurophysiol,* 104**,** 2713-29.

MOLKOV, Y. I., BACAK, B. J., DICK, T. E. & RYBAK, I. A. 2013. Control of breathing by interacting pontine and pulmonary feedback loops. *Front Neural Circuits,* 7**,** 16.

MOLKOV, Y. I., SHEVTSOVA, N. A., PARK, C., BEN-TAL, A., SMITH, J. C., RUBIN, J. E. & RYBAK, I. A. 2014a. A closed-loop model of the respiratory system: focus on hypercapnia and active expiration. *PLoS One,* 9**,** e109894.

MOLKOV, Y. I., ZOCCAL, D. B., BAEKEY, D. M., ABDALA, A. P., MACHADO, B. H., DICK, T. E., PATON, J. F. & RYBAK, I. A. 2014b. Physiological and pathophysiological interactions between the respiratory central pattern generator and the sympathetic nervous system. *Prog Brain Res,* 212**,** 1-23.

MOLKOV, Y. I., ZOCCAL, D. B., MORAES, D. J., PATON, J. F., MACHADO, B. H. & RYBAK, I. A. 2011. Intermittent hypoxia-induced sensitization of central chemoreceptors contributes to sympathetic nerve activity during late expiration in rats. *J Neurophysiol,* 105**,** 3080-91.

MONNIER, A., ALHEID, G. F. & MCCRIMMON, D. R. 2003. Defining ventral medullary respiratory compartments with a glutamate receptor agonist in the rat. *J Physiol,* 548**,** 859-74.

MONTANDON, G., QIN, W., LIU, H., REN, J., GREER, J. J. & HORNER, R. L. 2011. PreBotzinger complex neurokinin-1 receptor-expressing neurons mediate opioid-induced respiratory depression. *J Neurosci,* 31**,** 1292-301.

MORAES, D. A., ABDALA, A. P., MACHADO, B. H. & PATON, J. F. 2014a. Functional connectivity between Bötzinger complex glycinergic neurons and parafacial late-expiratory neurons for expiratory and sympathetic control (712.17). *The FASEB Journal,* 28.

MORAES, D. J., DA SILVA, M. P., BONAGAMBA, L. G., MECAWI, A. S., ZOCCAL, D. B., ANTUNES-RODRIGUES, J., VARANDA, W. A. & MACHADO, B. H. 2013. Electrophysiological properties of rostral ventrolateral medulla presympathetic neurons modulated by the respiratory network in rats. *J Neurosci,* 33**,** 19223-37.

MORAES, D. J., DIAS, M. B., CAVALCANTI-KWIATKOSKI, R., MACHADO, B. H. & ZOCCAL, D. B. 2012a. Contribution of the retrotrapezoid nucleus/parafacial respiratory region to the expiratory-sympathetic coupling in response to peripheral chemoreflex in rats. *J Neurophysiol,* 108**,** 882-90.

MORAES, D. J. & MACHADO, B. H. 2015. Electrophysiological properties of laryngeal motoneurones in rats submitted to chronic intermittent hypoxia. *J Physiol,* 593**,** 619-34.

MORAES, D. J., MACHADO, B. H. & PATON, J. F. 2014b. Specific respiratory neuron types have increased excitability that drive presympathetic neurones in neurogenic hypertension. *Hypertension,* 63**,** 1309-18.

MORAES, D. J., ZOCCAL, D. B. & MACHADO, B. H. 2012b. Medullary respiratory network drives sympathetic overactivity and hypertension in rats submitted to chronic intermittent hypoxia. *Hypertension,* 60**,** 1374-80.

MORAES, D. J. A., BONAGAMBA, L. G. H., DA SILVA, M. P., PATON, J. F. R. & MACHADO, B. H. 2017. Role of ventral medullary catecholaminergic neurons for respiratory modulation of sympathetic outflow in rats. *Sci Rep,* 7**,** 16883.

MORGADO-VALLE, C., BACA, S. M. & FELDMAN, J. L. 2010. Glycinergic pacemaker neurons in preBotzinger complex of neonatal mouse. *J Neurosci,* 30**,** 3634-9.

MULKEY, D. K., STORNETTA, R. L., WESTON, M. C., SIMMONS, J. R., PARKER, A., BAYLISS, D. A. & GUYENET, P. G. 2004. Respiratory control by ventral surface chemoreceptor neurons in rats. *Nat Neurosci,* 7**,** 1360-9.

MULLEN, R. J., BUCK, C. R. & SMITH, A. M. 1992. NeuN, a neuronal specific nuclear protein in vertebrates. *Development,* 116**,** 201-11.

NAGARAJAN, R. P., PATZEL, K. A., MARTIN, M., YASUI, D. H., SWANBERG, S. E., HERTZ-PICCIOTTO, I., HANSEN, R. L., VAN DE WATER, J., PESSAH, I. N., JIANG, R., ROBINSON, W. P. & LASALLE, J. M. 2008. MECP2 promoter methylation and X chromosome inactivation in autism. *Autism Res,* 1**,** 169-78.

NEWMAN-TANCREDI, A., MARTEL, J. C., ASSIE, M. B., BURITOVA, J., LAURESSERGUES, E., COSI, C., HEUSLER, P., BRUINS SLOT, L., COLPAERT, F. C., VACHER, B. & CUSSAC, D. 2009. Signal transduction and functional selectivity of F15599, a preferential post-synaptic 5-HT1A receptor agonist. *Br J Pharmacol,* 156**,** 338-53.

OERTEL, B. G., SCHNEIDER, A., ROHRBACHER, M., SCHMIDT, H., TEGEDER, I., GEISSLINGER, G. & LOTSCH, J. 2007. The partial 5-hydroxytryptamine1A receptor agonist buspirone does not antagonize morphine-induced respiratory depression in humans. *Clin Pharmacol Ther,* 81**,** 59-68.

OKATY, B. W., FRERET, M. E., ROOD, B. D., BRUST, R. D., HENNESSY, M. L., DEBAIROS, D., KIM, J. C., COOK, M. N. & DYMECKI, S. M. 2015. Multi-Scale Molecular Deconstruction of the Serotonin Neuron System. *Neuron,* 88**,** 774-91.

ONIMARU, H., IKEDA, K. & KAWAKAMI, K. 2008. CO2-sensitive preinspiratory neurons of the parafacial respiratory group express Phox2b in the neonatal rat. *J Neurosci,* 28**,** 12845-50.

ONIMARU, H., IKEDA, K., MARIHO, T. & KAWAKAMI, K. 2014. Cytoarchitecture and CO(2) sensitivity of Phox2b-positive Parafacial neurons in the newborn rat medulla. *Prog Brain Res,* 209**,** 57-71.

PAGLIARDINI, S., JANCZEWSKI, W. A., TAN, W., DICKSON, C. T., DEISSEROTH, K. & FELDMAN, J. L. 2011. Active expiration induced by excitation of ventral medulla in adult anesthetized rats. *J Neurosci,* 31**,** 2895-905.

PATON, J. F. 1996a. The ventral medullary respiratory network of the mature mouse studied in a working heart-brainstem preparation. *J Physiol,* 493 ( Pt 3)**,** 819-31.

PATON, J. F. 1996b. A working heart-brainstem preparation of the mouse. *J Neurosci Methods,* 65**,** 63-8.

PAXINOS, G. & WATSON, C. 2007. *The Rat Brain In Sterotaxic Coordinates,* London, UK, Elsevier.

PERCY, A. K. 2016. Progress in Rett Syndrome: from discovery to clinical trials. *Wien Med Wochenschr,* 166**,** 325-32.

PHILLIPS, R. S., JOHN, T. T., KOIZUMI, H., MOLKOV, Y. I. & SMITH, J. C. 2019. Biophysical mechanisms in the mammalian respiratory oscillator re-examined with a new data-driven computational model. *Elife,* 8.

PIERREFICHE, O., SCHWARZACHER, S. W., BISCHOFF, A. M. & RICHTER, D. W. 1998. Blockade of synaptic inhibition within the pre-Botzinger complex in the cat suppresses respiratory rhythm generation in vivo. *J Physiol,* 509 ( Pt 1)**,** 245-54.

PIPER, M. & HOLT, C. 2004. RNA translation in axons. *Annu Rev Cell Dev Biol,* 20**,** 505-23.

POLTER, A. M. & LI, X. 2010. 5-HT1A receptor-regulated signal transduction pathways in brain. *Cell Signal,* 22**,** 1406-12.

PRABHAKAR, N. R., PENG, Y. J., YUAN, G. & KUMAR, G. K. 2006. Reactive oxygen species facilitate oxygen sensing. *Novartis Found Symp,* 272**,** 95-9; discussion 100-5, 131-40.

PTAK, K., YAMANISHI, T., AUNGST, J., MILESCU, L. S., ZHANG, R., RICHERSON, G. B. & SMITH, J. C. 2009. Raphe neurons stimulate respiratory circuit activity by multiple mechanisms via endogenously released serotonin and substance P. *J Neurosci,* 29**,** 3720-37.

RADOCAJ, T., MUSTAPIC, S., PRKIC, I., STUCKE, A. G., HOPP, F. A., STUTH, E. A. & ZUPERKU, E. J. 2015. Activation of 5-HT1A receptors in the preBotzinger region has little impact on the respiratory pattern. *Respir Physiol Neurobiol,* 212-214**,** 9-19.

RAKOCZY, R. J. & WYATT, C. N. 2018. Acute oxygen sensing by the carotid body: a rattlebag of molecular mechanisms. *J Physiol,* 596**,** 2969-2976.

RAMANANTSOA, N., HIRSCH, M. R., THOBY-BRISSON, M., DUBREUIL, V., BOUVIER, J., RUFFAULT, P. L., MATROT, B., FORTIN, G., BRUNET, J. F., GALLEGO, J. & GORIDIS, C. 2011. Breathing without CO(2) chemosensitivity in conditional Phox2b mutants. *J Neurosci,* 31**,** 12880-8.

RAMIREZ, J. M. & BAERTSCH, N. 2018a. Defining the Rhythmogenic Elements of Mammalian Breathing. *Physiology (Bethesda),* 33**,** 302-316.

RAMIREZ, J. M. & BAERTSCH, N. A. 2018b. The Dynamic Basis of Respiratory Rhythm Generation: One Breath at a Time. *Annu Rev Neurosci,* 41**,** 475-499.

RAMIREZ, J. M., WARD, C. S. & NEUL, J. L. 2013. Breathing challenges in Rett syndrome: lessons learned from humans and animal models. *Respir Physiol Neurobiol,* 189**,** 280-7.

RASMUSSEN, M., KONG, L., ZHANG, G. R., LIU, M., WANG, X., SZABO, G., CURTHOYS, N. P. & GELLER, A. I. 2007. Glutamatergic or GABAergic neuron-specific, long-term expression in neocortical neurons from helper virus-free HSV-1 vectors containing the phosphate-activated glutaminase, vesicular glutamate transporter-1, or glutamic acid decarboxylase promoter. *Brain Res,* 1144**,** 19-32.

RAY, R. S., CORCORAN, A. E., BRUST, R. D., KIM, J. C., RICHERSON, G. B., NATTIE, E. & DYMECKI, S. M. 2011. Impaired respiratory and body temperature control upon acute serotonergic neuron inhibition. *Science,* 333**,** 637-42.

REN, J., DING, X. & GREER, J. J. 2015. 5-HT1A receptor agonist Befiradol reduces fentanyl-induced respiratory depression, analgesia, and sedation in rats. *Anesthesiology,* 122**,** 424-34.

RICHTER, D. W. 1982. Generation and maintenance of the respiratory rhythm. *J Exp Biol,* 100**,** 93-107.

RICHTER, D. W., BISCHOFF, A., ANDERS, K., BELLINGHAM, M. & WINDHORST, U. 1991. Response of the medullary respiratory network of the cat to hypoxia. *J Physiol,* 443**,** 231-56.

RICHTER, D. W., LALLEY, P. M., PIERREFICHE, O., HAJI, A., BISCHOFF, A. M., WILKEN, B. & HANEFELD, F. 1997. Intracellular signal pathways controlling respiratory neurons. *Respir Physiol,* 110**,** 113-23.

RICHTER, D. W., MANZKE, T., WILKEN, B. & PONIMASKIN, E. 2003. Serotonin receptors: guardians of stable breathing. *Trends Mol Med,* 9**,** 542-8.

RICHTER, D. W. & SMITH, J. C. 2014. Respiratory rhythm generation in vivo. *Physiology (Bethesda),* 29**,** 58-71.

ROSIN, D. L., CHANG, D. A. & GUYENET, P. G. 2006. Afferent and efferent connections of the rat retrotrapezoid nucleus. *J Comp Neurol,* 499**,** 64-89.

ROSS, C. A., RUGGIERO, D. A., PARK, D. H., JOH, T. H., SVED, A. F., FERNANDEZ-PARDAL, J., SAAVEDRA, J. M. & REIS, D. J. 1984. Tonic vasomotor control by the rostral ventrolateral medulla: effect of electrical or chemical stimulation of the area containing C1 adrenaline neurons on arterial pressure, heart rate, and plasma catecholamines and vasopressin. *J Neurosci,* 4**,** 474-94.

RUBIN, J. E., SHEVTSOVA, N. A., ERMENTROUT, G. B., SMITH, J. C. & RYBAK, I. A. 2009. Multiple rhythmic states in a model of the respiratory central pattern generator. *J Neurophysiol,* 101**,** 2146-65.

RYBAK, I. A., ABDALA, A. P., MARKIN, S. N., PATON, J. F. & SMITH, J. C. 2007. Spatial organization and state-dependent mechanisms for respiratory rhythm and pattern generation. *Prog Brain Res,* 165**,** 201-20.

RYBAK, I. A., SHEVTSOVA, N. A., PATON, J. F., DICK, T. E., ST-JOHN, W. M., MORSCHEL, M. & DUTSCHMANN, M. 2004. Modeling the ponto-medullary respiratory network. *Respir Physiol Neurobiol,* 143**,** 307-19.

SAETHER, K., HILAIRE, G. & MONTEAU, R. 1987. Dorsal and ventral respiratory groups of neurons in the medulla of the rat. *Brain Res,* 419**,** 87-96.

SAHU, A., GOPALAKRISHNAN, L., GAUR, N., CHATTERJEE, O., MOL, P., MODI, P. K., DAGAMAJALU, S., ADVANI, J., JAIN, S. & KESHAVA PRASAD, T. S. 2018. The 5-Hydroxytryptamine signaling map: an overview of serotonin-serotonin receptor mediated signaling network. *J Cell Commun Signal,* 12**,** 731-735.

SAMACO, R. C., MANDEL-BREHM, C., CHAO, H. T., WARD, C. S., FYFFE-MARICICH, S. L., REN, J., HYLAND, K., THALLER, C., MARICICH, S. M., HUMPHREYS, P., GREER, J. J., PERCY, A., GLAZE, D. G., ZOGHBI, H. Y. & NEUL, J. L. 2009. Loss of MeCP2 in aminergic neurons causes cell-autonomous defects in neurotransmitter synthesis and specific behavioral abnormalities. *Proc Natl Acad Sci U S A,* 106**,** 21966-71.

SAMACO, R. C., MCGRAW, C. M., WARD, C. S., SUN, Y., NEUL, J. L. & ZOGHBI, H. Y. 2013. Female Mecp2(+/-) mice display robust behavioral deficits on two different genetic backgrounds providing a framework for pre-clinical studies. *Hum Mol Genet,* 22**,** 96-109.

SCHMID, D. A., YANG, T., OGIER, M., ADAMS, I., MIRAKHUR, Y., WANG, Q., MASSA, S. M., LONGO, F. M. & KATZ, D. M. 2012. A TrkB small molecule partial agonist rescues TrkB phosphorylation deficits and improves respiratory function in a mouse model of Rett syndrome. *J Neurosci,* 32**,** 1803-10.

SCHMID, K., BOHMER, G. & GEBAUER, K. 1991. Glycine receptor-mediated fast synaptic inhibition in the brainstem respiratory system. *Respir Physiol,* 84**,** 351-61.

SCHREIHOFER, A. M. & GUYENET, P. G. 1997. Identification of C1 presympathetic neurons in rat rostral ventrolateral medulla by juxtacellular labeling in vivo. *J Comp Neurol,* 387**,** 524-36.

SCHREIHOFER, A. M. & GUYENET, P. G. 2002. The baroreflex and beyond: control of sympathetic vasomotor tone by GABAergic neurons in the ventrolateral medulla. *Clin Exp Pharmacol Physiol,* 29**,** 514-21.

SCHREIHOFER, A. M. & GUYENET, P. G. 2003. Baro-activated neurons with pulse-modulated activity in the rat caudal ventrolateral medulla express GAD67 mRNA. *J Neurophysiol,* 89**,** 1265-77.

SCHREIHOFER, A. M., STORNETTA, R. L. & GUYENET, P. G. 1999. Evidence for glycinergic respiratory neurons: Botzinger neurons express mRNA for glycinergic transporter 2. *J Comp Neurol,* 407**,** 583-97.

SCHREIHOFER, A. M., STORNETTA, R. L. & GUYENET, P. G. 2000. Regulation of sympathetic tone and arterial pressure by rostral ventrolateral medulla after depletion of C1 cells in rat. *J Physiol,* 529 Pt 1**,** 221-36.

SCHWARZACHER, S. W., WILHELM, Z., ANDERS, K. & RICHTER, D. W. 1991. The medullary respiratory network in the rat. *J Physiol,* 435**,** 631-44.

SEGERS, L. S., NUDING, S. C., DICK, T. E., SHANNON, R., BAEKEY, D. M., SOLOMON, I. C., MORRIS, K. F. & LINDSEY, B. G. 2008. Functional connectivity in the pontomedullary respiratory network. *J Neurophysiol,* 100**,** 1749-69.

SHERMAN, D., WORRELL, J. W., CUI, Y. & FELDMAN, J. L. 2015. Optogenetic perturbation of preBotzinger complex inhibitory neurons modulates respiratory pattern. *Nat Neurosci,* 18**,** 408-14.

SHEVTSOVA, N. A., BUSSELBERG, D., MOLKOV, Y. I., BISCHOFF, A. M., SMITH, J. C., RICHTER, D. W. & RYBAK, I. A. 2014. Effects of glycinergic inhibition failure on respiratory rhythm and pattern generation. *Prog Brain Res,* 209**,** 25-38.

SHEVTSOVA, N. A., MANZKE, T., MOLKOV, Y. I., BISCHOFF, A., SMITH, J. C., RYBAK, I. A. & RICHTER, D. W. 2011. Computational modelling of 5-HT receptor-mediated reorganization of the brainstem respiratory network. *Eur J Neurosci,* 34**,** 1276-91.

SHI, Y., STORNETTA, R. L., STORNETTA, D. S., ONENGUT-GUMUSCU, S., FARBER, E. A., TURNER, S. D., GUYENET, P. G. & BAYLISS, D. A. 2017. Neuromedin B Expression Defines the Mouse Retrotrapezoid Nucleus. *J Neurosci,* 37**,** 11744-11757.

SILVA, J. D. N., OLIVEIRA, L. M., SOUZA, F. C., MOREIRA, T. S. & TAKAKURA, A. C. 2020. GABAergic neurons of the medullary raphe regulate active expiration during hypercapnia. *J Neurophysiol,* 123**,** 1933-1943.

SILVA, J. N., OLIVEIRA, L. M., SOUZA, F. C., MOREIRA, T. S. & TAKAKURA, A. C. 2019. Distinct pathways to the parafacial respiratory group to trigger active expiration in adult rats. *Am J Physiol Lung Cell Mol Physiol,* 317**,** L402-L413.

SILVA, J. N., TANABE, F. M., MOREIRA, T. S. & TAKAKURA, A. C. 2016. Neuroanatomical and physiological evidence that the retrotrapezoid nucleus/parafacial region regulates expiration in adult rats. *Respir Physiol Neurobiol,* 227**,** 9-22.

SIMMS, A. E., PATON, J. F., PICKERING, A. E. & ALLEN, A. M. 2009. Amplified respiratory-sympathetic coupling in the spontaneously hypertensive rat: does it contribute to hypertension? *J Physiol,* 587**,** 597-610.

SMEETS, E. E., JULU, P. O., VAN WAARDENBURG, D., ENGERSTROM, I. W., HANSEN, S., APARTOPOULOS, F., CURFS, L. M. & SCHRANDER-STUMPEL, C. T. 2006. Management of a severe forceful breather with Rett syndrome using carbogen. *Brain Dev,* 28**,** 625-32.

SMITH, J. C., ABDALA, A. P., BORGMANN, A., RYBAK, I. A. & PATON, J. F. 2013. Brainstem respiratory networks: building blocks and microcircuits. *Trends Neurosci,* 36**,** 152-62.

SMITH, J. C., ABDALA, A. P., KOIZUMI, H., RYBAK, I. A. & PATON, J. F. 2007. Spatial and functional architecture of the mammalian brain stem respiratory network: a hierarchy of three oscillatory mechanisms. *J Neurophysiol,* 98**,** 3370-87.

SMITH, J. C., ABDALA, A. P., RYBAK, I. A. & PATON, J. F. 2009. Structural and functional architecture of respiratory networks in the mammalian brainstem. *Philos Trans R Soc Lond B Biol Sci,* 364**,** 2577-87.

SMITH, J. C., ELLENBERGER, H. H., BALLANYI, K., RICHTER, D. W. & FELDMAN, J. L. 1991. Pre-Botzinger complex: a brainstem region that may generate respiratory rhythm in mammals. *Science,* 254**,** 726-9.

SNIECIKOWSKA, J., GLUCH-LUTWIN, M., BUCKI, A., WIECKOWSKA, A., SIWEK, A., JASTRZEBSKA-WIESEK, M., PARTYKA, A., WILCZYNSKA, D., PYTKA, K., POCIECHA, K., CIOS, A., WYSKA, E., WESOLOWSKA, A., PAWLOWSKI, M., VARNEY, M. A., NEWMAN-TANCREDI, A. & KOLACZKOWSKI, M. 2019a. Novel Aryloxyethyl Derivatives of 1-(1-Benzoylpiperidin-4-yl)methanamine as the Extracellular Regulated Kinases 1/2 (ERK1/2) Phosphorylation-Preferring Serotonin 5-HT1A Receptor-Biased Agonists with Robust Antidepressant-like Activity. *J Med Chem,* 62**,** 2750-2771.

SNIECIKOWSKA, J., NEWMAN-TANCREDI, A. & KOLACZKOWSKI, M. 2019b. From Receptor Selectivity to Functional Selectivity: The Rise of Biased Agonism in 5-HT1A Receptor Drug Discovery. *Curr Top Med Chem,* 19**,** 2393-2420.

SONG, G. & POON, C. S. 2009. Lateral parabrachial nucleus mediates shortening of expiration during hypoxia. *Respir Physiol Neurobiol,* 165**,** 1-8.

SONG, G., TIN, C. & POON, C. S. 2015. Multiscale fingerprinting of neuronal functional connectivity. *Brain Struct Funct,* 220**,** 2967-82.

SONG, G., XU, H., WANG, H., MACDONALD, S. M. & POON, C. S. 2011. Hypoxia-excited neurons in NTS send axonal projections to Kolliker-Fuse/parabrachial complex in dorsolateral pons. *Neuroscience,* 175**,** 145-53.

SOTELO, C., CHOLLEY, B., EL MESTIKAWY, S., GOZLAN, H. & HAMON, M. 1990. Direct Immunohistochemical Evidence of the Existence of 5-HT1A Autoreceptors on Serotoninergic Neurons in the Midbrain Raphe Nuclei. *Eur J Neurosci,* 2**,** 1144-1154.

SOUTHALL, D. P., KERR, A. M., TIROSH, E., AMOS, P., LANG, M. H. & STEPHENSON, J. B. 1988. Hyperventilation in the awake state: potentially treatable component of Rett syndrome. *Arch Dis Child,* 63**,** 1039-48.

SOUZA, G., KANBAR, R., STORNETTA, D. S., ABBOTT, S. B. G., STORNETTA, R. L. & GUYENET, P. G. 2018. Breathing regulation and blood gas homeostasis after near complete lesions of the retrotrapezoid nucleus in adult rats. *J Physiol,* 596**,** 2521-2545.

STETTNER, G. M., HUPPKE, P., BRENDEL, C., RICHTER, D. W., GARTNER, J. & DUTSCHMANN, M. 2007. Breathing dysfunctions associated with impaired control of postinspiratory activity in Mecp2-/y knockout mice. *J Physiol,* 579**,** 863-76.

STORNETTA, R. L. 2009. Neurochemistry of bulbospinal presympathetic neurons of the medulla oblongata. *J Chem Neuroanat,* 38**,** 222-30.

STORNETTA, R. L. & GUYENET, P. G. 1999. Distribution of glutamic acid decarboxylase mRNA-containing neurons in rat medulla projecting to thoracic spinal cord in relation to monoaminergic brainstem neurons. *J Comp Neurol,* 407**,** 367-80.

STORNETTA, R. L., INGLIS, M. A., VIAR, K. E. & GUYENET, P. G. 2016. Afferent and efferent connections of C1 cells with spinal cord or hypothalamic projections in mice. *Brain Struct Funct,* 221**,** 4027-4044.

STORNETTA, R. L., SEVIGNY, C. P. & GUYENET, P. G. 2002a. Vesicular glutamate transporter DNPI/VGLUT2 mRNA is present in C1 and several other groups of brainstem catecholaminergic neurons. *J Comp Neurol,* 444**,** 191-206.

STORNETTA, R. L., SEVIGNY, C. P., SCHREIHOFER, A. M., ROSIN, D. L. & GUYENET, P. G. 2002b. Vesicular glutamate transporter DNPI/VGLUT2 is expressed by both C1 adrenergic and nonaminergic presympathetic vasomotor neurons of the rat medulla. *J Comp Neurol,* 444**,** 207-20.

STOTT, L. A., HALL, D. A. & HOLLIDAY, N. D. 2016. Unravelling intrinsic efficacy and ligand bias at G protein coupled receptors: A practical guide to assessing functional data. *Biochem Pharmacol,* 101**,** 1-12.

SUN, Q. J., GOODCHILD, A. K., CHALMERS, J. P. & PILOWSKY, P. M. 1998. The pre-Botzinger complex and phase-spanning neurons in the adult rat. *Brain Res,* 809**,** 204-13.

SUN, Q. J., MINSON, J., LLEWELLYN-SMITH, I. J., ARNOLDA, L., CHALMERS, J. & PILOWSKY, P. 1997. Botzinger neurons project towards bulbospinal neurons in the rostral ventrolateral medulla of the rat. *J Comp Neurol,* 388**,** 23-31.

SZEREDA-PRZESTASZEWSKA, M. & KACZYNSKA, K. 2007. Peripheral 5-HT1A receptors are not essential for increased ventilation evoked by systemic 8-OH-DPAT challenge in anaesthetized rats. *Exp Physiol,* 92**,** 953-61.

TAKAKURA, A. C., MOREIRA, T. S., COLOMBARI, E., WEST, G. H., STORNETTA, R. L. & GUYENET, P. G. 2006. Peripheral chemoreceptor inputs to retrotrapezoid nucleus (RTN) CO2-sensitive neurons in rats. *J Physiol,* 572**,** 503-23.

TAN, E. M., YAMAGUCHI, Y., HORWITZ, G. D., GOSGNACH, S., LEIN, E. S., GOULDING, M., ALBRIGHT, T. D. & CALLAWAY, E. M. 2006. Selective and quickly reversible inactivation of mammalian neurons in vivo using the Drosophila allatostatin receptor. *Neuron,* 51**,** 157-70.

TAN, Z. Y., LU, Y., WHITEIS, C. A., SIMMS, A. E., PATON, J. F., CHAPLEAU, M. W. & ABBOUD, F. M. 2010. Chemoreceptor hypersensitivity, sympathetic excitation, and overexpression of ASIC and TASK channels before the onset of hypertension in SHR. *Circ Res,* 106**,** 536-45.

TANAKA, I., EZURE, K. & KONDO, M. 2003. Distribution of glycine transporter 2 mRNA-containing neurons in relation to glutamic acid decarboxylase mRNA-containing neurons in rat medulla. *Neurosci Res,* 47**,** 139-51.

TAUGHER, R. J., LU, Y., WANG, Y., KREPLE, C. J., GHOBBEH, A., FAN, R., SOWERS, L. P. & WEMMIE, J. A. 2014. The bed nucleus of the stria terminalis is critical for anxiety-related behavior evoked by CO2 and acidosis. *J Neurosci,* 34**,** 10247-55.

TAXINI, C. L., MOREIRA, T. S., TAKAKURA, A. C., BICEGO, K. C., GARGAGLIONI, L. H. & ZOCCAL, D. B. 2017. Role of A5 noradrenergic neurons in the chemoreflex

control of respiratory and sympathetic activities in unanesthetized conditions. *Neuroscience,* 354**,** 146-157.

TEPPEMA, L. J. & DAHAN, A. 2010. The ventilatory response to hypoxia in mammals: mechanisms, measurement, and analysis. *Physiol Rev,* 90**,** 675-754.

TIAN, G. F., PEEVER, J. H. & DUFFIN, J. 1999. Mutual inhibition between Botzinger-complex bulbospinal expiratory neurons detected with cross-correlation in the decerebrate rat. *Exp Brain Res,* 125**,** 440-6.

TOPORIKOVA, N. & BUTERA, R. J. 2011. Two types of independent bursting mechanisms in inspiratory neurons: an integrative model. *J Comput Neurosci,* 30**,** 515-28.

TOWARD, M. A., ABDALA, A. P., KNOPP, S. J., PATON, J. F. & BISSONNETTE, J. M. 2013. Increasing brain serotonin corrects CO2 chemosensitivity in methyl-CpG-binding protein 2 (Mecp2)-deficient mice. *Exp Physiol,* 98**,** 842-9.

VALIC, M., PECOTIC, R. & DOGAS, Z. 2008. Phrenic nerve activity is enhanced by 5-HT1A receptor agonist 8-OH-DPAT in spontaneously breathing anesthetized rats. *J Physiol Pharmacol,* 59**,** 17-25.

VALLBO, A. B., HAGBARTH, K. E. & WALLIN, B. G. 2004. Microneurography: how the technique developed and its role in the investigation of the sympathetic nervous system. *J Appl Physiol (1985),* 96**,** 1262-9.

VANTREASE, J. E., DUDEK, N., DONCARLOS, L. L. & SCROGIN, K. E. 2015. 5-HT1A receptors of the nucleus tractus solitarii facilitate sympathetic recovery following hypotensive hemorrhage in rats. *Am J Physiol Heart Circ Physiol,* 309**,** H335-44.

VARGA, A. G., REID, B. T., KIEFFER, B. L. & LEVITT, E. S. 2020. Differential impact of two critical respiratory centres in opioid-induced respiratory depression in awake mice. *J Physiol,* 598**,** 189-205.

VICARIO, I., RIGUAL, R., OBESO, A. & GONZALEZ, C. 2000. Characterization of the synthesis and release of catecholamine in the rat carotid body in vitro. *Am J Physiol Cell Physiol,* 278**,** C490-9.

VIDAL, B., BOLBOS, R., REDOUTE, J., LANGLOIS, J. B., COSTES, N., NEWMAN-TANCREDI, A. & ZIMMER, L. 2020. Pharmacological MRI to investigate the functional selectivity of 5-HT1A receptor biased agonists. *Neuropharmacology,* 172**,** 107867.

VIDAL, B., FIEUX, S., REDOUTE, J., VILLIEN, M., BONNEFOI, F., LE BARS, D., NEWMAN-TANCREDI, A., COSTES, N. & ZIMMER, L. 2018. In vivo biased agonism at 5-HT1A receptors: characterisation by simultaneous PET/MR imaging. *Neuropsychopharmacology,* 43**,** 2310-2319.

VIEMARI, J. C., ROUX, J. C., TRYBA, A. K., SAYWELL, V., BURNET, H., PENA, F., ZANELLA, S., BEVENGUT, M., BARTHELEMY-REQUIN, M., HERZING, L. B., MONCLA, A., MANCINI, J., RAMIREZ, J. M., VILLARD, L. & HILAIRE, G. 2005. Mecp2 deficiency disrupts norepinephrine and respiratory systems in mice. *J Neurosci,* 25**,** 11521-30.

WANG, F., FLANAGAN, J., SU, N., WANG, L. C., BUI, S., NIELSON, A., WU, X., VO, H. T., MA, X. J. & LUO, Y. 2012. RNAscope: a novel in situ RNA analysis platform for formalin-fixed, paraffin-embedded tissues. *J Mol Diagn,* 14**,** 22-9.

WANG, S., BENAMER, N., ZANELLA, S., KUMAR, N. N., SHI, Y., BEVENGUT, M., PENTON, D., GUYENET, P. G., LESAGE, F., GESTREAU, C., BARHANIN, J. & BAYLISS, D. A. 2013. TASK-2 channels contribute to pH sensitivity of retrotrapezoid nucleus chemoreceptor neurons. *J Neurosci,* 33**,** 16033-44.

WATTS, S. W., MORRISON, S. F., DAVIS, R. P. & BARMAN, S. M. 2012. Serotonin and blood pressure regulation. *Pharmacol Rev,* 64**,** 359-88.

WEESE-MAYER, D. E., LIESKE, S. P., BOOTHBY, C. M., KENNY, A. S., BENNETT, H. L., SILVESTRI, J. M. & RAMIREZ, J. M. 2006. Autonomic nervous system dysregulation: breathing and heart rate perturbation during wakefulness in young girls with Rett syndrome. *Pediatr Res,* 60**,** 443-9.

WENKER, I. C., ABE, C., VIAR, K. E., STORNETTA, D. S., STORNETTA, R. L. & GUYENET, P. G. 2017. Blood Pressure Regulation by the Rostral Ventrolateral Medulla in Conscious Rats: Effects of Hypoxia, Hypercapnia, Baroreceptor Denervation, and Anesthesia. *J Neurosci,* 37**,** 4565-4583.

WENKER, I. C., KRENEISZ, O., NISHIYAMA, A. & MULKEY, D. K. 2010. Astrocytes in the retrotrapezoid nucleus sense H+ by inhibition of a Kir4.1-Kir5.1-like current and may contribute to chemoreception by a purinergic mechanism. *J Neurophysiol,* 104**,** 3042-52.

WILLETTE, R. N., BARCAS, P. P., KRIEGER, A. J. & SAPRU, H. N. 1983. Vasopressor and depressor areas in the rat medulla. Identification by microinjection of L-glutamate. *Neuropharmacology,* 22**,** 1071-9.

WINTER, S. M., FRESEMANN, J., SCHNELL, C., OKU, Y., HIRRLINGER, J. & HULSMANN, S. 2009. Glycinergic interneurons are functionally integrated into the inspiratory network of mouse medullary slices. *Pflugers Arch,* 458**,** 459-69.

WITTMAN, S., ABDALA, A. P. & RUBIN, J. E. 2019. Reduced computational modeling of Kolliker-Fuse contributions to breathing patterns in Rett syndrome. *J Physiol*.

WOLF, H. K., BUSLEI, R., SCHMIDT-KASTNER, R., SCHMIDT-KASTNER, P. K., PIETSCH, T., WIESTLER, O. D. & BLUMCKE, I. 1996. NeuN: a useful neuronal marker for diagnostic histopathology. *J Histochem Cytochem,* 44**,** 1167-71.

YANG, C. F., KIM, E. J., CALLAWAY, E. M. & FELDMAN, J. L. 2020. Monosynaptic Projections to Excitatory and Inhibitory preBotzinger Complex Neurons. *Front Neuroanat,* 14**,** 58.

YANG, S. J., LEE, K. Z., WU, C. H., LU, K. T. & HWANG, J. C. 2006. Vasopressin produces inhibition on phrenic nerve activity and apnea through V(1A) receptors in the area postrema in rats. *Chin J Physiol,* 49**,** 313-25.

YOKOTA, S., TSUMORI, T., OKA, T., NAKAMURA, S. & YASUI, Y. 2008. GABAergic neurons in the ventrolateral subnucleus of the nucleus tractus solitarius are in contact with Kolliker-Fuse nucleus neurons projecting to the rostral ventral respiratory group and phrenic nucleus in the rat. *Brain Res,* 1228**,** 113-26.

YOKOYAMA, T., NAKAMUTA, N., KUSAKABE, T. & YAMAMOTO, Y. 2015. Serotonin-mediated modulation of hypoxia-induced intracellular calcium responses in glomus cells isolated from rat carotid body. *Neurosci Lett,* 597**,** 149-53.

YOUNG, J. I., HONG, E. P., CASTLE, J. C., CRESPO-BARRETO, J., BOWMAN, A. B., ROSE, M. F., KANG, D., RICHMAN, R., JOHNSON, J. M., BERGET, S. & ZOGHBI, H. Y. 2005. Regulation of RNA splicing by the methylation-dependent transcriptional repressor methyl-CpG binding protein 2. *Proc Natl Acad Sci U S A,* 102**,** 17551-8.

ZERA, T., MORAES, D. J. A., DA SILVA, M. P., FISHER, J. P. & PATON, J. F. R. 2019. The Logic of Carotid Body Connectivity to the Brain. *Physiology (Bethesda),* 34**,** 264-282.

ZHANG, G. R., LI, X., CAO, H., ZHAO, H. & GELLER, A. I. 2011a. The vesicular glutamate transporter-1 upstream promoter and first intron each support glutamatergic-specific expression in rat postrhinal cortex. *Brain Res,* 1377**,** 1-12.

ZHANG, X., SU, J., CUI, N., GAI, H., WU, Z. & JIANG, C. 2011b. The disruption of central CO2 chemosensitivity in a mouse model of Rett syndrome. *Am J Physiol Cell Physiol,* 301**,** C729-38.

ZHANG, Y. Q., GAO, X., HUANG, Y. L. & WU, G. C. 2000. Expression of 5-HT1A receptor mRNA in rat dorsal raphe nucleus and ventrolateral periaqueductal gray neurons after peripheral inflammation. *Neuroreport,* 11**,** 3361-5.

ZHAO, Z. Q., SCOTT, M., CHIECHIO, S., WANG, J. S., RENNER, K. J., GEREAU, R. W. T., JOHNSON, R. L., DENERIS, E. S. & CHEN, Z. F. 2006. Lmx1b is required for maintenance of central serotonergic neurons and mice lacking central serotonergic system exhibit normal locomotor activity. *J Neurosci,* 26**,** 12781-8.

ZHENG, Y., BARILLOT, J. C. & BIANCHI, A. L. 1991. Patterns of membrane potentials and distributions of the medullary respiratory neurons in the decerebrate rat. *Brain Res,* 546**,** 261-70.

ZOCCAL, D. B., BONAGAMBA, L. G., PATON, J. F. & MACHADO, B. H. 2009a. Sympathetic-mediated hypertension of awake juvenile rats submitted to chronic intermittent hypoxia is not linked to baroreflex dysfunction. *Exp Physiol,* 94**,** 972-83.

ZOCCAL, D. B., FURUYA, W. I., BASSI, M., COLOMBARI, D. S. & COLOMBARI, E. 2014. The nucleus of the solitary tract and the coordination of respiratory and sympathetic activities. *Front Physiol,* 5**,** 238.

ZOCCAL, D. B., PATON, J. F. & MACHADO, B. H. 2009b. Do changes in the coupling between respiratory and sympathetic activities contribute to neurogenic hypertension? *Clin Exp Pharmacol Physiol,* 36**,** 1188-96.

ZOCCAL, D. B., SILVA, J. N., BARNETT, W. H., LEMES, E. V., FALQUETTO, B., COLOMBARI, E., MOLKOV, Y. I., MOREIRA, T. S. & TAKAKURA, A. C. 2018. Interaction between the retrotrapezoid nucleus and the parafacial respiratory group to regulate active expiration and sympathetic activity in rats. *Am J Physiol Lung Cell Mol Physiol,* 315**,** L891-L909.

ZOCCAL, D. B., SIMMS, A. E., BONAGAMBA, L. G., BRAGA, V. A., PICKERING, A. E., PATON, J. F. & MACHADO, B. H. 2008. Increased sympathetic outflow in juvenile rats submitted to chronic intermittent hypoxia correlates with enhanced expiratory activity. *J Physiol,* 586**,** 3253-65.